SAPIENZA
UNIVERSITÀ DI ROMA

Dark Matter and Galactic Structures

EMJD

Dottorato di Ricerca in Fisica – 30 Ciclo

Candidate

Andreas Krut
ID number 1674166

Thesis Advisor

Remo Ruffini

Co-Advisor

Carlos R. Argüelles

A thesis submitted in partial fulfillment of the requirements
for the degree of Doctor of Philosophy in Physics

August 2018

Thesis defended on 05.10.2018
in front of a Board of Examiners composed by:

Volker Perlick (chairman)
Piero Rosati
Paolo Pani

Dark Matter and Galactic Structures
Ph.D. thesis. Sapienza – University of Rome

This thesis has been typeset by LaTeX and the Sapthesis class.

Version: October 19, 2018

Author's email: andreas.krut@icranet.org

Dedicated to
my family and friends

Abstract

The observational and theoretical analysis on different scales, ranging from galactic to cosmological, strongly indicates the necessity of dark matter in the Universe. Modern astrophysics therefore aims to reveal its nature, rather than its existence. Preferentially, it consist of particles beyond the standard model of particle physics.

In order to explain galactic structures without focusing on a particular particle candidate, a self-gravitating system, composed of massive fermions in spherical symmetry, is considered here. The finite mass distribution of such a component is obtained after solving the Einstein equation for a thermal and semi-degenerate fermionic gas, described by a perfect fluid in hydrostatic equilibrium and exposed to cutoff effects (e.g. evaporation). Within this more general approach a new family of density profiles arises which explains dark matter halo constraints of the Galaxy and provides at the same time an alternative to the central black hole scenario in SgrA*. This analysis narrows the allowed particle mass to $mc^2 \sim 48 - 345\,\mathrm{keV}$. It is bolstered by the successful application (for $mc^2 \sim 50\,\mathrm{keV}$) to different galaxy types from dwarfs to ellipticals, including disk galaxies from the SPARC data base.

The key result is that there is a continuous underlying dark matter distribution, covering the whole galactic extent. It governs the dynamics of the galactic center (e.g. nuclei) as well as the galactic halo. Based on the model predictions, it is clear that fermionic dark matter with particle masses in the keV regime is able to explain the relation between dark and baryonic components as well as dark components only. The radial acceleration correlation is reproduced here and represents the former group. Equally important is the natural outcome of the observationally confirmed link between a central dark object and its harboring dark matter halo. Interestingly, the very same dark matter distributions provide a satisfactory explanation for the constancy of the central dark matter surface density, valid for various galaxy types.

Contents

Preface

The history of Dark Matter (DM) dates back almost a century ago in the beginning of the 20th century. I start the thesis with a brief review about DM evidence on the different astrophysical and cosmological scales (see section 1.1). Each scale magnitude then is explained chronologically for a better understanding. It is followed by a summary of important galaxy parameter relation, covering baryonic as well as dark components (see section 1.2). Following the majority of the scientific community, then DM is necessary to explain those relations, including several phenomena. Therefore, a selected list of candidates, representing a historical relevance, is given in section 1.3. Additionally, apart from closing discrepancies between observations and theory (e.g. the nature of DM), of great interest is also the formation of structures in the Universe within the Big Bang context. The latter aims to reveal the origin of DM, see section 1.4. With the given background information I describe the objective of this thesis in section 1.5.

The key contribution to the question what is DM, is based here on a Fermionic Dark Matter (FDM) model including relativistic and evaporation effects. This model is introduced in chapter 2 and referred hereafter as the Ruffini-Argüelles-Rueda (RAR) model. It requires the Einstein solutions of a perfect fluid in thermal equilibrium (see section 2.1) and a lowered Fermi-Dirac phase space distribution function (see section 2.2). For a better understanding of the model, it is convenient to decompose the obtained mass distributions by limiting cases and other approximations, see section 2.3. I recommend to check this chapter to get used to the notation and symbols. Otherwise, see section 2.4 for a summary.

A more detailed analysis of the introduced dark matter model and especially the obtained mass distributions is provided in chapter 3. The strategy is to focus on the configuration parameters to give a better understanding of their role, see section 3.1. However, of more importance are probably physical parameters (e.g. mass, radius, density) which are considered very briefly in section 3.2. Though, the vast amount of possible physical parameters and in particular their combinations are too many to make a proper analysis. Therefore, only a few more relevant combination are shown with the aim to demonstrate the difference between configuration and physical parameters. Nevertheless, the whole chapter illustrates very well the rich configurations of the dark matter model. Only for low cutoff effects it is possible to reveal simple behavior of the mass distribution with respect to configuration parameter. Those trends are described by simple power laws which are derived also analytically for a better physical understanding, see section 3.3. A summary of the chapter is given in section 3.4.

The goal of the thesis is the application of the dark matter model to real galaxies from observations, see chapter 4. The starting point is the Milky Way because it provides the best resolved galaxy, covering a wide radial extent form the core to the halo (see section 4.1). This work clearly demonstrates that the RAR model with a cutoff is able to explain the whole radial extent of the Galaxy without spoiling the baryonic matter on intermediate scales. It is therefore natural to ask if the same model can describe other galaxy types. This question is successfully answered in section 4.2 with the application to typical dwarfs, spirals and ellipticals. The results

are bolstered in section 4.3 by fitting disk galaxies from the Spitzer Photometry & Accurate Rotation Curves (SPARC) data base. The key result is that there is an underlying DM distribution in galaxies, being able to explain dark-to-dark as well as reproduce dark-to-baryonic relations. This achievement provides a significant contribution to the nature of DM. A conclusion of this insight is given in section 4.4.

Finally, in chapter 5 I give a brief outlook about further possible applications of the RAR model to other specific galaxies (e.g. ultra-compact dwarfs). For instance, I emphasize indications to answer where the suspected, but currently missing, Intermediate Massive Black Holes (IMBHs) are populated. Although, this clearly will require more detailed investigations. On the higher mass range, the results suggest that the RAR model in combination with accretion physics may also well explain phenomena of Active Galactic Nuclei (AGN). An important task remains to answer the formation and evolution of galaxies in a cosmological setup, especially in combination with baryonic feedback effects.

Further helpful information are given in the following pages. A very brief appendix contains details about other DM models such as the Navarro-Frenk-White (NFW) model and a mass-dependent density profile for dark matter halos including the influence of galaxy formation. The latter is known as the DC14 model. Additionally, there I recall in short the exponential sphere and exponential disk models which are important for modeling baryonic structures (e.g. of Milky Way). After the appendix I summarize the most important abbreviations and symbols. These lists are complemented by the bibliography. Finally, the thesis I close with my acknowledgments.

DM studies from other approaches (not considered in this thesis)

The success of DM has elevated this concept to a remedy for several astronomical phenomena. From the long history numerous DM candidates and models have been suggested in order to alleviate discrepancies between observations and theory. During this process various methods and strategies have been developed to discriminate DM models, thanks to the rich creativity of the scientific community. While I will focus mainly on the rotation curve as the classical DM indicator, there are many other possible indications from gravitational lensing and dynamical friction. Regarding the latter approaches I will not go into details and to refer, for instance within the RAR model, to the work of Gómez and Rueda (2017) and Gómez et al. (2016) as well as references therein.

Logically speaking the flat rotation curve and other observed phenomenological structures, being in conflict with theory, belong to the class of DM indications (or hints). A parallel and important branch in the DM framework is the DM *detection*, direct and indirect. Note that the term *detection* within the DM framework is usually limited to the field of particle physics. For instance, the detection of particular extraterrestrial X-ray sources, which are believed to be the end result of particle interactions (e.g. annihilation) with at least one DM species. The mechanism of the X-ray production is speculative and those detections are therefore considered as indirect. In contrast, the definitive confirmation of DM would be a direct detection of DM in particle accelerators. It is important to emphasize here that experiments, with the aim of a direct DM detection, have been unsuccessful up to now. However, many believe — although not all — that this situation is just a matter of time.

The full spectrum of direct and indirect DM detection methods is an interesting topic. Nevertheless, the DM model I am going to introduce is a simplified model, based on self-gravitating fermions. No other interaction is considering besides the fulfillment of the Pauli principle and the Einstein equation. More important, the applications of this model are limited to classical DM indications (e.g. rotations curves) which do not require further self-interaction. Therefore, in order to understand the

context of the DM model, I will focus in the introduction mainly on the methods relevant for this thesis and briefly to other methods when necessary. I will skip completely the discussion about DM detections, what would be beyond the scope of this thesis, and refer the interesting reader to the detailed review written by Marrodán Undagoitia and Rauch (2016).

Convention, nomenclature and notation

In this thesis I don't imply a particular unit system (e.g. I don't consider $c = G = h = 1$). It is much more convenient to define an appropriate unit system for each model in order to simplify the equations. This approach has also the advantage to separate physical solutions and scaling factors, i.e. it makes the equations *dimensionless*. However, note that the term 'dimensionless' refers to a particular unit system which is not necessary unique. Thus, a proper unit system may reduce the amount of parameters. Nevertheless, in the end all parameters are required to obtain physical solutions (e.g. in SI units).

In the case of a single unit system, dimensionless variables are often introduced (e.g. $r' = r/R$ with R the scaling factor). But in order to handle different unit systems it turned out that it is (often) much more suitable *not* to introduce additional dimensionless variables. In short, it is sufficient to introduce to every variable a scaling factor and write a dimensionless *variable* then as a fraction (e.g. r/R). This is analogue to the notation of a differentiation with respect to a variable (e.g. $\frac{\mathrm{d}}{\mathrm{d}x}$). For unpracticed readers this notation might seem alien. But it has several advantages. It keeps the amount of symbols low. It simplifies the transformation into another unit system what is necessary or recommended sometimes. In my opinion it improves the readability of equations because it clearly simplifies the contained physics (e.g. emphasizes configuration parameter) without reducing too much information (e.g. constants are grouped in scaling factors). Further, the fraction notation makes it easier to identify possible approximations (e.g. $r/R \ll 1$).

Sometimes it is suitable to introduce new variables in order to emphasize its physical importance or just to simplify equations. Equivalent to the fraction notation it is often recommended to define the new variable as dimensionless. In this case it is not necessary to introduce a scaling factor and, therefore, keep the amount of symbols low. However, it is always possible to fall back to the fraction notation.

For completeness, in this thesis I use the Einstein convention where repeated indices are considered as a sum.

Code development

An essential part of my PhD was the development of a program in order to solve the differential equations of the introduced models in chapter 2. In particular, I was interested to develop a framework which allows to maintain existing models easily and produce fast results (e.g. plots) as well as has the possibility to add new models with a minimum of couplings. Initially, I was planning to write a chapter with all details. But till the end of my PhD the framework remained in a developing state which has not reach a satisfying status for a final version. Though it is able to produce results.

Instead, I want here to mention the basic concepts of the framework which represent many years of my continuous experience in software development. First of all, I use the concept of a *model* in order to describe a real physical *system*. Clearly, in this thesis the system I am interested in are galactic structures, in particular the distribution of dark matter. In next it is important to *select* properties or phenomenological effects (e.g. flat rotation curve, supermassive compact object) of the system which have to be covered by a model. This part is very crucial because it is not clear

if the selected properties belong to the same system (or sub-system). Consequently, the selection choice implies which effects are relevant, what is often not clear in the beginning and needs to be checked.

For example, the current paradigm in galactic structures says that every galaxy hosts a supermassive black hole in its center. The black hole then is surrounded by baryonic matter (e.g. disk) what itself is embedded in a halo composed of dark matter. This example contains presumably three independent components.

Here, I am mainly interested in the relativistic fermionic dark matter model with evaporation effects. In contrast to the BH paradigm the hypothesis of this thesis is that the supermassive compact object is composed of degenerate fermions rather than a black hole and that the halo is composed of the same fermionic particles, although in a diluted (non-degenerate) state. Thus, only one assumption is sufficient to explain two phenomena: An underlying semi-degenerate mass distribution composed of massive fermions.

Turning now to the model description it is important to say that a model may be described in many different ways. Following the description in chapter 2 each dark matter configuration may be described through only four parameters (e.g. m, β_0, θ_0, W_0). But this *parameter description* implies a given set of equations what is important to keep in mind.

In order to compare for example the mass distribution with measurements of the system or other models it is necessary to describe the solution in a common basis. This is usually done through a set of equations which map the set of parameters to a set of profiles, e.g. the mass profile $\{r, M(r)\}$. This *profile description* finally uses the standard basis units such as length (e.g. m or pc), mass (e.g. kg or $M_\odot$) and so on.

It is worth to emphasize that measurements of a system (e.g. observables) represent a model just like a model from a theory. The difference is that such a model uses a description basis based on physical properties (e.g. a ruler, a clock, etc.). This concept allows to compare theory and reality with the implication that the model inferred from measurements is considered as *true*.

In summary, we find in the descriptions of a physical system or model always the pattern of mapping one description into another one. Here I want to emphasize that every description demands a choice of a basis, e.g. a set of equations, a unit system, an alphabet, ...). In the field of data storage, for example, it is inevitable to define a unit system. This encoding seems to be a fundamental pillar of communication. In other words, it is not possible to communicate without a basis. The purpose of the framework thus is to rely on the fundamental mapping principle. The idea is not only to program the mapping of one description into another, but to provide a (simplified) infrastructure which allows to define such mappings easily.

For a better understanding of the framework I want to describe briefly a typical work flow in more details. Given is a set of parameters (e.g. m, β_0, θ_0 and W_0). Those parameters describe a dark matter distribution encoded in such parameters what implies a set of equation. The next step therefore is to decode those parameters (e.g. evaluate equations) in order to obtain, for example, a mass profile $\{r/R, M(r)/M\}$. As mentioned above, it is inevitable to predefine a unit system what is given implicitly in the set of equations. A different unit system would demand a different set of equations what does basically the same mapping despite some scaling factors. But instead of defining many sets of such equations it is more convenient to rely on a single set of equations and define it as fundamental. It is then possible to transform the predefined unit system simply by an additional set of equations, e.g. $R \mapsto$ m or $M \mapsto$ kg. Note, that the additional set is (usually) more simple since it transforms a unit system only by elementary operations (e.g. rescaling).

It turned out that the mapping principle and the definition of a fundamental basis for each description (e.g. parameter-like, profile-like) are convenient tools for working with models and analyzing them.

Chapter 1

Introduction

Till the end of 18th century only a few galaxies such as the Milky Way galaxy, the Andromeda galaxy and the Magellanic clouds were known. All other stars appeared as bright points. Some sharp and others blurred. The latter had been interpreted as nebula. In the middle of 19th century telescopes then had been improved to obtain higher resolutions. Good enough to see more details. For instance, the new observations showed clear spiral structures in the nebulae.

Thanks to further improvements, especially the Hubble Space Telescope (HST) in the end of 20th century, there is nowadays a much more detailed picture of nebulae, recognized as galaxies in meanwhile. Thus, following the Hubble classification, galaxies appear mainly in two types: ellipticals and spirals. Elliptical galaxies (E) differ only in the ellipticity, ranging from E0 (spherical) to E7 (oblate). Spirals are further classified in barred (SB) and non-barred (S), depending if they possess a distinct bar in the inner spiral arms. The galaxy type on transition from ellipticals to spirals is called lenticular and labeled as S0. All other galaxies which appear distorted, being neither elliptical nor spiral, are simply labeled as irregular galaxy (Irr).

It is important to emphasize that this morphological classification is based on the visible structure. But all galaxies have in common that they are embedded in a halo, composed of DM.

1.1 Evidence and indications of dark matter

Initially motivated to solve the distribution and kinematics of visible stars, the idea of dark matter originated from discrepancies between observations and prediction of standard Newtonian gravity applied to known baryonic components in galaxies. The technological progress in telescopes and observations methods gave evidence of dark matter on many scales, from local (sun neighborhood) up to cosmological (see Bertone and Hooper, 2016, for a detailed review).

In next the DM evidence on different scales will be recalled briefly, following a hierarchical order from the smallest known scales (local dark matter), to galactic, cluster and finally to cosmological scales. This order roughly correlates with the chronological indications from observations.

Complimentary to the well accepted evidences of dark matter an interesting hypothesis about dark matter in the galactic center will be explained in the end of this section.

Local dark matter

Early evidence of dark matter came from the motion of bright stars near the sun (Jeans, 1922; Oort, 1932). The results set an upper limit of the dark matter density which is about 50% of the local total density (0.1 - $0.2\,M_\odot/\mathrm{pc}^3$). Recent results, however, give

a much smaller local dark matter density of about 0.006 - $0.011\,M_{\odot}/\mathrm{pc}^3$ (Salucci et al., 2010; Sofue, 2012). Based on those modern estimations there is general consensus among scientists that only a small amount (up to 10%) of DM is required in the Galactic disk.

Note that the estimations depend on the precise distance of the sun to the galactic center, what is still a topic of discussion in the scientific community (Salucci et al., 2010).

Further historical data and details about the local dark matter as well as information about promising future surveys, giving a better picture about the sun's neighborhood (e.g. Gaia), is provided in the review by Read (2014).

Dark matter on galactic scales

Before the 1970s few indications of dark matter in other galaxies (e.g. M31 and M81) were already given based on mass-to-light measurements and a minor group of scientists was open to the possibility of a dark matter contribution. However, the conservative interpretation was an absorption-of-light phenomena in the outer region of the observed galaxies.

In the 70s till early 80s the necessity of dark matter was clearly confirmed in galaxies other than our Galaxy. Thanks to the new developed image tube spectrograph, it was possible to measure velocities far in the outer disc region. The observation of those extended galaxy rotation curves uncovered the so called *flat* rotation curve, where circular velocities are (nearly) constant or 'flat' on halo scales (Bosma, 1978; Einasto, Kaasik, and Saar, 1974; Rubin and Ford, 1970; Rubin, Ford, and Thonnard, 1980).

This phenomena was observed in several galaxies, what finally convinced the majority of the scientific community that a dark matter component is needed in the outer part of galaxies. In particular now, the flat rotation curve is the classical argument in favor for dark matter because baryonic matter inferred from light implies a Keplerian (decreasing) behavior what is in conflict with the observations (nearly flat).

Motivated by those observations, early numerical calculation for MW-like galaxies then demonstrated that they, indeed, need to be embedded in a spherical halo, composed of invisible matter, due to stability (Ostriker and Peebles, 1973). By the end of the 70s it was already concluded that the case for dark matter in the universe is very strong and becoming stronger (Faber and Gallagher, 1979).

In meanwhile it is clear that most galaxies, ranging from dwarfs to ellipticals, are embedded in a dark matter halo with a contribution depending on the galaxy type. This insight comes from the continuous and improved HI measurements (e.g. THINGS) in combination with $3.6\,\mu\mathrm{m}$ measurements of the Spitzer Space Telescope (SST).

For instance, it is very well observed and accepted that dwarf galaxies, mostly satellites of larger galaxies, have a compelling contribution of dark matter (more than 90%). Evaluation of the Milky Way satellites demonstrated that the faintest dwarfs are the most dark-matter-dominated galaxies known (Strigari et al., 2008).

Strong evidence of dark matter in spirals comes from extended HI regions in their disk structure. Estimations of dark matter contribution are comparable to the observed baryonic distribution, what poses a challenge to disentangle the gravitational effects in the inner halo (de Blok et al., 2008).

The amount of dark matter in ellipticals is less clear from star kinematics due to faint stars in the outermost regions. Better dark matter tracer in this case are the kinematics of galaxy satellites (star clusters and dwarf galaxies), diffuse X-ray observations and weak lensing. Especially the combination of the different methods, each covering a particular radial extent, provide sufficient evidence for dark matter.

Similar to spirals, it is concluded that dark and baryonic matter contributions are comparable in ellipticals (Hoekstra et al., 2005; Humphrey et al., 2006; Romanowsky and Kochanek, 2001).

Dark matter on group scales

Further evidence of dark matter on the next larger scale, compared to galactic scales, was already given by early galaxy cluster observations in the 1930s. Redshift measurements, especially in the COMA cluster, showed a large scatter in the apparent velocity of galaxies. On the other hand, with the help of the virial theorem — a novelty in astronomy on group scales — and few assumptions about the properties of the COMA cluster, it was possible to estimate its mass and, from there, an average velocity dispersion. This estimation, based on pure baryonic matter, was clearly one order of magnitude below the observed average velocity dispersion along the line-of-sight, being approx. $1000\,\mathrm{km/s}$. In the case of a confirmation of the assumptions, the conclusion would be that the COMA cluster exhibit dark matter in much greater amount than luminous matter (Zwicky, 1933, 1937).

In the following decades the distribution of dark matter in galaxy clusters remained unsatisfied, mainly due to little knowledge about those systems. Nevertheless, part of the 1970s revolution regarding dark matter in galaxies, an inspiring review about the status of the *missing mass problem* supported the presence of dark matter on both scales, galactic and group scales (Faber and Gallagher, 1979).

The situation changed with further progress in telescopes and observations methods, clearly. The probably most fascinating and compelling evidence for dark matter on group scales comes from mass distribution estimations of the *Bullet Cluster*, referring to two merging galaxy clusters, through gravitational lensing. Comparing the results with the analysis from X-ray emissions, a baryonic matter tracer, indicated a dark source of matter which should dominate the total mass of the cluster (Clowe et al., 2006).

Dark matter in the Universe

The whole concept of dark matter is bolstered from cosmological observations and is highly related to particle physics in the early Universe. Nevertheless, it is important to understand that throughout the 20th century the origin of various nuclear species remained a puzzle. Until the mid of that century it was clear that stars are the main producer of several elements. Fusion processes, such as the proton-proton chain and the carbon-nitrogen-oxygen cycle, explain well the stellar nucleosynthesis and provide also their dominant energy budget (Bethe, 1939).

An alternative although incomplete theory to stellar nucleosynthesis suggested that all nuclear species (light and heavy) may have been produced in the early Universe (Alpher, Bethe, and Gamow, 1948). But stellar nucleosynthesis was also lacking to explain, for instance, the observed helium abundance (Burbidge et al., 1957). The discovery of the Cosmic Microwave Background (CMB), what contains information about the early Universe, finally lead to an increased interest in Big Bang nucleosynthesis. Motivated to solve the origin of deuterium, which is not generated in stars, it was shown that the cosmological baryon density is limited to about 10% of the critical density (Burles and Tytler, 1998a,b; O'Meara et al., 2001; Reeves et al., 1973).

Modern cosmological observations, in particular the angular power spectrum of the CMB, further constrained the matter composition of the Universe. Following the recent analysis of the Wilkinson Microwave Anisotropy Probe (WMAP) mission and especially the subsequent Planck mission, both satellite-based surveys, lead to the conclusion that less than 20% of the matter in the Universe is baryonic (Hinshaw

et al., 2013; Planck Collaboration et al., 2016). This strong result nowadays represents the modern pillar for the existence of dark matter.

Dark matter in the central region of galaxies?

The structure of galaxies is often characterized by a supermassive and compact object in the galactic center. Based on Quasar observations and strong theoretical arguments, those galactic nuclei are usually associated with so called supermassive black holes (Lynden-Bell and Rees, 1971; Salpeter, 1964). In particular, when they show clear activities such as X-ray emission from accretion and jets. In that case the compact object is called an AGN, corresponding to active galaxies.

For inactive galaxies (e.g. Milky Way) supermassive objects are unveiled , for example, through stellar kinematics in the inner galaxy regions. Usually, no other explanation than a black hole was feasible to explain such large masses within such highly limited volumina. This conclusion is known as the *enclosed mass argument*. But limited measurements allowed a wider window for speculations about the nature of inactive galactic nuclei.

Apart from the favored Supermasive Black Hole (SMBH) scenario, a hypothetical star cluster in the inner region of the Milky way, for instance, was also in agreement with early observations in the 90s (Haller et al., 1996; Sanders, 1992). Nevertheless, continued observations of the galactic center over many years ruled out the star cluster scenario. Careful monitoring of single stars in the Galactic center, especially the S2 star with an orbital period of about 15.6 years, led to the conclusion that a supermassive and compact object, with a mass of about $4 \times 10^6\, M_\odot$ and enclosed within a diameter no more than $6 \times 10^{-4}\,\mathrm{pc}$ (about 17 light hours), is present in the center of the Milky Way (Gillessen et al., 2009a,b).

Before the confirmation of the central compact object, an interesting question was whether dark matter might contribute in a measurable way to the Galactic center. It was shown that the presence of a Black Hole (BH) can produce a so-called dark matter *spike* in the central region of the Galaxy (Gnedin and Primack, 2004; Gondolo and Silk, 1999). However, it turned out that the central mass contribution of such a DM spike is too small to be dynamically relevant (Vasiliev and Zelnikov, 2008).

For further details about the Galactic center (e.g. BH, nuclear star cluster and DM contribution) see the excellent review by Genzel, Eisenhauer, and Gillessen (2010). In next, an alternative scenario based on fermionic dark matter will be described briefly and in section 1.3 explained in more detail.

Hypothetical DM nucleus

Unsatisfied with the black hole and star cluster scenario, few scientist considered in the late 90s also the possibility that the massive and dark object might be composed entirely of dark matter (in constrast to simple contribution through a DM spike). To achieve a sufficient compactness they assumed degenerate neutrinos which would form a so called keV neutrino-ball (or Fermi-ball in general). At that time such an object was found to be massive and compact enough to mimic a SMBH, centered in Sagittarius A* (SgrA*), and solve the so called *blackness problem* (Tsiklauri and Viollier, 1998, and references therein).

Based on all the previous concluded insights about galactic structure and dark matter, it was just naturally to develop a connection between the dark matter in the halo and in the Galactic center. Thus, just a few years later, in the early 2000s, it was concluded that dark matter in both regions, core and halo, may be of the same kind (Bilic et al., 2002).

Though, the upcoming constraints from more recent observations (e.g. monitoring the full orbit of the S2 star) showed that the hypothesized quantum cores composed

of fermions, as modeled in Bilic et al. (2002) and Tsiklauri and Viollier (1998), did not reach the correct compactness. This led the Astronomical community to rule out such fermion-ball proposals (see Genzel, Eisenhauer, and Gillessen, 2010).

Only recently the idea of self-gravitating fermions was seriously further developed with the conclusion that the Milky Way may be embedded in a continuous underlying DM distribution, covering the whole observed Galactic extent (from core to halo), without spoiling the baryonic contribution on intermediate scales. Appreciating this novel achievement, yet, their fermionic dark matter model still could not alleviate the compactness problem, In summary, it was lacking to explain the Galactic center and the halo simultaneously (Argüelles and Ruffini, 2014; Ruffini, Argüelles, and Rueda, 2015).

More recently, it was shown that enhancing fermionic dark matter with either self-interaction (Argüelles et al., 2016) or cutoff effects in the phase-space distribution function (Argüelles et al., 2018) provides a mechanism to obtain a sufficient compactness for the quantum core in order to work as an alternative to the central BH scenario. Hence, those approaches solve the compactness problem what allows to explain the Galactic core and halo at the same time.

Nevertheless, the main question still remains whether there is a black hole or an horizonless compact object (e.g. Fermi-ball). Thus, a crucial understanding of galactic nuclei depends on their compactness. The Galactic center provides here an excellent laboratory to give further constraints. On theoretical ground, gravitational lensing allows to discriminate between a BH and fermionic compact object (Gómez et al., 2016). On observational ground, the Event Horizon Telescope (EHT) project, for instance, is aiming to observe optical distortions (branded as the *black halo shadow*) in close proximity of SgrA*, due to an assumed SMBH (Lobanov, 2017). First results are expected (very soon) in 2018, which will have certainly deeper insights in the very center of the Milky Way.

1.2 Galaxy parameter relations

The compelling evidence of dark matter in the Universe unveiled intricate relations between the distribution of dark matter and baryonic matter (stars and gas), which are still an important open question. Big efforts have been aiming to understand the relations between dark and/or baryonic components within completely independent approaches. Accordingly, universal relations involving different pairs of galaxy parameters (e.g. mass, velocity and density) have been unveiled for galactic structures. In particular, dark-to-baryonic relations have re-gained much attention on galaxy scales, from center to periphery, in the last decade in views of the many and rich datasets which cover a broad radial extent along the different galaxy types (Cappellari et al., 2011; Lelli, McGaugh, and Schombert, 2016; de Blok et al., 2008).

Among the several relations in the literature only a selected list of relations, which are relevant within the context of this thesis, will be explained in next.

M-σ relation

Starting in the galactic center, it was shown that the mass of the central compact object M correlates with the stellar velocity dispersion of the bulge σ (Ferrarese and Merritt, 2000). This $M - \sigma$ relation provided a simple method to estimate masses of most black holes in galactic centers due to the better accessibility of the velocity dispersion σ. The relation had also an important impact on the understanding of galactic structures. Since its discovery in 2000 supermassive objects were considered as main components in galaxy formation and evolution. In detail, the tightness of the

relation suggest that some kind of feedback acts to maintain the connection between the galactic nuclei and the bulge (Silk and Rees, 1998).

(baryonic) Tully-Fisher relation

Focusing on the outer part of a galaxy, Tully and Fisher (1977) demonstrated an empirical relationship between the stellar mass (or luminosity) and the maximal rotation velocity. Later it was shown that this Tully-Fisher relation holds even tighter when the gas component is added. Known as baryonic Tully-Fisher relation, it connects the total baryonic mass (stellar and gas) with the maximal rotation velocity (McGaugh et al., 2000).

Mass discrepancy acceleration relation

Keeping in mind that the maximal rotation velocity appears typically as a flat tail in the DM dominated regime, it is possible to connect the (baryonic) Tully-Fisher relation with dark matter. With this idea some authors focus on the mass discrepancy encoded in the magnitude $D = V_{\rm obs}^2/V_{\rm bar}^2$, where $V_{\rm obs}$ is the total observed velocity and $V_{\rm bar}$ is the inferred velocity of the baryonic component only. They found that for disk galaxies the mass discrepancy shows clearly a systematic increasing with decreasing centripetal acceleration of the baryonic component $a_{\rm bar} = V_{\rm bar}^2/r$ below a particular scale $\mathfrak{a}_0 \approx 1.2 \times 10^{-10} m/s^2$. Above $\mathfrak{a}_0$ dark matter becomes negligible with $D \approx 1$. This correlation is known as MDAR for mass discrepancy acceleration relation (McGaugh, 2004; McGaugh, 2014).

Radial acceleration correlation

An alternative representation of the dark-to-baryonic relation on halo scales is the so-called radial acceleration correlation (RAC) what connects the centripetal accelerations of the baryonic and total component. It turned out that this relation, equivalent to MDAR, is independent of the Hubble type. Thus, the relation is not limited to disk galaxies and holds also for other galaxy types (ellipticals, lenticulars, dwarfs spheroidals) what makes it a true universal law among morphology classification (Lelli et al., 2017). Despite a relatively large scatter, this relation implies a fundamental link between dark and baryonic matter on halo scales what corresponds to the low acceleration regime.

Ferrarese relation

Focusing on dark components only, Ferrarese (2002) found a link between the total DM mass of a galaxy and the mass of its massive and dark compact object in the galactic center. This relation covers many order of magnitudes in total DM mass, from $\sim 10^{11}\, M_\odot$ (spirals) to $\sim 10^{14}\, M_\odot$ (big ellipticals). The mass of the embedded compact objects ranges from $\sim 10^5\, M_\odot$ to $10^9\, M_\odot$. Note that it spans a link between the very inner and outer region of a galaxy, apparently without taking into account baryonic matter in between on intermediate scales (e.g bulge and disk).

Donato relation

Additionally, DM halos show a nearly constant surface density $\rho_0 r_h \approx 140^{+80}_{-30} M_\odot \mathrm{pc}^{-2}$, where ρ_0 is the central density of the halo core and r_h the one-halo-length-scale of the Burkert profile. This universal halo surface density law is valid over a range of 14 mag in luminosity and for all Hubble types (Donato et al., 2009). It is worth to mention that it focuses only on the outer region of galaxies (intermediate halo scales), being supposedly unaffected of the remaining matter distributions.

1.3 Dark matter candidates and modeling

The first indications of dark matter beginning of the 20th century had emphasized on the term *dark*, or similar adjectives like *invisible*, *hidden* or *missing*. The main assumption was that there is matter, including all known astrophysical material, that is too faint to be detected with available telescopes. Initially limited only to baryonic matter as the only dark matter candidate, this picture changed rapidly in the 80s when particle physicist started to be interested in astrophysics and vice versa. The outcome of this fruitful collaboration is the hypothesis that dark matter consist of at least one yet-unknown subatomic particle.

Today, *dark matter* has became a proper noun for the bulk of the Universe's matter, preferentially non-baryonic which doesn't emit any light and interact only weakly (if at all). Modern astrophysics therefore is not interested anymore in whether dark matter exists or not but rather to explain its nature, its distribution on different scales and its impact on the formation and evolution of structures.

Baryonic dark matter

Before the dawn of the great era of astro-particle physicists, dark matter was assumed to be of baryonic nature (i.e. protons, neutrons, electrons and photons). This category can be separated mainly into two groups: gas and Massive Compact Halo Objects (MACHOs). The first, a hot gas labeled *corona*, was proposed as a viable candidate just after the confirmation of dark matter in several galaxies in the 70s (Einasto, Kaasik, and Saar, 1974; Einasto et al., 1974). In meanwhile it became clear that gas alone does not solve the mass discrepancy in halos (Turner, 2003).

Alternatively or complementary to an extended and diluted gas, it was assumed the halo may be composed of faint but massive objects, covering a wide mass range. Various species were considered such as low massive stars (e.g. red, brown and white dwarfs), planet-sized objects without any light source, neutron stars and light absorbing black holes. The latter includes theoretically also primordial black holes which would have been produced in the early Universe (Hawking, 1975). Following the idea that condensed objects deflect light, the strategy then was to constrain the mass range of those MACHOs through the observation of gravitational microlensing events when they pass background stars. After several years of observations in the 90s it was concluded that the mean mass of MACHOs is between $0.15\,M_{\odot}$ and $0.9\,M_{\odot}$. Moreover, the results demonstrated that these objects cannot explain the entire dark matter in galactic halos but only a fraction of about 20% (Alcock et al., 2000).

The most stringent limits on baryonic dark matter comes from primordial nucleosynthesis. Such analysis is not only consistent with the MACHO measurements, it also excludes definitely baryonic matter (MACHOs and hot gas) as a dominant dark matter component (Steigman, 2006).

Massive neutrinos

Around 1980, when the concept of dark matter in galaxies was well accepted but traditional explanations were still puzzling, heavy neutrinos were proposed as a possible non-baryonic candidate (Ruffini and Stella, 1983; Tremaine and Gunn, 1979). These particles are neutral and interact only weakly what makes them appealing candidates for dark matter. Although neutrinos of the Standard Model of Particle Physics (SM) don't posses a rest-mass, the assumption of heavy neutrinos predicts the existence of so-called neutrino oscillations. Such an extension of the SM explains the transformation of an neutrino among the three known types, called flavor (electron, myon, tauon). The oscillations then are reflected in variations of the rest-mass (Pontecorvo, 1958).

Theoretical estimations about the distribution of massive neutrinos and photons in the early Universe give a particular ratio $(6/11)$, where the information about the photon density can be extracted from the temperature of the CMB (about $2.7\,\mathrm{K}$). Then, under the assumptions that the ratio holds until now, that massive neutrinos decouple relativistically from the primordial plasma and that they contribute entirely to the present dark matter it is possible to derive an upper bound of the order $10\,\mathrm{eV}$ (Cowsik and McClelland, 1972; Gershtein and Zel'dovich, 1966). On the other hand, double beta-decay laboratory experiments and cosmological measurements imply upper bounds of the order 0.1 - $1\,\mathrm{eV}$. This discrepancy indicates that heavy neutrinos cannot explain all the dark matter in the Universe (Gonzalez-Garcia and Nir, 2003; Hannestad, 2010).

In meanwhile, neutrino astronomy has become a well established observation tool which, for instance, helps to explore the interior of the sun. Also the predicted neutrino oscillation has been confirmed within different context. But the determination of the neutrino masses still remains a difficult task.

Weakly interacting massive particles (WIMPs)

In contrast and parallel to relativistic massive neutrinos in the early Universe, it was also considered the possibility of a non-relativistic decouple. This ansatz required the introduction of a hypothetical highly more massive particle which would interact only weakly. In order to compare the particle density of those hypothetical neutrinos with the observed matter density in the Universe, it is necessary to describe properly the decoupling process and its evolution till now. Thus, the evolution of the phase space distribution function with the Boltzmann equation in a Friedman-Robertson-Walker (FRW) model was studied. The results of this analysis then yielded a lower particle mass limit of about $2\,\mathrm{GeV}$ (Lee and Weinberg, 1977).

The introduced hypothetical neutrino, referred as Weakly Interacting Massive Particle (WIMP) is probably the most cited candidate among the WIMP framework. Other reasonable candidates are an outcome of the Supersymmetric Standard Model (SUSY), e.g. neutralino, gravitino and photino (Longair, 2008).

Sterile neutrino

Another group of possible dark matter candidates considers particles which don't feel any of the known fundamental forces of nature (e.g. weak, strong and electromagnetic) except gravity. This characteristic is termed *sterile* and opens a wider window of hypothetical particles beyond the standard model. But to be produced in the early Universe, those particles have to interact with other particles in some way. Therefore, various sterile neutrinos are postulated. Each of those species has a specific particle mass, depending on the production mechanism. In particular, such neutrinos may close the gap between massive neutrinos ($\lesssim 1\,\mathrm{eV}$) and WIMPs ($\gtrsim 2\,\mathrm{GeV}$).

Around 2000 and in the following years an increasing attention has received the so-called sterile right-handed neutrino in the keV mass scale as a plausible dark matter candidate (Asaka, Blanchet, and Shaposhnikov, 2005; Boyarsky, Ruchayskiy, and Shaposhnikov, 2009; Shaposhnikov, 2009; Shi and Fuller, 1999; Stasielak, Biermann, and Kusenko, 2007). Further details about neutrinos, their production mechanism and their impact on structure formation in the Universe is given in the excellent White Paper of Adhikari et al. (2017).

Fermionic dark matter

Massive neutrinos and many other fermionic species predicted or hypothesized by particle physics beyond the standard model (e.g. sterile neutrinos) enter in a wider

category named fermionic dark matter. Apart from specific particle properties, an important and common characteristic is their rest-mass what has a crucial impact on the distribution of dark matter.

Early constraints on the particle mass of fermionic dark matter are based on the phase space. For comparison with observations this theoretical concept requires the introduction of a coarse-grained phase space density which is defined as the average of the (microscopic or fine-grained) phase space density over a finite volume, containing sufficient amount of particles. Then, by following Liouville's theorem together with the concept of violent relaxation, it is possible to set an upper limit for the coarse-grained phase space density. The former predicts a constant phase space density over time while the shape of a finite volume may change. The latter, additionally, causes a phase space mixing, e.g. winding of finite volumina (Lynden-Bell, 1967). Therefore it is well motivated to argue that the primordial coarse-grained phase space density can only decrease. This behavior clearly sets an upper limit for the late-time coarse-grained phase space density.

Applied to galaxies and assuming that galactic halos are described by a so-called isothermal sphere, resembling classical Newtonian solutions with a Maxwellian velocity distribution, allows to estimate a lower limit for the particle mass by comparing the primordial and late-time coarse-grained phase space densities. This estimation depends on the (isotropic) velocity dispersion and the one-halo length scale, where the latter is defined at the so-called King radius (Binney and Tremaine, 2008). For typical spiral galaxies, with velocity dispersions around $100\,\mathrm{km/s}$ and one-halo length scale at the order of $1\,\mathrm{kpc}$, the comparison yields a minimal particle mass of the order $100\,\mathrm{eV}$ (Tremaine and Gunn, 1979). This result clearly rules out the possibility that massive neutrinos contribute significantly to dark matter halos. Moreover, if dark matter is fermionic then hypothetical particles beyond the standard model are required. This necessity marks the dawn of astro-particle physics in the 1980s.

Self-gravitating fermions

On a more general ground the distribution of fermionic dark matter in galactic systems is motivated by the most profound interest in classic astronomy: the distribution of stars. Due to the vast amount of stars in galaxies (10^5 to 10^{12}) it is more suitable to describe those stellar systems on the ground of classical statistical mechanics rather than celestial mechanics. A convenient approximation is to assume identical stars (e.g. point masses) throughout a stellar system.

In its simplest form, a self-gravitating gas in equilibrium, which is composed of identical particles, follows Boltzmann statistics. The solutions of this model, called the isothermal sphere, produce spatially unlimited mass distributions what has been known already since the beginning of the 20th century (Chandrasekhar, 1939, 1942). In the 1960s then more realistic solutions were obtained by studying the Fokker-Planck equation, considering the effects of collisional relaxation and tidal cutoff (e.g. evaporation). It was shown that stationary solutions of this kind can be well described by lowered isothermal sphere models. Such models are based on simple Maxwellian energy distributions which are lowered by a constant term, interpreted as an energy cutoff (King, 1966; Michie, 1963). An extension of this pioneering statistical analysis with thermodynamical considerations included the effects of violent relaxation what had important implications to the problem of virialization in galaxies (Lynden-Bell, 1967).

In analogy to stars it is possible to consider identical dark matter particles. With this idea a series of works in the 1980s and early 1990s changed the emphasis from self-gravitating stellar systems to systems composed of fermionic particles with the aim to describe galactic halos. Initially, the results provided simple isothermal solutions with quantum corrections due to the Fermi-Dirac distribution function (Ruffini and

Stella, 1983). Later also relativistic effects and the possible presence of a cutoff in the energy as well as in the angular momentum was taken into account (Gao, Merafina, and Ruffini, 1990; Ingrosso et al., 1992; Merafina and Ruffini, 1989).

Note, that finite and self-gravitating systems undergo a so called gravothermal catastrophe (Lynden-Bell and Wood, 1968). Although this concept was demonstrated for stellar systems it is valid also for dark matter, represented by a gas (Binney and Tremaine, 2008, chap. 7). This faithful evolution forms a singular isothermal sphere what corresponds to highly cuspy halos. Moreover, it produces throughout all radial extent a flat rotation curve (Binney and Tremaine, 2008, chap. 4).

The only way to stop the gravothermal catastrophe is to take into account quantum effects of the fermions. The Pauli principle causes a quantum pressure due to the increasing central degeneracy. Thus, during the collapse such a particle feedback stops the process, resulting in a stable configuration with a degenerate core embedded in a halo (Chavanis, 2002, 2006; Chavanis and Sommeria, 1998; Lynden-Bell and Lynden-Bell, 1977). Indeed, it has been shown that a self-gravitating system, composed of general neutrinos (massive or hypothetical) following the Fermi-Dirac statistics and stars, is in agreement with gravitationally bounded systems (Rephaeli, 1982).

A remarkable contribution in the understanding of these issues was given by studying generalized kinetic theories accounting for collisionless relaxation processes, what lead to a class of generalized Fokker-Planck equations for fermions. It was explicitly shown the possibility to obtain, out of general thermodynamic principles, a generalized Fermi-Dirac distribution function including an energy cutoff (Chavanis, 2004). It is worth to emphasize that this achievement extends the former results in the 1960s, from stars to quantum particles.

Semi-degenerate distribution

The early semi-degenerate solutions of a fermionic mass distribution in the 80s and 90s were applied mainly to explain DM halos. Nearly in parallel there was an idea that the mass concentration in the center of the Milky can be explained by a fermi ball, a quantum core composed of degenerate fermions, without making any connection to the fermionic dark matter in the halo.

Consequently, the possibility that dark matter in the Galactic halo as well as in the Galactic core may be of the same (fermionic) kind was first studied in Bilic et al. (2002) in the framework of Newtonian gravity. There they demonstrated that the Milky Way may posses a continuous dark matter distribution, from the center to the halo, with the possibility of a fermion core at the Galactic center as an alternative to the central BH of the same mass. However, upcoming constraints from more recent observations (e.g. S2 star) showed that the predicted quantum core did not reach the correct compactness with a mismatch by 2 orders of magnitude (Gillessen et al., 2009a,b).

More recently the problem of a fermionic quantum core embedded in the Galactic halo was revived (Argüelles and Ruffini, 2014; Argüelles et al., 2014; Ruffini, Argüelles, and Rueda, 2015; Siutsou, Argüelles, and Ruffini, 2015). But this time in the framework of general relativity with the hope of solving the compactness problem. No additional interaction was assumed for the fermions besides their fulfilling of quantum statistics and the system of relativistic gravitational equations. There, the underlying DM distribution was described by a self-gravitating system composed of massive fermions in spherical symmetry. Compared to the first attempt within the Newtonian framework they took into account a slightly higher mass of the Galactic nuclei (about $4 \times 10^6\, M_\odot$).

The extension of a fermionic dark matter model to general relativity implicated a critical core configuration what sets an upper limit for the core mass (Argüelles and Ruffini, 2014). This mass depends on the particle mass, $M_c^{\rm cr} \propto m^{-2}$, what known as

the Oppenheimer-Volkoff (OV) limit for neutron stars (Oppenheimer and Volkoff, 1939). Note that such a limit for semi-degenerate configurations is not present in the framework of Newtonian physics.

In conclusion, a very interesting outcome of the fermionic dark matter models — either in the framework of Newtonian physics or general relativity — is the possibility to explain the Galactic center through a degenerate quantum core as an alternative to the black hole scenario. Thus, given the apparent ubiquity of massive black holes at the centre of galaxies, the models were proposed as a viable possibility to establish a link between the dark central cores to dark matter halos within a unified approach.

It is important to emphasize that the combined constraints from core and halo raised the lower particle mass limit substantially to about $10\,\mathrm{keV}$ compared to the order of $100\,\mathrm{eV}$ from early phase space constraints.

Nevertheless, it turned out that relativistic effects are not sufficient to solve the compactness problem. Instead, the results indicated that further effects have to be taken into account in order to explain the Galactic core and halo simultaneously. In particular, constraints from the innermost S-stars (e.g. S2) required a mechanism to increase the compactness of the core.

Thus, the focus was put onto the core. A promising extension considered particle self-interactions but limited only to the nuclei while the halo is described by a classical isothermal sphere. The entire dark matter distribution in this model is therefore a combination of two regimes. When compared with observables along the entire galactic extent (core and halo), the solutions of this modified model narrowed remarkably the allowed particle mass window to about 47 – $350\,\mathrm{keV}$ (Argüelles et al., 2016).

Another approach includes cutoff effects (e.g. evaporation), although without self-interactions and limited to galactic halos on theoretical ground. It has been recently developed in Chavanis, Lemou, and Méhats (2015) as the so-called *Fermionic King* model (Chavanis, 2002, 2004, 2006, see also). However, that model does not take into account general relativistic effects which become important for the quantum cores approaching the critical mass for gravitational collapse.

Very recently, the idea of cutoff effects within the framework of general relativity has been successfully applied to the Milky Way in order to explain the Galactic center (a compact object centered in SgrA*) and the Galactic halo at the same time (Argüelles et al., 2018, see also section 4.1 of this thesis). The main result is that the Galaxy is embedded in a continues DM distribution, from the galactic center to the halo, without spoiling the intermediate baryonic matter (e.g. stars). Additionally, the Milky Way analysis yielded the particle mass window $mc^2 = 48$ – $345\,\mathrm{keV}$, similar to the results from the self-interaction approach. (The application of such a fermionic dark matter model including cutoff effects to galactic systems is the objective of this thesis. See section 1.5 for details.)

Bosonic dark matter

In contrast to fermionic dark matter there exist the possibility of bosonic dark matter in order to explain galactic halos. Following the work of Ruffini and Bonazzola (1969) the attention has been directed to the possible role of quantum statistics as opposed to the Boltzmannian description. Attention has correspondingly shifted from stars to elementary particles. There the case of bosons as well as fermions was considered. This also shifted the interest from the baryonic matter composing a star to a new field of interest, which has become since of great relevance, the dark matter components of galactic structures.

A first significant attempt was made by Baldeschi, Gelmini, and Ruffini (1983) who called attention on the possible role of self-gravitating bosons for explaining galactic halos. Their result suggested as a viable DM candidate low particle masses

down to 10^{-24} eV. This idea was further developed by a large number of authors. For a recent review of the initial work as well as the large number of intervening works see e.g. Hui et al. (2017), and references therein.

Interestingly, it is possible to make some general statements about the particle mass based on the phase space (similar to fermions) but without the necessity of any further distribution model (e.g. isothermal sphere). The only requirement is to respect the uncertainty principle ($\Delta p \Delta x \geq \hbar/2$) when particles with bosonic character occupy a given cell in the phase space (Lisanti, 2017).

The tightest bounds then can be inferred from the halo of dark matter dominated dwarf galaxies by interpreting the galactic halo as a condensed Bose-Einstein gas. Hence, more recent observational constraints set a lower limit of the order $10^{-22}\,\mathrm{eV}$. The bottom bound corresponds to Ultra-light scalar dark matter, also known as fuzzy dark matter (Hu, Barkana, and Gruzinov, 2000).

Modified Gravity

The introduction of dark matter, especially in the halo, implies the assumption that Newtonian laws of gravity are applicable on halo scales. Thus, it is important (and fair) to mention that dark-to-baryonic relations (e.g. MDAR) may encourage to modify laws of gravity beyond solar scales without the necessity for any hypothetical particles representing dark matter.

The most prominent modification was published in 1983. There, the introduction of Modified Newtonian Dynamics (MOND) was able to explain the flat rotation curves (Milgrom, 1983a,b,c). Following this idea it provides corrections below a particular acceleration (about $1.2 \times 10^{-10}\,\mathrm{m/s^2}$). Above that acceleration value the corrections are negligible and Newtonian Dynamics is recovered. Nevertheless, MOND has a couple of serious problems to be a realistic framework. First of all, this original approximation does not conserve momentum, angular momentum or energy. Initially it was also not intended to be consistent with general relativity.

In the following year, 1984, a first step was made towards a more realistic framework, where a modified Lagrangian formalism, so-called Aquadratic Lagrangian theory (AQUAL), was presented. This theory produces identical results to those of MOND (within 10%) and, more important, now preserved symmetries corresponding to the conservation of momentum, angular momentum and energy. The relativistic extension of this model is known as relativistic AQUAL or RAQUAL (Bekenstein and Milgrom, 1984).

Similar to the original MOND theory, its successors struggled to explain other physical phenomena, in particular gravitational lensing. But due to the lack of any direct dark matter particle detections in the following years (till now) the idea of a modified gravity framework on galactic scales was never abandoned. It took 20 years until a realistic theory was developed in 2004. This so-called TeVeS theory (for Tensor-Vector-Scalar gravity) contains two additional fields, three free parameters and one free function beyond those of general gravity (Bekenstein, 2004). These additions now compete with the various hypothetical particle species in the dark matter framework.

Further information about the various modified gravity theories, within a wider context not limited only to the necessity of dark matter, are given in the extensive review by Clifton et al. (2012).

1.4 Structure formation

The explanation of observed dark matter distributions (in Universe and galaxies), through particular DM candidates and models, represents only a snap-shot of their evolution. Therefore, the question about the formation and evolution of galactic structures sets constraints on the nature of dark matter. Already in early 80s it became clear that non-baryonic dark matter must be produced in the early Universe. Of interest is therefore if such specific particles (e.g. massive neutrino, sterile neutrino, WIMP), can reproduce the typical cosmological and galactic structures when following their evolution. This objective gained an even higher importance after the exclusion of baryonic dark matter as a viable candidate to explain dark matter phenomena.

Numerical simulations

An early attempt in the 1970s to study the formation of structures (e.g. galaxies) in an expanding Universe was to simulate the condensation of self-gravitating particles (Press and Schechter, 1974). Although the simulation was limited to 1000 particles, it was demonstrated that their evolution produces self-similar structures on different scales.

In the following years to the present an increase of computation power (e.g. by Moore's law) and advances in numerical methods made it possible to simulate larger amounts of particles, what increased the resolution of an evolving gas. Interestingly, the results of those N-body simulations showed that cosmological structures do not depend much on the nature of particles (e.g. massive neutrinos or WIMPs). Of significant importance for the evolution is the initial velocity distribution in the early Universe after their decoupling. Thus, it became usually to classify dark matter species based on the decoupling temperature.

Non-baryonic particle classification

The framework of the primordial nucleosynthesis has many degrees of freedom (e.g. particle interactions and decouple temperature) what allows for speculations of several particles beyond the standard model. For instance, it remains unclear when and how exactly the hypothetical particles have been produced. But a convenient approximation tells that the decoupling temperature of the primordial plasma depends on the particle mass and their interactions.

Light particles (e.g. massive neutrinos with masses $\lesssim 1\,\mathrm{eV}$) decouple early in a relativistic environment when the plasma is still hot. Such particles correspond to the so called Hot Dark Matter (HDM) scenario. In contrast, heavy particles (e.g. WIMPs with masses $\gtrsim 2\,\mathrm{GeV}$) decouple non-relativistically what corresponds to the Cold Dark Matter (CDM) scenario. Hence, dark matter particles in the intermediate mass scales are classified as Warm Dark Matter (WDM). Those particles (e.g. sterile neutrinos) can decouple relativistically albeit their relatively large masses due to different production mechanisms.

Dark matter evolution scenarios

At the largest scales (e.g. superclusters) N-body simulations predict a cosmological late-time structure which is even largely insensitive to the initial velocity distribution and, therefore, to the dark matter scheme. However, each scheme has a particular sequence how the Large Structure of the Universe is reached. For instance, the random motion of individual dark matter particles acts as a filter for primordial density fluctuations. The higher the velocities the higher the free-streaming length. This relation has a crucial impact on the structure formation on smaller scales.

Prediction of the HDM scenario tell that the growth of small-scale structures is suppressed because of the relativistic (or *hot*) velocities. As a consequence large structures are formed first, which then fall apart in smaller structures (Peebles, 1982; Schramm and Steigman, 1981). This top-down scenario of HDM is in stark contrast to the bottom-up scenario of CDM. Following the latter case, non-relativistic (or *cold*) velocities allow to form very low-mass halos (about 10^{-9} to $10^{-3}\,M_{\odot}$) in the early Universe. These small structures then merge with one another to build up larger and larger dark matter structures, following a hierarchical growing.

CDM paradigm

The comparison of different dark matter scenarios with observations was possible only in the beginning of the 1980s, when results of the CfA redshift survey had been released (Davis et al., 1982). This 3D survey of galaxies in the local Universe revealed first indications of the so-called *cosmic web*, a particular structure of matter on large scales ($\gtrsim 10\,\mathrm{Mpc}$) as predicted by the dark matter schemes. Looking at smaller scales (e.g. sup-cluster) the survey was good enough to identify significant structures which are in conflict with the HDM scenario (White, Frenk, and Davis, 1983). Shortly after this failure it was clear that CDM provides better agreements (Blumenthal et al., 1984; Davis et al., 1985).

In the mid 1990s the focus has shifted to galactic scales in order to study the formation of galactic structures in more detail. Based on high-resolution CDM simulation it was concluded that spherically dark matter density profiles can be fitted by a simple universal profile (Navarro, Frenk, and White, 1996). This derived formula became known as the NFW profile.

Small scale crisis

Despite the good agreement of CDM on large scales (e.g. the Large Structure of the Universe), there remain few problems on smaller scales, known as the small scale crisis.

Results from N-body simulations predict an increasing of the dark matter density in the inner halo towards the center. Those cuspy halos are in conflict with cored halos from dwarf galaxy observations, where the dark matter density converges towards the center to a constant and finite value. Galaxies of the latter type are clearly better fitted with an isothermal density profile rather than the NFW profile. However, the situation is not that simple since other observations show a higher diversity in the inner halo structure, where NFW is acceptable. A similar situation is present also in larger and brighter galaxies (e.g spirals) as well as in galaxy clusters. In summary, CDM simulations and observations showed a discrepancy in the inner halo structure what has become known as the *core-cusp* problem (de Blok, 2010).

Another prediction of CDM simulations is an over-abundance of subhalos due to the small free-streaming length. For instance, the predicted number of satellite galaxies for Milky Way like galaxies is at least one order of magnitude above the yet observed ones. The recent discovery of faint and ultra-faint dwarf galaxies in the first decade the 21st century has alleviated but not solved this *missing-satellite* problem (Klypin et al., 1999).

Additionally to the missing satellites, a further often mentioned discrepancy between observations and CDM simulations is the *too big to fail* problem which focuses on the most massive satellites. In contrast to the smaller and fainter (missing) galaxies, those outcomes are not only massive but also luminous and big. Too big for typical MW satellites while no mechanism would lead them to fail being visible (Boylan-Kolchin, Bullock, and Kaplinghat, 2011, 2012).

Possible solutions to the small scale crisis within CDM

Early attempts to identify the discrepancy between observations and CDM simulations were given at both fields. Some authors claimed that the inconsistencies could be due restricted observations such as poor resolution or systematic effects (van den Bosch and Swaters, 2001; van den Bosch et al., 2000). Others blamed faulty or fragile numerical simulations (Borriello and Salucci, 2001; de Blok, Bosma, and McGaugh, 2003; de Blok et al., 2001). Nowadays, those complaints are mostly inappropriate since modern observations methods have improved a lot to distinguish between cuspy and cored halos in many galaxies (Kuzio de Naray and Kaufmann, 2011). In parallel, numerical simulations have been validated successfully for convergence, showing that CDM density profiles are correctly determined (Diemand, Moore, and Stadel, 2004).

Nevertheless, the discrepancies remained what lead to the conclusion that their origin must be in the underlying physics of simulations. It is important to recall here that early CDM simulation where limited to gravitational interaction and dark matter only. The strongest suspicion, therefore, was the neglect of the obvious baryonic components. The inclusion of baryonic matter and its effects on the dark matter distribution is referred as baryonic feedback (e.g. supernovae or dynamical friction). For instance, it has been shown that feedback mechanism may flatten the inner density profile to transform cuspy halos into cored one. It turned out that a solution of the core-cusp problem through baryonic feedback has also a positive effect on the alleviation of the other discrepancies.

A different approach to solve the small scale crisis in CDM focused on Self-Interacting Dark Matter (SIDM). In this scenario cold dark matter particles, with rest masses in the range $1\ \mathrm{MeV}/c^2$ up to $10\ \mathrm{GeV}/c^2$, scatter elastically what leads to deviations in the inner halo structure compared to CDM prediction (Davé et al., 2001; Spergel and Steinhardt, 2000). It was further shown that constraints on the total cross-section over the particle mass (i.e. $\sigma/m \sim 0.1 - 100\ \mathrm{cm}^2/\mathrm{g}$) would generate shallower inner DM density profiles with a consequent reduction in the amount of substructures. Those observational effects in the inner halo regions therefore alleviated important problems of collisionless CDM simulations. More recent cosmological simulations within the CDM framework studied the effects of SIDM on density cores of galaxies and galaxy clusters. The conclusion is that cross-sections in the range $\sigma/m \sim 0.5 - 1\ \mathrm{cm}^2/\mathrm{g}$ are consistent with the observational constraints on larger scales (e.g. Peter et al., 2013; Rocha et al., 2013).

A detailed review of the CDM problems in numerical simulations as well as a wide list of possible solutions, including baryonic feedback and other approaches, are given by Del Popolo and Le Delliou (2017) and references therein. See also the review by Tulin and Yu (2018) with a focus on SIDM. For a didactic approach in galaxy formation the reader is refereed to Longair (2008).

WDM, an alternative solution to small scale crisis

Notwithstanding the importance of baryonic feedback mechanism and/or self-interactions in CDM simulations, the necessity of baryons and self-interactions for the formation of galactic structure is still an open topic. Instead of taking further effects into account, the alternative is to change to nature of dark matter.

For instance, particles in the WDM framework have a larger free-streaming length compared to CDM, due to lighter or *warmer* particles. Consequently, WDM could affect small structures by producing flatter velocity profiles and fewer subhalos. These properties provide the base for solving small scale problems of CDM without the introduction of baryonic matter nor any self-interactions (Angulo, Hahn, and Abel, 2013; Lovell et al., 2012).

Apart from the different velocity distribution of WDM, a further important effect on small scales (e.g. galactic) is expected when fermionic particles (e.g sterile neutrinos) are considered (Bode, Ostriker, and Turok, 2001). More important, in the context of collisionless relaxation the conclusion was that for self-gravitating system the neutrino mass has to be in the keV regime, giving a strong support for WDM (see e.g. Argüelles et al., 2018; Ruffini, Argüelles, and Rueda, 2015).

1.5 Objectives

Among the many different dark matter candidates, the objective of this thesis is to investigate galactic structures on the ground of fermionic dark matter. In detail, the open problem of intricate dark-to-baryonic as well as dark-to-dark relations is faced from a different and complementary perspective relying on semi-analytic approaches, compared to cosmological concepts (e.g. CDM) or modified gravity (e.g. MOND).

Thus, a finite self-gravitating system, composed of massive fermions in spherical symmetry, is considered. It is assumed that such a system describes well relaxed galaxies. Therefore, in order to obtain mass distributions of a thermal and semi-degenerate fermionic gas, it is necessary to solve the Einstein equation for a perfect fluid in hydrostatic equilibrium.

In summary, this proposed dark matter model is motivated by the original RAR model, as introduced by Ruffini, Argüelles, and Rueda (2015), and enhanced here by a cutoff in the particle energy space. Consequently, it provides novel mass distributions of dark matter, including a compact and degenerate core in the galactic center surrounded by a diluted halo with a cutoff. The cutoff is necessary to account for finite galaxy sizes and masses. Moreover, the new families of core-halo solutions with an overall re-distribution of the bounded dark matter and more stringent halo constraints of these novel configurations allow a higher compactness of the central cores in order to solve the compactness problem.

It will be shown that with this enhanced model, the RAR model with cutoff, produces a continuous underlying dark matter structure, being able to explain

- the Milky Way observables on the entire radial extent (from core to halo) simultaneously without spoiling the baryonic matter on intermediate scales.

It is important to emphasize that the results for particle masses in the range 48–$345\,\mathrm{keV}$ provide a compelling alternative to the black hole scenario in the Galactic center. Additionally, when applied to different galaxy types (from dwarfs to ellipticals) a particle mass of $48\,\mathrm{keV}$ naturally creates

- the observed relation between the central supermassive dark objects and the total DM galaxy mass (Ferrarese, 2002)
- the constancy of the *central* surface density (Donato et al., 2009).

Finally, based on spiral galaxies from the SPARC data base it will be demonstrated that the model reproduces

- the relation between the centripetal accelerations of baryonic components and total mass contribution, including dark matter.

This radial acceleration correlation clearly confirms a fundamental link between dark and baryonic matter as suggested by McGaugh, Lelli, and Schombert (2016a).

Chapter 2

Dark Matter model

Following Argüelles et al. (2018), Ingrosso et al. (1992), and Ruffini, Argüelles, and Rueda (2015), a self-gravitating system composed of massive fermions describes the dark matter distribution of a galaxy. Thus, the aim of this chapter is to recall fermionic mass distributions on theoretical ground. An analysis of the model itself for a better insight is given in the next chapter and the application to dark matter in galaxies is then provided in chapter 4.

Of general interest is a spherical mass distribution within the general relativity framework (section 2.1). This approach is the basis for the dark matter model, described by a phase space distribution function. In order to solve the problem of the self-gravitating system, a lowered Fermi-Dirac distribution function is adopted. (section 2.2). This choice describes a fermionic nature of dark matter while the lowering term is necessary to obtain distributions finite in mass and size. For a better understanding it is convenient to consider approximations (e.g. limiting behavior) which allow to decompose the rich solutions into more elementary components (e.g. fully degenerate core and isothermal sphere), see section 2.3. Finally, a summary of the fermionic dark matter model including cutoff effects is given in section 2.4.

2.1 Perfect fluid

We solve Einstein's field equation

$$\frac{G_{\mu\nu}}{R^{-2}} = \frac{T_{\mu\nu}}{\rho c^2} \tag{2.1}$$

for a fermionic gas represented by the stress tensor for a perfect fluid,

$$T^{\mu\nu} = \mathrm{diag}(\rho(r)c^2, P(r), P(r), P(r)) \tag{2.2}$$

The components of the stress tensor $T^{\mu\nu} \equiv T^{\mu\nu}(r)$ are the density $\rho(r)$ and the isotropic pressure $P(r)$. We assume that the fermions relax in a spherically symmetric hydrostatic equilibrium. Then, the metric $g_{\mu\nu}$ is given in the standard form

$$g_{\mu\nu} = \mathrm{diag}(\mathrm{e}^{2\nu(r)}, -\mathrm{e}^{2\lambda(r)}, -\mathrm{e}^{2\xi(r)}, -\mathrm{e}^{2\xi(r)}\sin^2\vartheta) \tag{2.3}$$

where $\nu(r)$, $\lambda(r)$ and $\xi(r)$ depend only on the radial coordinate r. The latter is defined by $\xi(r) = \ln r/R$ while the solutions for $\nu(r)$ and $\lambda(r)$ have to be found by solving eq. (2.1). The solution for $\lambda(r)$ is given by

$$\mathrm{e}^{-2\lambda(r)} = 1 - \frac{R}{r}\frac{M(r)}{M} \tag{2.4}$$

while the metric potential $\nu(r)$ is described by the relation

$$\frac{\mathrm{d}\nu}{\mathrm{d}r/R} = \frac{1}{2}\frac{R^2}{r^2}\left[\frac{M(r)}{M} + \frac{r^3}{R^3}\frac{P(r)}{\rho c^2}\right]\left[1 - \frac{R}{r}\frac{M(r)}{M}\right]^{-1} \tag{2.5}$$

The enveloped mass $M(r)$ within the radius r (hereafter simply the mass) is given through its derivative

$$\frac{\mathrm{d}}{\mathrm{d}r/R}\frac{M(r)}{M} = \frac{r^2}{R^2}\frac{\rho(r)}{\rho} \tag{2.6}$$

Ansatz for density and pressure

Density $\rho(r)$ and pressure $P(r)$ are described through a phase space distribution function in terms of statistical physics. Classically, the phase space distribution function is given with focus on the momentum space (Shapiro and Teukolsky, 2008, chap. 2.2). Since spherical symmetry is considered, it is more convenient to focus on the energy space with the particle energy ϵ (in units of mc^2). Energy and momentum are related locally through

$$\epsilon^2 = 1 + \frac{p^2}{m^2c^2} \tag{2.7}$$

allowing to derive an expression for the volume element d^3p in momentum space,

$$\mathrm{d}^3p = \frac{4}{\sqrt{\pi}}m^3\left[\pi c^2\right]^{3/2}\mathrm{d}^3\epsilon \tag{2.8}$$

with the symbol

$$\mathrm{d}^3\epsilon = \left[\epsilon^2 - 1\right]^{1/2}\epsilon\,\mathrm{d}\epsilon \tag{2.9}$$

Then, density and pressure are given by

$$\frac{\rho(r)}{\rho} = \frac{4}{\sqrt{\pi}}\int \epsilon f(r,\epsilon)\,\mathrm{d}^3\epsilon \tag{2.10}$$

$$\frac{P(r)}{\rho c^2} = \frac{4}{3\sqrt{\pi}}\int \left[1-\epsilon^{-2}\right]\epsilon f(r,\epsilon)\,\mathrm{d}^3\epsilon \tag{2.11}$$

where $\epsilon \geq 1$. The factor $1/3$ in eq. (2.11) comes from isotropy. No additional interaction is assumed for the fermions besides their fulfilling of quantum statistics and the relativistic gravitational equation.

Unit system

Here, we introduced the scaling factors R, M and ρ for length, mass and density to eliminate the particle mass and other physical constants from the equations. It is convenient to describe the scale factors in the Planck unit system. In particular, with the Planck mass $m_\mathrm{P} = \sqrt{\hbar c/G}$, the Planck length $l_\mathrm{P} = \sqrt{\hbar G/c^3}$ and the Planck density $\rho_\mathrm{P} = m_\mathrm{P}/l_\mathrm{P}^3$ we obtain a unit system with focus on the particle mass,

$$\log\frac{R}{l_\mathrm{P}} = \log C_R \; - 2\log\frac{m}{m_\mathrm{P}} \tag{2.12}$$

$$\log\frac{M}{m_\mathrm{P}} = \log C_M \; - 2\log\frac{m}{m_\mathrm{P}} \tag{2.13}$$

$$\log\frac{\rho}{\rho_\mathrm{P}} = \log C_\rho \; + 4\log\frac{m}{m_\mathrm{P}} \tag{2.14}$$

with the coefficients

$$C_R = g^{-1/2}\,\pi^{1/4}$$

$$C_M = \frac{1}{2}\,g^{-1/2}\,\pi^{1/4}$$

$$C_\rho = \frac{1}{8\pi}\,g\,\pi^{-1/2}$$

For mass and length we may use the equivalent relation $2GM/R = c^2$ and $M = 4\pi R^3 \rho$ where G is the gravitational constant and c is the speed of light. Further, $\hbar$ is the reduced Planck's constant, m is the particle mass and g is the particle degeneracy. For fermions we use $g = 2$.

2.1.1 Alternative picture

It will be helpful to consider a representation of the stress tensor by substituting the pressure. We keep the idea of a density (e.g. mass or energy) and describe the pressure

$$\frac{P(r)}{\rho c^2} = \frac{\rho(r)}{\rho}\frac{\sigma^2(r)}{c^2} \tag{2.15}$$

through the density $\rho(r)$ and the velocity dispersion $\sigma(r)$ defined by

$$\frac{\sigma^2(r)}{c^2} = \frac{\frac{1}{3}\int \frac{v^2}{c^2} h(r,\epsilon)\,\mathrm{d}^3\epsilon}{\int h(r,\epsilon)\,\mathrm{d}^3\epsilon} \tag{2.16}$$

where $\epsilon \geq 1$. The velocities are weighted and normalized by the particle energy distribution function

$$h(r,\epsilon) = \epsilon f(r,\epsilon) \tag{2.17}$$

what resembles a weighted phase-space distribution function. The denominator of eq. (2.16) is exactly the definition of the density $\rho(r)$ given by eq. (2.10). With eq. (2.17) and

$$\frac{v^2}{c^2} = 1 - \epsilon^{-2} \tag{2.18}$$

it is straightforward to show that the numerator is equivalent to the pressure defined by eq. (2.11). In this picture the pressure may be interpreted as an isotropic velocity dispersion where the velocities are weighted with the energy distribution function. The stress tensor becomes then $T^{\mu\nu} = \rho(r)\sigma^{\mu\nu}$ with the velocity dispersion tensor

$$\sigma^{\mu\nu} = \mathrm{diag}(1, \sigma^2(r), \sigma^2(r), \sigma^2(r)) \tag{2.19}$$

In next, we define two further variables which will help to understand the properties of the metric potential. It is very convenient to consider the compactness $\varphi(r)$ what is defined as the ratio of the Schwarzschild radius of the enclosed mass $M(r)$ over the corresponding radius. In the chosen unit system we simply find

$$\varphi(r) = \frac{R}{r}\frac{M(r)}{M} \tag{2.20}$$

Additionally, we define an *effective* velocity dispersion

$$\frac{\varsigma^2(r)}{c^2} = \gamma(r)\frac{\sigma^2(r)}{c^2} \tag{2.21}$$

with the substitution

$$\gamma(r) = \frac{\mathrm{d}\ln M(r)/M}{\mathrm{d}\ln r/R} \tag{2.22}$$

Both, compactness $\varphi(r)$ and *effective* velocity dispersion $\varsigma(r)$, allow to rewrite eq. (2.5) to

$$\frac{\mathrm{d}\nu}{\mathrm{d}\ln r/R} = \frac{1}{2}\left[\frac{\varphi(r)}{1-\varphi(r)}\right]\left[1 + \frac{\varsigma^2(r)}{c^2}\right] \tag{2.23}$$

Note that physical velocities ($v < c$) give the inequality

$$0 \leq \frac{\sigma^2(r)}{c^2} < \frac{1}{3} \tag{2.24}$$

Additionally with $\gamma(r) \in [0, 3]$, where the upper limit is given for a hypothetical constant density (see section 2.3.2 for details), yields immediately $\varsigma(r) < c$ what tells that the defined velocity dispersions, $\sigma(r)$ and $\varsigma(r)$, indeed describe physical velocities. Finally, it is worth to emphasize that the compactness is always smaller than one, $\varphi(r) < 1$, according to eq. (2.4) and that, interestingly, it is independent of the particle mass, following eqs. (2.12) and (2.13).

2.1.2 Proper circular velocity

Complimentary to density, pressure and mass profiles we are interested also in circular velocities (of test particles) around the center of the mass distribution relative to a non-moving observer. The proper four-velocity is defined as $v^\mu = \mathrm{d}x^\mu / \mathrm{d}\tau$ where $\mathrm{d}x^\mu$ is the distance measured in the local frame $(\mathrm{d}t, \mathrm{d}r, \mathrm{d}\theta, \mathrm{d}\varphi)$ and τ is the proper time of the observed particle. The Lagrangian for a test particle on a circular orbit ($\mathrm{d}r = 0$ and by symmetry $\vartheta = \pi/2$) is given by

$$\frac{2L(x^\mu, \dot{x}^\mu)}{c^2} = \mathrm{e}^{2\nu(r)} \left[\frac{\mathrm{d}t}{\mathrm{d}\tau}\right]^2 - \frac{r^2}{c^2}\left[\frac{\mathrm{d}\varphi}{\mathrm{d}\tau}\right]^2 \tag{2.25}$$

Of interest is only the radial component of the Euler-Lagrange equation,

$$0 = \mathrm{e}^{2\nu(r)} \frac{\mathrm{d}\nu}{\mathrm{d}r} \left[\frac{\mathrm{d}t}{\mathrm{d}\tau}\right]^2 - \frac{r}{c^2}\left[\frac{\mathrm{d}\varphi}{\mathrm{d}\tau}\right]^2 \tag{2.26}$$

Additionally, using the constraint $v^\mu v_\mu = c^2$ gives

$$1 = \mathrm{e}^{2\nu(r)} \left[\frac{\mathrm{d}t}{\mathrm{d}\tau}\right]^2 - \frac{r^2}{c^2}\left[\frac{\mathrm{d}\varphi}{\mathrm{d}\tau}\right]^2 \tag{2.27}$$

Finally, using eqs. (2.26) and (2.27) and solving for the proper velocity defined by $v(r) = r\,\mathrm{d}\varphi/\,\mathrm{d}\tau$ yields

$$\frac{v^2(r)}{c^2} = \frac{1}{\left[\dfrac{\mathrm{d}\nu}{\mathrm{d}\ln r/R}\right]^{-1} - 1} \tag{2.28}$$

Note the difference to the classic velocity defined in space through $v^i = \mathrm{d}x^i/\,\mathrm{d}t$ where all measurements (in particular the local time t) are done in the local frame. In that case it is easy to show that the speed of light describes the upper velocity limit. But here the proper circular velocity $v(r)$ is simply the momentum per unit mass. Since the momentum is not bounded this is also the case for the proper velocity in general. Besides, the proper velocity is sometimes also called celerity.

In the remaining part of this chapter we are interested in the proper circular velocity (hereafter simply *circular velocity*). But in the following chapters, of interest will be the *classical* circular velocity referred with the same symbol $v(r)$ and given by

$$\frac{v^2(r)}{c^2} = \frac{\mathrm{d}\nu}{\mathrm{d}\ln r/R} \tag{2.29}$$

2.1.3 Compactness limit

With the help of circular velocity it is possible to constrain the compactness even more than $\varphi(r) < 1$. Eliminating the metric potential in eqs. (2.23) and (2.28) and

solving for the compactness yields

$$\varphi(r) = \frac{\frac{v^2(r)}{c^2}}{\frac{1}{2}\left[1+\frac{v^2(r)}{c^2}\right]\left[3+\frac{\varsigma^2(r)}{c^2}\right]-1} \tag{2.30}$$

Keeping in mind that the proper circular velocity $v(r)$ is in general not bounded gives the upper limit

$$\varphi_{\max}(r) = \lim_{v(r)\to\infty}\varphi(r) = \frac{2}{3+\frac{\varsigma^2(r)}{c^2}} \tag{2.31}$$

An increase of the effective velocity dispersion decreases the maximal possible compactness. Hence, for $\varsigma(r) = 0$ we obtain the absolute maximum

$$\varphi(r) < \frac{2}{3} \tag{2.32}$$

On other hand, considering the upper limit of the effective velocity dispersion, $\varsigma(r) \to c$, gives the limit $\varphi(r) < 1/2$.

2.1.4 Hydrostatic equation

Additionally to (2.5) we remind that the stress tensor is divergence free and this leads to

$$\frac{\mathrm{d}\nu}{\mathrm{d}r/R} = -\left[\frac{\rho(r)}{\rho}+\frac{P(r)}{\rho c^2}\right]^{-1}\frac{\mathrm{d}}{\mathrm{d}r/R}\frac{P(r)}{\rho c^2} \tag{2.33}$$

Comparing eqs. (2.5) and (2.33) yields the well known Tolman-Oppenheimer-Volkoff (TOV) equation (Shapiro and Teukolsky, 2008, page 125)

$$\frac{\mathrm{d}}{\mathrm{d}r/R}\frac{P(r)}{\rho c^2} = -\frac{1}{2}\frac{R^2}{r^2}\left[\frac{\rho(r)}{\rho}+\frac{P(r)}{\rho c^2}\right]\left[\frac{M(r)}{M}+\frac{r^3}{R^3}\frac{P(r)}{\rho c^2}\right]\left[1-\frac{R}{r}\frac{M(r)}{M}\right]^{-1} \tag{2.34}$$

Analogue to eq. (2.23) we may write

$$\frac{\mathrm{d}\ln P/\rho c^2}{\mathrm{d}\ln r/R} = -\frac{1}{2}\frac{c^2}{\sigma^2(r)}\left[1+\frac{\sigma^2(r)}{c^2}\right]\left[\frac{\varphi(r)}{1-\varphi(r)}\right]\left[1+\frac{\varsigma^2(r)}{c^2}\right] \tag{2.35}$$

2.2 Lowered Fermi-Dirac distribution

In order to solve the metric potential (2.5) we consider the Fermi-Dirac distribution with an energy cutoff,

$$f(r,\epsilon) = \frac{1-\mathrm{e}^{[\epsilon-\varepsilon(r)]/\beta(r)}}{\mathrm{e}^{[\epsilon-\alpha(r)]/\beta(r)}+1} \tag{2.36}$$

for $\epsilon \leq \varepsilon(r)$. Note that the escape energy $\varepsilon(r)$ limits the upper bound in eqs. (2.10) and (2.11). Particles with an energy ϵ above the escape energy $\varepsilon(r)$ are too fast to be kept by the mass distribution. Thus, we may consider those particles as lost what causes a cutoff in the phase space (King, 1966).

The phase-space distribution function $f(r,\epsilon)$ contains a lot of information encoded in the temperature variable $\beta(r)$, the chemical potential $\alpha(r)$ and the cutoff energy $\varepsilon(r)$. They are defined by

$$\beta(r) = \frac{k_B T(r)}{mc^2} \tag{2.37}$$

$$\alpha(r) = 1+\frac{\mu(r)}{mc^2} \tag{2.38}$$

$$\varepsilon(r) = 1+\frac{E_\infty(r)}{mc^2} \tag{2.39}$$

All three parameters are related with the metric potential through the Tolman relation (Tolman and Ehrenfest, 1930), the Klein relation (Klein, 1949) and the conservation of energy (Merafina and Ruffini, 1989). In detail, we find

$$\frac{\mathrm{d}\ln\beta(r)}{\mathrm{d}r/R} = \frac{\mathrm{d}\ln\alpha(r)}{\mathrm{d}r/R} = \frac{\mathrm{d}\ln\varepsilon(r)}{\mathrm{d}r/R} = -\frac{\mathrm{d}\nu}{\mathrm{d}r/R} \tag{2.40}$$

Note, that $\alpha(r)$ and $\varepsilon(r)$ contain the rest mass. Hence, $\mu(r)$ is the chemical potential with rest mass subtracted, $E_\infty(r)$ is the kinetic particle escape energy, $T(r)$ is the temperature and k_B is the Boltzmann constant.

Degeneracy and cutoff variables

In next, it is convenient to introduce the degeneracy variable $\theta(r)$ and the cutoff variable $W(r)$, defined by

$$\theta(r) = \frac{\mu(r)}{k_B T(r)} \tag{2.41}$$

$$W(r) = \frac{E_\infty(r)}{k_B T(r)} \tag{2.42}$$

Chemical potential and cutoff energy become

$$\alpha(r) = 1 + \beta(r)\theta(r) \tag{2.43}$$

$$\varepsilon(r) = 1 + \beta(r)W(r) \tag{2.44}$$

Inserting these expressions in eq. (2.40) gives

$$\frac{\mathrm{d}\theta}{\mathrm{d}r/R} = \frac{\mathrm{d}W}{\mathrm{d}r/R} = -\frac{1}{\beta(r)}\frac{\mathrm{d}\nu}{\mathrm{d}r/R} \tag{2.45}$$

Initial condition

Each configuration of the mass distribution is characterized by the initial condition

$$M(0) = M_0, \quad \beta(0) = \beta_0, \quad \theta(0) = \theta_0, \quad W(0) = W_0 \tag{2.46}$$

It is important to mention here that no black holes at the galactic center are assumed, what gives the condition $M_0 = 0$. The remaining configuration parameters (β_0, θ_0, W_0) represent finite mass distributions composed of massive fermions in spherical symmetry. Every mass distribution is described equivalently through variables such like the metric potential $\nu(r)$ given by eq. (2.5), mass $M(r)$ given by eq. (2.6), density $\rho(r)$ given by eq. (2.10), pressure $P(r)$ given by eq. (2.11) or circular velocity $v(r)$ given by eq. (2.28). Are dimensionless solutions of interest, e.g by considering the unit system given by eqs. (2.12) to (2.14), then the three configuration parameters are sufficient. Thus, this approach is appropriate when only physical properties needed to be analyzed. But in order to compare physical observables with predictions of the model the particle mass m is necessary to provide physical properties in the right unit system (e.g. SI units). Then, physical variables depend on a set of four model parameters $(\beta_0, \theta_0, W_0, m)$. Therefore, it is important to keep in mind that the simplified notation focusing on the radial distance implies a given set of model parameters. For example, $M(r)$ is a synonym for $M(\beta_0, \theta_0, W_0, m, r)$ and describes actually a five parametric function. Analogue for other physical variables.

Solving eq. (2.40) with the above initial conditions yields

$$\frac{\beta(r)}{\beta_0} = \frac{\alpha(r)}{\alpha_0} = \frac{\varepsilon(r)}{\varepsilon_0} \tag{2.47}$$

or equivalent

$$\frac{1}{\beta_0} - \frac{1}{\beta(r)} = \theta(r) - \theta_0 = W(r) - W_0 \tag{2.48}$$

where $\alpha_0 = 1 + \beta_0\theta_0$ and $\varepsilon_0 = 1 + \beta_0 W_0$.

Remark: Note that the metric potential $\nu(r)$ is - in principle - not necessary for the mass distribution. Important is only the derivative of the metric potential. Thus, $\nu(r)$ may be considered as a synonym for the difference $\nu(r) - \nu_0$ with arbitrary ν_0.

Analysis of variables

After defining the initial condition, see eq. (2.46), it is interesting to look at the behavior of the variables for increasing radii. Density, pressure, mass and temperature are positive by definition. With this information we easily may conclude that the mass $M(r)$ and the metric potential $\nu(r)$ are monotonically increasing functions, $\mathrm{d}M/\,\mathrm{d}r \geq 0$ and $\mathrm{d}\nu/\,\mathrm{d}r \geq 0$. The equality is fulfilled at the center only where we exclude the formation of black holes, $M(r)/M > r/R$. This implies the exclusion of any singularities for the metric potential, $\mathrm{d}\nu/\,\mathrm{d}r < \infty$.

Hence, the temperature parameter $\beta(r)$, the chemical potential $\alpha(r)$ and the escape energy $\varepsilon(r)$ are monotonically decreasing functions, $\mathrm{d}\beta/\,\mathrm{d}r \leq 0$, $\mathrm{d}\alpha/\,\mathrm{d}r \leq 0$, $\mathrm{d}\varepsilon/\,\mathrm{d}r \leq 0$. According to eq. (2.45) this is also the case for the degeneracy and cutoff parameter, $\mathrm{d}\theta/\,\mathrm{d}r \leq 0$ and $\mathrm{d}W/\,\mathrm{d}r \leq 0$.

Finally, following eq. (2.34) we immediately find that the pressure $P(r)$ is also a monotonically decreasing function. Without showing in detail, we conclude that the density $\rho(r)$ provides the same characteristic.

Boundary condition

In next, it will be shown that the mass distributions are always finite in mass and size for finite central cutoff parameter W_0. As mentioned above, particles with an energy above the escape energy are considered as lost. In combination with the fact, that the escape energy $\varepsilon(r) = 1 + \beta(r)W(r)$ is a monotonic decreasing function, it immediately implies a finite surface radius r_s. Keep in mind that the surface radius has to be a function of the initial condition parameters and the particle mass, $r_s \equiv r_s(\beta_0, \theta_0, W_0, m)$. Beyond the surface radius no particles contribute to the mass distribution. Thus, at the surface the kinetic escape energy has to drop to zero such that any particle crossing the surface radius is considered as lost. Since we consider a hydrostatic equilibrium it implies that the same amount of particles coming from an outer basin beyond the surface radius (e.g. intergalactic medium) are caught by the mass distribution. Clearly, at the surface density and pressure drop to the corresponding values of that basin. Alternatively, the loss of particle (evaporation) is so slow that the hydrostatic equilibrium resembles quasi-stationary solutions. In any case, it is convenient to assume that the surface density and pressure are negligible such that $\rho(r_s) = P(r_s) = 0$. Thus, for a finite $W_0 > 0$ the monotonically decreasing cutoff parameter $W(r)$ always reaches the boundary condition $W(r_s) = 0$ within a finite surface radius. Then, in contrast to the initial condition given by eq. (2.46), it is suitable to consider the boundary condition

$$M(r_s) = M_s, \quad \beta(r_s) = \beta_s, \quad \theta(r_s) = \theta_s, \quad W(r_s) = 0 \tag{2.49}$$

Here, M_s is the total mass while β_s and θ_s are the surface values of the corresponding variables. The boundary condition parameters (M_s, β_s, θ_s) are equivalent to the initial condition parameters (β_0, θ_0, W_0). Clearly, since $\beta(r)$, $\theta(r)$ and $W(r)$ are monotonic

decreasing functions (as described above) we have the inequalities $\beta_0 > \beta_s$, $\theta_0 > \theta_s$ and $W_0 > 0$. Indeed, with eq. (2.48) we obtain

$$\beta_s = \frac{\beta_0}{1 + \beta_0 W_0} \tag{2.50}$$

$$\theta_s = \theta_0 - W_0 \tag{2.51}$$

Regarding the total mass, we may say only that it has to be a function of the initial condition parameters and the particle mass, $M_s \equiv M_s(\beta_0, \theta_0, W_0, m)$. Here, we see that the cutoff parameter W_0 has direct influence on the finiteness of the surface parameters. In particular, for the limiting case $W_0 \to \infty$, implying mass distribution infinite in mass and size, yields $\beta_s \to 0$ and $\theta_s \to -\infty$.

Besides the finiteness of the surface parameter, an interesting characteristic shows the temperature parameter. Considering limiting cases for the *escape well depth* given by the product $\beta_0 W_0$, we obtain

$$\beta_s \approx \begin{cases} \beta_0 & (\beta_0 W_0 \ll 1) \\ \dfrac{1}{W_0} & (\beta_0 W_0 \gg 1) \end{cases} \tag{2.52}$$

Thus, for shallow escape wells ($\beta_0 W_0 \ll 1$) the temperature doesn't change significantly. But for deep escape wells ($\beta_0 W_0 \gg 1$) the surface temperature is determined by W_0 only.

Alternatively to the surface of the mass distribution it is suitable to consider a different boundary condition not relying on the cutoff parameter, especially in the limiting case $W_0 \to \infty$. This alternative boundary condition yields a boundary radius $r_b < r_s$ with corresponding β_b and θ_b. The latter are related through

$$\beta_b = \frac{\beta_0}{1 + \beta_0(\theta_0 - \theta_b)} \tag{2.53}$$

2.3 Limiting cases and approximations

The fermionic model with cutoff generalizes two well known limiting cases: the infinitely deep potential well ($W(r) \to \infty$) and the diluted case ($\mathrm{e}^{\theta(r)} \ll 1$),

$$f(r, \epsilon) \approx \begin{cases} \left[\mathrm{e}^{[\epsilon - \alpha(r)]/\beta(r)} + 1\right]^{-1} & W_0 \to \infty \\ \left[\mathrm{e}^{[\varepsilon(r) - \epsilon]/\beta(r)} - 1\right] \mathrm{e}^{\theta_0 - W_0} & \theta_0 \ll -1 \\ \mathrm{e}^{[\alpha(r) - \epsilon]/\beta(r)} & W_0 \to \infty \text{ and } \theta_0 \ll -1 \end{cases} \tag{2.54}$$

For the first case, implying $W_0 \to \infty$, the Fermi-Dirac distribution is recovered (Gao, Merafina, and Ruffini, 1990; Merafina and Ruffini, 1989), for the second case, implying $\theta_0 \ll -1$, we obtain the relativistic version of the King model (see King (1966) for the Newtonian approach) and the third case is the combination of the two possible limits which describes the relativistic version of the Boltzmann statistics (see e.g. Binney and Tremaine (2008) for the Newtonian approach).

In following the condition $\theta_0 \ll 1$ will be used as a synonym for $\mathrm{e}^{\theta(r)} \ll 1$. Since $\theta(r)$ is a monotonic decreasing function it is sufficient to consider the central value because it is the maximal value. Note that the condition for the diluted case is well fulfilled already for $\theta_0 \lesssim -5$.

In this section the RAR model with cutoff ($W_0 < \infty$) will be compared with the Newtonian versions of eq. (2.54) to understand the model in contrast to the classical models. Additionally, for a better physical understanding it will be helpful to consider also the approximation of a uniform body ($\rho(r) \approx \rho_0$), the fully degenerate core ($f(r, \epsilon) \approx 1$) and low compactness ($\varphi(r) \ll 1$).

2.3.1 Low compactness and velocities

We want to simplify the metric potential $\nu(r)$, using the more suitable picture with compactness $\varphi(r)$ and velocity dispersion $\sigma(r)$ or, similar, effective velocity dispersion $\varsigma(r)$. Hence, in case of negligible compactness ($\varphi(r) \ll 1$) and velocities ($\sigma(r) \ll c$) the metric potential $\nu(r)$ given by eq. (2.23) may be approximated by

$$\frac{\mathrm{d}\nu}{\mathrm{d}r/R} \approx \frac{1}{2}\frac{R^2}{r^2}\frac{M(r)}{M} \tag{2.55}$$

Together with the mass given by eq. (2.6) the metric potential can be described through the Poissonian

$$\frac{R^2}{r^2}\frac{\mathrm{d}}{\mathrm{d}r/R}\left[\frac{r^2}{R^2}\frac{\mathrm{d}\nu}{\mathrm{d}r/R}\right] \approx \frac{1}{2}\frac{\rho(r)}{\rho} \tag{2.56}$$

Interestingly, the metric potential becomes independent of the mass $M(r)$ and pressure $P(r)$. The mass is given unchanged by eq. (2.6). But the pressure is described by the hydrostatic equation

$$\frac{\mathrm{d}}{\mathrm{d}r/R}\frac{P(r)}{\rho c^2} \approx -\frac{1}{2}\frac{R^2}{r^2}\frac{M(r)}{M}\frac{\rho(r)}{\rho} \tag{2.57}$$

what is an approximation of the TOV equation given by eq. (2.35). Finally, inserting eq. (2.55) in eq. (2.28) expanding for low compactness we recover the classical expression for the circular velocity,

$$\frac{v^2(r)}{c^2} \approx \frac{1}{2}\frac{R}{r}\frac{M(r)}{M} \tag{2.58}$$

The factor $1/2$ is because of the chosen unit system. However, with the relation $2GM = Rc^2$ it is straightforward to obtain the expression commonly given in literature, e.g. $v^2(r) = GM(r)/r$.

Note that relativistic effects are negligible for this approximation due to low compactness and velocities. Accordingly, the approximation of the proper circular velocity given by eq. (2.28) and the approximation of the classical circular velocity given by eq. (2.29) yield the same result, making no difference between those two definitions.

2.3.2 Uniform body

A uniform body is characterized through a (nearly) constant density $\rho(r) = \rho_0$. We consider a spherical uniform body with the surface radius r_s. In this case it is suitable to choose a unit system with focus on the density ρ_0. Thus, we introduce new scale factors for length and mass, like

$$\log\frac{R_0}{l_\mathrm{P}} = \log C_{R_0} \; -\frac{1}{2}\log\frac{\rho_0}{\rho_\mathrm{P}} \tag{2.59}$$

$$\log\frac{M_0}{m_\mathrm{P}} = \log C_{M_0} \; -\frac{1}{2}\log\frac{\rho_0}{\rho_\mathrm{P}} \tag{2.60}$$

with the coefficients

$$C_{R_0} = \frac{1}{\sqrt{8\pi}}$$

$$C_{M_0} = \frac{1}{2}\frac{1}{\sqrt{8\pi}}$$

Equivalently, the scale factors fulfill the relations $2GM_0 = R_0c^2$ and $M_0 = 4\pi R_0^3\rho_0$. Relative to the *relativistic* unit system this unit system is described through the density ratio ρ_0/ρ,

$$\left[\frac{R_0^2}{R}\right]^{-2} = \left[\frac{M_0^2}{M}\right]^{-2} = \frac{\rho_0}{\rho} \tag{2.61}$$

Then, with the solution for the mass

$$\frac{M(r)}{M_0} = \frac{1}{3}\frac{r^3}{R_0^3} \tag{2.62}$$

we obtain the hydrostatic equation

$$\frac{\mathrm{d}}{\mathrm{d}r/R_0}\frac{P(r)}{\rho_0 c^2} = -\frac{1}{6}\frac{r}{R_0}\left[1+\frac{P(r)}{\rho_0 c^2}\right]\left[1+3\frac{P(r)}{\rho_0 c^2}\right]\left[1-\frac{1}{3}\frac{r^2}{R_0^2}\right]^{-1} \tag{2.63}$$

where the radius is valid within the interval $[0, \sqrt{3}R_0]$. It is has a solution where it is better to express R_0 through the compactness $\varphi_s = \varphi(r_s)$ and the surface radius r_s. Following the definition of the compactness given by eq. (2.20) we find

$$\frac{r_s^2}{R_0^2} = 3\varphi_s \tag{2.64}$$

Then, the solution for the hydrostatic equation is given by

$$\frac{P(r)}{\rho_0 c^2} = -\frac{1 \pm \sqrt{\dfrac{1-\varphi_s\frac{r^2}{r_s^2}}{1-\varphi_s}}}{3 \pm \sqrt{\dfrac{1-\varphi_s\frac{r^2}{r_s^2}}{1-\varphi_s}}} \tag{2.65}$$

Buchdahl-Bondi limit

Of interest is the solution with a negative sign of the square root. Otherwise, eq. (2.65) would give negative pressure values for all radii (within the allowed interval) what is not physical. Instead, only real and positive values of the pressure are allowed. The maximal pressure is given at the center ($r = 0$) because pressure is a monotonic decreasing function. In particular, the condition $P(0) < \infty$ yields the well known Buchdahl-Bondi limit (Bondi, 1964; Buchdahl, 1959, 1966). This limit gives an upper limit for the compactness,

$$\varphi_s < \frac{8}{9} \tag{2.66}$$

Stronger constraints on the limit

According to eq. (2.15) pressure and velocity dispersion are equivalent in the case of a constant density,

$$\frac{P(r)}{\rho_0 c^2} = \frac{\sigma^2(r)}{c^2} \tag{2.67}$$

Then, following the inequality for the velocity dispersion given by eq. (2.24) we obtain the limit

$$\frac{P(r)}{\rho_0 c^2} < \frac{1}{3} \tag{2.68}$$

In summary, we find that for the mass distribution of a homogeneous perfect fluid the upper limit for the compactness decreases below the Buchdahl-Bondi limit,

$$\varphi_s < \frac{5}{9} \tag{2.69}$$

Comparing this result with the absolute compactness limit of $\varphi(r) < 2/3$, see eq. (2.32), tells that arbitrary combination of proper circular velocity $v(r)$ and effective velocity dispersion $\varsigma(r)$ are not allowed. For instance, when the proper circular velocity approaches infinity, $v(r) \to \infty$, then the effective velocity dispersion is bounded to $\varsigma^2(r) < 3/5$.

Schwarzschild radius

The above derived upper limits for compactness are maybe better to understand through the Schwarzschild radius. However, the ratio of surface and Schwarzschild radius is simply the inverse of the compactness as defined by eq. (2.20). Then, following the unit transformation given by eq. (2.61) gives $\varphi_s = r_{\rm Sch}/r_s$ with the corresponding Schwarzschild radius $r_{\rm Sch} \equiv r_{\rm Sch}(r_s) = 2GM(r_s)/c^2$. Therefore, the size of a uniform body (in units of $r_{\rm Sch}$) is restricted through

$$\frac{r_s}{r_{\rm Sch}} > \frac{9}{8} = 1.125 \tag{2.70}$$

Thus, the lower limit for the surface radius r_s is just above the corresponding Schwarzschild radius before the solutions become unphysical. For a uniform body composed of fermions the lower size limit is raised to

$$\frac{r_s}{r_{\rm Sch}} > \frac{9}{5} = 1.8 \tag{2.71}$$

Interestingly, this limit is above the Innermost Stable Circular Orbit (ISCO) for photons, $r_{\rm ISCO}/r_{\rm Sch} = 1.5$, describing the photon sphere.

Low compactness

For low compactness ($\varphi \ll 1$) the solution for the pressure simplifies to

$$\frac{P(r)}{\rho_0 c^2} \approx \frac{\varphi_s}{4}\left[1 - \frac{r^2}{r_s^2}\right] \tag{2.72}$$

However, these results are valid only for a theoretical uniform body. This condition is approximately fulfilled at the center far from any abrupt surface where the density drops immediately to zero. Instead, a relativistic density profile has a (slightly) decreasing behavior in the core with $\rho(r) \approx \rho_0$ for sufficient small radii, e.g. below a core radius $r < r_c$. This density behavior should raise the lower limit for a surface even more, although probably in an analytically more complicated way.

Low compactness and low velocity dispersion

In the case of low compactness, $\varphi(r_s) \ll 1$ or equivalent $r \ll R_0$, and low velocity dispersion, $\sigma(r) \ll c$, the hydrostatic equation simplifies to

$$\frac{\mathrm{d}}{\mathrm{d}r/R_0}\frac{P(r)}{\rho_0 c^2} \approx -\frac{1}{6}\frac{r}{R_0} \tag{2.73}$$

It has the solution

$$\frac{P(r)}{\rho_0 c^2} \approx \frac{P_0}{\rho_0 c^2} - \frac{1}{12}\frac{r^2}{R_0^2} \tag{2.74}$$

2.3.3 Fully degenerate core

The fully degenerate core is described by the approximation $f(r,\epsilon) \approx 1$. This condition is fulfilled for the degenerate case with $\theta_0 > 0$ (especially for $\theta_0 \gtrsim 10$) locally at the center ($r \approx 0$) or globally for low temperatures $\beta(r) \to 0$. Then, density and pressure simplify to (e.g. Shapiro and Teukolsky, 2008, chap. 2.3)

$$\frac{\rho(r)}{\rho} \approx \frac{1}{2\sqrt{\pi}} \left[2\varepsilon_\mathrm{F}(r)\kappa^3(r) + \varepsilon_\mathrm{F}(r)\kappa(r) - \ln\left[\varepsilon_\mathrm{F}(r) + \kappa(r)\right]\right] \tag{2.75}$$

$$\frac{P(r)}{\rho c^2} \approx \frac{1}{2\sqrt{\pi}} \left[\frac{2}{3}\varepsilon_\mathrm{F}(r)\kappa^3(r) - \varepsilon_\mathrm{F}(r)\kappa(r) + \ln\left[\varepsilon_\mathrm{F}(r) + \kappa(r)\right]\right] \tag{2.76}$$

with the substitution

$$\kappa(r) = \sqrt{\varepsilon_\mathrm{F}^2(r) - 1} \tag{2.77}$$

Here, $\varepsilon_\mathrm{F}(r) \geq 1$ is the Fermi energy (with rest-mass included) which is given either by the cutoff energy $\varepsilon(r)$ or the chemical potential $\alpha(r)$,

$$\varepsilon_\mathrm{F}(r) = \begin{cases} \alpha(r) & \alpha_0 \leq \varepsilon_0 \\ \varepsilon(r) & \alpha_0 > \varepsilon_0 \end{cases} \tag{2.78}$$

According to eq. (2.77) it is clear that the fully degenerate core is applicable only in the degenerate case $\theta(r) > 0$.

Low Fermi energy

For very low Fermi energies ($\varepsilon_\mathrm{F}(r) \approx 1$) the density becomes

$$\frac{\rho(r)}{\rho} \approx \frac{4}{3\sqrt{\pi}} \left[2\varepsilon_\mathrm{F}(r) - 2\right]^{3/2} \tag{2.79}$$

while the pressure simplifies to

$$\frac{P(r)}{\rho c^2} \approx \frac{4}{15\sqrt{\pi}} \left[2\varepsilon_\mathrm{F}(r) - 2\right]^{5/2} \tag{2.80}$$

Interestingly, the velocity dispersion, as defined by eq. (2.16), is then described by the Fermi energy,

$$\frac{\sigma^2(r)}{c^2} \approx \frac{2}{5}\left[\varepsilon_\mathrm{F}(r) - 1\right] \tag{2.81}$$

Then, the upper limit for the velocity dispersion, see eq. (2.24), yields an upper limit for the Fermi energy. Note, that the Fermi energy is a monotonic decreasing function. Expressing it through the central temperature and degeneracy parameter gives the inequality

$$\beta_0\theta_0 \ll \frac{5}{6} \tag{2.82}$$

This is equivalent to the low Fermi energy condition, $\varepsilon_\mathrm{F}(0) \approx 1$.

High Fermi energy

On the other hand, for very high Fermi energies ($\varepsilon_\mathrm{F}(r) \gg 1$) we find

$$\frac{\rho(r)}{\rho} \approx \frac{1}{\sqrt{\pi}} \left[\varepsilon_\mathrm{F}^4(r) + \frac{1}{2}\varepsilon_\mathrm{F}^2(r) - \frac{1}{2}\ln(2\varepsilon_\mathrm{F}(r))\right] \tag{2.83}$$

$$\frac{P(r)}{\rho c^2} \approx \frac{1}{3\sqrt{\pi}} \left[\varepsilon_\mathrm{F}^4(r) - \frac{3}{2}\varepsilon_\mathrm{F}^2(r) + \frac{3}{2}\ln(2\varepsilon_\mathrm{F}(r))\right] \tag{2.84}$$

Considering only the leading term we obtain the limits

$$\frac{P(r)}{\rho c^2} \approx \frac{1}{3}\frac{\rho(r)}{\rho} \approx \frac{1}{3\sqrt{\pi}}\left[\varepsilon_{\mathrm{F}}(r)\right]^4 \tag{2.85}$$

Thus, a fully degenerate core with high Fermi energies is similar to a diluted core described by an isothermal sphere which is described by a polytrope of index $n = \infty$ as well. The difference is that the velocity dispersion would approach one third of the speed of light,

$$\frac{\sigma^2(r)}{c^2} \approx \frac{1}{3} \tag{2.86}$$

This is exactly the upper limit as constraint by eq. (2.24).

2.3.4 Newtonian limit

For small kinetic energies, e.g. $p \ll mc$, the particle energy given by eq. (2.7) can be simplified by the expansion

$$\epsilon \approx 1 + \frac{1}{2}\frac{p^2}{m^2c^2} + \mathcal{O}(p^4) \tag{2.87}$$

The second term describes then classical particles. In addition, we consider shallow escape wells ($\beta_0 W_0 \ll 1$ or $\beta_0(\theta_0 - \theta_b) \ll 1$) what implies an isothermal distribution, $T(r) \approx T = \mathrm{const}$, according to eq. (2.52). Thus, we obtain the Newtonian approximation

$$\left[\epsilon - \alpha(r)\right]/\beta(r) \approx y^2 - \theta(r) \tag{2.88}$$

and analogue

$$\left[\epsilon - \varepsilon(r)\right]/\beta(r) \approx y^2 - W(r) \tag{2.89}$$

with the substitution

$$p^2 = 2mk_BTy^2 \tag{2.90}$$

The phase space distribution function becomes

$$f(r,y) \approx \frac{1 - \mathrm{e}^{y^2 - W(r)}}{\mathrm{e}^{y^2-\theta(r)} + 1} \tag{2.91}$$

with $y^2 < W(r)$. Then, density and pressure are given by

$$\frac{\rho(r)}{\rho_{\mathrm{B}}} \approx \frac{4}{\sqrt{\pi}}\int y^2 f(r,y)\,\mathrm{d}y \tag{2.92}$$

$$\frac{P(r)}{\rho_{\mathrm{B}}\sigma^2} \approx \frac{8}{3\sqrt{\pi}}\int y^4 f(r,y)\,\mathrm{d}y \tag{2.93}$$

For the velocity dispersion we obtain analogue to eq. (2.16) the expression

$$\frac{\sigma^2(r)}{\sigma^2} \approx \frac{\frac{2}{3}\int y^4 f(r,y)\,\mathrm{d}y}{\int y^2 f(r,y)\,\mathrm{d}y} \tag{2.94}$$

Here, the particle energy distribution function is approximately equal to the phase space distribution function, $h(r,y) \approx f(r,y)$, for low kinetic energies.

Change of the unit system

The substitution eq. (2.90) extracted the temperature from the distribution function $f(r, y)$. This affects all distribution function dependent variables. Instead of the temperature T it is more convenient to introduce the velocity dispersion constant σ defined by

$$\sigma^2 = \frac{k_B T}{m} \tag{2.95}$$

to eliminate the constant temperature in the equations. That constant has the dimension of a velocity and represents a new constraint which reduces the configuration parameter set by one. It fulfills the role of a scale factor analogue to the particle mass. Therefore, it is appropriate to introduce new scale factors for density, length and mass which include the particle mass as well the the velocity dispersion constant,

$$\log \frac{R_\text{B}}{l_\text{P}} = \log C_R \; - 2 \log \frac{m}{m_\text{P}} - \frac{1}{4} \log \frac{2\sigma^2}{c^2} \tag{2.96}$$

$$\log \frac{M_\text{B}}{m_\text{P}} = \log C_M \; - 2 \log \frac{m}{m_\text{P}} + \frac{3}{4} \log \frac{2\sigma^2}{c^2} \tag{2.97}$$

$$\log \frac{\rho_\text{B}}{\rho_\text{P}} = \log C_\rho \; + 4 \log \frac{m}{m_\text{P}} + \frac{3}{2} \log \frac{2\sigma^2}{c^2} \tag{2.98}$$

with the coefficients

$$C_R = g^{-1/2}\, \pi^{1/4}$$
$$C_M = \frac{1}{2}\, g^{-1/2}\, \pi^{1/4}$$
$$C_\rho = \frac{1}{8\pi}\, g\, \pi^{-1/2}$$

The density scale factor may be interpreted as the thermal de Broglie density $\rho_\text{B} = gm/\lambda_\text{B}^3$ with the thermal de Broglie wavelength $\lambda_\text{B} = h/\sqrt{2\pi m^2 \sigma^2}$. The scale factors for radius, mass and velocity fulfill the relations $GM_\text{B} = R_\text{B}\sigma^2$ and $M_\text{B} = 4\pi R_\text{B}^3 \rho_\text{B}$.

The relation between the *relativistic* and the *classic* unit systems is given by the temperature parameter β,

$$\left[\frac{\rho_\text{B}}{\rho}\right]^{2/3} = \left[\frac{R_\text{B}}{R}\right]^{-4} = \left[\frac{M_\text{B}}{M}\right]^{4/3} = \left[\frac{2\sigma}{c}\right]^2 = 2\beta \tag{2.99}$$

The substitution β is approximately the temperature variable $\beta(r)$. Because in the Newtonian case the temperature is approximately constant we may use $\beta(r) \approx \beta$.

Low compactness

The results of the fully degenerate core with low Fermi energies ($\beta_0\theta_0 \ll 1$) give the upper limits

$$\varphi(r) \lesssim \frac{12}{5}\beta_0\theta_0 \tag{2.100}$$

$$\varsigma(r) \lesssim \frac{6}{5}\beta_0\theta_0 \tag{2.101}$$

for compactness $\varphi(r)$ and effective velocity dispersion $\varsigma(r)$. This allows to apply the approximations for low compactness and velocities as derived in section 2.3.1. Following also the new unit system and eq. (2.45) we may describe the degeneracy $\theta(r)$ through the Poissonian

$$\frac{R_\text{B}^2}{r^2} \frac{\mathrm{d}}{\mathrm{d}r/R_\text{B}} \left[\frac{r^2}{R_\text{B}^2} \frac{\mathrm{d}\theta}{\mathrm{d}r/R_\text{B}}\right] \approx -\frac{\rho(r)}{\rho_\text{B}} \tag{2.102}$$

Analogue for the cutoff variable $W(r)$. For completeness, the mass $M(r)$ is given analogue to eq. (2.6),

$$\frac{\mathrm{d}}{\mathrm{d}r/R_\mathrm{B}}\frac{M(r)}{M_\mathrm{B}} = \frac{r^2}{R_\mathrm{B}^2}\frac{\rho(r)}{\rho_\mathrm{B}} \tag{2.103}$$

the hydrostatic equation by

$$\frac{\mathrm{d}}{\mathrm{d}r/R_\mathrm{B}}\frac{P(r)}{\rho_\mathrm{B}\sigma^2} \approx -\frac{R_\mathrm{B}^2}{r^2}\frac{M(r)}{M_\mathrm{B}}\frac{\rho(r)}{\rho_\mathrm{B}} \tag{2.104}$$

and the circular velocity by

$$\frac{v^2(r)}{\sigma^2} \approx \frac{R_\mathrm{B}}{r}\frac{M(r)}{M_\mathrm{B}} \tag{2.105}$$

Initial condition

To solve eq. (2.102) we consider the regular initial condition

$$\theta(0) = \theta_0 \quad \text{and} \quad \left.\frac{\mathrm{d}\theta}{\mathrm{d}r}\right|_0 = 0 \tag{2.106}$$

The second constraint follows from eq. (2.45). Analogue for $W(r)$.

Limiting cases

For the non relativistic cases we find the following limits for our fermionic model with cutoff,

$$f(r,y) \approx \begin{cases} \left[\mathrm{e}^{y^2-\theta(r)}+1\right]^{-1} & W_0 \to \infty \\ \left[\mathrm{e}^{W(r)-y^2}-1\right]\mathrm{e}^{\theta_0-W_0} & \theta_0 \ll -1 \\ \mathrm{e}^{\theta(r)-y^2} & W_0 \to \infty, \theta_0 \ll -1 \end{cases} \tag{2.107}$$

with $y^2 \leq W(r)$ for the second case ($\theta_0 \ll -1$) and $y^2 < \infty$ otherwise. The first limit describes a non-relativistic Fermi gas without cutoff what implies an unbounded mass distribution, the second limit describes a diluted Boltzmann gas with an energy cutoff, also known as the King model (King, 1966), and the third limit recovers the Boltzmann distribution which describes the isothermal sphere model (Binney and Tremaine, 2008).

2.3.5 Isothermal sphere model (non-relativistic)

The Isothermal Sphere (IS) is the most simple model regarding the approximation of the phase space distribution function (besides the fully degenerate core). Here, the distribution function, given by eq. (2.91), simplifies to the Boltzmann distribution

$$f(r,y) \approx \mathrm{e}^{\theta(r)-y^2} \tag{2.108}$$

for $W_0 \to \infty$ and $\theta_0 \ll -1$. Indeed, the latter condition is sufficiently fulfilled already for $\theta_0 \lesssim -5$. The solutions for density and pressure are given through the integral

$$\frac{4}{\sqrt{\pi}}\int_0^\infty y^{2n} f(r,y)\,\mathrm{d}y = \frac{2}{\sqrt{\pi}}\Gamma(n+1/2)\mathrm{e}^{\theta(r)} \tag{2.109}$$

where $n \in \mathbb{Z}^+$ and $\Gamma(n)$ is the gamma function. In summary, we obtain

$$\frac{\rho(r)}{\rho_\mathrm{B}} \approx \frac{P(r)}{\rho_\mathrm{B}\sigma^2} \approx \mathrm{e}^{\theta(r)} \tag{2.110}$$

Important to mention is that the IS gives a unique mass distribution (in an appropriate unit system) what is shown in next.

Change of unit system

We introduce an unit system which focuses on the central density ρ_0, similar to the unit system of the uniform body (see section 2.3.2), and the velocity dispersion constant σ. However, with eqs. (2.14), (2.98) and (2.110) we may describe the central density as

$$\log \frac{\rho_0}{\rho_\mathrm{P}} = \log C_\rho + \frac{3}{2} \log \frac{2\sigma^2}{c^2} + 4 \log \frac{m}{m_\mathrm{P}} + \theta_0 \tag{2.111}$$

Then, after few straightforward calculations we obtain finally

$$\log \frac{R_\mathrm{IS}}{l_\mathrm{P}} = \log C_R \; - \frac{1}{4} \log \frac{2\sigma^2}{c^2} \; - 2 \log \frac{m}{m_\mathrm{P}} \; - \frac{1}{2}\theta_0 \tag{2.112}$$

$$\log \frac{M_\mathrm{IS}}{m_\mathrm{P}} = \log C_M \; + \frac{3}{4} \log \frac{2\sigma^2}{c^2} \; - 2 \log \frac{m}{m_\mathrm{P}} \; - \frac{1}{2}\theta_0 \tag{2.113}$$

Equivalently, the scale factors fulfill the relations $GM_\mathrm{IS} = R_\mathrm{IS}\sigma^2$ and $M_\mathrm{IS} = 4\pi R_\mathrm{IS}^3 \rho_0$. With the new unit system density and pressure become

$$\frac{\rho(r)}{\rho_0} \approx \frac{P(r)}{\rho_0 \sigma^2} \approx \mathrm{e}^{\theta(r)-\theta_0} \tag{2.114}$$

Then, considering eq. (2.102) and inserting eq. (2.114) we obtain

$$\frac{R_\mathrm{IS}^2}{r^2} \frac{\mathrm{d}}{\mathrm{d}r/R_\mathrm{IS}} \left[\frac{r^2}{R_\mathrm{IS}^2} \frac{\mathrm{d}[\theta(r)-\theta_0]}{\mathrm{d}r/R_\mathrm{IS}} \right] \approx -\mathrm{e}^{\theta(r)-\theta_0} \tag{2.115}$$

what clearly shows that $\theta(r) - \theta_0$ has a unique solution regarding the shape of $\theta(r)$. Thus it has no configuration parameter and θ_0 may be separated from the equation into the unit system as was done.

Alternatively, with eq. (2.114) we may describe the isothermal mass distribution through the Poissonian for the density instead of the degeneracy parameter,

$$\frac{R_\mathrm{IS}^2}{r^2} \frac{\mathrm{d}}{\mathrm{d}r/R_\mathrm{IS}} \left[\frac{r^2}{R_\mathrm{IS}^2} \frac{\mathrm{d} \ln \rho(r)/R_\mathrm{IS}}{\mathrm{d}r/R_\mathrm{IS}} \right] \approx -\frac{\rho(r)}{\rho_0} \tag{2.116}$$

Parameter degeneracy

Radius and mass are determined through σ and ρ_0 only. The information about the particle mass m is in the velocity dispersion constant as well as in the central density. Both scale factors have a parameter degeneracy which prohibits to determine the particle mass with the IS model. For the central degeneracy we have a parameter degeneracy due to eq. (2.114), $\rho_0 \sim \sigma^3 m^4 \mathrm{e}^{\theta_0}$. For the length and mass scales we obtain similar proportionality relations, $R_\mathrm{B}^2 \sim \sigma m^4 \mathrm{e}^{\theta_0}$ and $M_\mathrm{B}^2 \sim \sigma^3 m^4 \mathrm{e}^{\theta_0}$. In particular, the unit system has the parameter degeneracy, meaning that all scale factors contain the product $m^4 \mathrm{e}^{\theta_0}$. This has the practical limitation that it is impossible to determine the particle mass uniquely within the IS model. For any particle mass m there is always a corresponding central degeneracy $\theta_0 \ll -1$. A similar problem has the velocity dispersion constant, $\sigma^2 \sim T/m$, with the temperature T and particle mass m.

Despite those limitations, the isothermal sphere model describes phenomenologically very well the cored behavior of a halo. It is also well approximated by the so called pseudo-IS and posses a particular but non-physical solution known as singular-IS. Both are commonly used because of their simplicity. The latter describes very well the flat rotation curves on halo scales but fails at core scales due to its singularity in the center (e.g. Binney and Tremaine, 2008; Chandrasekhar, 1967). In the following these approximations are described briefly in more detail.

Pseudo-IS

We consider the Poissonian given by eq. (2.115) together with the boundary conditions eq. (2.106). The regular initial conditions imply that near the center the degeneracy parameter has a parabolic behavior. This we see when $\theta(r)$ is expanded up to the second order,

$$\theta(r) - \theta_0 \approx -a\frac{r^2}{R_{\text{IS}}^2} \tag{2.117}$$

where a is the central curvature. In next, it is convenient to introduce slightly modified scale factors to simplify the equations. In particular, the parameter a will be separated into the unit system. In summary, we have

$$\log\frac{R_{\text{PS}}}{l_{\text{P}}} = \log C_R \; - \frac{1}{4}\log\frac{2\sigma^2}{c^2} \; - 2\log\frac{m}{m_{\text{P}}} \; - \frac{1}{2}\theta_0 \; - \frac{1}{2}\log a \tag{2.118}$$

$$\log\frac{M_{\text{PS}}}{m_{\text{P}}} = \log C_M \; + \frac{3}{4}\log\frac{2\sigma^2}{c^2} \; - 2\log\frac{m}{m_{\text{P}}} \; - \frac{1}{2}\theta_0 \; - \frac{3}{2}\log a \tag{2.119}$$

Equivalently, the scale factors fulfill the relations $aGM_{\text{PS}} = R_{\text{PS}}\sigma^2$ and $M_{\text{PS}} = 4\pi R_{\text{PS}}^3\rho_0$. Then, for the density profile ansatz, see eq. (2.114), follows the approximation

$$\frac{\rho(r)}{\rho_0} = \frac{1}{\mathrm{e}^{-[\theta(r)-\theta_0]}} \approx \frac{1}{1+\frac{r^2}{R_{\text{PS}}^2}} \tag{2.120}$$

where in the last step numerator and dominator have been expanded separately. For such a density function the mass $M(r)$ and the circular velocity $v(r)$ are given by

$$\frac{M(r)}{M_{\text{PS}}} = \frac{r}{R_{\text{PS}}}\left[1 - \frac{\arctan(r/R_{\text{PS}})}{r/R_{\text{PS}}}\right] \tag{2.121}$$

$$\frac{v^2(r)}{\sigma^2/a} = 1 - \frac{\arctan(r/R_{\text{PS}})}{r/R_{\text{PS}}} \tag{2.122}$$

Because an approximation for the density function was considered, we cannot use eq. (2.114) any longer for deriving the corresponding degeneracy parameter. Instead we have to go through the Poissonian given by eq. (2.115) together with the initial conditions given by eq. (2.106). We find the solution

$$a\left[\theta(r) - \theta_0\right] = 1 - \frac{\arctan(r/R_{\text{PS}})}{r/R_{\text{PS}}} - \frac{1}{2}\ln\left[1 + \frac{r^2}{R_{\text{PS}}^2}\right] \tag{2.123}$$

Singular-IS

The singular-IS is a particular solution of the Poissonian for the IS. In detail, we assume a power law for the density

$$\frac{\rho_n(r)}{\rho_0} = A\left[\frac{r}{R_{\text{IS}}}\right]^n \tag{2.124}$$

and insert it in eq. (2.116) what yields

$$\frac{\rho_n(r)}{\rho_0} = -n\left[\frac{r}{R_{\text{IS}}}\right]^{-2} \tag{2.125}$$

Comparing it with the power law ansatz gives the unique solution with the exponent $n = -2$ and the coefficient $A = 2$. Similar to pseudo-IS we introduce new scale factors

for length and mass which simplify the equations. The new unit system is simply the same as for the pseudo-IS model but with $a = 1/2$. To be precise, we define

$$\log \frac{R_{\text{SS}}}{l_{\text{P}}} = \log C_R \; - \frac{1}{4} \log \frac{2\sigma^2}{c^2} \; - 2 \log \frac{m}{m_{\text{P}}} \; - \frac{1}{2}\theta_0 \; + \frac{1}{2} \log 2 \tag{2.126}$$

$$\log \frac{M_{\text{SS}}}{m_{\text{P}}} = \log C_M \; + \frac{3}{4} \log \frac{2\sigma^2}{c^2} \; - 2 \log \frac{m}{m_{\text{P}}} \; - \frac{1}{2}\theta_0 \; + \frac{3}{2} \log 2 \tag{2.127}$$

Then, density, mass, circular velocity and degeneracy parameter are simply given by

$$\frac{\rho(r)}{\rho_0} = \frac{R_{\text{SS}}^2}{r^2} \tag{2.128}$$

$$\frac{M(r)}{M_{\text{SS}}} = \frac{r}{R_{\text{SS}}} \tag{2.129}$$

$$\frac{v^2(r)}{\sigma^2} = 2 \tag{2.130}$$

$$\left[\theta(r) - \theta_0\right]/2 = -\ln \frac{r}{R_{\text{SS}}} \tag{2.131}$$

In literature the singular isothermal sphere profile is better known in the form

$$\rho(r) = \frac{\sigma^2}{2\pi G r^2} \tag{2.132}$$

where the expressions for the scale factors have been inserted. Here, σ^2 is the isotropic velocity dispersion and G the gravitational constant.

2.4 Summary

Dark matter is considered as a self-gravitating system composed of massive fermions in a thermal equilibrium. For simplicity, it is assumed that the mass distribution has relaxed in a spherical symmetry. No additional interaction is assumed for the fermions besides the relativistic gravitational equation and their fulfilling of quantum statistics. Such a configuration is then described by a perfect fluid.

For a complete description of the problem we adopted a lowered Fermi-Dirac distribution for the fermions. Such a phase-space distribution takes into account the escape velocity of a given mass distribution. Thus, particles with higher velocities are considered as lost what is resembled by a cutoff in the distribution function.

Model description

The dark matter distribution is then described by variables such as the metric potential $\nu(r)$, the enclosed mass $M(r)$, the density $\rho(r)$, the pressure $P(r)$ and the circular velocity $v(r)$. Further suitable variables are the temperature parameter $\beta(r)$, chemical potential $\alpha(r)$ and escape energy $\varepsilon(r)$. Instead of the latter two it is more convenient to look at the degeneracy parameter $\theta(r)$ and cutoff parameter $W(r)$.

Each dark matter solution is then described by three configuration parameter (e.g. β_0, θ_0, W_0) and the particle mass m what was separated into the unit system. On theoretical ground we are also free to choose an initial mass M_0 at the center. However, it is important to emphasize that we consider mass distributions without any embedded black holes, given by $M_0 = 0$.

Special attention has to given to the cutoff parameter W_0, corresponding to the cutoff in the phase-space distribution function. With this parameter it is possible to control the finiteness of the mass distribution. In the limit $W_0 \to \infty$ we recover the Fermi-Dirac distribution, producing isothermal halos infinite in mass and size. (See chapter 3 for further details)

Model approximations

For finite cutoff parameter $W_0 < \infty$ but negative degeneracy parameter $\theta_0 \ll -1$ we obtain the relativistic version of the King model, describing a diluted gas with a cutoff. Further, in the limiting case $W_0 \to \infty$ the distribution function simplifies to the Boltzmann distribution, describing the so-called isothermal mass distribution. Note that the condition $\theta_0 \ll -1$ is a synonym for the diluted case, given for $\mathrm{e}^{\theta(r)} \ll 1$. It is very well fulfilled already for $\theta_0 \lesssim -5$.

It is worth to consider also approximations regarding the mass distribution independent of the phase-space distribution for a better understanding of the model. Thus, low compactness together with low velocities what simplifies the equations significantly.

A good description of the central region is given by the uniform body, characterized through a constant density. The size of such an object is limited at a radius where the pressure becomes zero and, therefore, depends on the central pressure. For physical solutions with finite pressure $P(r) < \infty$ there is a natural limit for the compactness of $\varphi_s < 8/9$, known as the Buchdahl-Bondi limit (Bondi, 1964; Buchdahl, 1959, 1966). Taking into account also constraints on the velocity dispersion, implies a finite upper limit for the pressure in contrast to the Buchdahl-Bondi limit. This stronger constraint lowers the maximal compactness to $\varphi_s < 5/9$.

An alternative description of the inner structure is given by the fully degenerate core, characterized by a constant phase-space distribution $f(r, \epsilon) = 1$. In this case it is convenient to consider a Fermi energy and distinguish further between low and high Fermi energies. Note, that the approximation of a fully degenerate core for low Fermi energies corresponds to a polytrope of index $n = 3/2$. For high Fermi energies we obtain instead an approximation what corresponds to a polytrope of index $n = \infty$. (see e.g. Binney and Tremaine, 2008).

The Newtonian case is motivated by small kinetic energies, e.g. $p \ll mc$. Taking also into account the results from the fully degenerate core for low Fermi energies ($\beta_0\theta_0 \ll 1$), justifies the approximations for low compactness and velocities. The main difference to the relativistic case is the constancy of a low temperature parameter $\beta(r) \approx \beta_0 \ll 1$, allowing to reduce the configuration parameter set by one. Thus, the temperature parameter becomes a scaling factor like the particle mass and may be separated into the unit system.

Relation with the isothermal sphere

The Newtonian approximation in combination with no cutoff ($W_0 \to \infty$) for a diluted gas ($\theta_0 \ll -1$) results in the isothermal sphere. It is possible to separate the degenerate parameter θ_0 into the unit system. Thus, this model posses no configuration parameter what resembles a unique mass distribution in a dimensionless description. Even more, such a heavy simplification causes a parameter degeneracy $m^4\mathrm{e}^{\theta_0}$ for the particle mass m and the degeneracy parameter θ_0.

The isothermal sphere model posses a particular but unphysical solution called singular isothermal sphere (singular-IS). This model is non-physical because of the singularity at the center. Additionally, it is spatially unbounded in size and mass just like the isothermal model (without cutoff). Despite the cautions for inner and outer halo structures, it is the simplest description of self-gravitating mass distribution, able to explain the observed flat rotation curves of galaxies at their halo (Binney and Tremaine, 2008). Indeed, according to the the singularity at the center, the singular-IS model is only applicable for large radii, $r \gg R_{\text{IS}}$. For more realistic (dark matter) mass distributions we have to consider numerical solutions of the more general IS.

The next more realistic yet still simple approximation is the so-called pseudo-IS. This model provides the same outer halo characteristics as the singular-IS. For large

distances the orbital velocity converges to a constant non-zero value, $v(r \to \infty)^2 = \sigma^2/a$. This it not surprising because for $r \gg R_{\rm PS}$ and $a = 1/2$ the singular-IS model is obtained. In the inner halo the density profile doesn't become singular, e.g. resembles cored instead of cuspy halos. The pseudo-IS model has been used to fit data of star clusters phenomenologically by King (1962).

Concluding remarks

Clearly, the introduced dark matter model is a mathematical idealization in which energy production and transport processes are disregarded. In that case the model describes a quasi-stationary system where its parameters (e.g. β_0, θ_0, W_0) may vary slowly with time. Further, we consider perfect spherical symmetry for simplicity while real astrophysical system may be regarded as anisotropic perturbations of the idealized picture which supports the main properties of a galactic system. Also, we neglect the contribution to the potential by the obviously present baryonic matter. This is certainly a good approximation for dwarf spheroidal galaxies which is composed mainly of DM. For the bigger systems like spirals and ellipticals it is less clear how strong baryonic matter affects the galactic structure. Therefore, the solutions develop so-called free DM halos. Another idealization regards the hard cutoff of the presented model where the density goes to zero at the surface radius rather than e.g. asymptotically to the density of the intergalactic medium (see following chapter for details about the cutoff effects). In that case we assume that beyond the surface radius the amount and flow of matter is so low that its contribution may be neglected.

Chapter 3

Analysis

In this chapter the RAR model will be analyzed to entangle its rich complexity and get familiar with the concept of a core, plateau, halo and surface. Similar to chapter 2, which focused on the model on mathematical ground, this chapter focuses on the analysis of the model itself without any application to galaxies. Nevertheless, in this chapter few definitions are motivated by galactic observations which will be suitable for the application of the model to the dark matter in galaxies, provided in chapter 4.

The main tools are the analysis of so-called one parametric families. The nomenclature of the family refers to the parameters which are fixed. We will distinguish between two types of families. The first type considers only the configuration parameters of the RAR model (e.g. β_0, θ_0 and W_0). The second type considers physical parameters (e.g. central density ρ_0, core mass M_c or surface radius r_s). The free parameter may be either a configuration or a physical parameter.

We start with the analysis of the configuration parameter in section 3.1. This will give a sufficient understanding how they affect the mass distribution. To entangle the rich complexity of the RAR model and for a better communication we will separate the set of each configuration parameter into three regimes. We will define a cold, a moderate and a hot regime for the central temperature parameter β_0. A diluted, a transition and a degenerate regime for the central degeneracy parameter θ_0. Finally, a weak, an intermediate and a strong regime for the central cutoff parameter W_0.

The analysis continues in section 3.2 with the focus on physical parameters, in particular which may be compared with observables theoretically.

Throughout the analysis of the families we will mainly focus on the density, velocity and mass profiles to give a good picture of the different solutions. These three variables are essential to understand the morphology of the mass distribution. For clarity, different pictures will be used, which have different purposes.

In the first part, the configuration parameter analysis, it is suitable to focus on so-called core, plateau and halo pictures. In these pictures the profiles will be plotted relative to the core, plateau and halo, respectively. This is equivalent to a change of the unit system. The advantage is a better picture of the morphology of the mass distribution.

The situation changes in the second part, the physical parameter analysis. Here, we may constraint directly particular values of the mass distribution. For example, fixing the central density is partially equivalent to the core picture. Note that the core picture is practically a change of the unit system and does not resemble necessary any constraints. The advantage here is that it is suitable enough to consider the so-called raw picture where the profiles are represented in the unit system (e.g. R, M, ρ) as defined in chapter 2. This picture makes the plots particle mass independent.

Complementary to the profiles it is convenient to reduce the amount of information towards few particular points. It allows to show many regimes of a family in an elegant and compact way. With the help of this analysis picture it is easier to

understand the morphology transitions.

The families provide universal laws within a specific regime. We will highlight the most interesting laws obtained numerically in the first two sections and compare them with laws derived analytically in section 3.3. Finally, a summary is given in section 3.4.

3.1 Configuration parameter

The RAR model is described by a set of four parameters $(m, \beta_0, \theta_0, W_0)$ where the particle mass m is simply a constant scaling factor. Thus, we may ignore the particle mass for theoretical investigations and focus only on the other three configuration parameters to calculate numerical solutions in a dimensionless approach. The procedure is as following: we vary only one parameter while others are fixed to reveal its effect on the characteristics of the mass distribution. The analysis will be divided in two parts.

The first part deals with RAR solutions without cutoff ($W_0 \to \infty$) to get used with the concept of *core*, *plateau* and *halo*. At this point we want to introduce a degenerate core radius r_c and halo core radius r_h which will be called simply *core* and *halo* radius in next. Additionally it is convenient to introduce a *plateau* radius r_p, another important characteristic of the model. The core, halo and plateau radii are defined through the extrema of the rotation curve:

core The core radius r_c is defined at the first maxima in the rotation curve

plateau The plateau radius r_p is defined at the lowest minima in the rotation curve (usually first minima)

halo The halo radius r_h is defined at the maxima after the plateau in the rotation curve (usually second maxima)

It is then suitable to divide these semi-degenerate mass distribution in a core ($0 \leq r \lesssim r_c$), followed by a plateau ($r_c \lesssim r \lesssim r_h$) and a halo ($r_h \lesssim r \lesssim r_s$).

The second part considers finite cutoff parameter values which requires the additional concept of a *surface*. A surface implies that the mass distributions are bounded at the surface radius. We adopt the following definition:

surface The surface radius r_s is defined as the radius where the density drops to zero. This is equivalent to $W(r_s) = 0$.

Thus, a surface is always given for a finite cutoff parameter, $W_0 < \infty$.

We want to emphasize that the definitions of the core, plateau and halo radii are suitable for solutions with a degenerate core embedded in a clearly defined isothermal halo, namely $\theta_0 \gtrsim 15$. However, depending on the initial conditions there exist solutions of a core-only (without a halo) and halo-only solutions (without a degenerate core). Of course, there are also transitions between those regimes where a core and/or a halo are not clearly identified.

3.1.1 Solutions without cutoff: β_0 family

We start by we varying the degeneracy parameter θ_0 for a fixed temperature parameter $\beta_0 = 10^{-6}$ within the cold regime ($\beta_0 \lesssim 10^{-4}$).

In fig. 3.1 the solutions are plotted relative to the plateau for better clarity. Hence, the radii are given in units of the plateau radius r_p, densities in units of the plateau density $\rho_p \equiv \rho(r_p)$, velocities in units of the plateau velocity $v_p \equiv v(r_p)$ and masses in units of the plateau mass $M_p \equiv M(r_p)$. In this picture the morphology from the degenerate regime ($\theta_0 \in [15, 50]$) to the diluted regime ($\theta_0 \lesssim -5$) with a transition

regime $\theta_0 \in [-5, 15]$) is best visible. The nomenclature of the regimes refers to the central degeneracy θ_0.

In summary, the mass distributions are composed of two main components: a core and a halo. A plateau links these two components. It is worth to emphasize that in the degenerate regime all RAR solutions have a very similar core and halo. In comparison to the diluted regime, the sharp eye will notice that the diluted core has the same shape as the halo in the degenerate regime. This is not surprising since we know that the degeneracy variable $\theta(r)$ is a monotonic decreasing function. Therefore, all semi-degenerate solutions with $\theta_0 \gtrsim 15$ have $\theta(r) \ll -1$ beyond a radius r. In that regime the mass distributions have necessary the same shape as when we would consider an entire diluted mass distribution with $\theta_0 \ll -1$.

The upper limit of $\theta_0 = 50$ was chosen arbitrary for clarity. Solutions for higher θ_0 clearly exist which would produce more compact cores. On the other hand, there is indeed a lower limit of $\theta_0 \approx 15$, although slightly blurred. Solutions with θ_0 below that blurred limit begin to deform the halo such that their profiles (e.g. density) would not overlap in the halo. Thus, there is a transition regime in the range $\theta_0 \sim -5 - 15$ where the concept of a core and halo seems to be not appropriate anymore. This becomes obvious when the RAR solutions ($\theta_0 \gtrsim 15$) are compared with the isothermal sphere ($\theta_0 \ll -1$). The halo of the isothermal sphere is defined at the first maxima in the rotation while the halo of the RAR solution is defined as the second maxima.

Alternative presentations give a deeper understanding of the morphology when the solutions are plotted relative to the core or halo. In those cases it is appropriate to focus only on the degenerate regime for $\theta_0 \in [15, 50]$ and compare the solutions with a fully degenerate core (see fig. 3.2) and an isothermal sphere (see fig. 3.3). In the core picture all RAR solutions have very similar degenerate cores, well described by a fully degenerate core, but provide different halos. In the halo picture all RAR solutions have very similar halos, well described by the isothermal sphere, but provide different cores.

The most interesting solutions are given in the cold and degenerate regime ($\beta_0 \lesssim 10^{-4}$ and $\theta_0 \gtrsim 15$). There, the density profiles can be separated into four intervals:

(I) a degenerate quantum core with nearly constant density followed by

(II) a steep fall and

(III) an almost constant plateau which changes to

(IV) a Boltzmannian power law tail.

The rotation curve can be classified similarly. The intervals are basically given by alternating power laws. It starts with

(I) an almost constant degenerate core up to the first maxima followed by

(II) a Keplerian power law up to the lowest minima, then changes to

(III) an almost constant and diluted halo up to the second maxima which

(IV) changes to a flat rotation curve.

A similar classification is also present in the mass profiles and other variables.

In the transition regime ($\theta_0 \sim -5 - 15$) the steep fall (II) and the plateau (III) become less distinct. Looking at the rotation curve it is still possible to define a core and a halo based on the maxima. But the core (close to the first maxima) is not well described by a fully degenerate core anymore and the halo (close to the second maxima) is not well described by the isothermal sphere, either.

At the bottom bound of the transition regime (for $\theta_0 \ll -1$) the mass distributions become completely diluted and are well described by the isothermal sphere. In

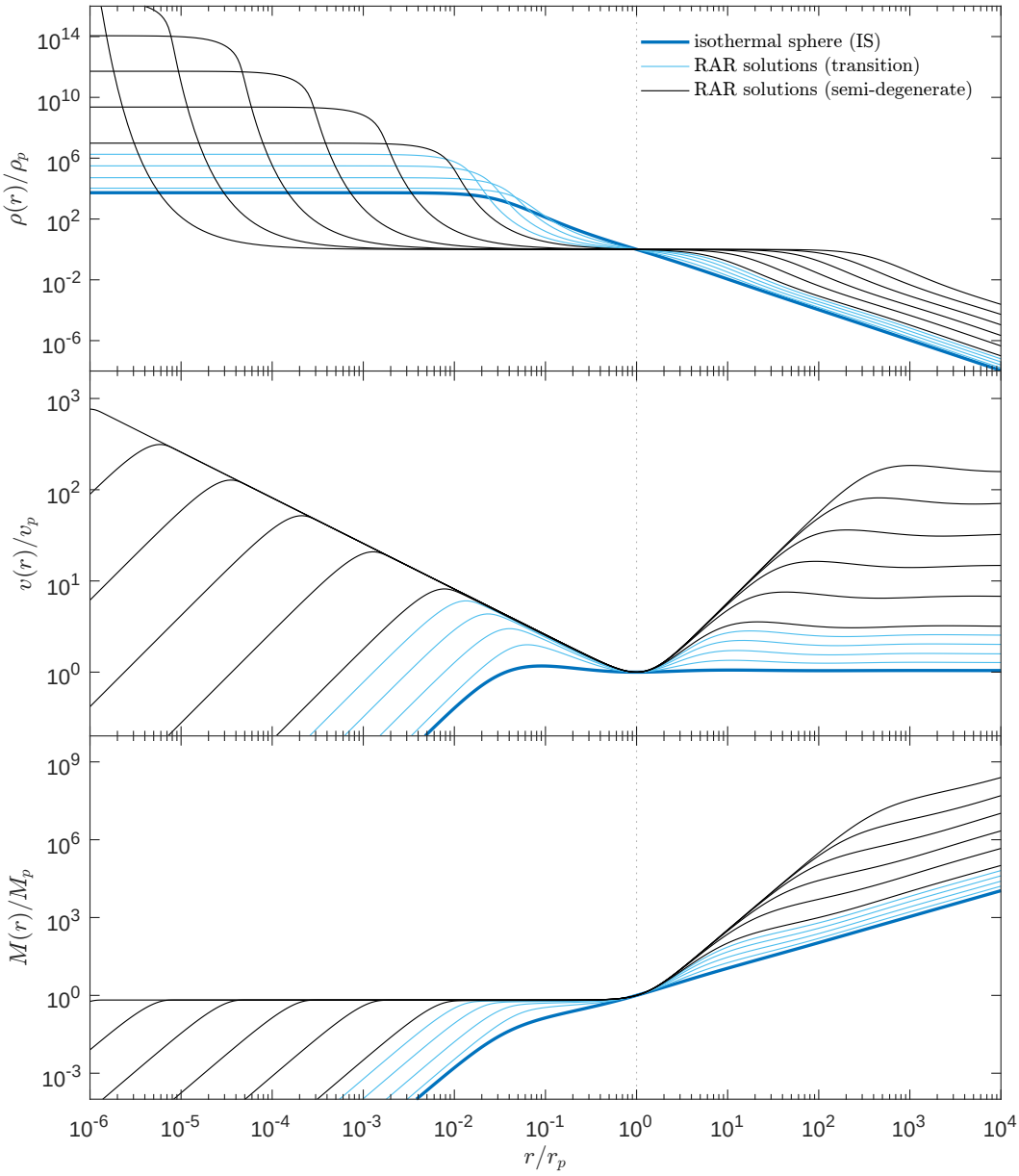

Figure 3.1. Degeneracy parameter analysis illustrated with density, velocity and mass profiles for $\theta_0 \in [-5, 50]$ and $\beta_0 = 10^{-6}$. In the degenerate regime $\theta_0 \in [15, 50]$ RAR solutions with a distinct core and halo are shown. In this regime each core is well describes by a fully degenerate core (not shown) and each halo by the isothermal sphere (not shown). The transition regime is given for $\theta_0 \in [-5, 15]$ where core and halo become less distinct. Also the plateau becomes cuspy in the density profile. Note that radii are given in units of the plateau radius, densities in units of plateau density, velocities in units of the plateau velocity and masses are given in units of the plateau mass. In this picture all RAR solutions (thin solid lines) overlap in the plateau what links the core and the halo. The vertical line highlights the location of the plateau radius defined at the first minima in the rotation curve of RAR solutions.

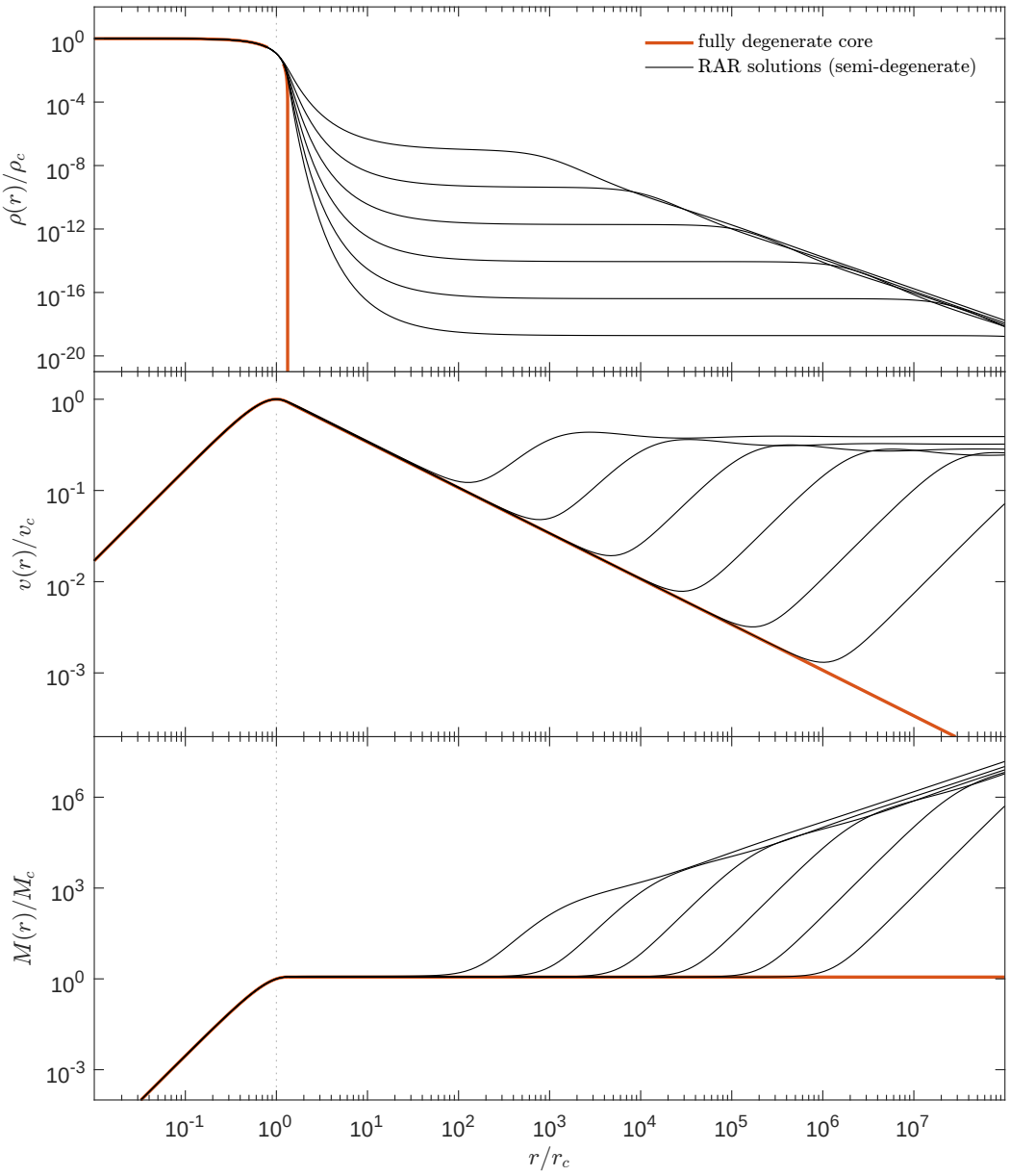

Figure 3.2. Degeneracy parameter analysis illustrated with density, velocity and mass profiles for $\theta_0 \in [15, 50]$ and $\beta_0 = 10^{-6}$. Note that radii are given in units of the core radius, densities in units of central density, velocities in units of the core velocity and masses are given in units of the core mass. In this picture all RAR solutions (thin solid lines) overlap in the core which is very well described by fully degenerate core (red thick line). The vertical line highlights the location of the core radius defined at the first maxima in the rotation curve of RAR solutions.

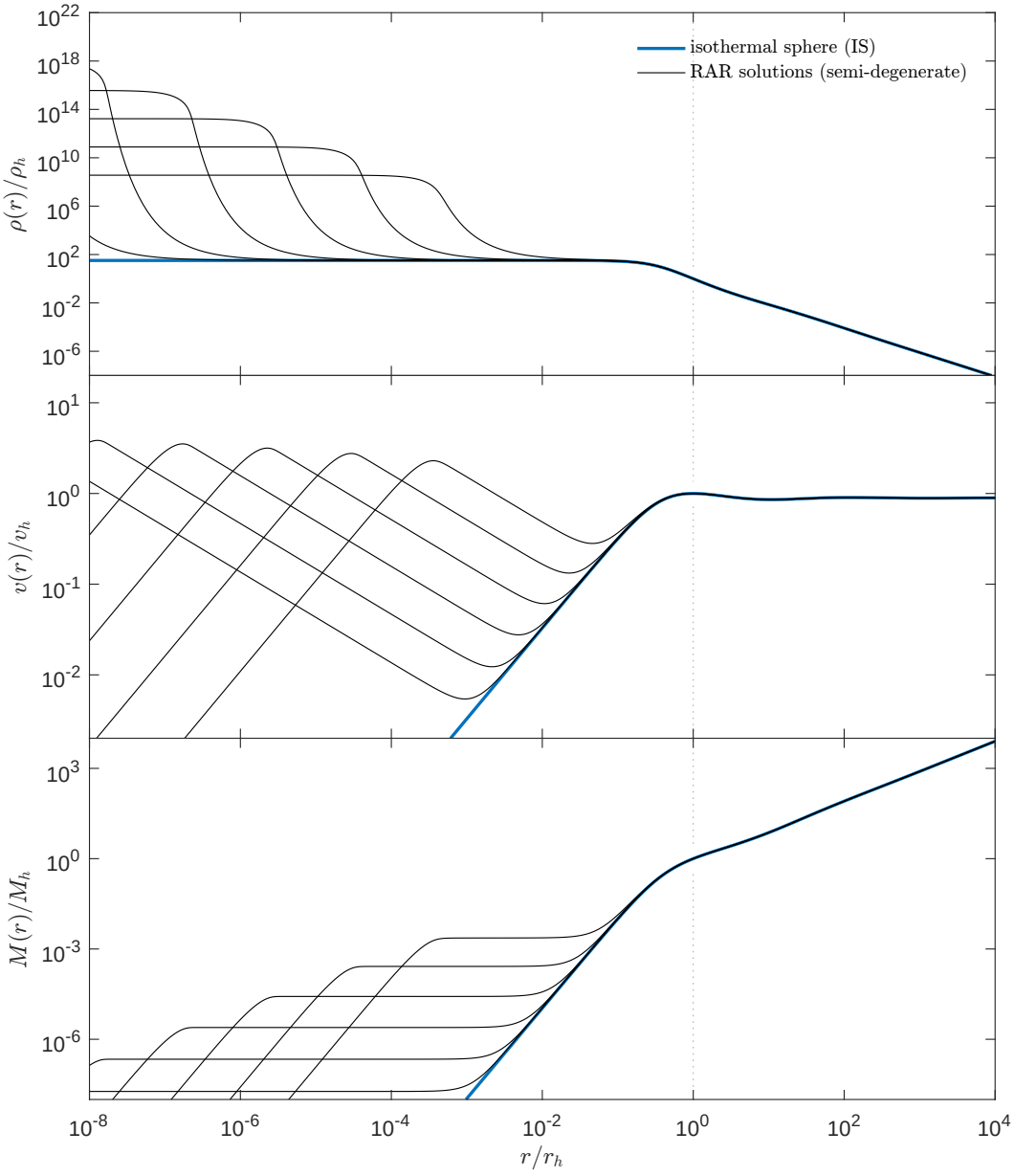

Figure 3.3. Degeneracy parameter analysis illustrated with density, velocity and mass profiles for $\theta_0 \in [15, 50]$ and $\beta_0 = 10^{-6}$. Note that radii are given in units of the halo radius, densities in units of halo density, velocities in units of the halo velocity and masses are given in units of the halo mass. In this picture all RAR solutions (thin solid lines) overlap in the halo which is very well described by the isothermal sphere (blue thick line). The vertical line highlights the location of the halo radius defined at the second maxima in the rotation curve of RAR solutions. For the isothermal sphere the halo is defined at the first maxima.

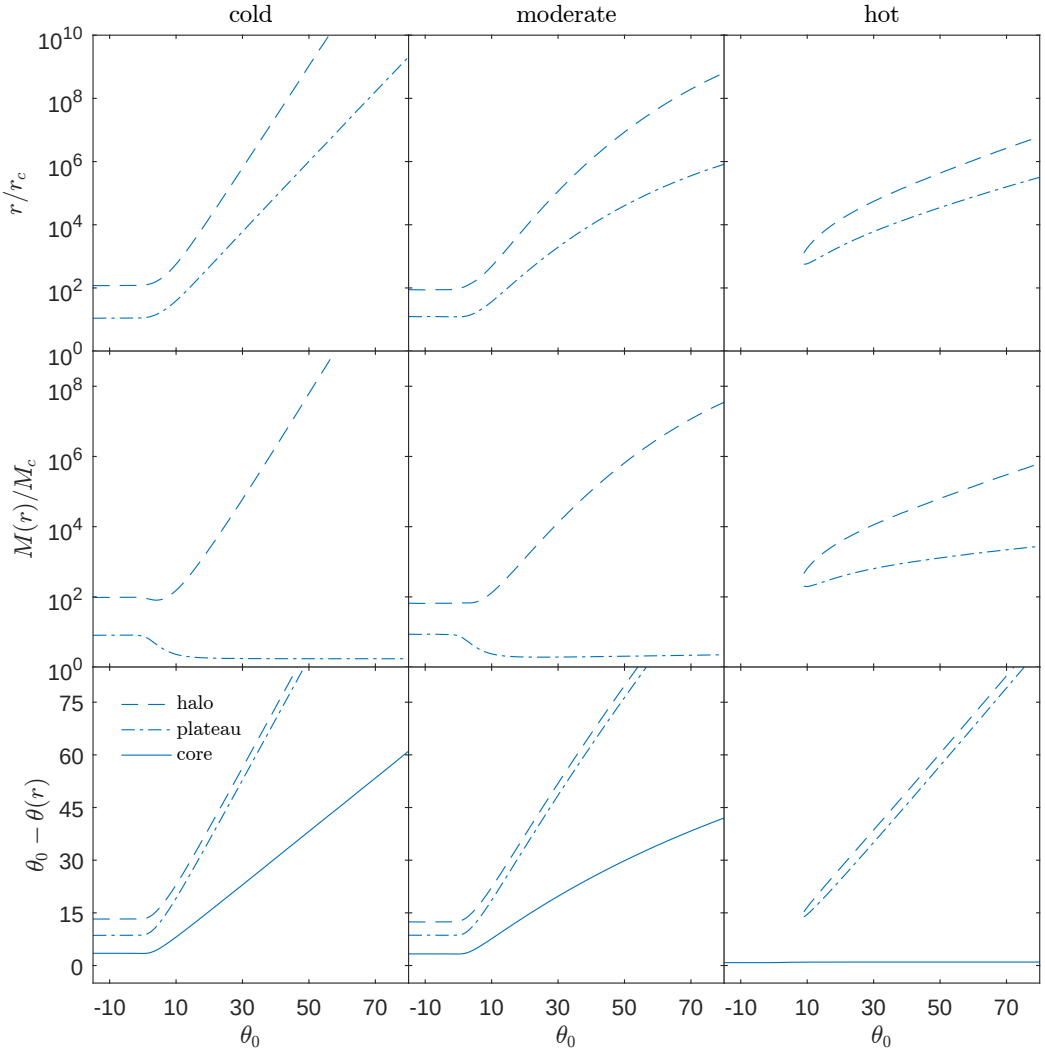

Figure 3.4. Degeneracy parameter analysis illustrated with particular values of the radius, mass and degeneracy variables for three different temperature regimes: low temperature regime with $\beta_0 = 10^{-6}$ (left), a transition regime with $\beta_0 = 10^{-2}$ (middle) and a high temperature regime with $\beta_0 = 1$ (right). The values of interest are obtained at the core, plateau and halo. Note that radii are given in units the core radius and masses in units of the core mass.

this diluted regime we find a diluted core instead of degenerate core (I) which changes to the Boltzmannian tail (IV) without developing a steep fall nor any plateau. Instead, comparing the semi-degenerate solutions ($\theta_0 \gtrsim 15$) with the diluted solutions ($\theta_0 \lesssim -5$) we may interpret the plateau of the semi-degenerate solutions as the core of the diluted solutions.

To get an even better understanding of the morphology of the core, plateau and halo it is suitable to focus explicitly on them instead on the entire profiles. To be precise, we will focus on the values extracted at the first extrema of the rotation curve and label them simply *core*, *plateau* and *halo* - in analogy to the definitions above. Thus, in fig. 3.4 the information is reduced to those quantities. This provides a good picture of the transition from the degenerate to the diluted regime. The evolution is shown for varying the central degeneracy parameter θ_0 and three different temperature regimes (cold, moderate and hot) described by given β_0 values. The results are presented relative to the core similar to the presentation of the profiles in the core picture. Note, that the concept of a core and halo in combination with a plateau makes sense only for solutions with a degenerate core embedded in a diluted halo. This is the case for $\theta_0 \gtrsim 15$.

In the cold regime ($\beta_0 \lesssim 10^{-4}$) illustrated for $\beta_0 = 10^{-6}$ there are two clear degeneracy regimes (diluted and degenerate) visible. They are connected through the transition regime in the intermediate range $\theta_0 \sim -5 - 15$. For $\theta_0 \lesssim -5$ the morphology of the core, plateau and halo does not change. Their ratios remain constant. This regime represents the diluted regime and is very well described by the isothermal sphere. For $\theta_0 \gtrsim 15$ we obtain the degenerate regime where the morphology changes with θ_0 following power laws. Increasing the temperature to $\beta_0 = 10^{-2}$ (within the moderate regime, $10^{-4} \lesssim \beta_0 \lesssim 1$) does not change the diluted regime significantly. But the degenerate regime is not described by simple power laws anymore. The entire topology changes for high temperatures (hot regime, $\beta_0 \gtrsim 1$), illustrated for $\beta_0 = 1$. In this case the diluted regime is described by a core only. There is no plateau or halo. Those characteristics appear only in the transition regime and remain in the degenerate regime.

3.1.2 Solutions without cutoff: θ_0 family

We turn now to the case where we vary the central temperature parameter β_0 for a given central degeneracy parameter of $\theta_0 = 30$ in the degenerate regime. The solutions can be divided into three regimes: cold, moderate and hot. Here, the nomenclature refers to the central temperature implying thermal effects on the mass distribution.

In the cold regime ($\beta_0 \lesssim 10^{-4}$) RAR solutions with a distinct core and halo are practically indistinguishable, see fig. 3.5. In this regime the core is well described by a fully degenerate core (not shown) and the halo by the isothermal sphere (not shown). This unique mass distribution (for a given θ_0) is compared with a moderate and hot regime. The transition between the latter two regimes is well defined by a minimal central density ρ_0/ρ_p. The moderate regime ($\beta_0 \sim 10^{-4} - 1$) shows thermal effects which decrease the core (e.g. density, mass and radius) as well as the halo relative to the plateau. In the hot regime ($\beta_0 \gtrsim 1$) the halo varies just slightly while the core forms an extended flat rotation curve. In summary, high temperatures blur the mass distribution. The core and halo become less dense and compact compared to the plateau. Also, high temperatures transform the halo from a cored shape (given as a plateau in the cold regime) to a cuspy shape.

A focused picture on the core, plateau and halo is given through the analysis for the three degeneracy regimes (diluted, transition, degenerate) as shown in fig. 3.6. All solutions show a constant halo to core and plateau to core ratio for low temperatures. Qualitatively, the exact values depend on the central degeneracy θ_0. Thermal effects

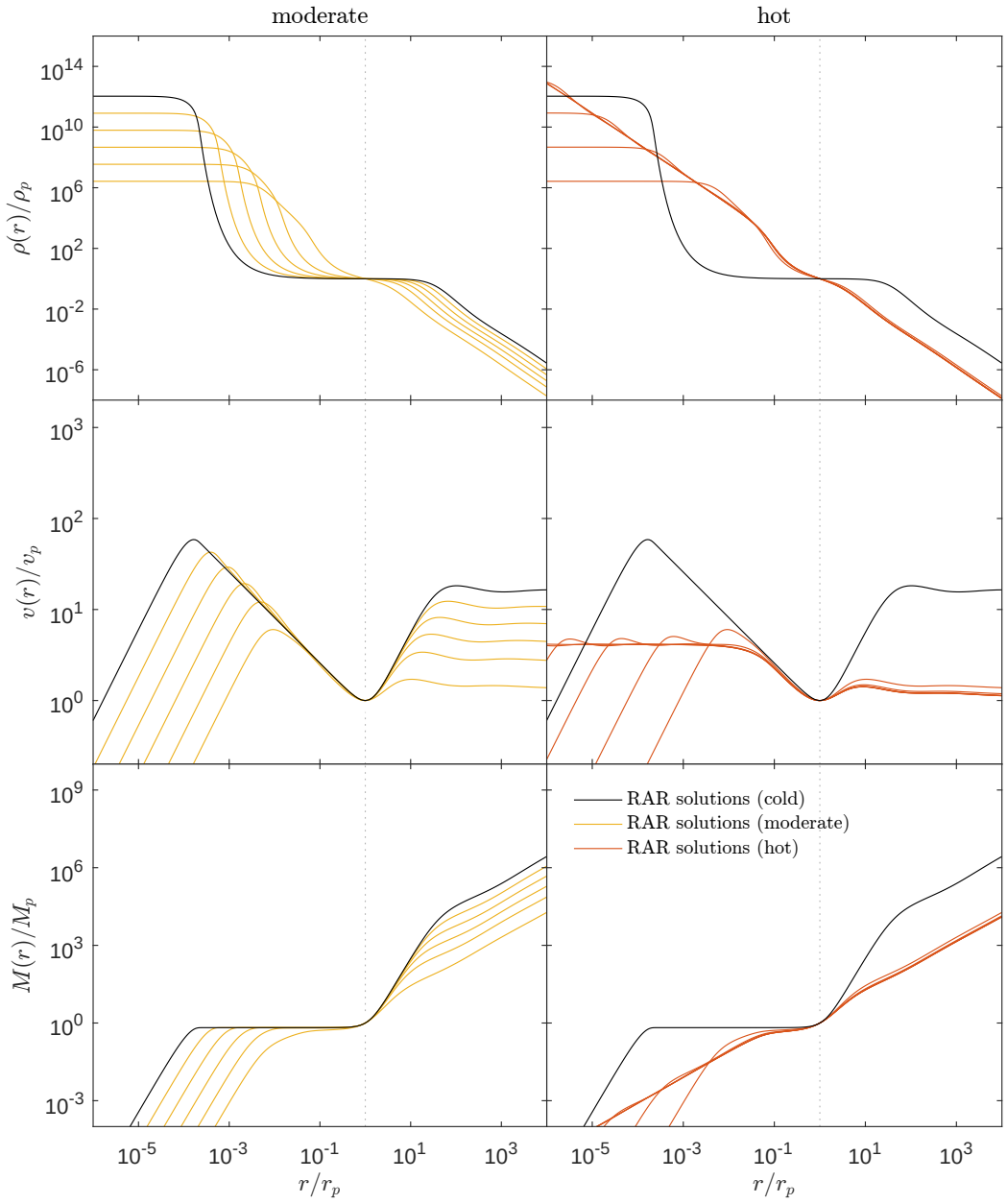

Figure 3.5. Temperature parameter analysis illustrated with density, velocity and mass profiles for $\theta_0 = 30$ and $\beta_0 \leq 10^2$. In the cold regime $\beta_0 \lesssim 10^{-4}$ RAR solutions (solid black line) with a distinct core and halo are practically indistinguishable. In this regime the core is well described by a fully degenerate core (not shown) and the halo by the isothermal sphere (not shown). This unique mass distribution (for a given θ_0) is compared with an intermediate and hot regime. The transition between those two regimes is marked by an minimal central density ρ_0/ρ_p. The moderate temperature regime, $\beta_0 \sim 10^{-4} - 1$, shows thermal effects which decrease the core as well as the halo relative to the plateau. In the hot regime, $\beta_0 \gtrsim 1$, the halo varies just slightly while the core forms an extended flat rotation curve. Note that radii are given in units of the plateau radius, densities in units of plateau density, velocities in units of the plateau velocity and masses are given in units of the plateau mass. In this picture all RAR solutions (thin solid lines) overlap in the plateau what links the core and the halo. The vertical line highlights the location of the plateau radius defined at the lowest minima in the rotation curve of RAR solutions.

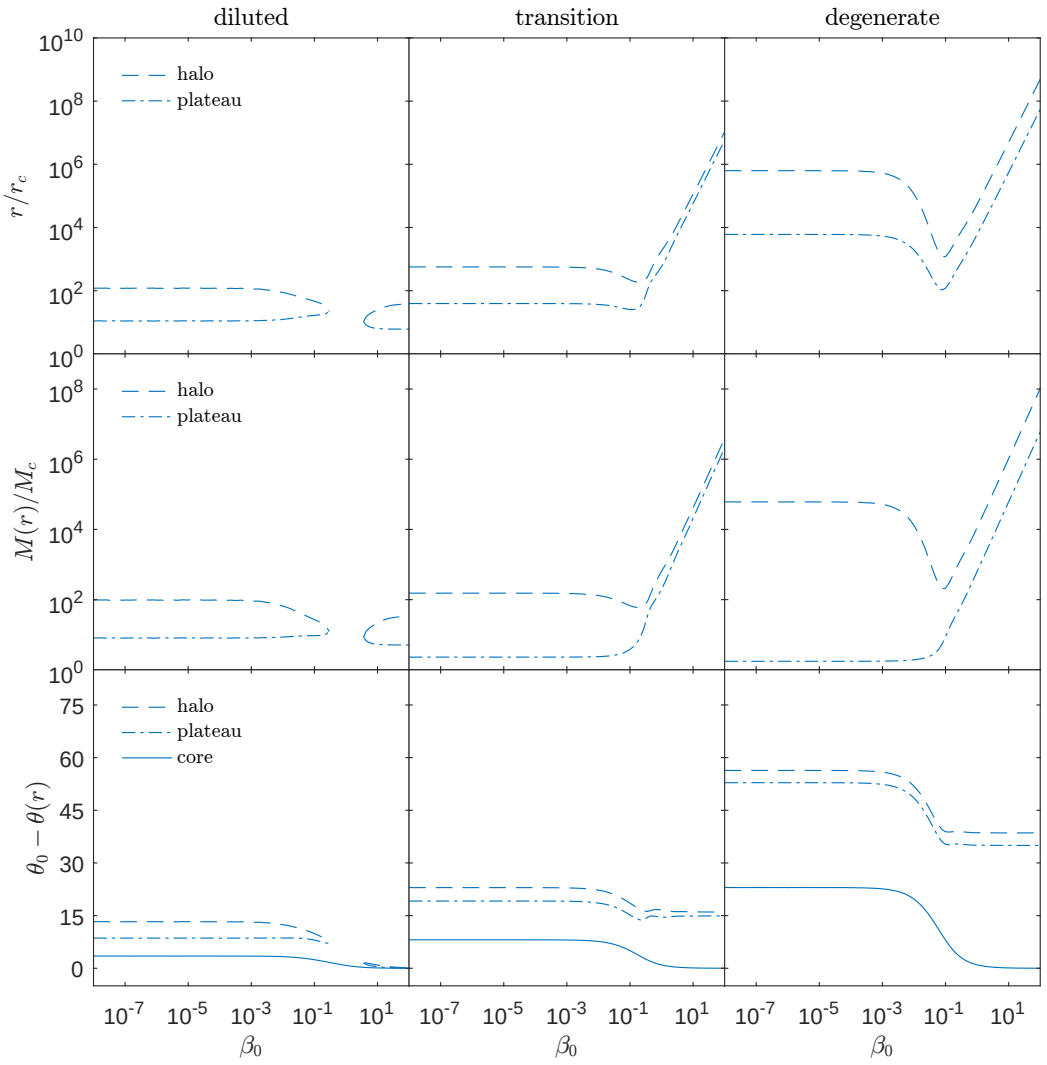

Figure 3.6. Temperature parameter analysis illustrated with particular values of the radius, mass and degeneracy variables for three different degeneracy regimes: diluted regime with $\theta_0 = -20$ (left), a transition regime with $\theta_0 = 10$ (middle) and a degenerate regime with $\theta_0 = 30$ (right). The values of interest are obtained at the core, plateau and halo. Note that radii are given in units of the core radius and masses in units of the core mass.

start to appear for $\beta_0 \gtrsim 10^{-4}$. In this moderate regime the degenerate core (within degenerate regime) shows a smooth transition into a hot regime, $\beta_0 \gtrsim 1$, with clear power laws. For less degenerate solutions the halo shrinks faster than the plateau relative to the core. This trend has the effect that halo and plateau merge for solutions in the moderate and diluted regime with the conclusion that no halo and plateau are identified anymore. A halo and plateau appear again in the hot regime which converge to a constant value relative to the core.

The interpretation of the temperature parameter is as following. For low temperatures quantum pressure is dominant and prevents the core from a collapse. Variation in the temperature do not change the morhology of the mass distribution significantly. Only in the moderate regime thermal effects start to be of the same order as quantum effects, and surpass them in the hot regime.

The strong thermal effects in the hot regime produce also flat rotation curve at the core, similar to the flat rotation curve of the halo in the cold regime. The characteristic is an oscillation with low amplitudes. This is the reason why the plateau has been defined at the lowest minima in the rotation curve.

3.1.3 Solutions with cutoff: β_0-θ_0 family

After discussing the β_0 and θ_0 family without cutoff we are interested in solutions with a cutoff described by a finite cutoff parameter $W_0 < \infty$. We start by varying the cutoff parameter for a fixed temperature parameter of $\beta_0 = 10^{-6}$ (cold regime) and a fixed degeneracy parameter of $\theta_0 = 20$ (degenerate regime). The solutions of this family (e.g. the parameter space) can be divided into three regimes: cored, cuspy and deficit. The nomenclature refers to the characteristics of the halo. Note that the corresponding W_0 intervals depend on the chosen θ_0 value. Additionally to the three main regimes it is convenient to introduce two more regimes describing limiting cases, such as the Fermi-Dirac limit ($W_0 \to \infty$) and the fully degenerate core. In summary, we define the following regimes

$W_0 \to \infty$	Fermi-Dirac limit (unbounded mass distributions)
$W_{\rm cr} < W_0 < \infty$	finite and cored halo regime
$W_0 \approx W_{\rm cr}$	critical regime with surface effects causing cuspy halos
$\theta_0 \lesssim W_0 < W_{\rm cr}$	degenerate core with an envelope representing a halo deficit
$0 < W_0 \lesssim \theta_0$	fully degenerate core

Thus, the interpretation of the cutoff parameter my be described as the strength of the evaporation, see fig. 3.7 for details.

For no evaporation ($W_0 \to \infty$) the mass distribution is spatially infinite and the Boltzmannian tail (IV) shows a $\rho \sim r^{-2}$ behavior in the density profile. Of more interest is the cored regime ($W_0 \gg \theta_0$) where the outer halo is described by a lowered isothermal sphere.

For high but finite values of the cutoff parameter (very weak evaporation) the mass distribution is bounded at the surface radius far beyond the halo. After the surface radius we can simply use Keplerian mechanics. The surface radius is approx. proportional to W_0. The lower W_0 the smaller the surface radius (relative to the core radius). But the inner structures (core and plateau) remain unaffected. Very similar to the case without a cutoff we may separate the mass distribution into four intervals: (I) a degenerate core (II) followed by steep fall and (III) an extended plateau. The difference is in the Boltzmannian tail (IV) which gets shortened, resulting in finite mass distributions. The lower W_0 the shorter the tail.

By decreasing the cutoff parameter the halo starts to evaporate more and more what simply tightens the mass distribution (surface radius decreases). There is a local surface radius minimum when W_0 becomes low enough such that evaporation effects start to affect also the inner parts of the halo (relative to the unaffected degenerate core). For decreasing W_0 the surface radius begins to increase again and the halo becomes cuspy. This transformation happens for degenerate values close to the plateau value θ_p, representing a critical cutoff value ($\theta_p \approx W_{\rm cr}$). Only in that narrow window of the cutoff parameter the linear power law after the steep fall (in the density profiles) is present, see fig. 3.7. The transition from a cored to a cuspy halo ends when the plateau and halo radii merge to a saddle point in the rotation curve.

We choose this particular point because dark matter dominated galaxies necessary require a maximum in the rotation curve on halo scales (see chapter 4 for details). This is equivalent with a plateau in the density profile. Without the maximum/plateau the solutions would imply that galaxies should be dominated by dark matter entirely what is in conflict with observations. Whether such mass distributions indeed exist or may exist is another question. Hence, this definition might be appropriate in an astrophysical context. Nevertheless, the cuspy regime could be also extended to a local maximum of the surface radius. However, both definitions are almost equivalent and the differences are most probably negligible, in particular compared to the core.

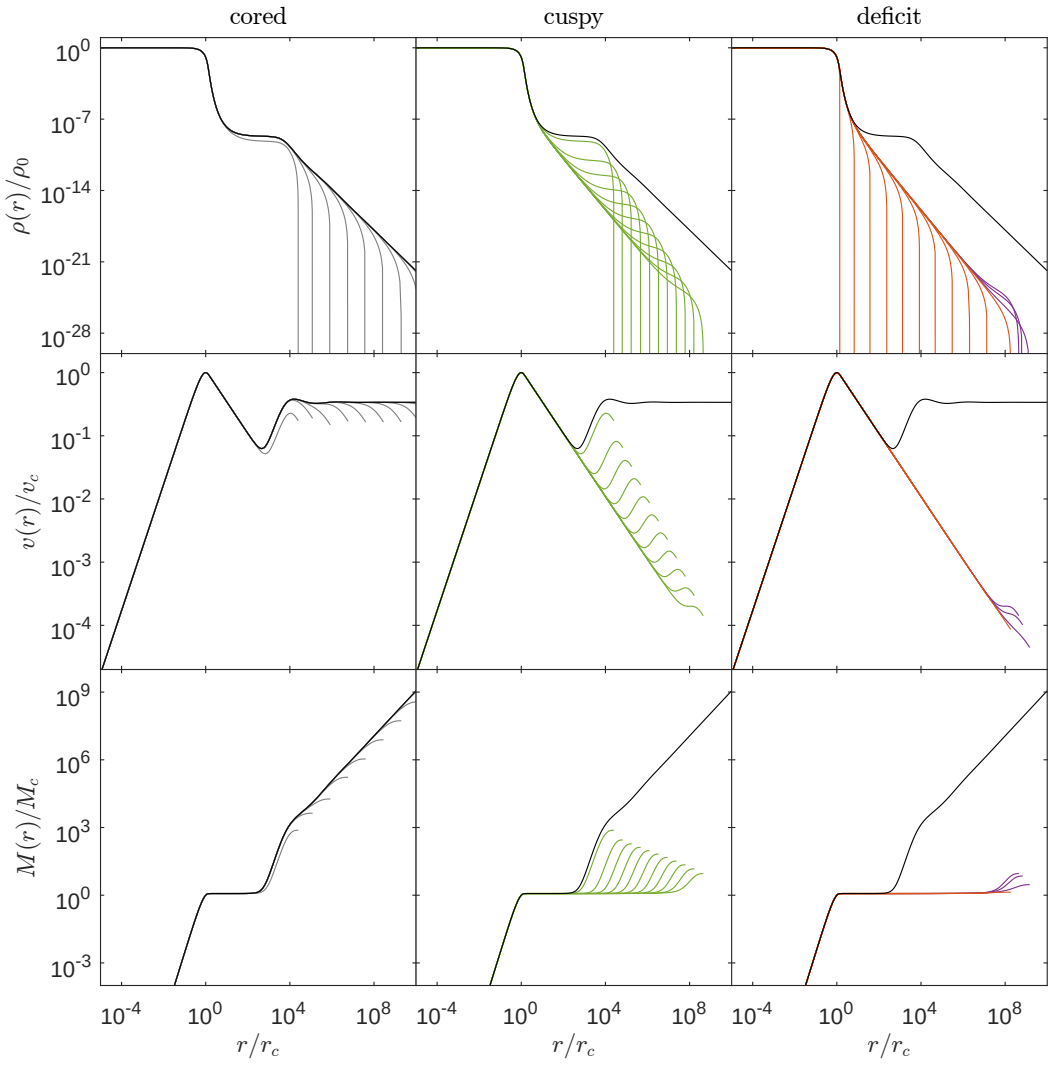

Figure 3.7. Cutoff parameter analysis illustrated with density, velocity and mass profiles for $W_0 \in [17.7, 76.4]$, $\beta_0 = 10^{-6}$ and $\theta_0 = 20$. There are three main regimes: (**left**) for high central cutoff values, $W_0 \gg \theta_0$ the outer halo is described by an lowered isothermal sphere. The surface radius is approx. proportional to W_0. The lower W_0 the smaller the surface radius (relative to the core radius). (**middle**) There is a local surface radius minimum when W_0 becomes low enough such that the halo gets affected. For decreasing W_0 the surface radius begins to increase again and the halo becomes cuspy. This transition from cored to cuspy halo ends when the plateau and halo radii merge to a saddle point in the rotation curve. (**right**) After the saddle point the surface radius continues to increase a bit more but with a *halo deficit*. Finally, after a local maximum in the cuspy regime the halo gets disrupted for decreasing W_0. Note that radii are given in units of the central density ρ_0, velocities are given in units of the core velocity (maximum) and masses are given in units of the core mass. In each plot the limiting solution ($W_0 \to \infty$) is plotted as a solid black line for comparison.

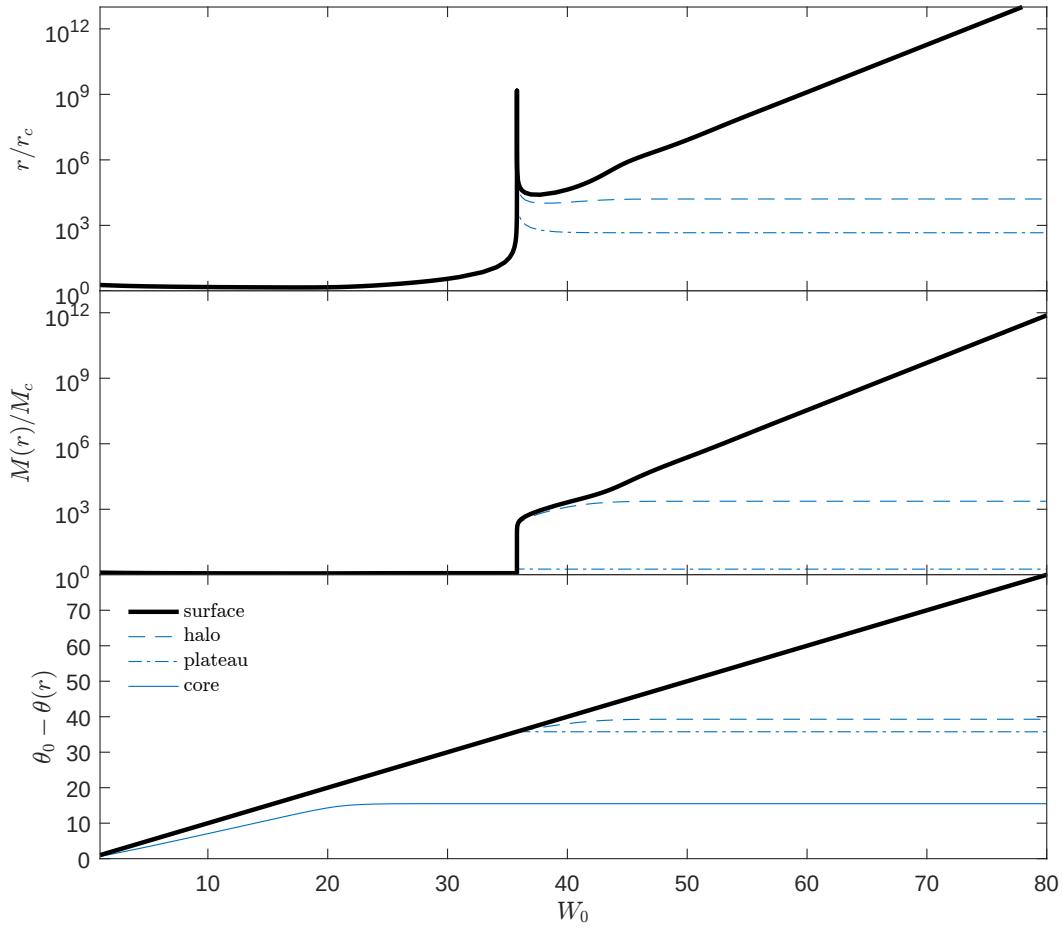

Figure 3.8. Cutoff parameter analysis illustrated with particular values of the radius, mass and degeneracy variables for $\beta_0 = 10^{-6}$ and $\theta_0 = 20$. Those values are obtained at the core, plateau, halo and surface. There are three main regimes: for high central cutoff values, $W_0 \gg \theta_0$ the outer halo is described by an lowered isothermal sphere. The surface radius follows a power law. There is a local surface radius minimum when W_0 becomes low enough such that the halo gets affected. It follows a sharp peak characterizing the transition from cored to cuspy halos. This transition ends with the *halo deficit* regime. The particular mass values follow a similar behavior as for the radius except the sharp peak. In the halo deficit regime the total mass is dominated by the core. The different transition points become clear in the analysis of the degeneracy parameter. Note that radii are given in units of the central density ρ_0, velocities are given in units of the core velocity (maximum) and masses are given in units of the core mass.

A further decreasing of W_0 finally starts to affect also the cuspy halo similar to the evaporation of the outer halo in the cored regime. But in this case we don't find a transformation of the halo into another form. Instead, the decreasing cutoff parameter corresponds to stronger evaporation of the mass distribution causing a halo deficit. We label it a deficit in the context of the surface radius relative to the core. Thus, we obtain a degenerate core with an evaporating envelope which may be interpreted as a cuspy halo without developing a maximum in the rotation curve on halo scales. For $W_0 \lesssim \theta_0$ the halo gets completely evaporated and a fully degenerate core remains. Lower W_0 values would even affect the core but qualitatively the shape remains the same.

A clearer picture of the different regimes is given in fig. 3.8. Especially the peak in the surface radius, representing solutions with cuspy halos, is one of the most interesting results of the dark matter model. In this narrow regime is it possible to vary the compactness of the core.

The different regimes are well understood through the bottom panel, showing the degeneracy at the core, plateau, halo and surface. The thick black line, representing the value $W_0 = \theta_0 - \theta_s$, acts as an upper limit. Reducing W_0 and therefore the difference $\theta_0 - \theta_s$ has an effect on the halo and plateau when W_0 is low enough. Note that the degeneracy variable is a monotonic decreasing function. Thus, the degeneracy at the surface has to be lower than at the halo, and the latter lower than at the plateau. A surface degeneracy below the halo or even the plateau value necessary requires a decreasing at those positions. Interestingly, there is a critical $W_{\rm cr} > 0$ where the plateau and halo merge, resulting in a halo deficit. There still remains an envelope around the degenerate core which may be interpreted as a halo. But this halo is not compatible anymore with the halo defined through the second maxima in the rotation curve. Finally, for $W_0 \sim \theta_0$ there is clearly the effect on the core what represents the transition into a new regime, the fully degenerate core.

3.1.4 Solutions with cutoff: β_0-W_0 family

A similar morphology to the β_0-θ_0 family we obtain by varying the degeneracy parameter θ_0 for a fixed temperature parameter $\beta_0 = 10^{-6}$ (cold regime) and a fixed cutoff parameter $W_0 = 36$, see fig. 3.9. For low but positive central degeneracy values a degenerate core is formed together with a long ranged isothermal halo showing a flat rotation curve. Due to the finite cutoff parameter the flat rotation curve transforms into a Keplerian tail. Instead, for high central degeneracies only a fully degenerate core remains. Thus, the most general density profile (for the low temperature regime) can be separated into four intervals very similar to the solutions without cutoff. The only difference is a smoothly truncated Boltzmannian power law tail in the weak cutoff regime. The truncated tail is visible as a change towards a Keplerian power law in the rotation curve.

According to fig. 3.10 the degeneracy parameter can be classified in three main regimes considering a finite cutoff parameter: A diluted regime, a degenerate regime with halo and a degenerate regime without halo. For high central degeneracy ($15 \lesssim \theta_0 < \theta_{cr}$) a distinct quantum core is formed while for the diluted case ($\theta_0 \lesssim -5$) no such core can be clearly identified. Instead, in the diluted case only a halo is present where its core is defined as the first maxima in the rotation curve. The intermediate case ($-5 \lesssim \theta_0 \lesssim 15$) can be considered as a transition between those two regimes. The degenerate regime with halo ends for a critical central degeneracy θ_{cr} what actually depends on the cutoff parameter. For higher central degeneracies ($\theta_0 > \theta_{cr}$) a degenerate core remains with a diluted envelope which may be interpreted as a halo but a different one as the halo defined through the second maxima in the rotation curve. Finally, higher $\theta_0 \gtrsim W_0$ values produce solution very well described with a fully degenerate core.

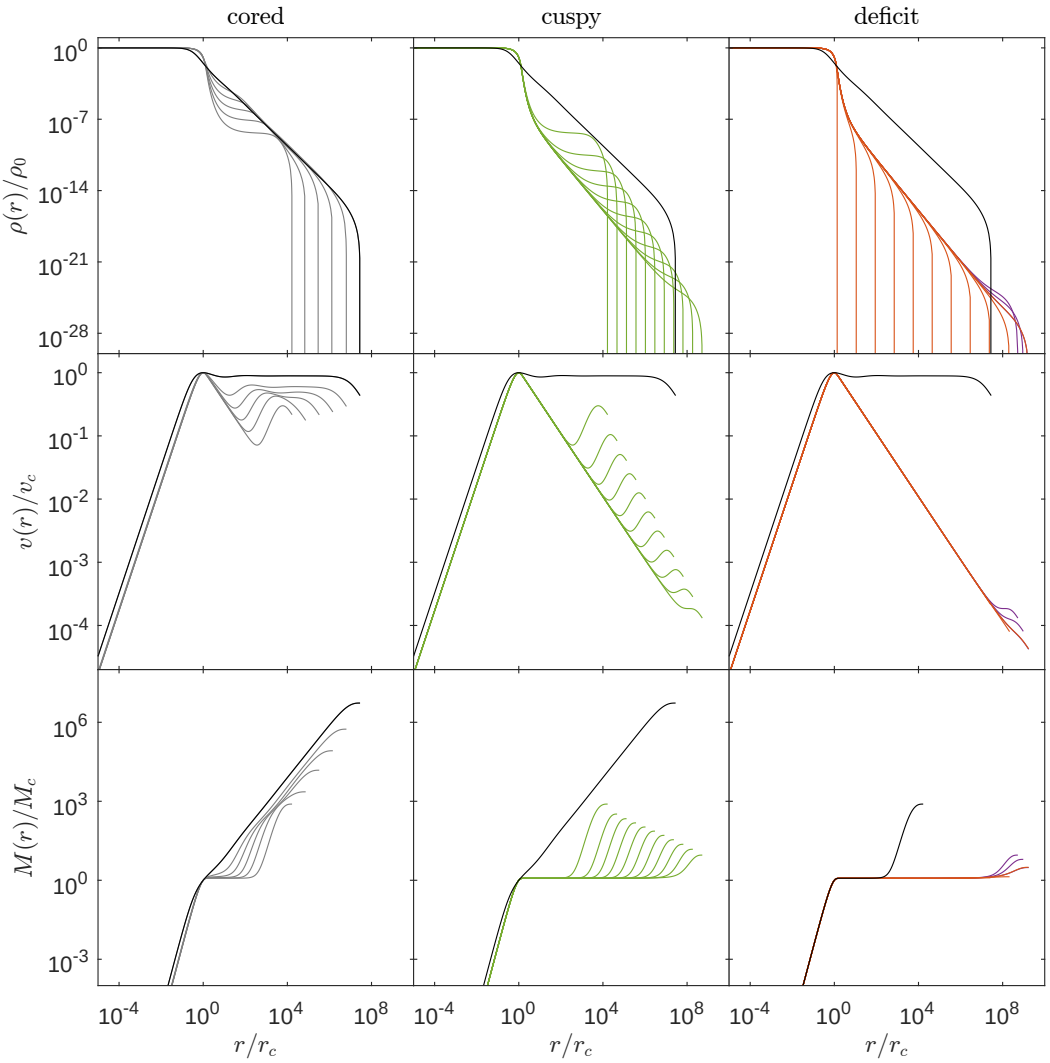

Figure 3.9. Degeneracy parameter analysis illustrated with density, velocity and mass profiles for $\theta_0 \in [-3.6, 40]$, $\beta_0 = 10^{-6}$ and $W_0 = 36$. There are three main regimes: (**left**) for low central degeneracy values, $\theta_0 \ll -1$ the mass distribution is well described by an isothermal sphere with cutoff. The cutoff is characterized through W_0. For increasing θ_0 a degenerate core followed by an plateau is clearly formed, in particular for $\theta_0 > 0$. Simultaneously the surface radius and density of the formed plateau decrease. The maximal cored halo (longest plateau) is obtained when the surface radius reaches a local minimum. (**middle**) For increasing θ_0 the halo gets affected such that the morphology from the isothermal halo to a cored halo continues to a cuspy halo. This transition ends when the plateau and halo radii merge to a saddle point in the rotation curve. (**right**) After the saddle point the surface radius continues to increase a bit more but with a *halo deficit*. Finally, after a local surface radius maximum in the cuspy regime the halo gets disrupted for increasing θ_0. Note that radii are given in units of the central density ρ_0, velocities are given in units of the core velocity (maximum) and masses are given in units of the core mass. In each plot the limiting solution ($\theta_0 \ll -1$) is plotted as a solid black line for comparison.

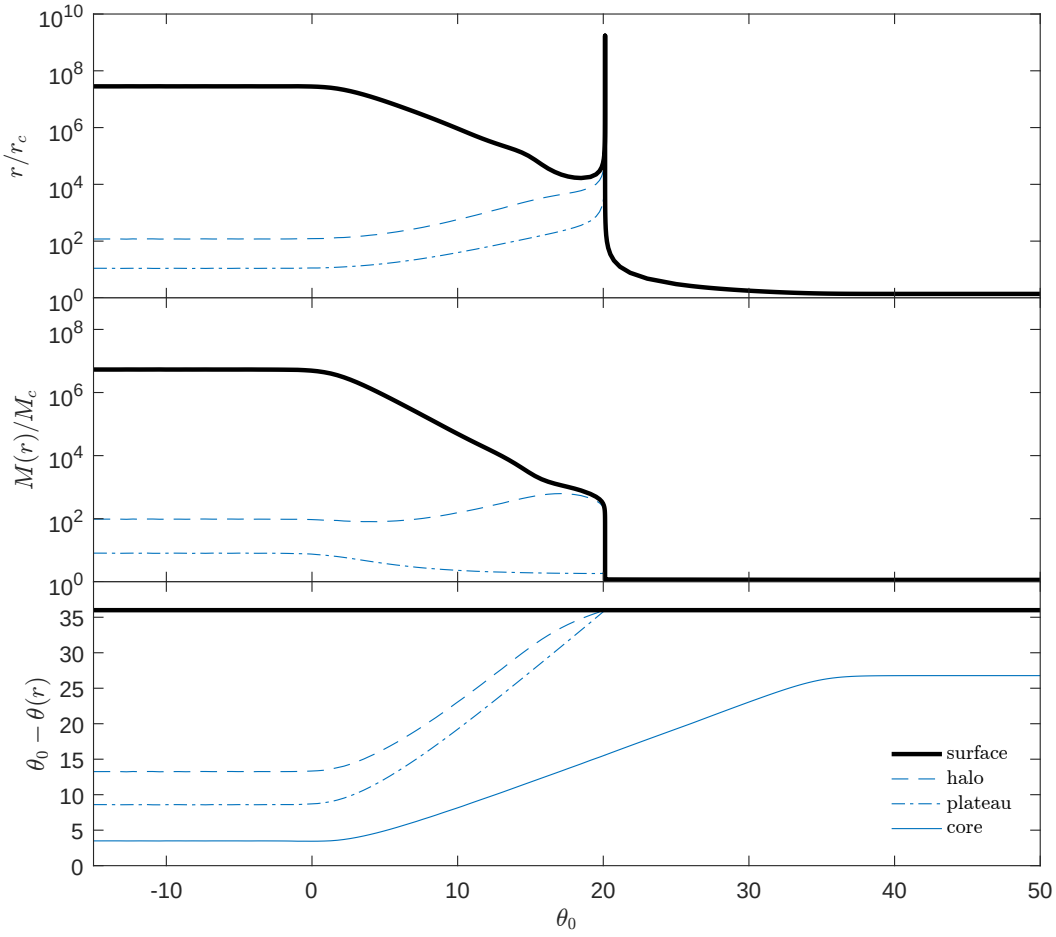

Figure 3.10. Degeneracy parameter analysis illustrated with particular values of the radius, mass and degeneracy variables for $\beta_0 = 10^{-6}$ and $W_0 = 36$. Those values are obtained at the core, plateau, halo and surface. There are three main regimes: for low central degeneracy values, $\theta_0 \ll -1$ the mass distribution is well described by an isothermal sphere with cutoff. There is a local surface radius minimum when different $W_0 - \theta_0$ becomes low enough such that the halo gets affected. It follows a sharp peak characterizing the transition from cored to cuspy halos. This transition ends with the *halo deficit* regime. The particular mass values follow a similar behavior as for the radius except the sharp peak. In the halo deficit regime the total mass is dominated by the core. The different transition points become clear in the analysis of the degeneracy parameter. Note that radii are given in units of the central density ρ_0, velocities are given in units of the core velocity (maximum) and masses are given in units of the core mass.

Note, that the morphology of the mass distribution given by this family is very similar to the β_0-θ_0 family. Therefore the arguments explaining the regimes are very similar as well. The only difference are the solutions in the cored regimes due to the different central degeneracy values and the finite cutoff parameter. Lower θ_0 values make the core more diluted and transform the halo from a cored into a cuspy one. Those diluted cuspy-like solutions are different to the mass distributions in the cuspy regime which are characterized through a degenerate core embedded in a cuspy halo with a different power law (see top middle panel of fig. 3.9).

Interesting is the critical regime $\theta_0 \approx \theta_{\rm cr}$ with a peak where the halo becomes highly cuspy on the transition to the deficit regime. This behavior is related to the plateau and can be explained only by considering the central degeneracy together with the cutoff parameter. Here, the cutoff parameter $W_0 \leq \theta_0 - \theta_x$ gives the limit for the difference of the central degeneracy θ_0 and any other degeneracy value θ_x. The equality is given at the surface radius according to eq. (2.51), $W_0 = \theta_0 - \theta_s$. For fixed cutoff parameter (and fixed central temperature) there exists a critical central degeneracy θ_{cr} such that the surface degeneracy is given approx. at the plateau. But since the degeneracy parameter is always decreasing according to eq. (2.45) the degeneracy at the surface radius is always smaller than at any other radius, especially smaller compared to halo and plateau. Keeping in mind that for finite cutoff parameter the mass distribution is bounded at a finite radii it implies that the plateau and the halo have to merge at the critical central degeneracy. That behavior is clearly seen in the bottom panel of fig. 3.10. Considering the rotation curve it means that the minima of the plateau and the maxima of the halo merge to a saddle point with a finite surface radius.

In summary, we want to separate the above discussed cases in the following regimes according the chosen central degeneracy:

$\theta_0 \lesssim$ -5	diluted regime (diluted core with halo)
-5 $\lesssim \theta_0 \lesssim$ 15	transition regime (core and halo are less distinct)
15 $\lesssim \theta_0 \lesssim \theta_{\rm cr}$	degenerate regime with halo (core becomes more degenerate while surface radius decreases)
$\theta_0 \approx \theta_{\rm cr}$	critical regime with surface effects
$\theta_{\rm cr} < \theta_0 \lesssim W_0$	degenerate regime without halo
$W_0 \lesssim \theta_0$	fully degenerate regime

We want to note that the critical central degeneracy does depend on the cutoff parameter. Therefore, for an infinitely deep potential well ($W_0 \to \infty$) the critical central degeneracy goes to infinity. In that case only the first three regimes (diluted, transition and degenerate) remain. Hence, without any evaporation there are no surface effects possible, prohibiting the formation of cuspy halos and fully degenerate cores.

3.1.5 Solutions with cutoff: θ_0-W_0 family

In next, we analyze the θ_0-W_0 family by varying the central temperature parameter β_0 for fixed central degeneracy and cutoff parameter. The density, mass and degeneracy profiles for $\theta_0 = 20$ and $W_0 = 50$ are plotted in fig. 3.11. Here, it is convenient to consider the plateau picture to illustrate the morphology of the mass distributions. The solutions represent the weak regime ($\theta_0 \ll W_0$) and are very similar to the θ_0 family without cutoff ($W_0 \to \infty$).

Of more interest are solutions in the intermediate regime ($\theta_0 \lesssim W_0$) illustrated with $\theta_0 = 20$ and $W_0 = 28$, see fig. 3.12. In that case it is better to consider the core

picture. Thus, in the cold regime ($\beta_0 \lesssim 10^{-4}$) the solutions develop fully degenerate cores. An increase of the temperature allows to form a diluted envelope around the core. These envelopes become cuspy halos in the moderate regime ($10^{-4} \lesssim \beta_0 \lesssim 1$). A further increase of the central temperature transforms the cuspy halos to cored halos. Finally, in the hot regime ($\beta_0 \gtrsim 1$) the cored halos do not change much but the core develops an extended flat rotation curve similar to the one of the isothermal sphere.

Interestingly, for the first θ_0-W_0 combination the solution do not develop cuspy halos. But reducing the W_0 value, for example, changes the mass distribution in the cold regime and allows to emerge two distinct moderate regimes instead of one. Such solutions are presented in the core picture, see fig. 3.12. For clarity, the hot regime is is not shown which is very similar to the hot regime with a higher W_0 value, see fig. 3.11.

A better understanding of the morphology of the θ_0-W_0 family is given by the analysis as shown in fig. 3.13. The core, plateau and halo values of the degeneracy variable $\theta(r)$ again provide the right information to distinguish between three cutoff regimes: a weak ($\theta_0 \ll W_0$), an intermediate (e.g. $\theta_0 \lesssim W_0$) and a strong regime (e.g. $\theta_0 \gtrsim W_0$). Additionally, varying the central temperature parameter develops different temperature regimes (e.g. cold, moderate and hot). These regimes are characterized through different core, plateau, halo and surface radii (relative to the core).

The weak regime is very similar to the θ_0 family without cutoff ($W_0 \to \infty$). The only difference is a surface radius far beyond the halo radius. This weak regime does not affect the inner halo. An increase of the cutoff parameter reduces the surface radius, what affects the inner structures by *pushing* the halo and the plateau to lower values.

In the intermediate regime, where the cutoff effect is not too strong, the surface radius is low enough such that halo and plateau merge together. This may happen for example in the cold regime, depending on the chosen θ_0-W_0 combination. However, an increase of the central temperature affects the surface radius. Important to emphasize is that a plateau and halo appear again above a specific temperature in the moderate regime. The transition from the cold to the moderate regime develops first cuspy halos which become cored with higher temperatures. Then, the intermediate and hot regime is very similar again to the weak and hot regime despite a reduced surface radius.

A great difference is given in the strong regime. Here, the surface radius is so low that it remains below the plateau and halo radius (compared to the weak regime) for any central temperature. Only in the strong and hot regime a plateau and halo are identified again. However, they follow another behavior compared to the weak and intermediate regimes.

Regarding the temperature parameter we classify three regimes independent of the cutoff parameter:

$\beta_0 \lesssim 10^{-4}$	cold regime (low temperature where quantum effects dominate)
$10^{-4} \lesssim \beta_0 \lesssim 1$	moderate regime (transition from cold to hot regime where thermal effects appear)
$1 \lesssim \beta_0$	hot regime (high temperature with clear thermal effects)

By fixing the core radius the interpretation is as following. In the cold regime the temperature is low and the thermal pressure therefore negligible. Only the dominant quantum pressure prevents the mass distribution from a collapse. In the cold regime the solution do not change significantly by varying the central temperature parameter, independent of the chosen θ_0-W_0 combination. In the moderate regime thermal

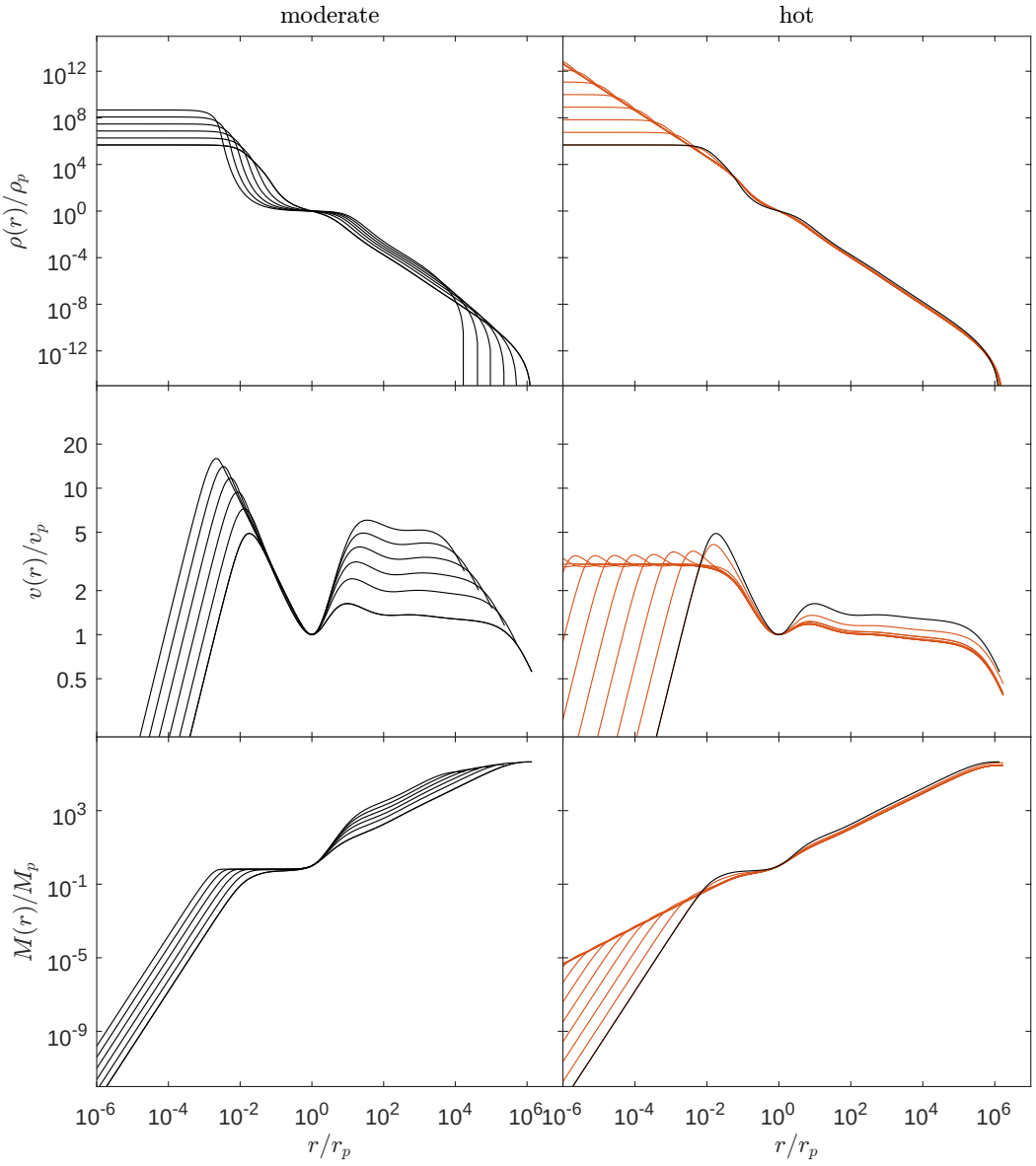

Figure 3.11. Temperature parameter analysis illustrated with density, velocity and mass profiles for $\beta_0 \in \left[10^{-9}, 10^{2}\right]$, $\theta_0 = 20$ and $W_0 = 50$. The solution are plotted relative to the plateau to focus on the morphology of the core and halo. There are two main regimes: moderate ($10^{-4} \lesssim \beta_0 \lesssim 1$) and hot ($\beta_0 \gtrsim 1$). There is also a uni solution in the cold regime ($\beta_0 \lesssim 10^{-4}$) visible in the left panel. Note, that for the chosen parameters, which represent here the *weak cutoff regime*, the solutions do not develop cuspy halos.

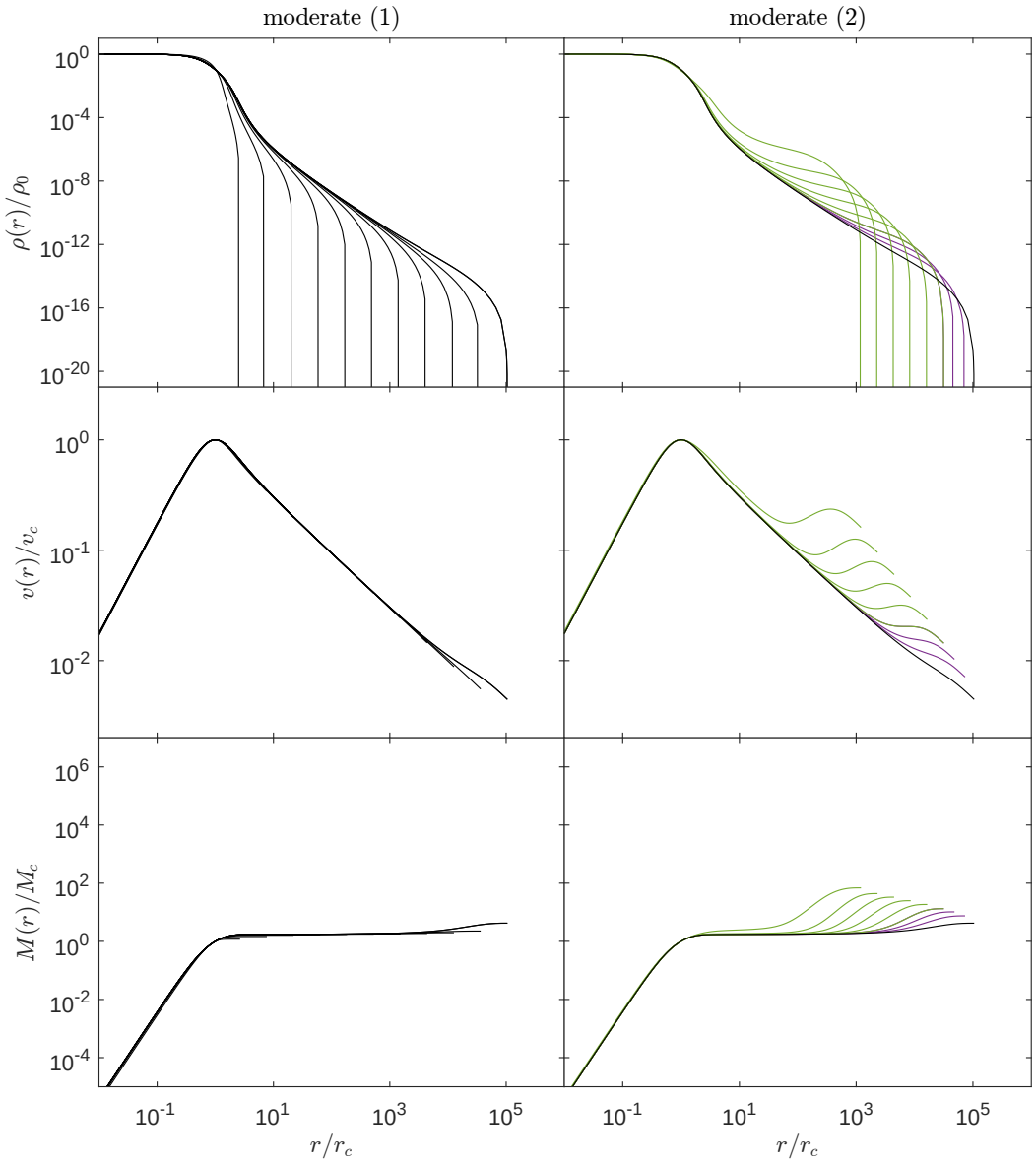

Figure 3.12. Temperature parameter analysis illustrated with density, velocity and mass profiles for $\beta_0 \in \left[10^{-5}, 1\right]$, $\theta_0 = 20$ and $W_0 = 28$. The solution are plotted relative to the core to focus on the morphology of the plateau and halo. For clearity the hot regime is not shown. Of more interest are two moderate regimes: $10^{-5} \lesssim \beta_0 \lesssim 10^{-1}$ and $10^{-1} \lesssim \beta_0 \lesssim 1$. There is a unique solution (independent of β_0) in the cold regime (here $\beta_0 \lesssim 10^{-5}$. That solution is well described by a fully degenerate core. Note, that for the chosen parameters, which represent here the *intermediate cutoff regime*, the solutions develop cuspy halos.

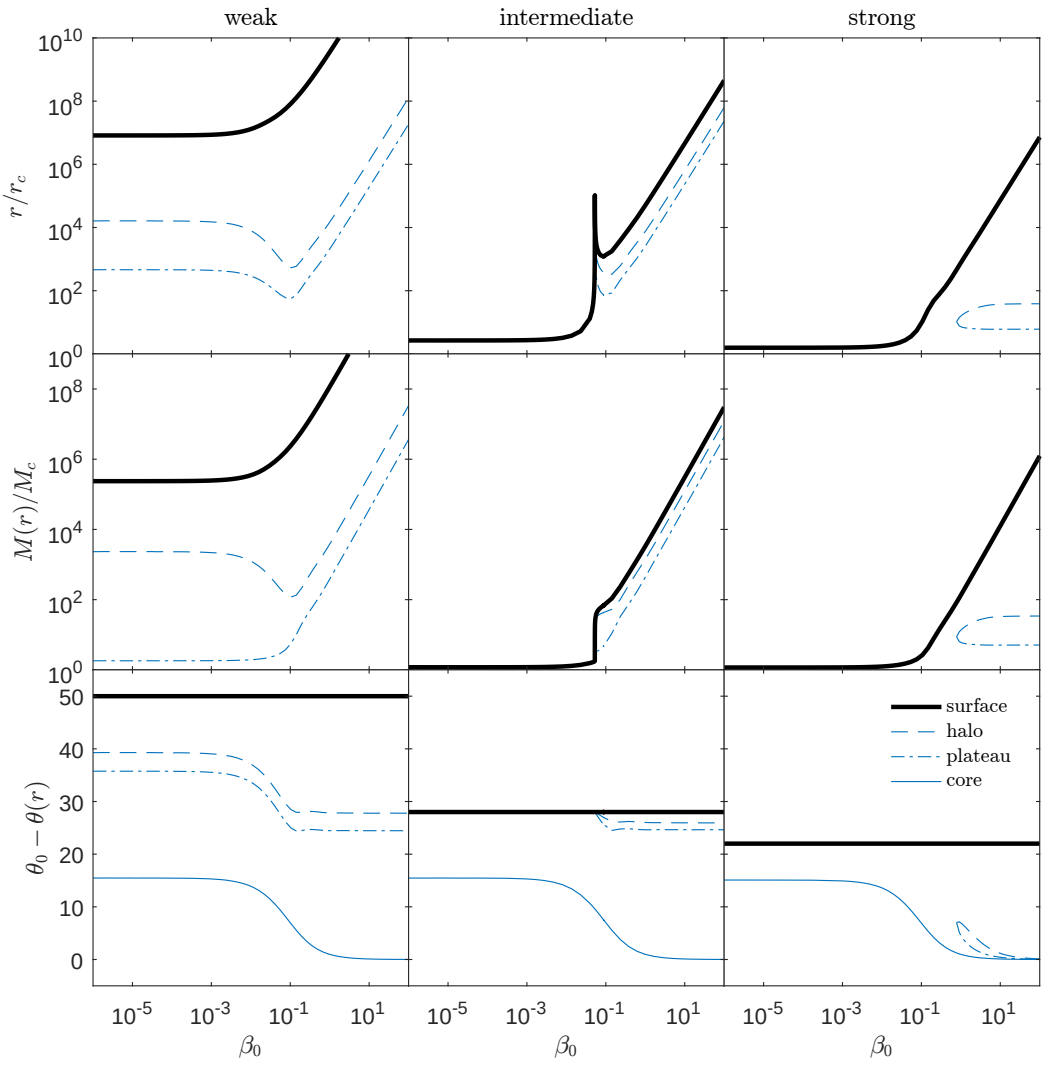

Figure 3.13. Temperature parameter analysis illustrated with particular values of the radius, mass and degeneracy variables for $\theta_0 = 20$ and three different cutoff parameter representing three regimes: $W_0 = 50$ (weak), $W_0 = 28$ (intermediate) and $W_0 = 22$ (strong). Those values are obtained at the core, plateau, halo and surface.

pressure starts to blow up the mass distribution while interestingly the halo and plateau shrink on the contrary. However, for sufficient high temperatures also the halo and plateau blow up. That behavior simplifies in the hot regime to a simple power law unless the cutoff effect is not too strong.

3.2 Physical parameter

In the previous section it was shown that the configuration parameters do not show a simple relation with physical parameters like central density, core mass and halo radius. In this section we therefore focus on solution families with fixed physical parameters and one free parameter. The free parameter can be either a physical parameter as well or a configuration parameter.

The basic strategy is to describe the core and the halo, each with a constraint. For example, the central density ρ_0 and the core mass M_s are clearly parameters describing the core. On the other hand, parameters like the halo radius r_h and surface radius r_s are two different ways to describe the halo. Important is to keep in mind that the plateau may also constraint either the core or the halo. Thus, the plateau

mass M_p is a good alternative to the core mass. And the plateau density is ideal in describing the inner halo without constraining the outer halo.

Focusing only on the density, velocity and mass variables, the number of possible families are too many to discuss them all in this thesis. This would take into account families with only one fixed parameter, mainly for solutions without cutoff. The number increases for solutions with a finite cutoff when two fixed parameters have to be combined. Therefore, we will discuss here only a couple of families (with and without cutoff) for demonstrative purpose.

Another difference to the previous section is the way how profiles are presented. Here, we will use the so-called *raw* picture instead of a core, plateau or halo picture. In this raw picture the variables are plotted in the unit system as introduced in chapter 2. Therefore, the representation of the solutions becomes particle mass independent. In this case the results directly show how the entire morphology changes within a family.

Finally, we want to note that the chosen (dimensionless) parameter values are somewhat arbitrary and are only for the propose of illustrating the morphology of families. The comparison with real observation is given in the next chapter.

3.2.1 Solutions without cutoff: ρ_0 family

From the fully degenerate analysis, implying $\theta_0 > 0$ (see section 2.3.3), we know that the core depends mainly on the Fermi energy, equivalent to the product $\beta_0\theta_0$. This parameter degeneracy allows different configurations for a given core, what we describe through a given central density ρ_0/ρ. Note, that we are interested in the central density ρ_0 in units of the scale factor ρ, corresponding to the raw unit system.

In this case we don't need anymore the presentation of the RAR solutions in a core, plateau or halo picture which imply a given particle mass. For example, when the central temperature parameter β_0 is fixed then the solutions can have the very same core (e.g. central density ρ_0) only when the central degeneracy parameter θ_0 and the particle mass m are changed.

Therefore, in fig. 3.14 all solutions are valid for any particle mass. The only constraint is the central density (given in a mass dependent unit system). This family shows three regimes: (1) A degenerate regime with a clear degenerate core, a plateau and a diluted halo. (2) A transition regime with less distinct cores and halos. (3) A diluted regime with a diluted core followed by a Boltzmannian tail without developing an extended plateau.

The regimes are better visible in the analysis picture, see fig. 3.15. Their morphology is very similar to the θ_0 family without cutoff. The difference is in the diluted regime $\theta_0 \lesssim -5$ where the central temperature rises significantly. These high temperature produces thermal effects such that below a specific θ_0 value no plateau and halo are identified anymore. Compare section 3.1.2.

The core size remains constant in the degenerate regime, increases in the transition regime and converges to a constant values again in the diluted regime. Although we described the core through ρ_0 we still obtain a significant change in the core. First, it is worth to emphasize that ρ_0 just constraints the *inner* structure of the core (e.g. it does not take into account the one-core scale at the first extrema in the rotation curve). Second, the correlation with the outer core structure is different in the degenerate regime (e.g. fully degenerate core) than in the diluted regime (e.g. isothermal sphere).

Well correlated to the size are the core mass and velocity. High θ_0 values produces extended plateaus, pushing the halo to larger scales. There is a local minimum in core size in the transition regime. Lower θ_0 values imply higher temperatures what increase the halo in the same way as the core. The interpretation is that thermal pressure blows up the entire mass distribution.

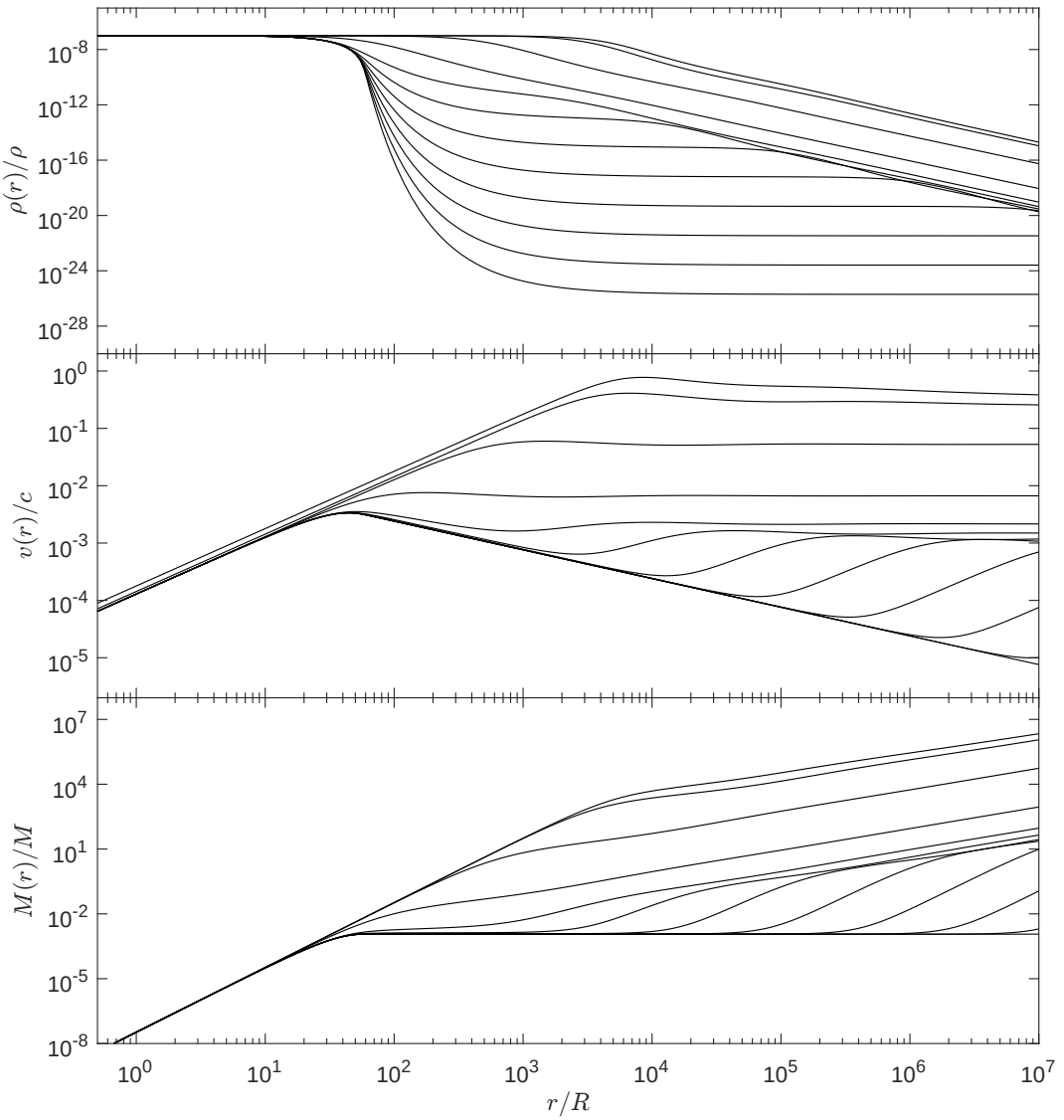

Figure 3.14. Family of solutions with a fixed central density, $\rho_0/\rho = 10^{-7}$, illustrated with density, velocity and mass profiles. Note that radius, mass and density are given in a particle mass dependent unit system (R, M and ρ). The velocity is given units of the speed of light. In this picture the shown family becomes particle mass independent. There are three regimes visible: (1) A degenerate regime with a clear degenerate core, a plateau and a diluted halo. (2) A transition regime with less distinct core and halo. (3) A diluted regime with a diluted core followed by a Boltzmannian tail without developing a plateau.

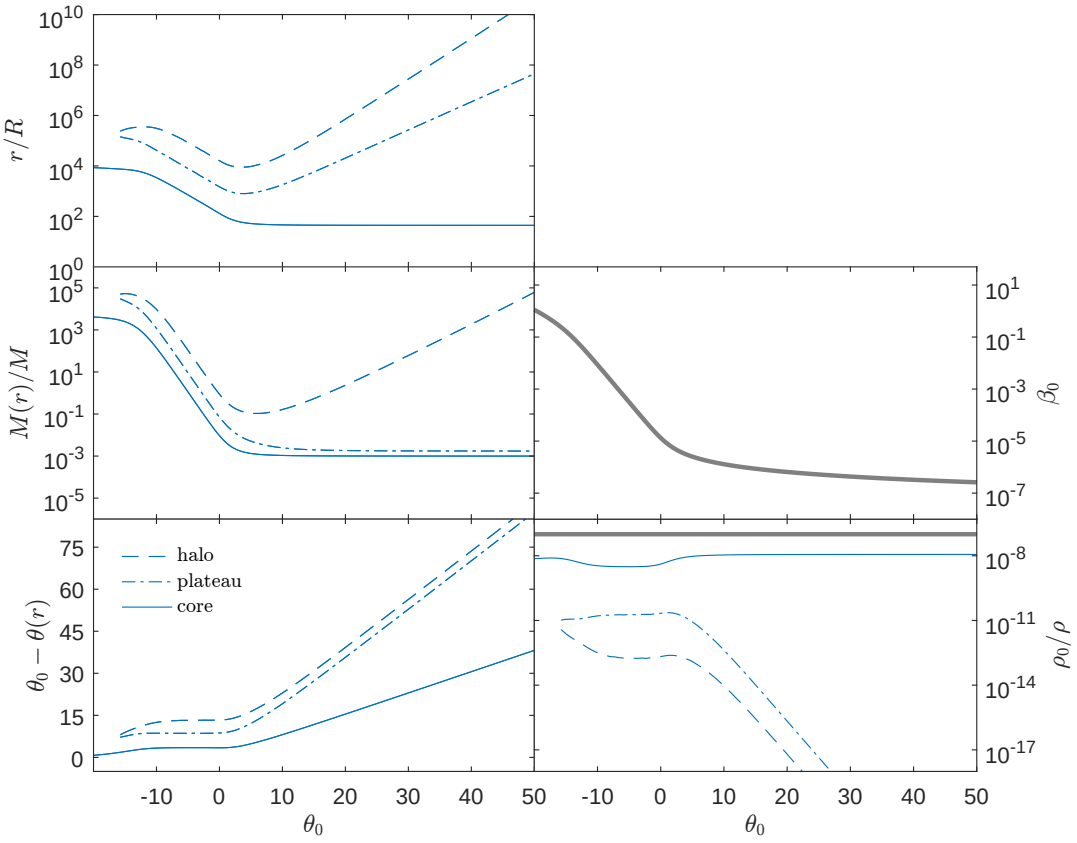

Figure 3.15. Parameter analysis of the ρ_0 family (without cutoff) illustrated with particular values of the radius, mass and degeneracy variables. The values of interest are obtained at the core, plateau and halo. Note that radius and density are given in a particle mass dependent unit system (R and ρ). There are three regimes visible: (1) A degenerate regime with a clear degenerate core, a plateau and a diluted halo. (2) A transition regime with less distinct core and halo. (3) A diluted regime with a diluted core followed by a Boltzmannian tail without developing a plateau.

In the diluted regime, with very low central degeneracy and corresponding high temperatures, strong thermal effects soften the mass distribution such that no halo and plateau are identified anymore (the corresponding minima and maxima merge to a saddle point).

3.2.2 Solutions without cutoff: ρ_p family

Similar to the ρ_0 family we are interested also in the ρ_p family where we fix the plateau density defined at the plateau radius, $\rho_p = \rho(r_p)$. This parameter is appropriate to characterize the inner halo. In fig. 3.16 are few solutions shown to illustrate the morphology of the family. For clarity the configuration window was chosen mostly in the degenerate regime with $\theta_0 \in [2.7, 50]$.

Interestingly, in the density profile the solutions seem to go through a particular point at the plateau. However, this behavior is not present in other profiles, such as the velocity and mass profiles. Although, the plateau radius does not change in the degenerate regime and decreases slightly in the transitions regime. Note that in the diluted regime there is no degenerate core what makes it superfluous to talk about a plateau.

Of more interest is the morphology of the core and the outer halo. Since we constraint with ρ_p only the plateau (e.g. the inner halo), this allows some freedom for other structures. Thus, the solutions here cover a wide range of core-halo distributions

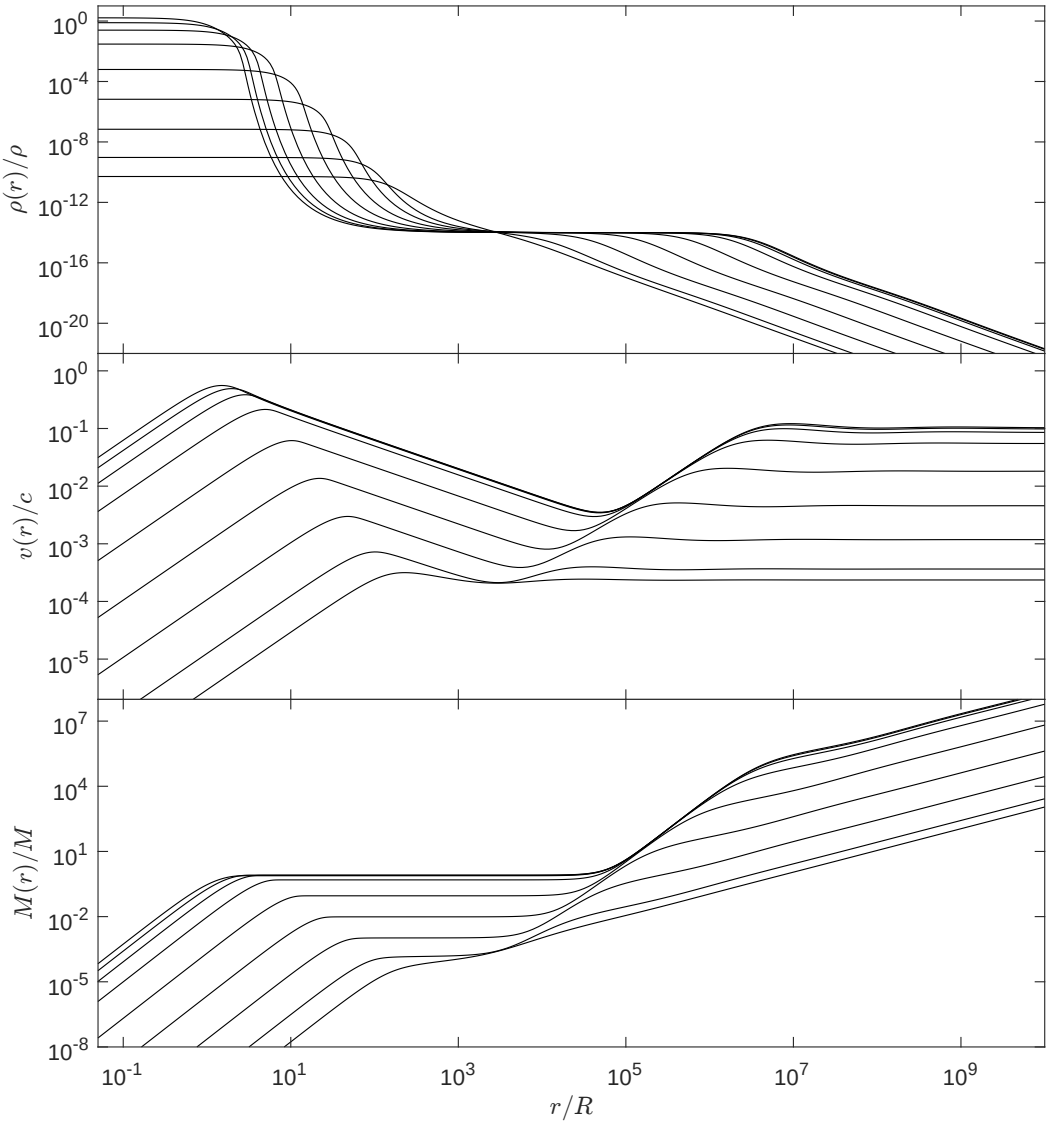

Figure 3.16. Family of solutions with a fixed plateau density ($\rho_p/\rho = 10^{-14}$) illustrated with density, velocity and mass profiles. Note that radius and density are given in a particle mass dependent unit system (R, M and ρ). The velocity is given units of speed of light. In this picture the shown family becomes particle mass independent.

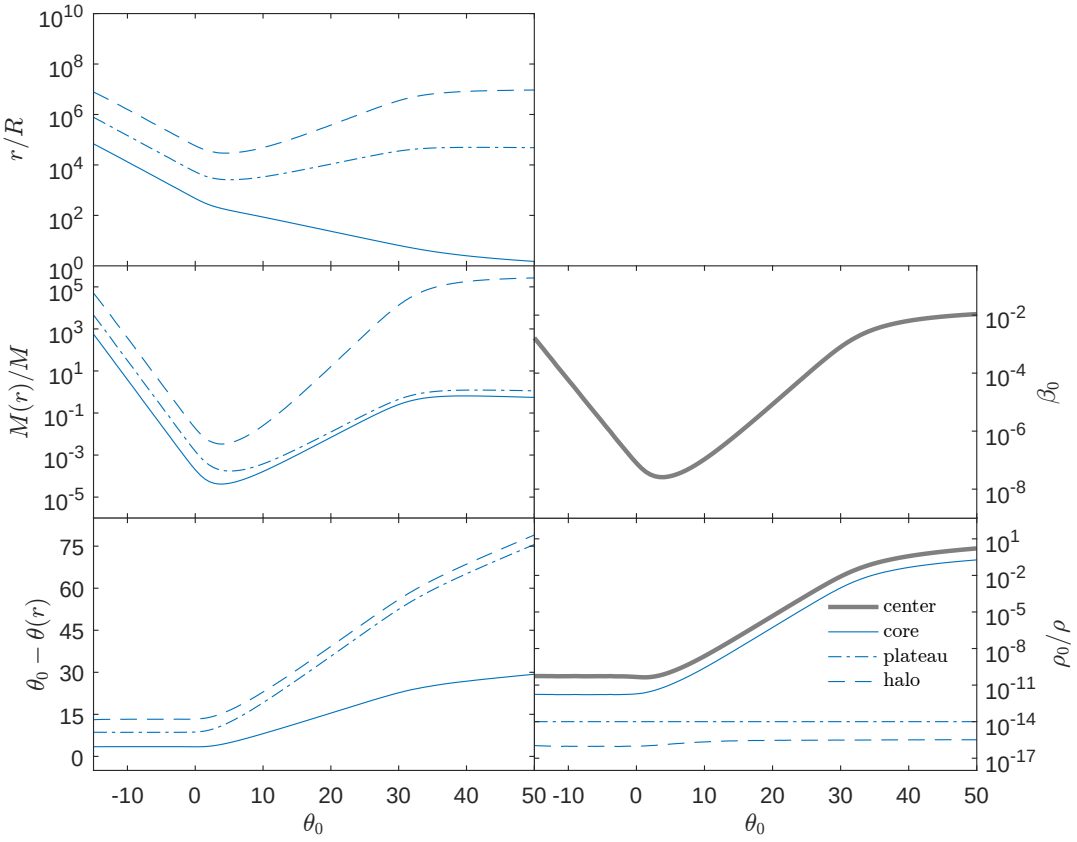

Figure 3.17. Parameter analysis of the ρ_p family (without cutoff) for $\rho_p/\rho = 10^{-14}$. On the left column the family is illustrated with particular values of the radius, mass and degeneracy variables. On the right column are particular values of density and temperature parameter. The values of interest are obtained at the core, plateau and halo. If availbale also at the center. Note that radius, mass and density are given in a particle mass dependent unit system (R, M and ρ).

with significant changes in the core and halo. In summary, the higher the central density the more extended is the plateau, corresponding to larger and more massive halos.

A better picture of the morphology is given in fig. 3.17, where values at the center, core, plateau and halo were extracted from the solutions. Also, in that analysis it is possible to look at a wider θ_0-window without losing clarity. In this picture we identify three regimes: A diluted regime for $\theta_0 \lesssim 0$, a transition regime for $\theta_0 \in [0, 35]$ which covers partially the degenerate regime and a saturation regime for $\theta_0 \gtrsim 35$ where the solutions seem to converge to a particular distribution.

3.2.3 Solutions with cutoff: ρ_0-ρ_p family (CoPla)

After analyzing the ρ_0 and ρ_p families, both without cutoff, we are heading now to the ρ_0-ρ_p family, where we fix the central and plateau densities. Here, we introduce the cutoff parameter W_0 which acts also as a free parameter. The family is illustrated for the combination $\rho_0/\rho = 10^{-7}$ and $\rho_p/\rho = 10^{-17}$. The central density acts here as a characteristic for the core while the plateau density represents the inner halo. Note that there are no constraints for the outer halo which limit the mass distribution in size and mass. In summary, this family falls in the category *core-plateau* constraints (alias CoPla).

The solutions of this family are given in fig. 3.18. The majority may be assigned to the degenerate regime with a degenerate core, followed by a steep fall, a plateau

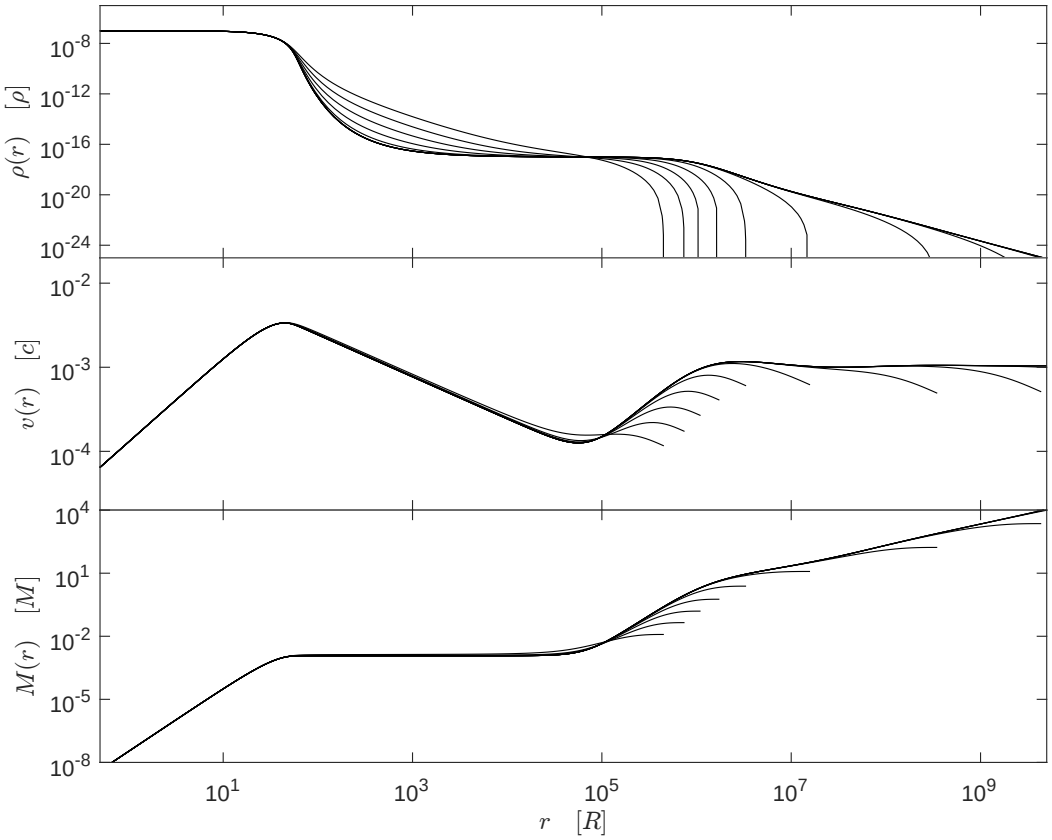

Figure 3.18. Family of solutions with fixed central and plateau density, $\rho_0/\rho = 10^{-7}$ and $\rho_p/\rho = 10^{-17}$, illustrated with density, velocity and mass profiles. Note that radius, mass and density are given in a particle mass dependent unit system (R, M and ρ). The velocity is given units of the speed of light. In this picture the shown solutions are particle mass independent. W_0 is a free parameter here. The predicted solutions are mainly in the degenerate regime, developing a degenerate core, a plateau and a halo. On the bottom edge of the W_0-intervall the solution touch the transition regime with developing cuspy plateaus. There are no solutions in the diluted regime.

and halo. There is already visible a clear correlation between the size of the mass distribution and the cuspiness of the plateau. The solution with the most cuspy plateau is given at the bottom edge of the W_0 interval which touches the transition regime, developing less distinct cores.

A better picture of the morphology and how W_0 affects here the mass distribution is given in fig. 3.19. Interestingly, this family shows just two simple regimes: a regime without and one with surface effects, both mostly in the degenerate regime.

For high W_0 values, the morphology does not change significantly. The central temperature and degeneracy, β_0 and θ_0, remain constant, simply because in this weak regime the cutoff does not affect the core, characterized through the product $\beta_0\theta_0$. Only the outer halo shrinks in size. The lower W_0 the smaller the surface radius (relative to the core).

Surface effects start to appear when W_0 reaches values close to the degeneracy difference between core and halo. This initiates the transformation from a cored to a cuspy halo and ends when the halo merges with the plateau. Because we lose the characteristic of a plateau, as defined above, nothing can be told with certainty about the possible extrapolation of this family beyond this point.

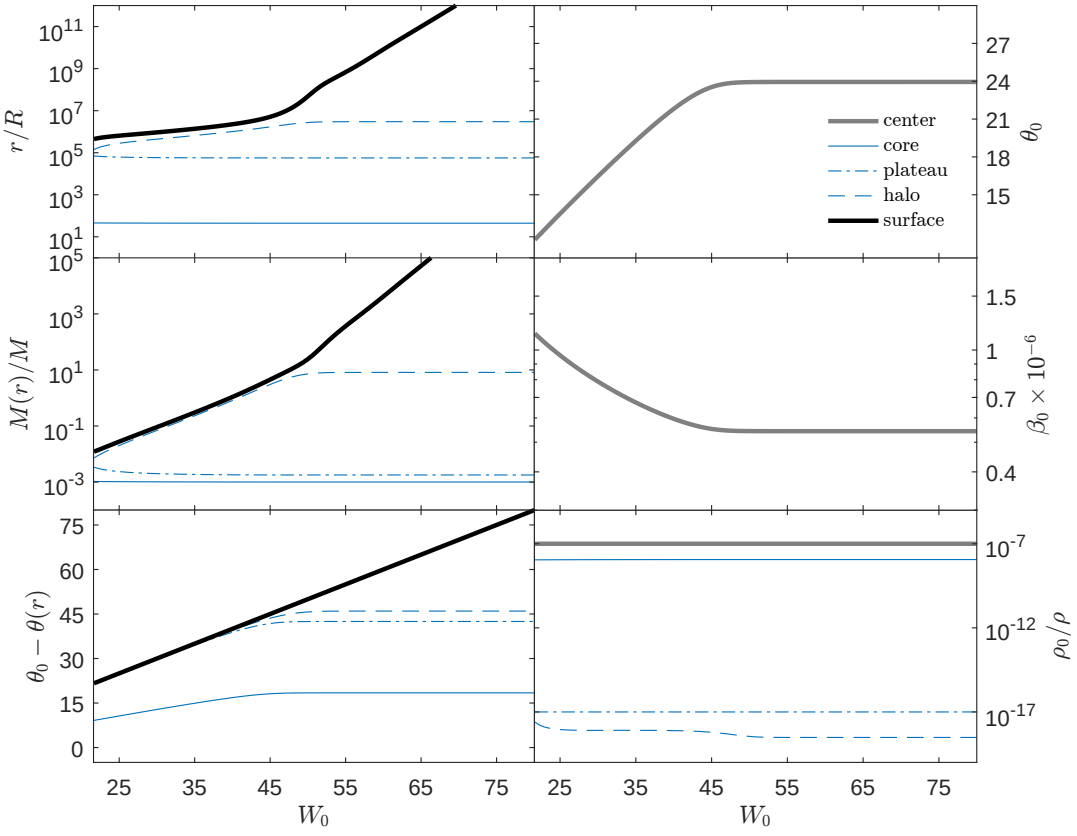

Figure 3.19. Parameter analysis of the ρ_0-ρ_p family with $\rho_0/\rho = 10^{-7}$ and $\rho_p/\rho = 10^{-17}$. The cutoff parameter W_0 has been choosen as the free parameter. On the left column the family is illustrated with particular values of the radius, mass and degeneracy variables. On the right column are particular values of density, temperature parameter and degeneracy parameter. The values of interest are obtained at the core, plateau and halo. If available also at the center and surface. Note that radius, mass and density are given in a particle mass dependent unit system (R, M and ρ).

3.2.4 Solutions with cutoff: M_p-M_s family (BiKe)

Due to the lack of resolution and sensitivity of telescopes, observations are hardly able to discover the galactic center (with a possible compact core) and can barely see the faint stars far at the outer halo to determine a distinct surface radius. Nevertheless, we assume here that a fermionic mass distribution has a specific core mass as well as a specific total mass without knowing the precise values. Therefore, we focus on the important role of the plateau, what resembles a good characteristic of the core mass, and the fact that our dark matter model provides bounded mass distributions. The latter implies the assumption that inter-galactic matter beyond the surface is diluted enough to be neglected.

In other words, we assume the following boundary conditions: $M(r_p) = M_p$ and $M(r_s) = M_s$. Here, r_p is the plateau radius defined at the lowest minima in the rotation curve and r_s is the surface radius where the density drops to zero. Thus, the plateau mass M_p describes well the Keplerian regime after the core and M_s, the entire mass of the bounded mass distribution, describes clearly the Kepleriean regime beyond the surface radius.

The outer Keplerian regime is easy to understand. Outside of the bounded mass distribution, where no matter is present or the matter contribution is negligible, the dynamics are given by simple Keplerian dynamics. The inner Keplerian regime requires an extended plateau which implies an approximately constant mass for a relatively wide range. Thus, in that range the dynamics of stars follow Keplerian dynamics, too.

In summary, the mass distribution is characterized by two Keplerian regimes: one after the core and one after the surface. Of interest is the morphology of such mass distributions, constraint by M_p and M_s. For this Bi-Keplerian family (or simply BiKe) it is convenient to find the right temperature β_0 and the right cutoff parameter W_0 for a given central degeneracy θ_0.

In fig. 3.20 a set of solutions with $M_p/M = 4 \times 10^{-3}$ and $M_s/M = 10^2$ is shown for the range $\theta_0 \in [7, 40]$. For clarity the solutions for $\theta_0 < 7$ are hidden. Thus, in this family the degeneracy parameter covers a wide range, producing solutions in different regimes. The first few plots represent the transition regime with less distinct cores and halos. But with increasing θ_0 the mass distributions emerge more degenerate cores and diluted halos, both connected through more extended plateaus. Interestingly, the *range* of the plateau seems to be limited by the chosen M_p-M_s combination. For relatively high central degeneracies the density profiles develop a power law after the steep fall. And after the power law regime the solutions develop a nearly unique halo characterized through a core, represented by the plateau, followed by a Bolzmannian tail with a strong cutoff.

A better understanding of the different regimes is given in fig. 3.21. Following those results three clear regimes are identified which do not necessary overlap with the θ_0 regimes defined above (diluted, transition, degenerate). Here, we find a diluted regime but for $\theta_0 \lesssim 0$, a semi-degenerate regime with weak evaporation for $\theta_0 \sim 0 - 30$ and a semi-degenerate regime with strong evaporation for $\theta_0 \gtrsim 30$.

In the diluted regime the mass distributions do not change significantly. It becomes more interesting in the semi-degenerate regime with weak evaporation. Due to the fixed surface mass we find that the surface radius remains also nearly constant in that regime. But the halo and plateau radii keep increasing for increasing θ_0. A similar trend is given in the mass analysis. Because we have fixed the plateau and surface mass, the halo mass is bounded by those constraints. Therefore, there has to be a new regime when the halo mass reaches values close the to surface mass. This regime corresponds to a mass distribution with a strong cutoff.

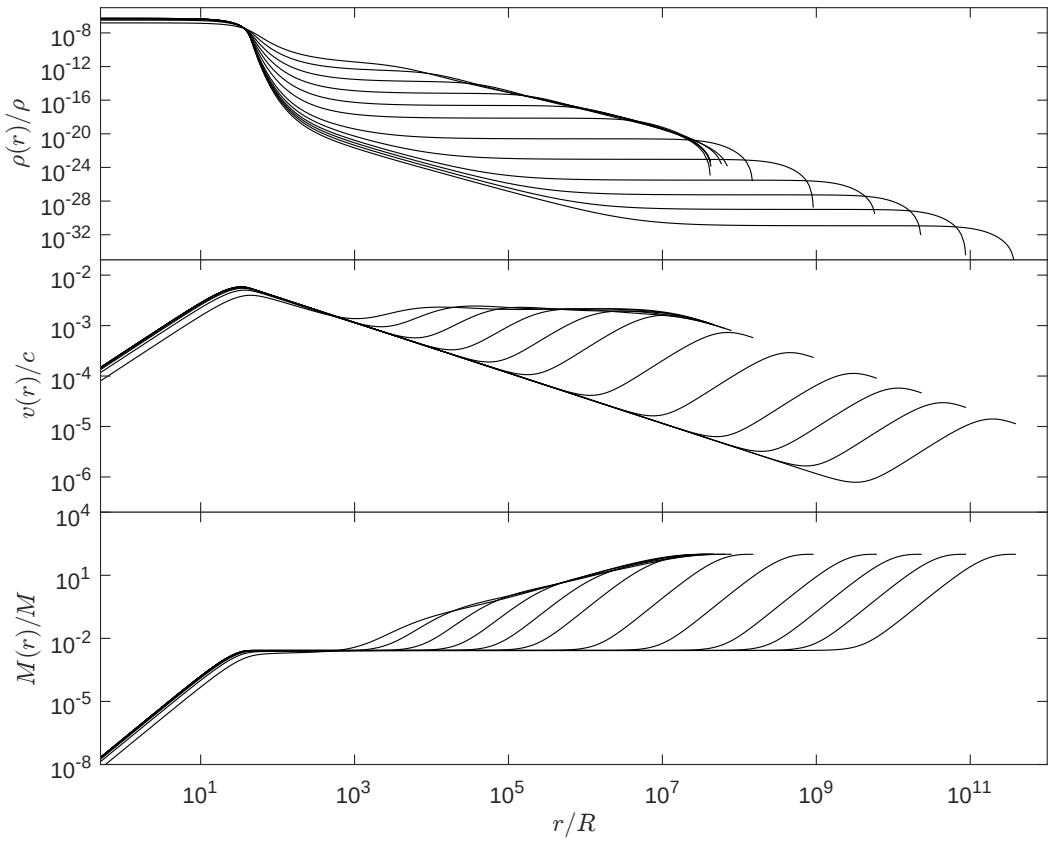

Figure 3.20. Family of solutions with fixed plateau and surface mass, $M_p/M = 4 \times 10^{-3}$ and $M_s/M = 10^2$, illustrated with density, velocity and mass profiles. Note that radius, mass and density are given in a particle mass dependent unit system (R, M and ρ). The velocity is given units of the speed of light. In this picture the shown solutions are particle mass independent. Because θ_0 covers a wide range of values the solutions show (1) a degenerate regime with a clearly degenerate core, a plateau and a diluted halo, (2) a transition regime with less distinct core and halo and (3) a diluted regime with a diluted core followed by a Boltzmannian tail (with a cutoff) without developing a plateau. The latter is not shown for clarity.

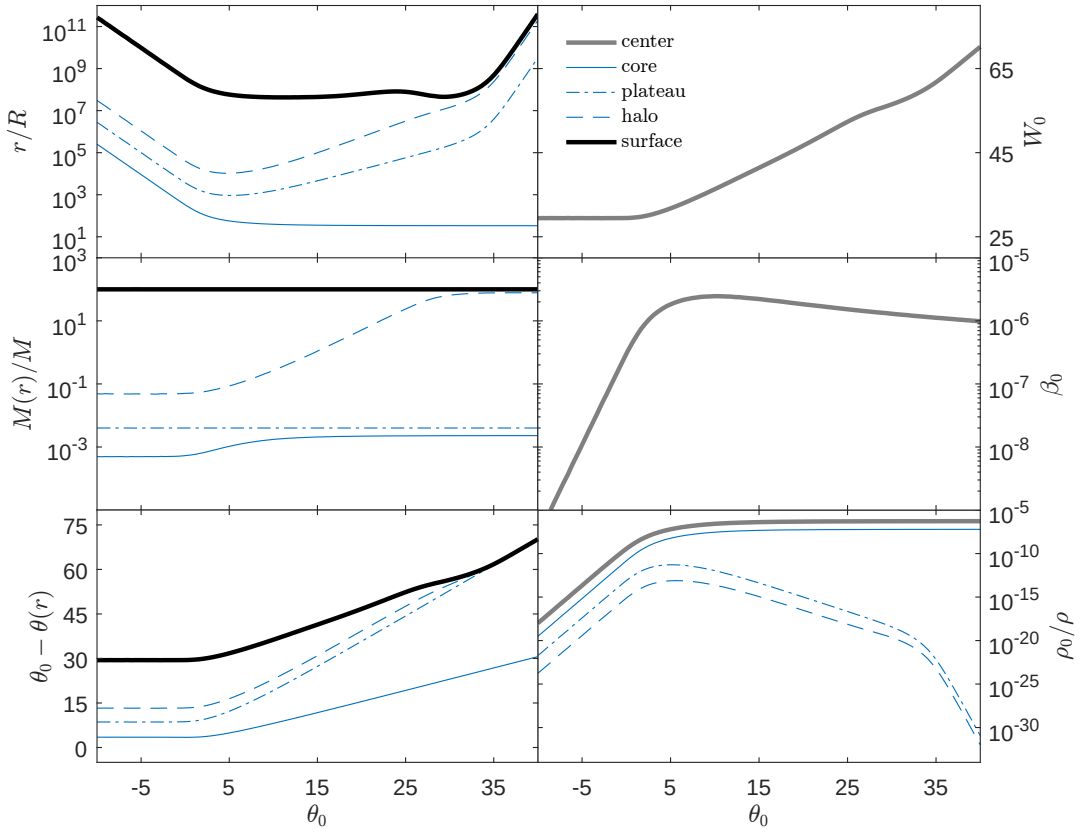

Figure 3.21. Parameter analysis of the M_p-M_s family with $M_p/M = 4\times10^{-3}$ and $M_s/M = 10^2$. On the left column the family is illustrated with particular values of the radius, mass and degeneracy variables. On the right column are particular values of density, temperature parameter and cutoff parameter. The values of interest are obtained at the core, plateau and halo. If available also at the center and surface. Note that radius, mass and density are given in a particle mass dependent unit system (R, M and ρ).

3.3 Universality laws within the model

We proceed now to analyze the core and halo of the model. The core is defined at the first maxima of the rotation. The halo is defined at the second maxima. In particular, we are interested in the relation between those characteristics.

We start by analyzing core and halo separately. Both are approximated by a uniform body. The difference is the central degeneracy θ_0. Thus, the core is very well approximated by a fully degenerate core while the halo is approximated by an isothermal sphere. Remember that the fully degenerate core is applicable only for a positive central degeneracy ($\theta_0 > 0$) and the isothermal sphere only for negative values ($\theta_0 < 0$).

To avoid confusion between the two different central degeneracies (positive and negative) we will in following refer with the symbol θ_0 to the fully degenerate core, implying $\theta_0 > 0$. This is a convenient choice because θ_0 is a monotonic decreasing function. Therefore, the sub-index '0' refers intuitively to the central value. Then after a drop follows a plateau resembling the inner halo. Thus, the degeneracy value at the plateau represents the central value of a isothermal sphere. In following this plateau value will be labeled with θ_p, implying $\theta_p < 0$.

3.3.1 Isothermal halo

The halo is described by an isothermal sphere with $\theta_p \ll -1$ and $\beta_0 \ll 1$. However, the inner halo (also called *halo core*) may be approximated by an uniform body. Thus, with eqs. (2.62), (2.74) and (2.110) we eliminate density and pressure in the hydrostatic equation. Then, solving for the core radius and mass, here r_h and $M_h = M(r_h)$, by considering the boundary condition $P(r_h) = 0$ gives

$$\log \frac{r_h}{l_{\rm P}} \approx \log C_R \; - \frac{1}{4} \log \frac{2\sigma^2}{c^2} \; - 2 \log \frac{m}{m_{\rm P}} \; - \frac{1}{2}\theta_p \; + \frac{1}{2} \log 6 \tag{3.1}$$

$$\log \frac{M_h}{m_{\rm P}} \approx \log C_M \; + \frac{3}{4} \log \frac{2\sigma^2}{c^2} \; - 2 \log \frac{m}{m_{\rm P}} \; - \frac{1}{2}\theta_p \; + \frac{3}{2} \log 6 - \log 3 \tag{3.2}$$

Further, eliminating central degeneracy θ_p and particle mass m gives

$$\frac{M_h}{m_{\rm P}} \left[\frac{r_h}{l_{\rm P}}\right]^{-1} \approx \frac{2\sigma^2}{c^2} \tag{3.3}$$

where we have described the scaling factors in Planck units. It is important to note that σ here belongs to the diluted case and describes a lower bound of central temperature parameter describing the corresponding degenerate core, $\beta_0 \geq \sigma^2/c^2$. Alternatively, eliminating the velocity dispersion constant σ gives

$$\frac{M_h}{m_{\rm P}} \left[\frac{r_h}{l_{\rm P}}\right]^{3} \approx \frac{36\pi}{g^2} \left[\frac{m^4}{m_{\rm P}^4} \mathrm{e}^{\theta_p}\right]^{-2} \tag{3.4}$$

Here, we see clearly the degenerate factor $m^4 \mathrm{e}^{\theta_p}$. This parameter degeneracy makes it impossible to extract any precise information about the particle mass since we may fit the halo with any diluted central degeneracy $\theta_p \ll -1$. Though, because the isothermal sphere implies an upper limit for θ_p it is possible to find a lower limit for the particle mass,

$$\left[\frac{m}{m_{\rm P}}\right]^{8} \lesssim \frac{36\pi}{g^2} \left[\frac{M_h}{m_{\rm P}}\right]^{-1} \left[\frac{r_h}{l_{\rm P}}\right]^{-3} \mathrm{e}^{-2\theta_p} \tag{3.5}$$

It is worth to remind that the condition for the isothermal sphere is already fulfilled for $\theta_p \lesssim -5$, resembling an appropriate upper bound.

3.3.2 Fully degenerate core

In next we focus on the fully degenerate case at low Fermi energies ($\varepsilon_{\mathrm{F}}(r) \approx 1$) and approximate the degenerate core by an uniform body. With eqs. (2.62), (2.74), (2.79) and (2.80) we eliminate density and pressure. Then solving for core radius r_c and core mass M_c by considering the boundary condition $P(r_c) = 0$ gives

$$\log \frac{r_c}{l_{\mathrm{P}}} \approx \log C_R \; - 2 \log \frac{m}{m_{\mathrm{P}}} \; - \frac{1}{4} \log \left[2\varepsilon_{\mathrm{F}}(0) - 2\right] \quad + \log \frac{3}{\sqrt{5}} \; + \frac{1}{4} \log \pi \tag{3.6}$$

$$\log \frac{M_c}{m_{\mathrm{P}}} \approx \log C_M \; - 2 \log \frac{m}{m_{\mathrm{P}}} \; + \frac{3}{4} \log \left[2\varepsilon_{\mathrm{F}}(0) - 2\right] \; + \log \frac{12\sqrt{5}}{25} \; + \frac{1}{4} \log \pi \tag{3.7}$$

Here, it is worth to emphasize that core radius and mass depend only on the central Fermi energy. In the low temperature case $\beta(r) \ll 1$ that energy is given by $\varepsilon_{\mathrm{F}}(0) = 1 + \beta_0\theta_0$. Eliminating the Fermi energy gives an expression for the particle mass depending only on the core radius and mass,

$$\left[\frac{m}{m_{\mathrm{P}}}\right]^8 \approx \frac{162}{125} \frac{\pi^2}{g^2} \left[\frac{M_c}{m_{\mathrm{P}}}\right]^{-1} \left[\frac{r_c}{l_{\mathrm{P}}}\right]^{-3} \tag{3.8}$$

This relation allows to determine the particle mass from information about the core.

3.3.3 Core-Halo relation

In next we give the core-halo relations for radius and mass. Comparing the relations for the halo and core we find

$$\ln \frac{r_h}{r_c} \sim -\frac{1}{2}\theta_p - \frac{1}{4} \ln \theta_0 \tag{3.9}$$

$$\ln \frac{M_h}{M_c} \sim -\frac{1}{2}\theta_p - \frac{3}{4} \ln \theta_0 \tag{3.10}$$

For a complete description we need an equation of state between the central and plateau degeneracy. On the other hand, we may use those relations to eliminate either one of the two degeneracy parameter. Thus, the degeneracy values are given by the halo mass and radius and the corresponding values for the core. With eqs. (3.4) and (3.8) we find that the information about the plateau degeneracy is encoded in the relation between core and halo,

$$\mathrm{e}^{-2\theta_p} \approx \frac{9\pi}{250} \frac{M_h}{M_c} \left[\frac{r_h}{r_c}\right]^3 \tag{3.11}$$

Indeed, this equation truly describes the connecting nature of the plateau, linking the core with the halo.

Among all the different regimes, only the cold and degenerate regime without cutoff ($\beta_0 \lesssim 10^{-4}$, $\theta_0 \gtrsim 15$, $W_0 \to \infty$) shows an universal character where the solutions do not depend on the central degeneracy. Numerically, we find simple power laws for the core-halo relations,

$$\frac{r_h}{r_c} \approx 8.67 \times 1.45^{\theta_0} \tag{3.12}$$

$$\frac{M_h}{M_c} \approx 1.35 \times 1.42^{\theta_0} \tag{3.13}$$

In all other regimes, especially for finite cutoff values, the relations become more complicated.

3.4 Summary

In this chapter we have analyzed the rich morphology of diluted, semi-degenerate and fully degenerate mass distributions, obtained from the introduced dark matter model. The shape of the solutions are described by three configuration parameters (β_0, θ_0, W_0).

Essential for the understanding are density, mass and velocity profiles. Clearly, the fermionic dark matter model shows a rich behavior in the profiles mainly due to a finite cutoff parameter. The basic strategy was to analyze those profiles, in particular by looking at particular values at center, core, plateau, halo and surface. A better insight in the morphology of the various regimes provides the extraction of those particular values from the profiles.

Regime classification

In the first section, we have systematically analyzed how the three configuration parameters affect the solutions. For didactic reasons, it is convenient to start with the RAR model without cutoff ($W_0 \to \infty$). In that case only the central degeneracy and the central temperature are free parameters. The results suggest to divide each parameter space into three regimes. The degeneracy parameter shows a diluted ($\theta_0 \lesssim -5$), a transition ($-5 \lesssim \theta_0 \lesssim 15$) and a degenerate regime ($\theta_0 \gtrsim 15$). Similarly, the temperature parameter shows a cold ($\beta_0 \lesssim 10^{-4}$), a moderate ($10^{-4} \lesssim \beta_0 \lesssim 1$) and a hot regime ($\beta_0 \gtrsim 1$).

The most general solutions here are in the cold and degenerate regime. In that regime, the mass distributions develop a degenerate core embedded in a diluted halo. Since the degeneracy variable is a monotonic decreasing function we clearly find that the diluted halo is well described by an isothermal sphere, represented in the cold and diluted regime. The degenerate core, on the other hand, is well described by a fully degenerate core. Both, core and halo, are connected through a plateau. Based on this general solutions we have adopted typical one-length scales for a core, plateau and halo, defined through the extrema of the rotation curve.

The complexity of the model increases once finite values of the cutoff parameter are considered. The mass distribution becomes finite in mass and size, leading to the adoption of a surface radius. Depending on the θ_0-W_0 combination different surface effects occur. Thus, the W_0 parameter space shows a weak ($W_0 \gg \theta_p$), an intermediate ($W_0 \gtrsim \theta_p$) and a strong regime ($W_0 < \theta_p$) additionally to the regimes of the temperature and degeneracy parameter. A slightly different classification refers to the halo type which is cored for high cutoff values ($W_0 > \theta_p$) but becomes cuspy for lower values ($W_0 \gtrsim \theta_p$). For even lower cutoff values ($W_0 < \theta_0$) the cuspy halo starts to evaporate, leaving a degenerate core with an envelope what represents a particular halo. The characteristic of such a halo is the lack of a maxima in the rotation curve on halo scales what permits to use the definition of the one-halo length scale, leading to a halo deficit.

Role of configuration parameters

The regime classification of the three configuration parameters showed that their role cannot be strictly assigned to observables like central density, core mass or surface radius (or their ratios, respectively). It becomes even more tangled compared to the simpler Fermi-Dirac limit with $W_0 \to \infty$. Although each parameter shows a role tendency.

The product $\beta_0\theta_0$ has a great influence on the central region and high central degeneracies θ_0 are necessary to form a degenerate core, independent of the cutoff parameter. But a finite cutoff parameter W_0 starts to affect the outer halo in the

weak regime and becomes very aggressive in the strong evaporation regime until only a fully degenerate core remains. The temperature parameter β_0 has mainly an effect on the circular velocity. But in the cold regime it is mostly irrelevant for the qualitative shape of the profiles (it may be reduced to a scaling factor). A low temperature remains approx. constant what explains the scaling behavior of a low temperature parameter. For moderate temperatures thermal effects start to act at the central region. That transition ends in the high temperature regime where the halo is not affected anymore by an increase of the central temperature. Interestingly, in that high temperature regime the rotation curve develops a flat rotation curve with oscillations on core scales similar to the flat rotation curve of the halo in the cold regime. That is the reason why we define the plateau as the smallest minima in the rotation curve. Although, a plateau barely exists in the hot regime considering the density profile. Finally, for a well chosen set of configuration parameters the variation of the central temperature parameter (for given θ_0 and W_0 values) may develop cuspy profiles.

Role of physical parameters

A relatively brief analysis was done for physical parameters due to the large number of possible family candidates. Therefore, we have focused only on few families with somewhat arbitrary values for demonstrative purpose. In the first part (solutions without cutoff) two families were analyzed: one describing the core through ρ_0 and another one describing the halo through ρ_p. In the second part (solutions with cutoff) two different families were considered. Both had one constraint for the core and one for the halo.

The analysis of the physical parameter families showed that the configuration parameter change in general. This leads to solutions in many different regimes within one family. Also, the analysis clearly demonstrates that there are inner and outer structures for core and halo. A connecting element is the plateau.

Thus, the central density ρ_0 constraints the inner core structure, leaving core mass and size unconstrained. Similar behavior is given for the plateau density ρ_p, what constraints the inner halo structure but leaves the outer halo (e.g. surface) unconstrained. In contrast, the plateau mass M_p describes very well the outer core structure but leaves some freedom for the central density. Again, a similar behavior is given by constraining the total mass M_p with the difference that it leaves a huge freedom for the inner structures (e.g. core).

Dependent on the constraints it is convenient to choose for each family its specific free parameter. For example, for the M_p-M_s family it is suitable to choose θ_0 because such a family does not constraint the inner core structure. In contrast, for the ρ_0-ρ_p family it is suitable to choose W_0 because such a family does not constraint the outer halo structures. For the latter note that $W_0 = \theta_0 - \theta_s$ may be interpreted as a characteristic for the outer halo. But keep in mind that the θ_0-W_0 combination is crucial.

Parameter relations of a fermionic DM mass distribution

On theoretical ground it is possible to find relations for core and halo, e.g. for their mass and size. Those relations take into account the model parameters, including the particle mass. Note that the core was approximated by an uniform and fully degenerate core while the halo by an uniform and isothermal sphere.

For the halo we find a dependency on particle mass m, velocity dispersion constant σ and the *central* degeneracy θ_p. The latter corresponds to the plateau for solutions with a core embedded in a diluted halo. Most important, the halo is characterized by the parameter degeneracy $m^4 \mathrm{e}^{\theta_p}$. Thus, the halo of a fermionic mass

distribution may be explained with $\theta_p \lesssim -5$ and a particle mass without an upper limit.

The core, on the other hand, depends on the particle mass m and the Fermi energy, described by the product $\beta_0\theta_0$. The latter allows to develop the same core (e.g. mass or size) but different halos. More important is the fact, that the core provides clear information about the particle mass in contrast to the halo.

Considering both, core and halo, allows to break the parameter degeneracies. Though, the ratio of halo to core size as well as the ratio of halo to core mass depend on the degeneracies at the plateau and center. It is important to emphasize here that those degeneracies follow a relation, depending on the chosen parameter set. Only for the cold and degenerate regimes without a cutoff we find relations based on numerical calculations. All other regimes show a highly non-linear behavior.

Regime exclusion

In summary, the fermionic dark matter model provides various different regimes regarding the three configuration parameter (β_0, θ_0, W_0). The aim of the analysis in this chapter was to illustrate a complete picture of the possible equilibrium configuration of self-gravitation fermions. For better clarity the solutions where subdivided into different regimes. The question now is which of those regimes are relevant for known physical systems. As will be demonstrated in the next chapter, few regimes may be excluded based on observational constraints.

However, it is important to emphasize in advance that the hot and degenerate regime ($\beta_0 \geq 1$ for $\theta_0 \geq 15$) is excluded, based on stability analysis. Argüelles, Ruffini, and Fraga, 2014 showed that the quantum core of a semi-degenerate mass distribution composed of fermions posses a critical mass corresponding to a central temperature parameter in the moderate regime. For larger values of the temperature parameters the quantum core becomes unstable.

Although the analysis was done for fermionic dark matter without evaporation effects (e.g. without a cutoff) it is clear that the same results are applicable for the dark matter model with cutoff as introduced here. This is based on the characteristics of the cutoff parameter which affects mainly the outer halo and therefore leaves the quantum core undisturbed.

Concluding remarks

Finally, it is worth to mention that for classifying the radial extent of the semi-degenerate solutions the introduction of a core, a plateau and a halo was very helpful. All this characteristics are defined through the extrema of the rotation curve. However, the rotation curve is not the only convenient candidate with appropriate criteria (e.g. extrema). Interesting alternatives with a similar topology are the derivative of the mass, $\mathrm{d}M(r)/\,\mathrm{d}r$, and the compactness, $M(r)/r$. Both are independent of the particle mass. On theoretical ground, the derivative of the metric potential and the derivative of the degeneracy parameter satisfy the criteria as well. Even more, the derivative of the degeneracy parameter provides two maxima only in the degenerate regime (here $\theta_0 \gtrsim 10$), making it an exciting candidate for analytic purpose.

Chapter 4

Application

After recalling the fermionic dark matter model including cutoff effects (hereafter RAR model) in chapter 2 and providing in chapter 3 its analysis for a better understanding, the aim of this chapter is its application to different galaxy types. The results are supported by the work presented in Argüelles et al. (2018).

Section 4.1 starts with the analysis of the well resolved Milky Way galaxy what provides crucial implications for the dark matter particle mass. With the new knowledge section 4.2 continues to analyze other galaxy types, such as typical dwarfs, spirals and ellipticals. Including results from the Milky Way I show also that the RAR model is able to explain universal galaxy relations. In section 4.3 a third work compares the RAR model with two other phenomenological dark matter models within a set of galaxies from the SPARC data base. Finally, in section 4.4 I provide a discussion of the main results of our work and further comment on where it stands with respect to the current affairs of cosmological DM and structure formation. Especially, its potentiality to solve some of the actual discrepancies within the standard Λ Cold Dark Matter (ΛCDM) and Λ Warm Dark Matter (ΛWDM) cosmologies will be indicated.

4.1 Milky Way

We show here that the gravitational potential of the new quantum core, embedded at the centre of the DM halo, explains the observed dynamics of the surrounding gas and stars in the Galactic center without the necessity of introducing a central BH. This result is based on a recent and extensive observational study of the Milky Way rotation curves (Sofue, 2013), complemented by the central S-star cluster data (Gillessen et al., 2009b) and the analysis of the Sagittarius stream on outer halo scales (Gibbons, Belokurov, and Evans, 2014).

About two decades ago an idea arose that dark matter could play an important role in below pc scales. After the discovery of the M-σ relation it became clear that supermassive objects are embedded in the center of the hosting galaxy, making them them favorite candidates for black holes. However, many of them remain dark without showing the typical characteristics like X-ray emission and jets to be classified as black holes. And that's the point where fermionic dark matter becomes interesting. By considering quantum particles the supermassive compact objects at the center of galaxies may be described by degenerate fermions forming a so called *fermi ball* (sometimes also *neutrino ball*) and giving an alternative to the black halo paradigm (Argüelles and Ruffini, 2014; Tsiklauri and Viollier, 1998). Focusing only on the quantum core it is possible to derive an upper and lower bound for the particle mass. With this approach De Paolis et al. (2001) found a particle mass in the range from 11 keV up to 787 keV for a core mass of $M_c = 2.6 \times 10^6 M_\odot$. The following analysis further narrows the allowed particle mass range.

The adopted observational constraints are explained and summarized in section 4.1.1. It is followed by detailed results in section 4.1.2. In particular, implications are shown for the dark matter distribution and the particle mass it is composed of.

4.1.1 Observational constraints

We consider here the extended high resolution rotation curve data of the Galaxy as provided in Sofue (2013). It ranges from few pc up to several hundred kpc, covering different baryonic structures such as the bulge and disk. Information about the galactic center (at sub-parsec scales) is provided through the orbital data of the seven best resolved S-cluster stars taken from Gillessen et al. (2009b). Complimentary data about the outer halo ($r \gtrsim 10\,\mathrm{kpc}$) is given by Gibbons, Belokurov, and Evans (2014) who analyzed the Sagittarius stream to constrain the Milky Way galaxy mass. Accordingly, the matter components of the Galaxy can be divided in four independent mass distribution laws, governed by different kinematics and dynamics:

- The central region ($r \sim 10^{-4}$ – $2\,\mathrm{pc}$) consists of young S-stars and molecular gas. It follows a Keplerian law $v \propto r^{-1/2}$, whose dynamics is dictated by a dark and compact object centred in SgrA*.
- An intermediate spheroidal Bulge structure ($r \sim 2$ – $10^3\,\mathrm{pc}$) is composed mostly of older stars. Both, inner and a main component, are explained by the exponential spheroid model. It presents a maximum bump in the velocity curve of $v \approx 250\,\mathrm{km/s}$ at $r \sim 0.4\,\mathrm{kpc}$.
- An extended flat disk ($r \sim 10^3$ – $10^4\,\mathrm{pc}$) includes a star forming region (dust and gas), whose surface mass density is described by an exponential law.
- A spherical halo ($r \sim 10^4$ – $10^5\,\mathrm{pc}$) is dominated by DM and presents a velocity peak of $v \approx 160\,\mathrm{km/s}$ at about $r \sim 30\,\mathrm{kpc}$. The outer halo shows a decreasing density tail steeper than r^{-2}.

Our analysis will thus cover in total more than nine orders of magnitude of radial extent with stellar and dark mass components. The total rotation curve allows to link those components.

The objective now is to fit the Milky Way data with contributions from our dark matter model in order to find solutions consistent with the observationally constrained DM halo of the Galaxy. Simultaneously, we require a quantum core mass $M_c \equiv M(r_c)$ enclosed within the S2 star pericentre $r_{p(S2)} = 6 \times 10^{-4}\mathrm{pc}$. The latter sets a lower limit for the core radius, $r_c < r_{p(S2)}$, defined at the first maxima in the rotation curve. In summary, we adopt

- $M_c = 4.2 \times 10^6\, M_\odot$ (Gillessen et al., 2009b)
- $M(12\,\mathrm{kpc}) = 5 \times 10^{10}\, M_\odot$ (Sofue, 2013)
- $M(40\,\mathrm{kpc}) = 2 \times 10^{11}\, M_\odot$ (Gibbons, Belokurov, and Evans, 2014)

These constraints we use to determine the model parameters, e.g. (β_0, θ_0, W_0) for a given particle mass m (at keV scales), with the least-square fitting method.

4.1.2 Results

Following the standard assumption in the literature that baryonic and dark matter interact only gravitationally, we have reproduced the rotation curve of the Milky Way galaxy by combining stellar components together with our dark matter contribution,

$$v^2_{\mathrm{tot}}(r) = v^2_{\mathrm{b}}(r) + v^2_{\mathrm{d}}(r) + v^2(r) \tag{4.1}$$

The total (inner + main) bulge circular velocity $v_{\rm b}(r)$ was calculated with the same model parameters as in Sofue (2013). For the disk $v_{\rm d}(r)$ we have performed the calculations with model parameters slightly changed with respect to those given in Sofue (2013), where the NFW DM profile was assumed. We do this change to improve the fit of the observational data when adopting our DM profile. Finally, the novel DM contribution was computed numerically by

$$\frac{v^2(r)}{c^2} = \frac{{\rm d}\nu}{{\rm d}\ln r/R} \tag{4.2}$$

The key result of our work, summarized in fig. 4.1, is that there is a continuous underlying DM distribution covering the whole observed Galactic extent. It governs the dynamics of the halo (above $r \gtrsim 10\,{\rm kpc}$) as well as the Galactic center (sub-parsec) without spoiling the intermediate region dominated by the baryonic components (bulge+disk).

Core–halo distribution

The DM density solution shows a division of three physical regimes: core, plateau and halo. The quantum core of almost constant density is governed by quantum degeneracy. It is followed by a sharp decrease, where quantum corrections are still important, and an intermediate region with an extended plateau. For high particle masses a power law emerges after the sharp decrease what transitions into the extended plateau. In that case the halo is characterized by a modified Boltzmannian density tail showing a behavior $\rho \propto r^{-n}$ with $n > 2$. On the other hand, for low particle mass the halo is well explained by the isothermal sphere, showing a regular $\rho \propto r^{-2}$ behavior.

The different regimes in the density profiles are also manifest in the DM rotation curve. A linearly increasing circular velocity $v(r) \propto r$ reaches a maximum at the quantum core radius r_c. It follows a Keplerian power law, $v(r) \propto r^{-1/2}$, with decreasing behavior representing the transition from quantum degeneracy to the dilute regime. After a minimum, highlighting the plateau, the circular velocity continues with a linear trend again until reaching the second maximum at r_h, which we adopt as the one-halo scale length in our model. The remaining behavior is consistent with the power law density tail for the given particle mass. For heavy particles the rotation curves changes into a Keplerian power law at the surface radius r_s. For light particles the solution develop the typical flat rotation curve of the isothermal sphere.

Comparing these results with the results in the analysis chapter, we find that the solutions cover the cold, degenerate and weak regime for low particle masses. In contrast, for high particle masses the solutions are mainly in the moderate, degenerate and intermediate regime, implying the necessity of thermal and surface effects.

Halo boundary

The DM contribution to the Galactic halo becomes necessary above ~ 7 kpc. This is in agreement with the DM model-independent observational analysis by Iocco, Pato, and Bertone (2015). According to our model the Milky Way outermost DM halo behavior is subjected to the cutoff condition $W(r_s) = 0$ with $r_s \approx 50\,{\rm kpc}$. Note that we considered here only solutions with compact enough cores (see blue lines in fig. 4.1). It is clear that such a DM halo mass distribution must be also in agreement with the dynamical constraints set by the Galactic satellite dwarf observations, e.g. the Sagittarius (Sgr) dwarf satellite.

Indeed, such observational constraints have been recently considered in Gibbons, Belokurov, and Evans (2014). They showed that their fulfillment requires a total

Galaxy mass of $M_{\rm tot}(50{\rm kpc}) \approx 3 \times 10^{11}\, M_\odot$. This in agreement with our results where $\sim 80\%$ of the total mass is dark according to our model (i.e. $M(r_s) \approx 2.3 \times 10^{11}\, M_\odot$).

Constraints on the total (virial) Galaxy mass from the Sgr dwarf stream may imply even larger values of $M_{\rm tot}(100\,{\rm kpc}) \approx 4 \times 10^{11}\, M_\odot$ (Belokurov et al., 2014; Gibbons, Belokurov, and Evans, 2014). Nevertheless, this stream motion of tidally disrupted stars is likely related with merging processes that date back to the DM halo formation of the Galaxy (Lynden-Bell and Lynden-Bell, 1995). However, our modeling does not include mergers nor dynamical DM accretion from environment what may likely increase the Galaxy mass during its whole evolution.

Particle mass limits

The fermion mass range $mc^2 \leq 7.6\,{\rm keV}$ is firmly ruled out by the present analysis. For this lowest particle mass the solutions differ only in the outer halo, mostly beyond any observables.

In the intermediate range $mc^2 \sim 7.6$ – $48\,{\rm keV}$ the theoretical rotation curve is not in conflict with any of the observed data and DM inferences in Sofue (2013). But the compactness of the quantum core is not enough to be an alternative to the central BH scenario.

There is a fermion mass range $mc^2 \sim 48$ – $345\,{\rm keV}$ with corresponding accompanying parameters (θ_0, β_0, W_0), whose associated solutions explain the Galactic DM halo while providing at the same time an alternative for the central BH. The lower bound in m is imposed by the dynamics of the stellar S-cluster, while the upper bound corresponds to the last stable configuration before reaching the critical mass for gravitational collapse ($M_c^{cr} \sim m^{-2}$, see also Argüelles and Ruffini (2014)). The critical configuration has a core radius $r_c \approx 4\, r_{\rm Sch}$ with $r_{\rm Sch}$ the Schwarzschild radius associated to a BH of $4.2 \times 10^6\, M_\odot$ (see also Argüelles, Ruffini, and Fraga (2014)).

Following the analytical approximation for a lower particle mass limit, given by eq. (3.8), we obtain $mc^2 \geq 35.9\,{\rm keV}$ for the core mass of $M_c = 4.2 \times 10^6 M_\odot$ within the inner most pericentre, $r_c \leq 6 \times 10^{-4}\,{\rm pc}$, given by the S2 star. The upper particle mass limit we obtain for the highest possible compactness of $M(r)/r \leq 5/9$, see chapter 2. Applied at the core, with $r_c/l_{\rm P} \geq 9/5 \times 2M_c/m_{\rm P}$, we find $mc^2 \leq 446\,{\rm keV}$. Therefore, the obtained range $mc^2 \sim 48$ – $345\,{\rm keV}$ is also well in agreement with the analytically determined.

When looking at the baryonic structures only, then the full rotation curve (solid red line in fig. 4.1) is in good agreement with observations of Sofue (2013) within the observational uncertainty. For the full mass range $mc^2 \sim 7.6$ – $345\,{\rm keV}$ all our theoretical DM distributions produce Keplerian rotation curves at $r \lesssim 2\,{\rm pc}$. This in agreement with the innermost gas data points obtained in Sofue (2013) who had indeed pointed out that this Keplerian trend can be only dominated by a dark central object with a negligible baryonic contribution.

Additionally, in all solutions the minimum in the DM rotation curve *coincides* with the absolute maximum of $v_{\rm rot}$ (i.e. the bulge peak) attained at $r \approx 0.4\,{\rm kpc}$. This peculiar fact should provide more enlightening clues for a deeper understanding of the complex ensemble history of the baryonic stellar bulge on top of the previously formed DM structure, characterized by the core-halo distribution.

Further constraints

The above full particles mass range depend highly on the chosen set and number of constraints. For instance, there is a small transition regime at about 10 keV where the evaporation effects become less distinct such that the halo transforms towards an isothermal sphere. The limiting case corresponds to the lower limit of the particle mass window, $mc^2 = 7.6\,{\rm keV}$ and is achieved for $W_0 \to \infty$. Due to the different halos

the solutions in that narrow regime (7.6 keV up to approx. 10 keV) are not comparable anymore with the solutions for particles masses above ~ 10 keV.

Therefore, a possible further constraint (e.g. the surface mass or radius) may be adopted for lower particle masses such that the solution produce the same halo. But in that case it is necessary to relax the core mass constraint. Otherwise the problem is over-constraint and no solutions exist.

Nevertheless, for such a change of constraint the results a consistent. For particle masses $mc^2 \lesssim 10$ keV the solution develop the right halo but are not able to form cores with the right mass. More important, the solution produce an overshoot in the inner rotation curve. The smaller the particle mass the, larger the overshoot.

Baryonic matter modeling

The overshoot in the observed inner-rotation curve implies that the lower limit to the fermion mass will hold also for different and more accurate inner-baryonic models (e.g. Portail et al., 2017), which — in any case — change the total inner-rotation curve only by a small percentage with respect to the one used in this work. In addition, for these relatively low particle masses below 10 keV, and due to the overshooting in the inner-bulge velocity region, it is clear that these solutions only fulfill the chosen halo boundary conditions and do not provide an alternative to the central BH in SgrA*.

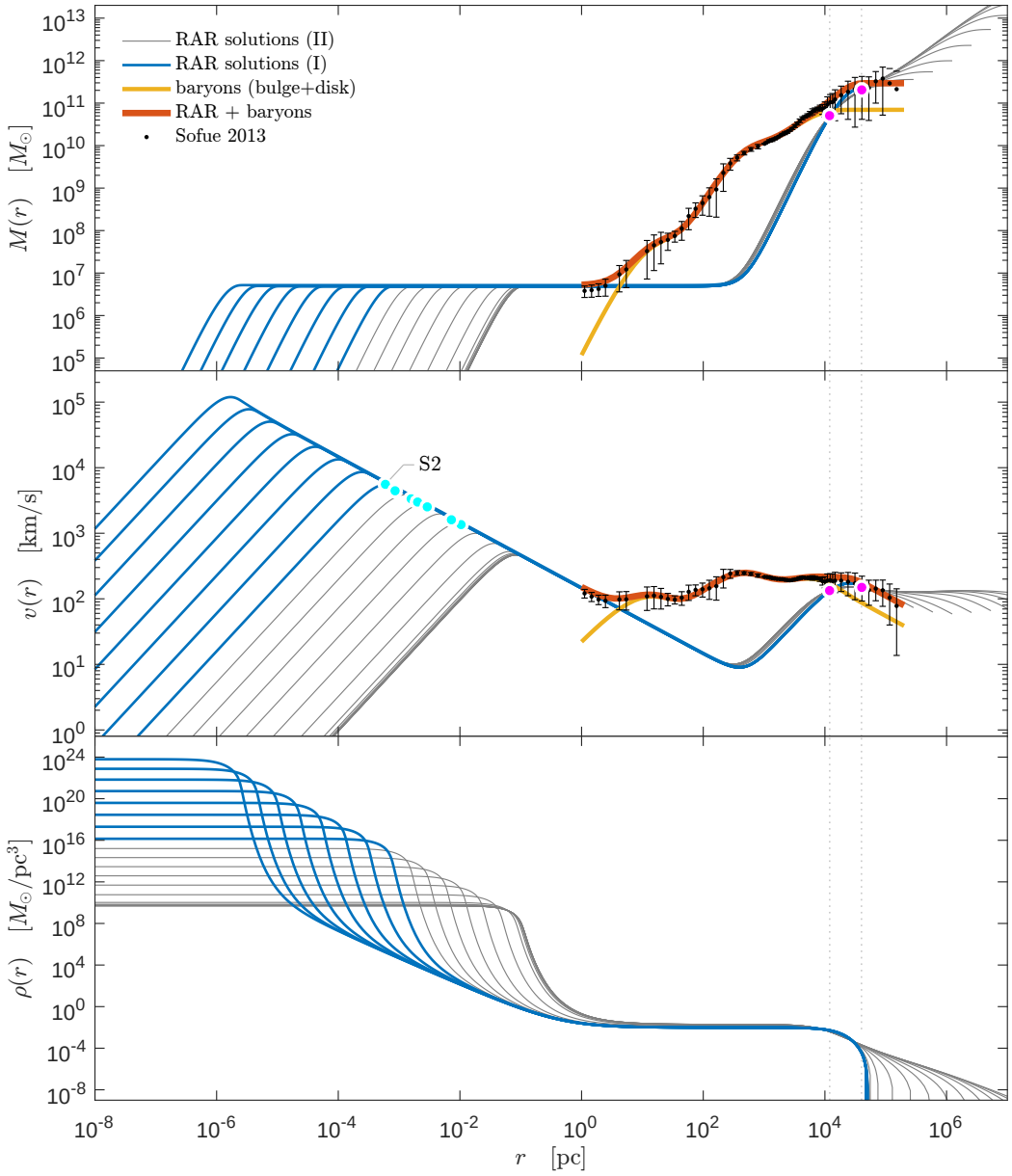

Figure 4.1. Theoretical mass profiles (upper panel), rotation curves (middle panel) and density profiles (lower panel) for different DM fermion masses in the keV region. The solutions are in agreement with all the Milky Way observables, such as the dynamics of S2 stars and kinematic data of the baryonic structures (from $\sim 10^{-3}$ pc to $\sim 10^{5}$ pc). The continuous thick-red curve represents the total rotation curve, composed of all baryonic components (yellow line) and the dark component (blue lines). Only in the range $mc^2 = 48$–$345\,\mathrm{keV}$ (blue lines) the developed quantum core is able to mimic the dynamics of the S-cluster stars. Lower particle masses (gray lines) produce the right core mass but with a too low compactness. Blue points represent the eight best resolved S-cluster stars (Gillessen et al., 2009b), whose positions in the plot indicates the *effective* circular velocity at pericentre (i.e. without considering the ellipticity of the orbits). In the inner bulge region ($r \sim 2 - 10^2$ pc) the large velocity error bars of about ± 20–30% are mainly due to non-circular motions, while in the halo region there are larger observational errors bars of up to $\sim 50\%$ due to systematics (Sofue, 2013).

4.2 Dwarfs, spirals and ellipticals

It is now natural to ask whether or not the RAR model can explain the observational properties of other types of galaxies, in the same range of DM particle mass obtained above. We therefore proceed to show how, for a fixed particle mass m, our model leads to an extensive three-parametric (θ_0, β_0, W_0) family of dark halos with parameters ranging from the ones of dwarf to the ones of elliptical galaxies, harboring at the same time a semi-degenerate core at each center.

It is important to stress that in the case of our Galaxy, analyzed in section 4.1, we identified three relevant *observable* conditions, thanks to the vast amount of rotation curve data from the center (Gillessen et al., 2009b; Sofue, 2013), to the halo (Sofue, 2013), to the periphery (Belokurov et al., 2014; Gibbons, Belokurov, and Evans, 2014). Thus, we constraint a dark core mass and two intermediate dark halo masses out of which the three (free) model parameters (β_0,θ_0,W_0) were obtained for different particle masses m in the keV range.

On the contrary, when dealing with different galaxy types, located far away from us, the observational inferences of the DM content are limited to a narrow window of galaxy radii, usually lying just above the baryonic dominance region (i.e. typically up to several half-light radii). Generally, there is no observational access. Neither for the possible detection of a dark compact object at the centre nor for constraining the boundary of the DM halo at the virial radius scale.

4.2.1 Observational constraints

In this work we adopt a similar methodology as for the Milky Way, but limited to radial halo extents where observational data is available, allowing to constraint the DM halo mass in a model independent/dependent manner. In particular, we will select as the only boundary conditions, taken from observables, a characteristic halo mass $M_h \equiv M(r_h)$ and a halo radius r_h. The latter is defined as the location of the maximum of the halo rotation curve which we adopt as the one-halo scale length of our model. Thus, we define now the parameters adopted for the different DM halos as constrained from observations in typical dwarf spheroidal (dSph), spiral and elliptical galaxies.

Typical dSph galaxies

We consider the eight best resolved dwarf satellites of the Milky Way, as analyzed in Walker et al. (2009) by solving the Jeans equations for large (stellar) kinematic data sets including orbital anisotropy.

There, it was reported a DM model-independent evidence of a maximum-circular velocity (v_{max}) in the DM halo of the Fornax dwarf (see fig. 2 in Walker et al., 2009). Such an evidence was found by comparing the theoretical projected dispersion velocity (from Jeans equation) with the observed one through a Markov-Chain-Monte-Carlo method. A 4-parametric generalized Hernquist mass model for the halo was considered, allowing either for cored or cuspy density profiles depending on the free parameters. The best fit to v_{max} was found independently of the free parameters couple which control the DM shapes (i.e. in a DM independent way).

In the other seven cases evidence for a DM circular velocity peak was found, assuming either cuspy (e.g. NFW) or cored (e.g. cored-Hernquist) DM halo density profiles.

In all eight cases the inferred radii and masses at the maximum circular halo velocity (supported by data) are $r_{\max(d)} \equiv r_{h(d)} \sim$ few 10^2 pc and $M(r_{\max(d)}) \equiv M_{h(d)} \sim$ few $10^7 M_\odot$. Those values are valid for a cored-Hernquist DM profile assumption, similar to the RAR profiles here presented (see e.g. Argüelles et al.,

2016; Ruffini, Argüelles, and Rueda, 2015 for the RAR halo fits to isothermal and Burkert profiles respectively). Somewhat larger values, $r_{\max(d)} \sim 1\text{kpc}$ and for $M(r_{max(d)}) \sim 1 \times 10^8 M_\odot$, are obtained for cuspy profiles. Though, the latter is disfavored with respect to cored profiles for dSph as recently reviewed in Bullock and Boylan-Kolchin (2017).

Thus, as allowed by data, we adopt throughout this work the following fiducial values for the characteristic DM halo properties for typical dSphs:

$$r_{h(d)} = 400\,\text{pc} \tag{4.3}$$
$$M_{h(d)} = 3 \times 10^7\, M_\odot \tag{4.4}$$

Typical spiral galaxies

Besides the Milky Way, as analyzed in section 4.1, we consider some nearby disk galaxies observed in high resolution from the THINGS data sample (de Blok et al., 2008), where DM model-independent evidence for a maximum in the halo rotation curves is provided. Such an evidence is obtained by accounting for stellar and gas baryonic components (thanks to the inclusion of infrared data from the *Spitzer* telescope) in addition to the (total) observed rotation curve from the HI tracers. With the help of the observed rotation curve v_{obs} and the corresponding build up of mass models for the baryonic components $v^2_{bar} = \Upsilon_* v^2_* + v^2_{gas}$ (with Υ_* the stellar mass-to-light ratio) they calculate along the full observed data coverage the DM halo contribution through $v^2_{halo} = v^2_{obs} - v^2_{bar}$.

This analysis provides support for a clear evidence of a maximum in the circular velocity, shown for galaxies with extended enough data coverage which mainly correspond to the larger and more luminous (see gray curves within fig. 63 in de Blok et al. (2008)). The maximum values for radii and velocity in the more luminous galaxies ($M_B \lesssim -20$) are expected to be bounded from above and below as 10 kpc $\lesssim r_{\max(s)} \lesssim 80$ kpc and 70 km/s $\lesssim v(r_{\max(s)}) \lesssim 310$ km/s. This further implies masses in the range $1 \times 10^{10} M_\odot \lesssim M(r_{\max(s)}) \lesssim 2 \times 10^{12} M_\odot$. The reported bounds for $r_{\max(s)} \equiv r_{h(s)}$ and $v(r_{\max(s)})$, implying $M(r_{\max(s)}) \equiv M_{h(s)}$, are based on NFW models together with data support up to $\approx 50\,\text{kpc}$.

Thus, as allowed by data, we adopt throughout this work the following fiducial values for the characteristic DM halo properties for typical spirals:

$$r_{h(s)} = 50\,\text{kpc} \tag{4.5}$$
$$M_{h(s)} = 1 \times 10^{12}\, M_\odot \tag{4.6}$$

Typical elliptical galaxies

We consider a small sample of elliptical galaxies from Hoekstra et al. (2005), studied via weak lensing signals, and further analyzed in Donato et al. (2009) by providing halo mass models for the tangential shear of the distorted images. We also include the iconic case of the largest and closest elliptical galaxy M87 as studied in Romanowsky and Kochanek (2001), accounting for combined halo mass tracers such as stars, globular clusters (GCs) and X-ray data. While kinematical measurements (e.g. GCs) can probe distances up to several tens of kpc, X-ray and weak lensing data can reach much further distances up to several hundreds of kpc. The latter allows for DM model-dependent evidence of maximum circular velocities on halo scales where data supports.

The DM profiles (i.e. Burkert or NFW), used to obtain best fits to the full data coverage in the galaxies, provide the following maxima values: $r_{\max(e)} \equiv r_{h(e)} \approx 100$ kpc

and $M(r_{\max(e)}) \equiv M_{h(e)} \approx 10^{12} M_\odot$ (in the case of the more luminous ellipticals with $M_B < -20$) up to $\approx 10^{13} M_\odot$ (in the case of M87).

Thus, as allowed by data, we adopt throughout this work the following fiducial values for the characteristic DM halo properties for typical ellipticals:

$$r_{h(e)} = 90 \text{ kpc} \tag{4.7}$$
$$M_{h(e)} = 5 \times 10^{12} M_\odot \tag{4.8}$$

Method

It is important to stress that the galactic halo values, here adopted for each type of (representative) galaxy, are such that

- they correspond to DM dominated halos as carefully checked in each observational work cited above.
- they do not account for the (total) virial DM mass due to natural observational limitations, but they rather represent the DM halo characteristics somewhat outside the region of baryon dominance.

The outermost DM halo masses, $M_{\rm tot}$ (obtained at the border r_s), are an outcome of the RAR family of astrophysical solutions, and can be considered as a prediction of our theory (see below and table 4.1).

Once the *observables* (r_h, M_h) are chosen for each galaxy type, we calculate systematically the solutions for the relevant example of $mc^2 = 48\,\text{keV}$. The chosen particle mass, motivated by the Milky Way analysis, describes a third constraint for the four-parametric RAR model.

The aim is to find only solutions, represented through the configuration parameter (β_0, θ_0, W_0), which match the halo constraints r_h and M_h with a tolerance $\tau = 10^{-3}$ under the conditions

$$\left|1 - \frac{M_h(\beta_0, \theta_0, W_0, m)}{M_h}\right| + \left|1 - \frac{r_h(\beta_0, \theta_0, W_0, m)}{r_h}\right| \leq \tau \tag{4.9}$$

Here, the observable constraints for each galaxy type are given in the denominator. They are compared with the predictions given in the numerator.

Notice that the halo constraints necessarily imply astrophysical solutions, which develop a maximum in the halo rotation curve. Additionally, we request to the solutions one extra (underlying) physical condition, hereafter the *critical core* condition: the compact-core is stable or non-critical (i.e. it does not collapse to a BH). These conditions define the full window of astrophysically allowed RAR-family solutions. Importantly, the two halo constraints provide a one-parametric family within the full ranges of the three configuration parameters (β_0, θ_0, and W_0). Thus, the obtained values lay along a one-dimensional curve in the configuration space and are limited from below and above, see section 4.2.3 for further details.

4.2.2 Results

The RAR model provides for each galaxy type, represented through the constraints (r_h, M_h), a continuous set of solutions which is illustrated as a blue shaded region in fig. 4.2. In particular, we show five benchmark solutions, labeled with their central densities (from black to magenta, roughly enveloping the blue shaded regions), for DM mass distributions $M(r)$, rotation curves $v(r)$ and density profiles $\rho(r)$. All solutions have been calculated for the relevant example of $mc^2 = 48\,\text{keV}$. They encompass a window of possible M_c and $M_{\rm tot}$ values for each galaxy type (see

table 4.1 for numerical values), bounded from above and below as dictated by the astrophysical and *critical core* conditions.

The continuous magenta curves represent the critical solutions, reaching the limiting core mass $M_c^{cr} \approx 2.2 \times 10^8 M_\odot$ which is achieved only for typical spiral and elliptical galaxies. The dashed magenta curve indicates the limiting (non-critical) solutions for typical dwarfs, where no maximum halo rotation curve is present (halo maximum and plateau minimum merge to a saddle point). The black curves correspond to the solutions acquiring the lowest possible central density ρ_0 but with a cut-off affecting the outer halo tails. These solutions develop more and more extended density tails resembling isothermal-like solutions, corresponding to $\rho \propto r^{-2}$ at large radii. The limiting case $W_0 \to \infty$ resembles fully isothermal solutions, infinite in mass and size, as obtained in the original version of the model (Ruffini, Argüelles, and Rueda, 2015).

The astrophysical conditions imposed to the solutions put no limit on the maximum value of W_0. Unless no other observational constraint is available (for a given galaxy) regarding the ending trend in the shape of the density tail, W_0 can increase indefinitely. Indeed, the larger W_0 the lesser the hardness in the falling-down shape of density profiles beyond r_h and the larger the surface radius r_s. Of course, at some point r_s (and consequently $M_{\rm tot}$) will be excessively large to represent any reliable astrophysical halo. Therefore, those RAR solutions must be discarded as physical ones. We show, for completeness, at bottom left of fig. 4.2 (black lines) the full plethora of density tails, corresponding with the specific minimum core mass solutions for each galaxy type.

Thus, dark halos from dSph till normal elliptical galaxies can be explained with regular and continuous distributions of $mc^2 \sim 50\,{\rm keV}$ fermions without massive BHs at their centres, alternatively harboring compact quantum cores with masses in the range

- $M_c \in (3.8 \times 10^3 M_\odot, 4.3 \times 10^6 M_\odot)$ for typical dSphs
- $M_c \in (4.5 \times 10^5 M_\odot, 2.2 \times 10^8 M_\odot)$ for typical spirals and
- $M_c \in (9.8 \times 10^5 M_\odot, 2.2 \times 10^8 M_\odot)$ for typical ellipticals.

The smaller the dark halos (from dSphs to typical ellipticals), the lesser their masses and the lesser their core compactness, and viceversa. This tendency ends at the larger (i.e. more extended) DM halos, having a core of critical mass which is described in more detail by the continuous-magenta solutions for typical spiral and elliptical galaxies in fig. 4.2. Additionally, the trend can be checked by comparing the group of values in columns 8 with 5 and 6 among the different galaxy types in table 4.1.

The quantum core masses M_c, the total halo masses $M_{\rm tot}$ and the (consequent) associated window for the plateau densities ρ_p (defined at the minimum of the RAR rotation curve and inherent to each of the RAR solutions), have to be considered as explicit predictions of the RAR model. These predicted values will be then contrasted in more details within the context of the $M_{\rm BH}$-$M_{\rm tot}$ relation and the constancy of the *central* surface DM density in section 4.2.4, as a consistency check of the model.

We describe in next the predicted morphological trends of the DM RAR profiles and main characteristics of each galaxy type. The reader is referred to section 4.2.3 for a full description of the limiting predicted properties in terms of the free model parameters.

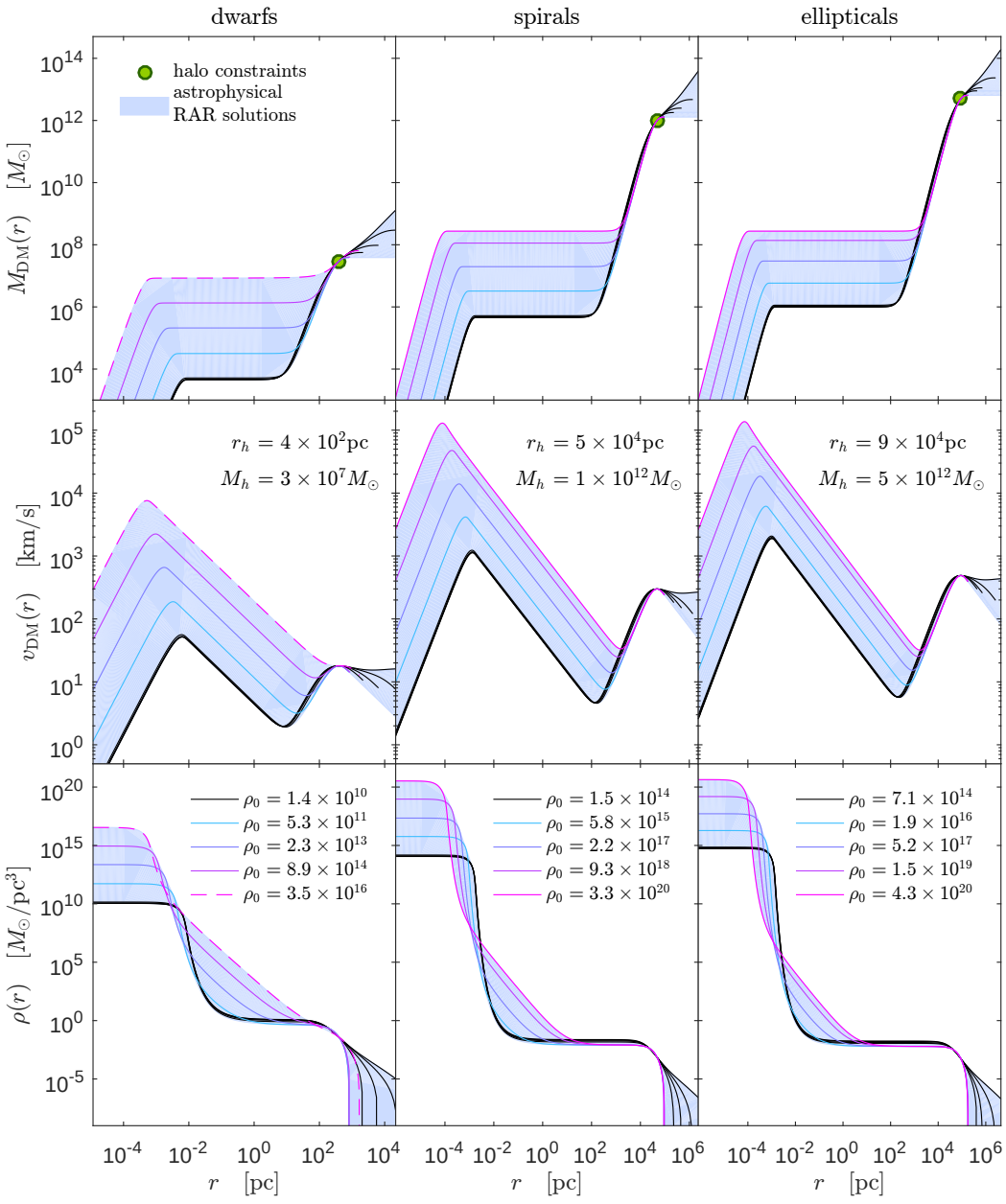

Figure 4.2. Astrophysical RAR solutions, for the relevant case of $mc^2 = 48\,\mathrm{keV}$, fulfill observationally given DM halo restrictions (r_h, M_h) for typical dwarf (left), spiral (middle) and elliptical galaxies (right). Shown are density profiles (bottom), rotation curves (middle) and DM mass distributions (top). The full window for each galaxy type is illustrated by a blue shaded region and enveloped approx. by 5 benchmark solutions inside. The continuous-magenta curves, occurring only for spiral and elliptical galaxies, indicates the critical solutions which develop compact critical cores (before collapsing to a BH) of $M_c^{cr} = 2.2\times10^8\,M_\odot$. The dashed-magenta curves for dwarfs are limited (instead) by the astrophysical necessity of a maximum in the halo rotation curve. The bounding black solutions correspond to the ones having the minimum core mass (or minimum ρ_0) which in turn imply larger cutoff parameters. Thus, these solutions develop more extended density tails, where $\rho \propto r^{-2}$ is the limiting isothermal density tail achieved when $W_0 \to \infty$.

ρ_0 ($M_\odot$/pc^3)	β_0	θ_0	W_0	M_c ($M_\odot$)	r_c (pc)	$M_{\rm tot}$ ($M_\odot$)	r_s (pc)	ρ_p ($M_\odot$/pc^3)
DWARFS ($M_h = 3 \times 10^7 M_\odot$, $r_h = 4 \times 10^2$ pc)								
1.1×10^{10}	1.4×10^{-9}	23.8	∞	3.9×10^3 (§)	6.3×10^{-3}	∞	∞	1.2×10^0
5.3×10^{11}	1.8×10^{-8}	24.5	43.9	2.7×10^4	3.3×10^{-3}	3.9×10^7	8.2×10^2	4.4×10^{-1}
2.3×10^{13}	2.6×10^{-7}	21.1	37.7	1.8×10^5	1.8×10^{-3}	3.9×10^7	8.1×10^2	4.5×10^{-1}
8.9×10^{14}	3.6×10^{-6}	17.7	31.8	1.1×10^6	9.6×10^{-4}	4.0×10^7	8.7×10^2	4.4×10^{-1}
3.5×10^{16}	4.5×10^{-5}	16.1	29.3	7.0×10^6 (†§)	5.2×10^{-4}	6.4×10^7	1.7×10^3	4.1×10^{-2}
SPIRALS ($M_h = 1 \times 10^{12} M_\odot$, $r_h = 5 \times 10^4$ pc)								
1.1×10^{14}	4.0×10^{-7}	40.9	∞	3.9×10^5 (§)	1.3×10^{-3}	∞	∞	2.4×10^{-2}
5.8×10^{15}	5.4×10^{-6}	41.6	73.2	2.8×10^6	6.9×10^{-4}	1.3×10^{12}	9.8×10^4	8.3×10^{-3}
2.2×10^{17}	6.5×10^{-5}	38.5	67.6	1.7×10^7	3.8×10^{-4}	1.3×10^{12}	9.6×10^4	8.2×10^{-3}
9.3×10^{18}	8.3×10^{-4}	35.8	62.3	9.7×10^7	1.9×10^{-4}	1.3×10^{12}	9.6×10^4	8.2×10^{-3}
3.3×10^{20}	6.7×10^{-3}	39.6	64.4	2.2×10^8 (†)	7.8×10^{-5}	1.3×10^{12}	9.6×10^4	8.2×10^{-3}
ELLIPTICALS ($M_h = 5 \times 10^{12} M_\odot$, $r_h = 9 \times 10^4$ pc)								
5.4×10^{14}	1.1×10^{-6}	43.3	∞	8.5×10^5 (§)	1.0×10^{-3}	∞	∞	1.8×10^{-2}
1.9×10^{16}	1.1×10^{-5}	44.3	77.9	5.1×10^6	5.7×10^{-4}	6.5×10^{12}	1.9×10^5	6.3×10^{-3}
5.2×10^{17}	1.1×10^{-4}	41.6	72.9	2.6×10^7	3.3×10^{-4}	6.4×10^{12}	1.8×10^5	6.2×10^{-3}
1.5×10^{19}	1.0×10^{-3}	39.7	68.7	1.2×10^8	1.7×10^{-4}	6.4×10^{12}	1.8×10^5	6.2×10^{-3}
4.3×10^{20}	6.7×10^{-3}	45.5	73.0	2.2×10^8 (†)	7.2×10^{-5}	6.4×10^{12}	1.8×10^5	6.2×10^{-3}

Table 4.1. Free RAR model parameters for the 5 benchmark sets of DM profiles given in fig. 4.2, for the case of $mc^2 = 48\,\mathrm{keV}$, together with the DM masses (M_c, $M_{\rm tot}$) and radii (r_c, r_s), as well as central and plateau densities (ρ_0, ρ_p) for each galaxy type from typical dSph to elliptical galaxies. The (†) symbol reads for the critical core mass value M_c^{cr} just before reaching the gravitational collapse, while the (†§) symbol indicates the maximum core mass for dwarfs corresponding to the solutions without maximum in the halo rotation curve. Instead, the (§) symbol reads for the minimum quantum core mass for each galaxy type associated with the limited isothermal-like solutions.

Typical dSph galaxies

The predicted family of dwarf solutions, resembling the given *observable* halo restrictions $M_{h(d)} = 3 \times 10^7\, M_\odot$ and $r_{h(d)} = 400\,\mathrm{pc}$ for the relevant case of $mc^2 = 48\,\mathrm{keV}$, is explicitly shown in fig. 4.2 (left column). The difference in morphology among the dwarf family solutions, presented through the $M(r)$, $v(r)$, and $\rho(r)$ profiles, can be explained according to the behavior of the RAR model configuration parameters (β_0,θ_0,W_0).

It turns out that the temperature parameter β_0 is the main responsible for changes in the central core while the couple (θ_0, W_0) is the main responsible to variations in the halo region. From lower to larger central temperatures β_0, the solutions develop central cores which are more massive, have larger central velocity peaks and become more compact and denser. Moving forward in radius, this trend translates into more massive inner-halos with more extended decreasing Keplerian velocities before reaching the standard rising halo behavior until r_h. At the same time they acquire less sharp density transitions from compact-core to dilute-halo with less pronounced plateaus (see blue-shaded regions in left column of fig. 4.2).

The softer core-halo transitions for $\rho(r)$ as β_0 rises imply a *cuspier* behavior for the inner-halo densities while the difference between minimum and maximum halo rotation velocities reduces. This continuous trend in morphology ends in a maximum (non-critical) core mass $M_c^{\max} \approx 7.0 \times 10^6 M_\odot$, characterized by an overall cuspy inner halo with absence of a plateau before reaching the outer halo tail. Correspondingly, the inner-halo rotation curve is governed by a very extended Keplerian behavior, finishing in a small halo decreasing part without developing any maximum.

Interestingly, at such limiting solutions the density and velocity curves acquire a peculiar saddle point transition from inner-halo to diluted-tail, which is a distinct feature of the smallest galaxies here studied (indicated in the dashed-magenta line in fig. 4.2). This feature is not present in larger spiral or elliptical galaxies.

The total halo (extension and mass) are mainly governed by the cutoff parameter W_0 as already explained in chapter 3 and section 4.1. In general, the larger W_0 the more massive and more extended the dark halo, and viceversa. However, this trend is not present in the solutions very near the maximum core mass, in which the moderate central temperature effects start compete with surface effects, induced by the lowest W_0 values. The latter produces larger total halo masses relative to the minimum one (see section 4.2.3).

Finally, the monotonic relation between W_0 and β_0 (for β_0 not close to maximum), obtained in this observationally constrained family of solutions (see the β_0-W_0 projection plane in fig. 4.5), directly implies that for all $W_0 \gtrsim 50$ we have a $\beta_0^{\min}$, defining a minimum core mass of $M_c^{\min} \approx 4.4 \times 10^3 M_\odot$ (which can be also checked in top-right panel of fig. 4.6). Conversely, the existence of a $\beta_0^{\max}$, set by the (threshold) solution without a maximum in the halo rotation curve, will necessarily define through the above monotonic relation a W_0 value low enough to set the minimum total halo mass as $M_{\mathrm{tot}}^{\min} \approx 3.9 \times 10^7 M_\odot$ (see dashed-magenta curve in figs. 4.2 and 4.6 corresponding with the empty-magenta dot in fig. 4.5).

Before closing this section, we proceed to further analyze the meaning of the astrophysical condition of requesting the presence of a maximum in the halo rotation curve (i.e. the dashed-magenta curves in fig. 4.2). Even though there is no phenomenological DM profile in the literature which can lead to a halo rotation curve without a maximum, it is worthy to see in a more explicit way to which unphysical results it may lead. The aim is thus to link our typical Sculptor-like solutions with a proper observable such as the (projected) dispersion velocity ($\hat{\sigma}$) arising from Jeans analysis (as the one applied for dwarfs in Walker et al. (2009)), to be then compared with the corresponding data. For this we assume our RAR DM mass profile $M(r)$ and a Plummer profile for the stellar (surface) density (with the corresponding r_{half} and

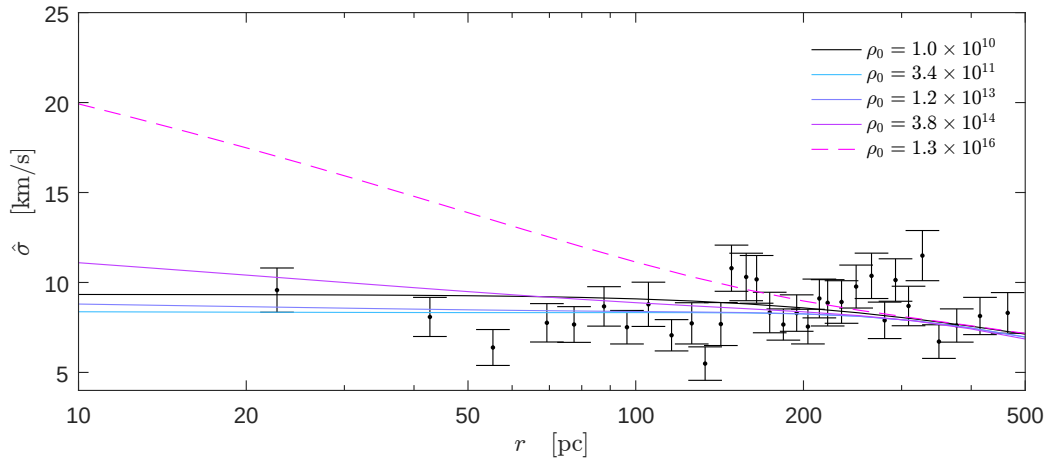

Figure 4.3. Comparison between the observed (projected) dispersion velocity ($\hat{\sigma}$) of Sculptor, taken from (Walker et al., 2009), against the same magnitude as predicted by a standard Jeans analysis. The latter uses the RAR benchmark solutions for the mass distribution $M(r)$ as shown in fig. 4.2. Notice the fast rise in the inner-halo region (at $\sim$ few 10 pc) due to the cuspy RAR halo with $\rho_0 = 1.3 \times 10^{16}$, implying a clear data mismatch in the case of this limiting dashed-magenta solution.

orbital anisotropy for stellar components adopted in Walker et al. (2009) for Sculptor). This is done for the five different benchmark solutions as given in fig. 4.2. From this (back-of-the-envelope) comparison, which is shown in fig. 4.3, it turns out that while all of our solutions provide reasonable fits on halo scales (somewhat similar to the cored-halo profile assumed in Walker et al. (2009)), there is a clear mismatch (of nearly a factor 2) through the more central inner-halo scales (see dashed-magenta curve in fig. 4.3). This clear difference occurs for the solutions with central temperatures close to $\beta_0^{\max}$, i.e. the ones having exceedingly large Keplerian velocity cores reaching inner halo scales of few ~ 10 pc. Notice that much refined fits to the data could be obtained within the RAR model, if many more halo observables are used to obtain $M(r)$ besides the two generic restrictions here applied.

In summary, astrophysical solutions for dwarf galaxies may reach large DM core masses near $M_c^{\max} \approx 7 \times 10^6 M_\odot$, corresponding to overall cuspy halo profiles. On the other hand, solutions with the minimum core mass $M_c^{\min} \approx 4.4 \times 10^3 M_\odot$ correspond to solutions with larger total halo masses, unbounded by the isothermal halo without surface effects.

Typical spiral and elliptical galaxies

The predicted family of solutions, resembling the given *observable* halo restrictions of $M_{h(s)} = 1 \times 10^{12}\, M_\odot$ and $r_{h(s)} = 50$ kpc for spirals and $M_{h(e)} = 5 \times 10^{12}\, M_\odot$ and $r_{h(e)} = 50$ kpc for ellipticals for the relevant case of $mc^2 = 48$ keV, are explicitly shown in fig. 4.2 (center and right column respectively). In complete analogy to the dwarf galaxies the free configuration parameters (β_0,θ_0,W_0) of these larger galaxies follow similar relations among them.

Same effects in the morphology behavior of the profiles are present but with one important difference. These typical galaxies here always reach the critical core mass $M_c^{cr} \approx 2.2 \times 10^8 M_\odot$ with a minimum total halo mass $M_{\rm tot}^{\min} \sim 10^{12}$ which is now well above M_c for all the solutions. Therefore, the density profiles always develop extended (inner-halo) plateaus with a clear maximum in the halo rotation curves (see benchmark curves at bottom-right of fig. 4.2). That is different to what may occur for dwarf galaxies as analyzed above.

The minimum core mass solutions for both kind of galaxies are again set, analogously to the case of dwarf galaxies, by the existence of a minimum β_0 as W_0 increases $\gtrsim 80$. We then obtain a minimal core mass of $M_c^{\min} \approx 5 \times 10^5 M_\odot$ for spirals and $M_c^{\min} \approx 10^6 M_\odot$ for ellipticals.

Particle mass dependence

In the case of typical dark halos in normal spiral and elliptical galaxies a particle mass of $mc^2 = 48\,\mathrm{keV}$ provides the maximum (critical) core mass of $M_c^{cr} = 2.2 \times 10^8 M_\odot$. If the mass is instead shifted to larger values, say $mc^2 \sim 100\,\mathrm{keV}$, a different three-parametric (θ_0, β_0, W_0) family of solutions arises, able to reproduce DM halo observables from dwarf to spiral/elliptical galaxies. But now the maximum (critical) core mass decreases to $M_c^{cr} \sim 10^7 M_\odot$. These new solutions have exactly the same core-halo behavior as those in fig. 4.2 with similar windows of *predicted* core and total halo mass (M_c and M_{tot}) but ending at the lower critical core mass as indicated above.

More generally, the fermion mass range $48\,\mathrm{keV} \lesssim mc^2 \lesssim 345\,\mathrm{keV}$, as obtained from the Milky Way analysis in section 4.1, implies stable DM quantum cores with masses up to the critical values. The lower particle mass the higher the critical core mass. Thus, the corresponding range is $4.2 \times 10^6 M_\odot \lesssim M_c^{cr} \lesssim 2.2 \times 10^8 M_\odot$ due the particle mass dependence $M_c^{cr} \propto m^{-2}$ (see Argüelles and Ruffini, 2014).

About the critical core mass

The concept of critical core mass M_c^{cr} can be formally achieved by finding the maximum (turning point) in a ρ_0 vs. M_c diagram, as was shown in the context of the original RAR model, i.e. for $W_0 \to \infty$ (see Argüelles and Ruffini (2014) and references therein). Labeled here as the *critical-core* condition, this concept applies in the same way for the actual RAR model with cutoff ($W_0 < \infty$), see fig. 4.4.

Accordingly, typical spiral and elliptical galaxies reach the critical core mass (e.g the turning point at a critical density), corresponding to a critical temperature parameter β_0^{cr}. For typical dwarfs, on the other, the maximal temperature is set by the astrophysical condition, such as requiring a maximum in the rotation curve on halo scales. This limits the maximal core mass (and central density), being far away from the critical value.

About the role of the degeneracy and cut-off parameters in the core-halo morphology of RAR solutions

The fact that higher compactness of the core is obtained by increasing the temperature parameter, while maintaining a rather low degeneracy, is understood by the semi-degenerate nature of our fermionic solutions in contrast with a fully degenerate regime. The combination of the finite-temperature effects and the monotonically decreasing change (from positive to negative values) of the degeneracy parameter with the distance (see e.g. central panel of fig. 1 in Ruffini, Argüelles, and Rueda, 2015) are the responsible for the clear *dense quantum core - Boltzmannian tail* behavior of the density profiles in fig. 4.2. Once in the diluted regime, and for solutions which are still away from becoming critical, a small increase in W_0 has important effects on the RAR halo scales: the larger the cutoff parameter W_0, the more massive and more extended the galaxy gets as can be directly checked in fig. 4.2 from dSphs to ellipticals, respectively.

This fact is better understood through the role of the escape energy in the Fermi-like distribution function (2.36). The larger the escape energy $\varepsilon(r) \neq \infty$, the larger the momentum (and energy) space the particles can occupy at any radius. Note,

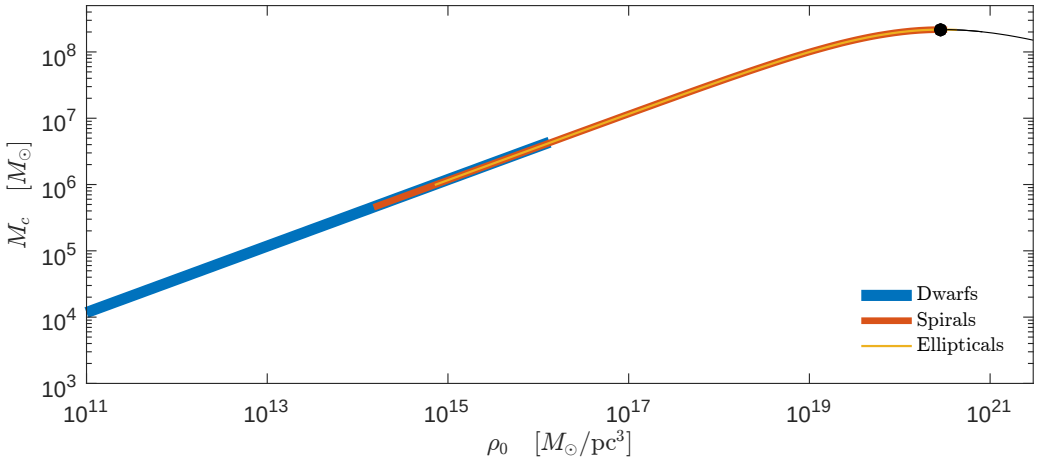

Figure 4.4. Explicit calculation of the ρ_0-M_c parameter space within the RAR model for $mc^2 = 48\,\mathrm{keV}$ in the case of typical dwarf (blue line), spiral (red line) and elliptical galaxies (yellow line). Each galaxy type is described by given halo observable conditions (M_h and r_h). Notice the case of spiral and elliptical galaxies where a critical DM core mass $M_c^{cr} = 2.2 \times 10^8\, M_\odot$ is reached at the maximum of the curve, when studied through the turning point criterion for core collapse in the ρ_0-M_c plane, see e.g. Argüelles and Ruffini (2014).

the escape energy is proportional to the cutoff parameter $W(r)$. In consequence, the solution cover more extended total spatial extensions before $W(r)$ reaches 0 at the surface radius r_s.

4.2.3 Parameter space analysis

Here we show how the halo observable constraints (r_h,M_h) together with the additional *critical-core* condition define the limiting values of the free sets of RAR configuration parameters (β_0,θ_0,W_0) for the different galaxy types. Specifically fig. 4.5 shows the full curves in the (β_0, θ_0, W_0)-space for $mc^2 = 48$ keV. Each galaxy is represented through a coloured 1-dimensional line, i.e. in thick blue (dwarfs), red (spirals) and yellow (ellipticals). We also include along each line the sets of the 5 benchmark RAR solutions, given in fig. 4.2, through dots in corresponding colours. This correspondence shows clearly the ranges of β_0, θ_0, and W_0, encompassing all the astrophysical RAR solutions.

About the 1-dimensional curves of free RAR model parameter space

The fact that the halo scale radius r_h sets a specific morphological point in the RAR solutions (i.e. as in $v(r)$, $M(r)$, $\beta(r)$, $\theta(r)$, etc.), it must necessarily depend on the specific choice of the initial conditions, i.e. $r_h = r_h(\beta_0, \theta_0, W_0, m)$. This functional dependence, together with $M_h = M_h(\beta_0, \theta_0, W_0, m) \equiv M(\beta_0, \theta_0, W_0, m, r_h)$, clearly defines a 1-dimensional curve in the (β_0, θ_0, W_0) RAR configuration parameter space once m, M_h and r_h are given (i.e. 4 free parameters and 3 constraints).

The number of free parameters of the model may be reduced to three when the particle mass m is set (i.e. in the range $48\,\mathrm{keV} \lesssim mc^2 \lesssim 345\,\mathrm{keV}$ as obtained in section 4.1). This approach requires only 2 constraints, such as r_h and M_h. Notice that in this case a narrow 2-dimensional region would arise in the (β_0, θ_0, W_0)-space if only one constraint (i.e. $M(r)$ with $r \neq r_h$ a hypothetically well constrained halo scale-length) is applied instead of the two constraints used in this work. Nevertheless, many of the solutions in this (more) extended family will certainly provide worst

fits to the baryonic data (as e.g. for the case of $\hat{\sigma}$ in dSphs) than the solutions here presented, considering less observable constraints were used.

Limiting behavior in the parameter sets

The effects of the RAR parameter sets in the corresponding RAR solutions explain the limiting values in the core mass M_c, the total mass $M_{\rm tot}$ and plateau density ρ_p. The maximum and minimum DM masses, predicted by the RAR model, have associated maximum and minimum in the predicted ρ_p values, as explicitly shown in fig. 4.6.

The importance of those predicted windows for each galaxy type reflect universal relations between galaxy parameters. Thus, the predicted windows of M_c and $M_{\rm tot}$ masses reflect the Ferrarese Universal relation (Ferrarese, 2002) while the predicted ρ_p window reflects the constancy of the *central* surface DM density in galaxies (Donato et al., 2009). Both relations are discussed in detail in section 4.2.4.

The main responsible for the increase of the quantum-core mass, i.e. from $\sim 10^3 M_\odot$ in dSphs to $\sim 10^8 M_\odot$ in typical spirals and ellipticals, is the temperature parameter β_0, which can vary about six orders of magnitude among the different galaxy types. Instead, the pair (θ_0, W_0) remains around the same order-of-magnitude values and is mainly relevant to the DM halo physics. For the latter compare fig. 4.2 and fig. 4.5, together with values in table 4.1.

The temperature parameter β_0 is limited from above by its critical value $\beta_0^{\rm cr}$ for the case of typical spiral and elliptical galaxies. That limit is set by the *critical core* condition. For higher values the RAR solutions become gravitationally unstable and lead to the gravitational collapse of the quantum core. In the case of typical dwarf galaxies the temperature is limited by its maximum value $\beta_0^{\rm max}$. That limit, on the other hand, is set by the (threshold) solution without a maximum in the halo rotation curve, corresponding to highly cuspy halos. Thus, while $\beta_0^{\rm cr}$ sets the critical core mass M_c^{cr} for typical spiral and elliptical galaxies, the $\beta_0^{\rm max}$ sets the $M_c^{\rm max}$ for typical dSphs. See fig. 4.6 and table 4.1 for numerical values for each galaxy type.

At the same time, a specific minimal temperature parameter $\beta_0^{\rm min}$ (for all galaxy types) is implied by the linear relation between the configuration parameters (β_0, θ_0, W_0), as seen in fig. 4.5 and the corresponding projection-planes (for β_0 not close to its maximum). For large enough W_0 values (and beyond) the solutions develop isothermal halo tails without affecting the inner structures through surface effects. Especially, the core remains constant, what resembles here mainly constant β_0 and θ_0 values. Thus, large enough W_0 values set all the possible total halo masses $M_{\rm tot}$, although unbounded from above because W_0 may grow up to infinity. But those solutions correspond to the minimal temperature $\beta_0^{\rm min}$ which produce minimal DM core masses.

The existence of a $\beta_0^{\rm cr}$ for spirals and ellipticals (and $\beta_0^{\rm max}$ for dwarfs), will necessarily define through the above monotonic relation a low enough W_0 value to set the minimal total halo mass for each galaxy type. In the case of spirals and ellipticals that minimum correlates with the maximal (critical) temperature $\beta_0^{\rm cr}$. The correlation does not apply for dwarfs due to the strong surface effects close to the maximal temperature $\beta_0^{\rm max}$, see fig. 4.6.

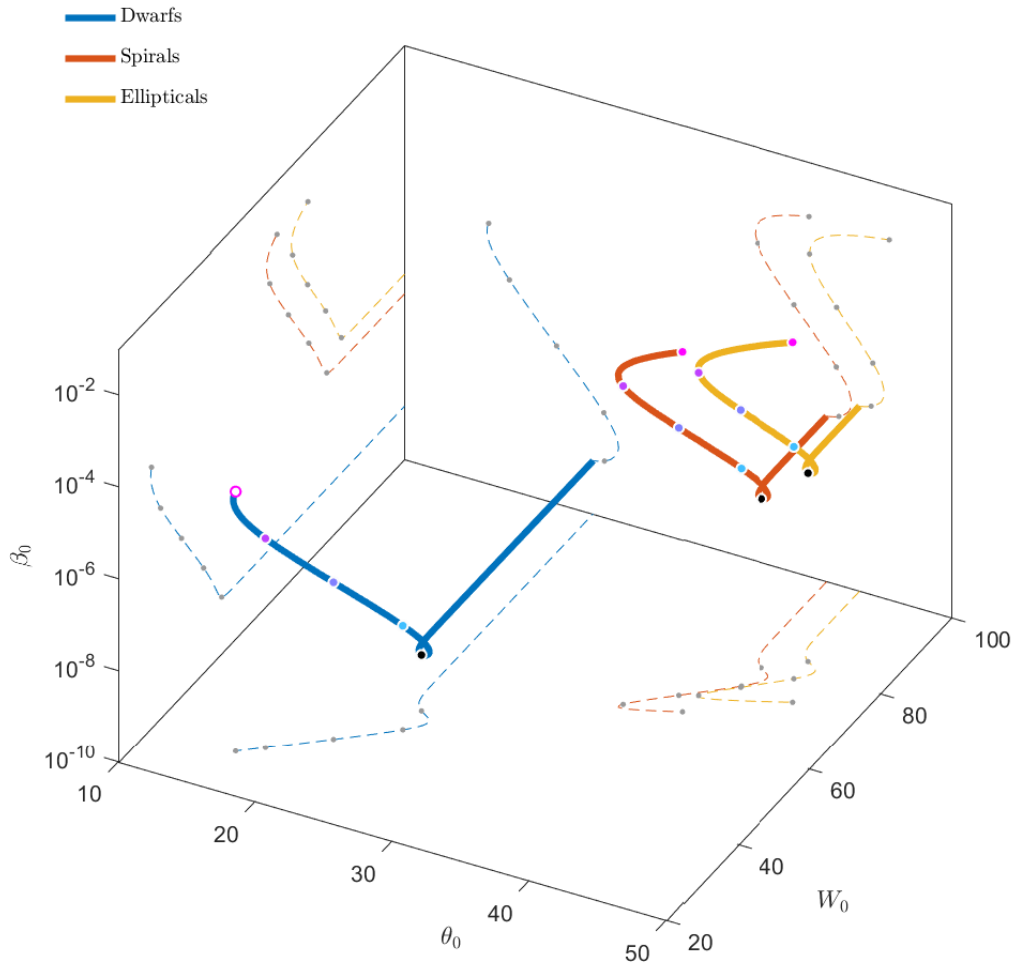

Figure 4.5. Full astrophysical ranges of the configuration parameters for $mc^2 = 48\,\mathrm{keV}$. Specific observational halo constraints (M_h and r_h) for each galaxy type define 1-dimensional curves in the (β_0, θ_0, W_0)-space. Each coloured dot along each thick line has its corresponding RAR benchmark solution (for $M(r)$, $v(r)$ and $\rho(r)$) in fig. 4.2. The limiting filled-magenta dots correspond to the critical solutions for spirals and ellipticals while the empty-magenta dot is associated with the limiting (non-critical) solution for typical dwarfs. The latter is set by the (threshold) solution without developing a maximum in the halo rotation curve. The straight line behaviour in all cases correspond to solutions having the minimum core mass (or minimum ρ_0), as well as achieving the more extended density tails as can be seen from fig. 4.2. These solutions develop isothermal-like tails, ending in the standard isothermal density tail $\rho \propto r^{-2}$ for infinitely large cut-off parameter W_0.

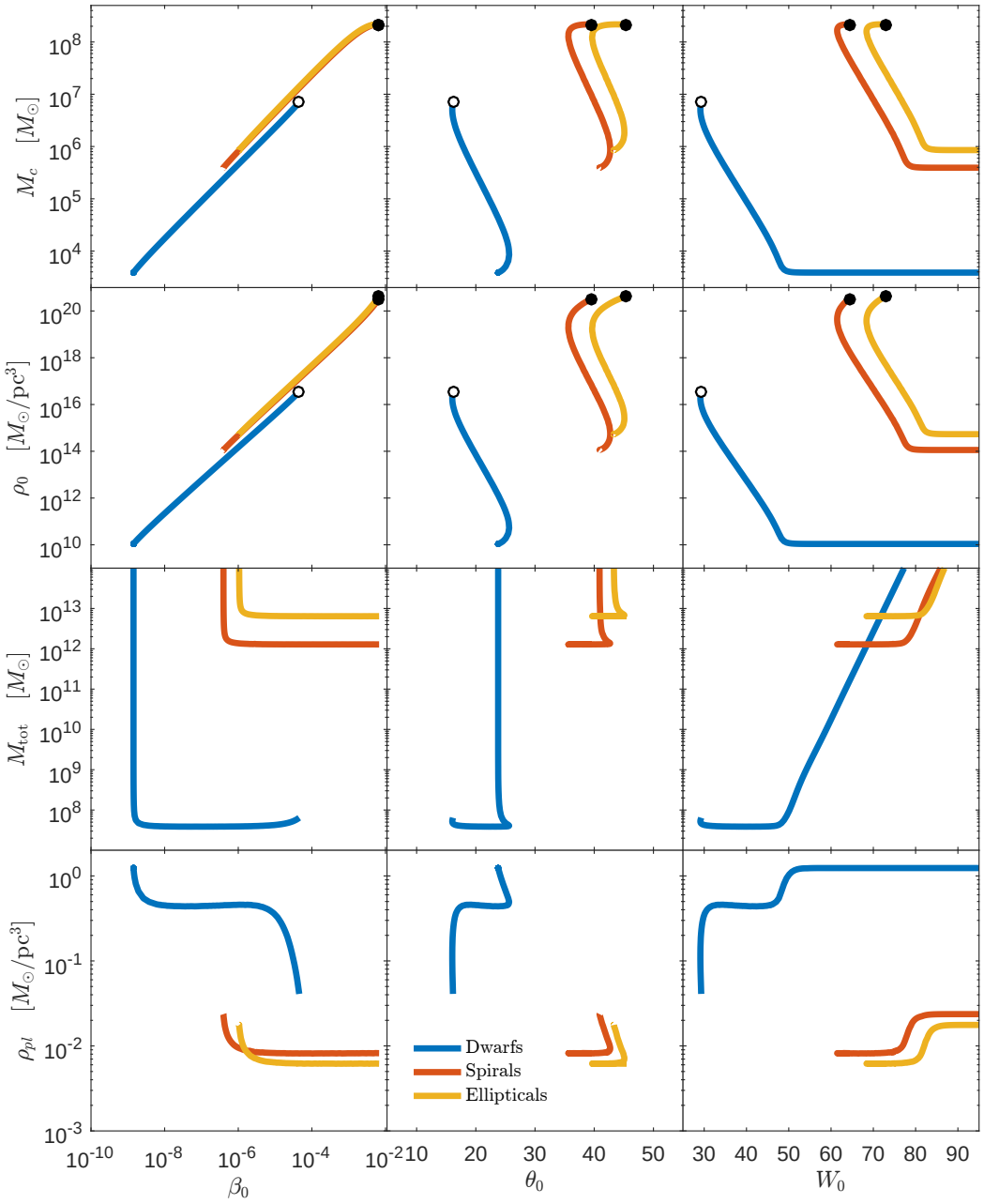

Figure 4.6. Full display of RAR magnitudes (ρ_0,M_c,M_{tot}, and ρ_p) for $mc^2 = 48\,\mathrm{keV}$ as a function of β_0 (left column), θ_0 (central column) and W_0 (right column). Shown are three typical galaxy types (dwarfs, spirals, ellipticals) which are constrained by halo observables (M_h and r_h). The existence of a critical core mass of $M_c^{cr} = 2.2 \times 10^8 M_\odot$, for the case of typical spiral and elliptical galaxies, is denoted by a filled black dot. In the case of dwarfs there is only a maximum value β_0^{max} (with associated M_c^{max}) and denoted by an empty black dot. Notice also the larger plateau density ($\sim 10^{-1} M_\odot/\mathrm{pc}^3$). This is typical for the more compact dwarf galaxies (on inner-halo scales) with respect to the corresponding much lower values for larger spiral or elliptical galaxies, see e.g. Walker et al. (2009).

4.2.4 Galaxy parameter correlations

In the previous sections we have successfully compared and contrasted the solutions of the RAR model with a wide range of galactic observables. The versatility of the physical solutions also accounts for the (real) physical spread observed in the correlation between dark halo mass vs. dark central object mass. We turn now to analyze if the RAR model agrees with the following observational correlations:

- The $M_{\rm BH} - M_{\rm tot}$ relations with $M_{\rm BH}$ the mass of the compact dark object at the centre of galaxies and $M_{\rm tot}$ the total DM halo mass (Bogdán and Goulding, 2015; Ferrarese, 2002; Kormendy and Bender, 2011).

- The constancy of the *central* surface DM density in galaxies, e.g. $\rho_{0D} r_0 \approx 140^{+80}_{-50}\, M_\odot\, {\rm pc}^{-2}$. It spans about 14 orders of magnitude in absolute magnitude (M_B), where ρ_{0D} and r_0 are the *central* DM halo density at the one-halo-scale-length of the Burkert profile (Donato et al., 2009).

In order to show this, we use the full family of astrophysical RAR solutions (i.e. contained within the blue-shaded region of fig. 4.2) for typical dSphs, spiral and elliptical galaxies. Such solutions cover the maximal free parameter space (β_0,θ_0,W_0) for each galaxy type as constrained by the halo observables (r_h, M_h) for the particle mass $mc^2 = 48\,{\rm keV}$ together with the *critical core* condition. Correspondingly, a well defined window of predicted masses $(M_c, M_{\rm tot})$ is obtained. As we show below, the knowledge of the corresponding values of the plateau density ρ_p is also important for the analysis of the *central* surface DM density relation.

We can proceed now to make a consistency check of the predictions of the RAR model by contrasting them within the physical observed spread of the correlations. Notice that the constancy of the *central* surface DM density deals only with DM halos while the $M_{\rm BH} - M_{\rm tot}$ relations correlate both, the central and total halo dark object masses. Traditionally, the central compact dark objects are assumed as SMBHs. But here we interpreted them as DM quantum cores with the exception of the supermassive objects of active galaxies.

Mass relation between central core and total halo

Concerning the $M_{\rm BH} - M_{\rm tot}$ relations, we show the predicted $(M_c, M_{\rm tot})$ values for different galaxy types (from dwarfs to ellipticals) together with the observationally inferred best-fit relations found in Bogdán and Goulding (2015) and Ferrarese (2002). The inferred relations are limited to the region where data supports, i.e. the so-called *Ferrarese window* as shown shown in fig. 4.7, and coincides well with the prediction for spirals and ellipticals. Those two galaxy types cover the (horizontal) spread of the *observed* correlation. In addition, it extends out of it, indicating a window of predicted masses by the RAR model, not yet observed. The Milky Way RAR solution is also plotted for completeness, showing a good agreement as well.

The case of typical dwarf galaxies is located at the lower end of the $(M_c, M_{\rm tot})$ plane, beyond the *Ferrarese window*. It is worth to stress that no observational data exist yet in that part of the correlation and thus the obtained results are predictions of the RAR model (i.e the blue curve at the bottom of fig. 4.7).

Additional verification of the above predictions of the RAR model needs the observational filling of the gaps in the $(M_c, M_{\rm tot})$ plane from dwarfs all the way up to ellipticals. This is partially done for disk galaxies from the SPARC data base, see section 4.3.

It is appropriate at this point to recall that the majority of the values of $M_{\rm BH}$ in the observed $M_{\rm BH} - M_{\rm tot}$ relation have been obtained through the so-called $M_{\rm BH} - \sigma_*$ relation, with σ_* the bulge dispersion velocity (Ferrarese and Merritt, 2000; Gebhardt

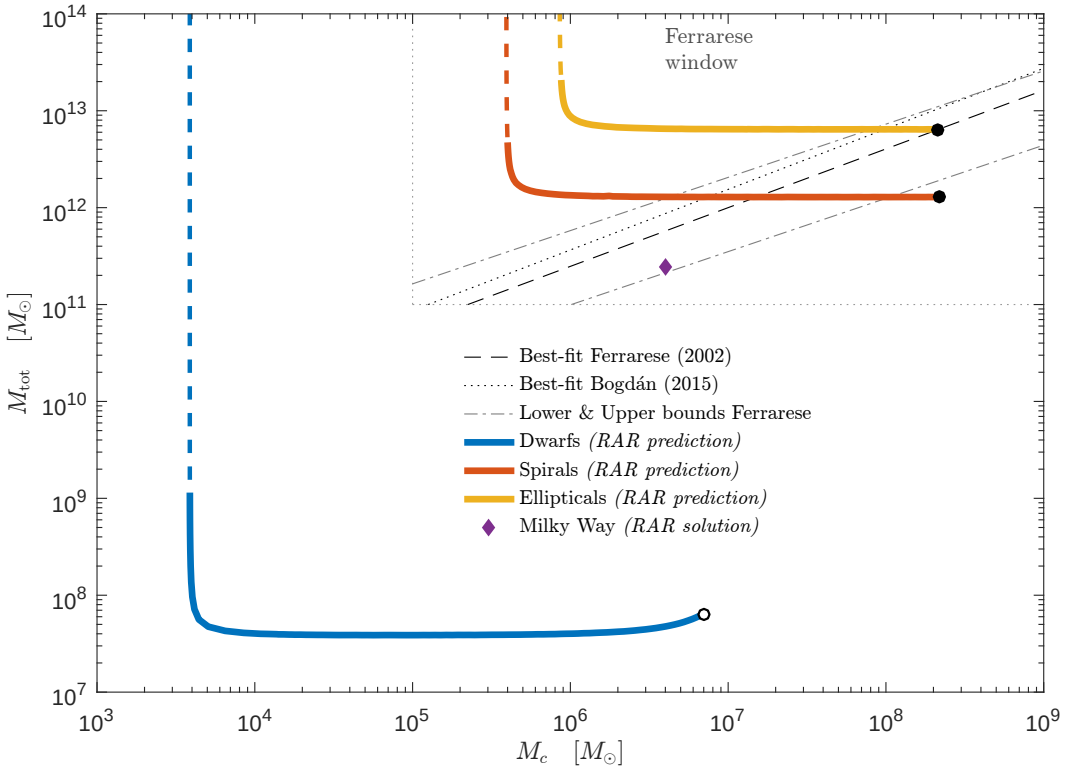

Figure 4.7. Prediction of the M_c-$M_{\rm tot}$ relations within three parametric RAR model (for $mc^2 = 48\,\mathrm{keV}$). The different *predicted* lines read for each galaxy type in correspondence with the astrophysical RAR solutions as given in fig. 4.2. The results show the ability to be in agreement with the different $M_{\rm BH} - M_{\rm tot}$ relations, as considered in the literature, and explicited in this picture box. While the red and yellow RAR prediction lines (i.e. spiral and elliptical galaxies), together with the Milky Way solution, can fit within the 'observable Ferrarese window', the blue RAR prediction for dwarfs is located at the lower end of the M_c-$M_{\rm tot}$ plane, where data do not support. The filled-black dots correspond to the critical core masses M_c^{cr}, and the empty-black dot indicates the limiting maximum core mass for dwarfs $M_c^{\rm max}$. Notice that the vertical trend in the colour lines correspond to RAR solutions having the minimum core mass (or minimum ρ_0) which in turn implies the larger cutoff parameters W_0. Those solutions develop more extended and more massive halos. Such trend ends in an infinite halo mass when the limiting $\rho \propto r^{-2}$ isothermal RAR tail is reached, unless some (extra) virial condition is imposed to them (e.g. typically setting a minimum threshold density at about $\sim 200\rho_{\rm cr}$ to any profile, where $\rho_{\rm cr}$ is the critical density of the Universe). Solutions with total masses exceeding such constraint are shown here in dashed.

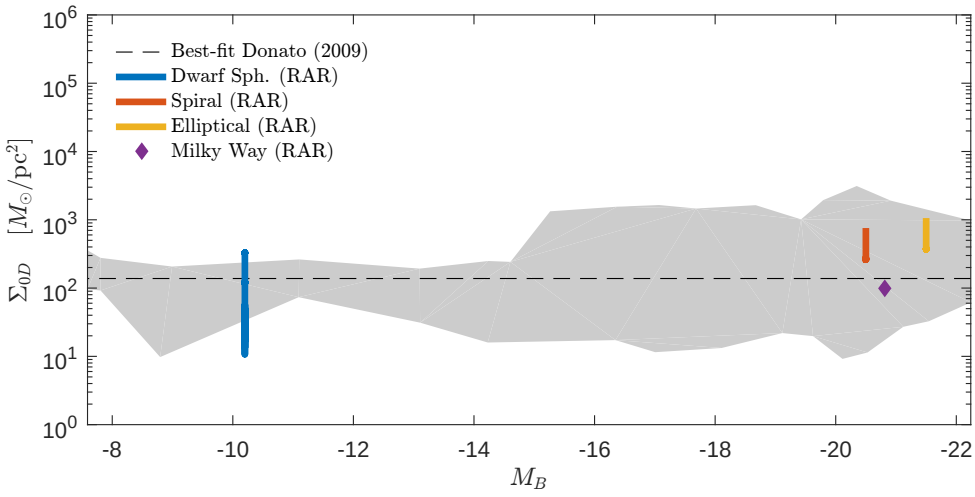

Figure 4.8. The surface DM density as predicted by the RAR model (see vertical colour lines) for each galaxy type in correspondence with the astrophysical solutions (i.e. blue-shaded regions in fig. 4.2). The dashed horizontal line represents the Universal relation from the best fit of the data as found by Donato et al., 2009. The dark-gray region indicates the delimited area by the $3-\sigma$ error bars of all the data points. The result shows the ability of the three parametric RAR model (for $mc^2 = 48\,\mathrm{keV}$) to be in agreement with the DM surface density observations.

et al., 2000; Gültekin et al., 2009). The M_{tot} values were there calculated at the virial radius within a Navarro-Frenk-White DM model (Ferrarese, 2002), while in our case they were obtained at the surface radius r_s of the RAR model equilibrium configurations.

DM surface density relation

Regarding the *central* surface DM relation, we first take from the literature the values for the blue absolute magnitude M_B, corresponding to each typical galaxy within each galaxy type considered above. Thus we adopt $M_B \approx -10.2$ for typical dSphs (Irwin and Hatzidimitriou, 1995), $M_B \approx -20.8$ for the Milky Way (Karachentsev et al., 2004), $M_B \approx -20.5$ for typical spirals (de Blok et al., 2008) and $M_B \approx -21.5$ for typical ellipticals (Hoekstra et al., 2005).

Then, in order to calculate the DM surface density $\Sigma_{0D} = \rho_{0D}\, r0$ in each case, we simply realize that the equivalent of the Burkert central density ρ_{0D} would correspond to the density of the plateau ρ_p within the RAR model. The relation between both one-halo scale lengths is given by $r_0 \approx 2/3\, r_h$, where r_h is fixed for each galaxy type according to the imposed halo constraints. For the corresponding family of ρ_p values see table 4.1 and fig. 4.6.

We thus calculate the product $2/3\, \rho_p\, r_h$ for each theoretical profile in the case $mc^2 = 48\,\mathrm{keV}$, including the Milky Way, and finally contrast the pair (M_B, Σ_{0D}) with the observational relation found by Donato et al. (2009).

The results are very good in agreement with the observed relation, see fig. 4.8. For simplicity, the latter is displayed as the overall dark-grey region delimited (or enveloped) within the $3-\sigma$ error bars along all the data points considered in Donato et al. (2009). The predicted surface density (solid lines), for the adopted M_B values, are located within the expected data region. Interestingly, results of the RAR model show a mild increasing behavior with decreasing M_B. This trend resembles the analogous universal relation presented in Boyarsky et al. (2009a) where larger elliptical galaxies were included in the analysis, contrary to the sample presented in Donato et al. (2009).

DWARFS: FORNAX ($M(0.3\,\mathrm{kpc}) = 7.0 \times 10^6 M_\odot$, $M(1.7\,\mathrm{kpc}) = 9.9 \times 10^7 M_\odot$)					
ρ_0 ($M_\odot/\mathrm{pc}^3$)	1.4×10^{10}	3.9×10^{11}	1.1×10^{13}	3.2×10^{14}	1.0×10^{16}
β_0	1.4×10^{-9}	1.3×10^{-8}	1.4×10^{-7}	1.5×10^{-6}	1.6×10^{-5}
θ_0	27.4	27.5	24.6	21.4	20.2
W_0	53.5	49.0	43.6	38.1	36.2
M_c ($M_\odot$)	4.3×10^3	2.3×10^4	1.2×10^5	6.6×10^5	3.8×10^6
r_c (pc)	6.1×10^{-3}	3.5×10^{-3}	2.0×10^{-3}	1.1×10^{-3}	6.4×10^{-4}
M_{tot} ($M_\odot$)	$\geq 1.3 \times 10^8$	9.9×10^7	9.9×10^7	10.0×10^7	2.1×10^8
r_s (pc)	$\geq 5.4 \times 10^3$	2.1×10^3	2.0×10^3	2.1×10^3	4.9×10^3
ρ_p ($M_\odot/\mathrm{pc}^3$)	8.3×10^{-2}	7.4×10^{-2}	7.3×10^{-2}	6.5×10^{-2}	1.3×10^{-2}

Table 4.2. Free RAR model parameters (with $mc^2 = 48\,\mathrm{keV}$) for the 5 benchmark sets of DM profiles, as shown in fig. 4.9. They fulfill the observational constraints ($M(0.3\,\mathrm{kpc}) = 7.0 \times 10^6 M_\odot$, $M(1.7\,\mathrm{kpc}) = 9.9 \times 10^7 M_\odot$) for the Fornax dwarf as given in Walker et al. (2009). The characteristic DM masses and radii, given here , have to be compared with those given in table 4.1 for typical dSphs. Importantly, the predicted M_c, M_{tot} and ρ_p values, by the RAR model in this case, are very similar to the ones obtained for the case of the other halo constraints (r_h, M_h). This indicates the robustness in the RAR predictions.

4.2.5 Robustness of the RAR model predictions

The allowed choice for observational constraints at the rotation curves maxima (r_h, M_h), are here selected in order to have a convenient and unique prior to be used across the entire galaxy zoo. Nevertheless, more precise observational halo mass constraints can be obtained at other typical radial halo scales (though somewhat close to r_h), depending on the galaxy type. For example, in the case of dSphs, the halo mass is observationally better constrained at r_{300} (i.e at 300 pc, very close to r_{half} for Milky Way satellites) as shown in Strigari et al. (2008). Including spiral and elliptical galaxies, other typical one-halo scale lengths (such as the Burkert halo scale-length) are appropriate as reported in Donato et al. (2009).

With the aim to analyze the robustness of the RAR model predictions, we further investigate which are the effects on the free RAR model parameters when changing the halo constraints (r_h, M_h) to the (observationally) better constrained couple $(M(r_{300}), M(r_{last}))$. Here, r_{last} is the last observed data point, as reported in (Walker et al., 2009), allowing for a good fit of $M(r_{last})$. These constraints represent the case of typical dSphs.

The results show a mild shift between the new set of astrophysical RAR solutions, illustrated as a light-red shaded region in fig. 4.9, with respect to the one already found in fig. 4.2 (displayed as grey-shaded region in fig. 4.9). Correspondingly, we found similar sets of free RAR free model parameters for the new benchmark solutions, as explicited in table 4.2, which should be compared with those in table 4.1. The main conclusions from the alternative constraints are very similar to conclusions from the halo constraints (r_h, M_h). Thus, we obtain similar effects on the predicted DM magnitudes (such as M_c, M_{tot} and ρ_p) for the differently chosen boundary halo conditions. This maintains intact the main predictions as provided through the halo constraints (r_h, M_h).

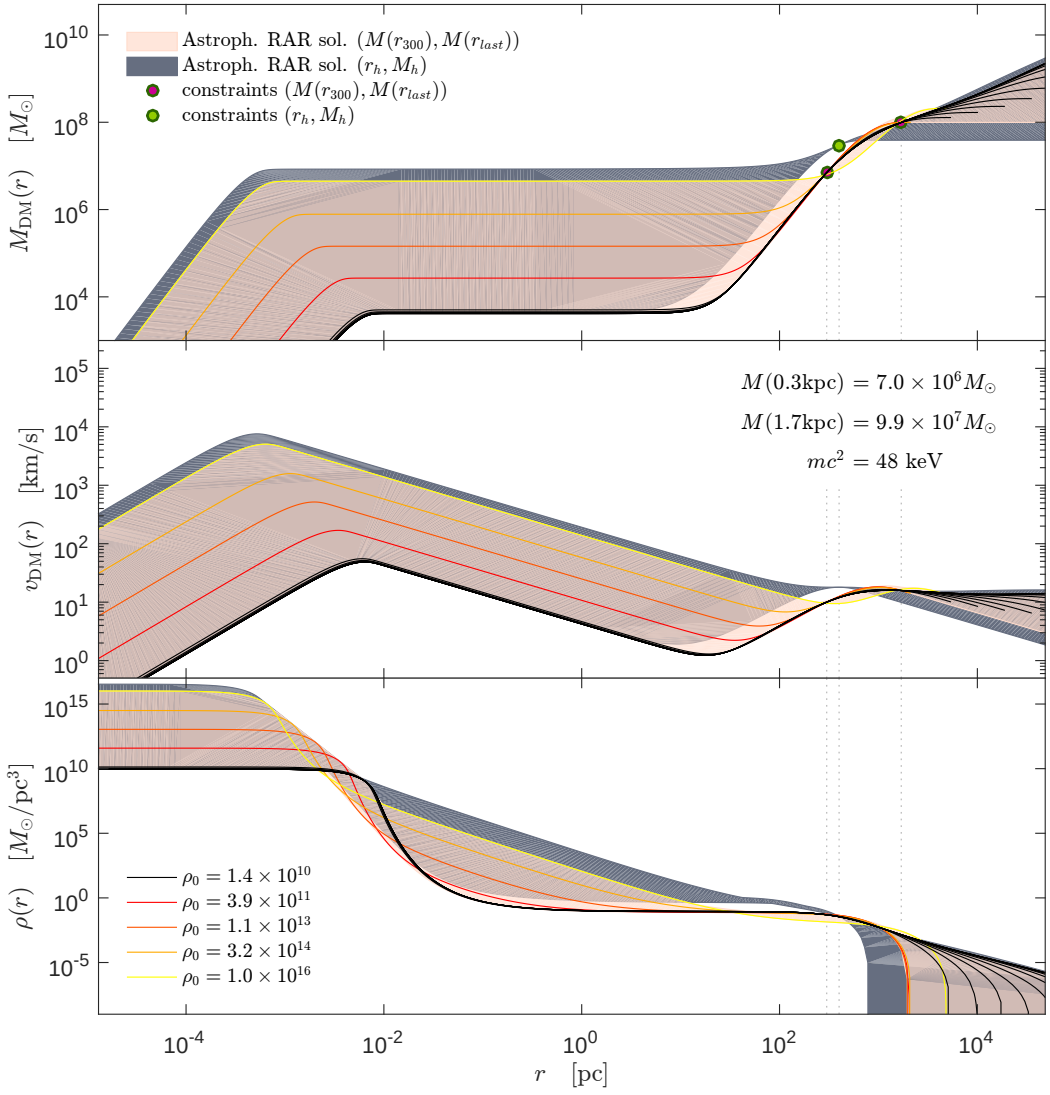

Figure 4.9. Comparison between the full window of the astrophysical RAR solutions, as obtained by using the (r_h, M_h) halo constraints (gray shaded regions, coinciding with the bluish region in fig. 4.2), with those fulfilling the alternative halo constraints $(M(r_{300}), M(r_{last}))$, represented by the light-red shaded regions. The latter belongs to the Fornax dwarf as given in Walker et al. (2009). There is a mild shift in the position of the maximum-circular velocities (roughly a factor 2) between both kind of families. Though, such positions (i.e $r_{\rm max}$), appearing in the light-red family of RAR solutions, can be achieved with different Hernquist models. The maximal velocity $v_{\rm max} \approx 18$ km/s, on the other hand, is exactly obtained in both cases.

4.3 SPARC galaxies

It is the purpose of this section to extend the applicability of the RAR model to universal relations which include both dark and baryonic structural galaxy parameters. We center our attention here in the radial acceleration correlation (McGaugh, Lelli, and Schombert, 2016b), broadening the extent of applicability of the RAR solutions from those including only DM as analyzed before.

We thus consider a filtered SPARC sample of 124 galaxies, covering 2369 data points in total. In order to check the goodness of fit for the RAR model we apply non-linear least square statistical analysis, making also the same kind of analysis for NFW and DC14 models in order to properly compare among them. The task is then not only to compare between the different approaches but to see what more information can be gained by inspecting the behavior in the (free) physical parameter space of the RAR model depending on some galaxy characteristics.

Thus, regarding the radial acceleration correlation, fundamental deviations are present when inspecting single galaxies. The analysis of the much better resolved Milky Way helps to understand the origin of those deviations. According to our RAR model we predict a different behavior in the very low acceleration regime and even an increase of the dark matter acceleration in the high acceleration regime after the baryonic matter dominated region. The latter is in contrast to the proposed empirical formula by McGaugh, Lelli, and Schombert (2016a), since their result focus only on halo scales. The increase is due to the degenerate dark matter core in the galactic center, a fundamental feature of RAR model. Exactly these overall dark matter induced deviations are a satisfying explanation of the large scatter in the empirical radial acceleration correlation based on the average of many spiral galaxies.

In section 4.3.1 we describe the SPARC database, data selection, the halo models we use to fit the inferred DM rotation curve of each galaxy given in the SPARC sample and the fitting methods. The four parametric RAR model is applied for a fixed particle mass ($50\mathrm{keV/c^2}$) what reduces the number of free parameters by one. For comparison we consider the NFW model, a two parametric empirical model motivated from N-body simulations (Navarro, Frenk, and White, 1996), and the DC14 model, a baryonic feedback motivated halo model with three free parameters (Cintio et al., 2014).

In section 4.3.2 we present the results of the SPARC analysis, perform a goodness of model analysis to compare the competing dark matter models and give a satisfying explanation for the scatter shower in the acceleration correlation based on the prototype NGC0055 and the better resolved Milky Way. A more detailed best-fit analysis for two more prototypes, DDO161 and NGC6015, gives a better picture about the characteristics of the inferred DM rotation curves within the context of the RAR model. Finally, we predict relations for different pairs of structural galaxy parameters for the 50keV-RAR model. Of special interest are the M_{BH}-M_{tot} relation (Bogdán and Goulding, 2015; Ferrarese, 2002; Kormendy and Bender, 2011) and the constancy of the *central* DM surface density (Donato et al., 2009). Here, we are going to enhance these relations with predictions inferred from disk galaxies of the SPARC data base.

4.3.1 Methodology

This work uses the new Spitzer Photometry and Accurate Rotation Curves (SPARC) database. It includes $3.6\,\mu\mathrm{m}$ near-infrared and $21\,\mathrm{cm}$ observations. The former traces the stellar distribution (bulge and disk) while the latter traces the atomic gas distribution and provides velocity fields from which the rotation curves are derived. See Lelli, McGaugh, and Schombert (2016) for a complete description of the SPARC database.

Data selection

The SPARC data is distributed in separated files and can be found at http://astroweb.cwru.edu/SPARC/. Specific information about each galaxy (i.e Hubble type, inclination etc) are provided in the file Table1.mrt. The information we are interested in, like galactocentric radius r and rotation curves V, are provided in the file Table2.mrt.

In detail, we extract the observed circular velocity $V_{\rm obs}$ and the baryonic contribution $V_{\rm bar}$, composed of a bulge ($V_{\rm b}$), disk ($V_{\rm d}$) and gas component ($V_{\rm g}$). The bulge and disk components are inferred from surface brightness observations for a given mass-to-light ratio. In summary, the baryonic component is given by

$$V_{\rm bar}^2 = \Upsilon_{\rm b} V_{\rm b}^2 + \Upsilon_{\rm d} V_{\rm d}^2 + V_{\rm g}^2 \tag{4.10}$$

For convenience, the velocities $V_{\rm b}$ and $V_{\rm d}$ are provided for a mass-to-light ratio of $1\,M_\odot/L_\odot$ what does not represent the real value for a galaxy. Since the mass-to-light ratio is just a constant scaling factor we may correct the velocities simply with the mass-to-light *ratio factors* Υ_b and Υ_d for bulge and disk (in units of $M_\odot/L_\odot$). Then the rotation curve for each component traces immediately its centripetal acceleration $a = V^2/r$.

For the data selection we proceed similar as was done by McGaugh, Lelli, and Schombert (2016b). Thus, we want to note that we consider same mass-to-light ratios since the following data selection output depends on the values. For all bulges we choose $\Upsilon_{\rm b} = 0.7$ and for all disks $\Upsilon_{\rm g} = 0.5$ as convenient average representatives. Further, we exclude all galaxies with a bad quality flag ($Q = 3$) and face-on galaxies with an inclination $i < 30°$. Then we exclude all points with a velocity error greater than 10% and all points where the baryonic velocity is greater than 95% of the observed velocity. The latter affects mainly data points in the inner region which is dominated by baryonic matter and strongly depend on the chosen mass-to-light factors. Afterwards, we exclude all remaining galaxies with less then 6 data points and obtain 124 galaxies (out of 174) with 2396 points (of 3355) in total.

Halo models

Following the standard assumption in the literature, that baryonic and dark matter do not interact each other, the total velocity is simply given by

$$V_{\rm tot}^2 = V_{\rm bar}^2 + v_{\rm DM}^2 \tag{4.11}$$

Here, $v_{\rm DM}$ is a theoretical dark matter component. Three competing dark matter models (RAR, NFW, DC14) will be explained in next and compared in the following section.

The RAR model is introduced in chapter 2. Besides the configuration parameters (β_0, θ_0, W_0), this model is described also by the particle mass m which is necessary to provide right physical properties for the obtained configurations. In this work the particle mass is set to $m = 50{\rm keV/c^2}$ as a promising candidate motivated by the Milky Way analysis (see section 4.1) and the application to different galaxy types from dwarfs to ellipticals (see section 4.2).

The NFW and DC14 model are two phenomenological dark matter models, determined from numerical CDM simulations. The DC14 model may be considered as in extension of the NFW model, because it takes into account more realistic feedback mechanism. See appendix A.1 for more details.

Data fitting

We fit the inferred DM rotation curve, $V^2_{\rm DM} = V^2_{\rm obs} - V^2_{\rm obs}$, with the Levenberg–Marquardt (LM) algorithm to find a χ^2 minima. The quantity χ^2 is calculated by

$$\chi^2(\boldsymbol{p}) = \sum_{i=1}^{N} \left[\frac{V_i - v(r_i, \boldsymbol{p})}{\sigma_i} \right]^2 \tag{4.12}$$

with N the number of data points, V_i is the set of circular velocity data, r_i is the corresponding set of radius data, $v(r_i, \boldsymbol{p})$ is the predicted circular velocity at radius r_i for the model parameter vector $\boldsymbol{p}$ and σ_i is the uncertainty for V_i.

For the RAR model, $\boldsymbol{p} = (\theta_0, W_0, \beta_0, m)$, we vary the three free parameter (θ_0, W_0, β_0) for a fixed particle mass m. Due to numerical stability improvements we consider the cutoff parameter $W_0 = 1.73\theta_0 + 1.07 + 10^{\omega}$ to make sure our fitting algorithm obtains only solutions with a halo (for approx. $W_0 < 1.73\theta_0 + 1.07$ the halo gets disrupted and only a degenerate core remains). Phenomenally, we can vary the cutoff through the cutoff parameter W_0 and the steepness through the degeneracy parameter θ_0. The latter is only possible within the transition regime ($\theta_0 \in [-5, 15]$). For high degeneracy, $\theta_0 > 15$, we obtain a cored halo with a degenerate core. For these degenerate solutions we propose a particle mass of $m = 50\mathrm{keV/c^2}$ as a promising candidate (Argüelles et al., 2018).

The NFW model describes a fixed cuspy halo with two free scaling parameter, e.g. $\boldsymbol{p} = (R_N, \rho_N)$. Therefore, that model can not explain the variation of the inner RC steepness or the variation in the cutoff. Instead, it is expected that NFW covers the rotation curves well on average due to its wide maxima bump.

The DC14 model, e.g. $\boldsymbol{p} = (X, R_N, \rho_N)$, has the additional parameter X compared to NFW which affects the inner steepness and the maxima bump width simultaneously.

For the LM fitting algorithm we need well chosen initial values to ensure convergence. Because that algorithm finds only local minima we choose 100 parameter sets randomly within a range. For the RAR model we have $\theta_0 \in [25, 45]$, $\beta_0 = [10^{-8}, 10^{-5}]$ and $\omega \in [0, 2]$. For NFW we have $R_N \in [10^1, 10^4]$, and $\rho_N = [10^{-4}, 10^{-1}]$. For the DC14 model we choose the same ranges as for the NFW model. Also, according to Katz et al. (2016) we may bound the initial values of the additional parameter to $X \in [-3.75, -1.3]$. These ranges are no restrictions such that the fitting algorithm may find solutions beyond the boundaries.

4.3.2 Results

Here, we reproduce the radial acceleration correlation and perform a goodness of model analysis for our RAR model as well as for NFW and DC14. We demonstrate that the acceleration behavior for individual galaxies is more intricate what becomes obvious after changing the perspective of the acceleration correlation. Finally, we present correlations for different pairs of structural galaxy parameter.

Acceleration correlations

The radial acceleration correlation (hereafter RAC) compares the total acceleration $a_{\rm tot}$, implying all matter contribution, with the baryonic component $a_{\rm bar}$, see top panels of fig. 4.10. The correlation in this projection ($a_{\rm tot}$-$a_{\rm bar}$) is well described by McGaugh's empirical fit McGaugh, Lelli, and Schombert (2016b),

$$a_{\rm tot} = \frac{a_{\rm bar}}{1 - \mathrm{e}^{-\sqrt{a_{\rm bar}/\mathfrak{a}_0}}} \tag{4.13}$$

with the only parameter

$$\mathfrak{a}_0 \approx 1.20 \times 10^{-10} \mathrm{m/s^2} \tag{4.14}$$

It clearly shows a deviation from the linear correlation, inferred from spiral galaxies, in the low acceleration regime ($a_{\mathrm{bar}} \ll \mathfrak{a}_0$), what is dominated by dark matter. In the high acceleration regime ($a_{\mathrm{bar}} \gg \mathfrak{a}_0$), where baryonic matter dominates, the linear relation is recovered.

An equivalent representation of the link between baryonic and total components is given by the mass discrepancy acceleration relation (hereafter MDAR). It is usually defined as the ratio between the total velocity and the baryonic velocity, $D = V_{\mathrm{tot}}/V_{\mathrm{bar}}$. With $a = v^2/r$ this relation is equivalent to $D = a_{\mathrm{tot}}/a_{\mathrm{bar}}$ and the results are illustrated in the bottom panels of fig. 4.10. In the limiting case of spherical mass distributions and with $a = \frac{\mathrm{d}\Phi}{\mathrm{d}r}$ the relation may be linked to the enclosed masses through $D = M_{\mathrm{tot}}/M_{\mathrm{bar}}$.

According to our results we conclude that all considered models (RAR,NFW,DC14) are able to reproduce the acceleration correlations (RAC and MDAR). Qualitatively, they look similarly good compared to the empirical correlation (4.13) inferred from original SPARC data. Especially, the deviation in the low acceleration regime look adequate, representing the dark matter dominated region. Unsurprisingly, the linear relation in the high acceleration regime, representing the baryonic matter dominated region, is reproduced as well. This is obvious because the DM halo models predict mass profiles with negligible DM contribution in the inner disk region towards the bulge.

Indeed, according to some authors RAC and MDAR does not show any new physics and may be explained within the ΛCDM framework (Keller and Wadsley, 2016; Navarro et al., 2016; Salucci, 2016). Based on modern cosmological simulations, Keller and Wadsley (2016) predict even a redshift dependency of the acceleration parameter $\mathfrak{a}_0$ what emphasizes that the correlation is universal only regarding the morphological classification.

Both, the RAC and MDAR, have been criticized that their representation focus only on the low acceleration regime where dark matter dominates. Therefore, Chae, Bernardi, and Sheth (2017) suggested to compare the baryonic component, a_{bar}, with the ratio of the baryonic and dark matter components, $a_{\mathrm{DM}}/a_{\mathrm{bar}}$, what gives also information about dark matter in the intermediate acceleration regime. They clearly realized that the original representation of RAC/MDAR shows a fundamental link on halo scales but simultaneously obscures the relation between dark and baryonic matter on inner halo scales. Therefore, any DM model independent of the inner shape (cored or cuspy) would reproduce the linear relation in the baryon dominated region.

Following that argument we suggest a similar approach. Thus, we want to emphasize that it is more convenient to connect directly the dark matter component, $a_{\mathrm{DM}} = a_{\mathrm{obs}} - a_{\mathrm{bar}}$, with the baryonic counterpart a_{bar}. This reveals more information about the relation between baryonic and dark matter ranging from the low acceleration up to the high acceleration regime. Especially details about the DM acceleration in the baryon dominated part are unveiled. In this presentation we find (on a first glimpse) a linear correlation in the loglog-plot rather than the empirical fit proposed by McGaugh, Lelli, and Schombert (2016b). The important fact remains that a radial acceleration correlation is found and ranges from a DM dominated region to a baryonic matter dominated region, see middle panels of fig. 4.10. Contrasted with the original representation we noticed an increased scatter (in form of a *scatter shower*) in the high acceleration regime which we are going to analyze in more detail.

Finally, it is worth to note that regardless of the presentation (a_{tot} or a_{DM}) it is difficult to compare the different DM models quantitatively with respect to the acceleration correlation found in the SPARC database due to the increased scatter. Qualitatively they all are able to explain that correlation. In next, the strategy therefore

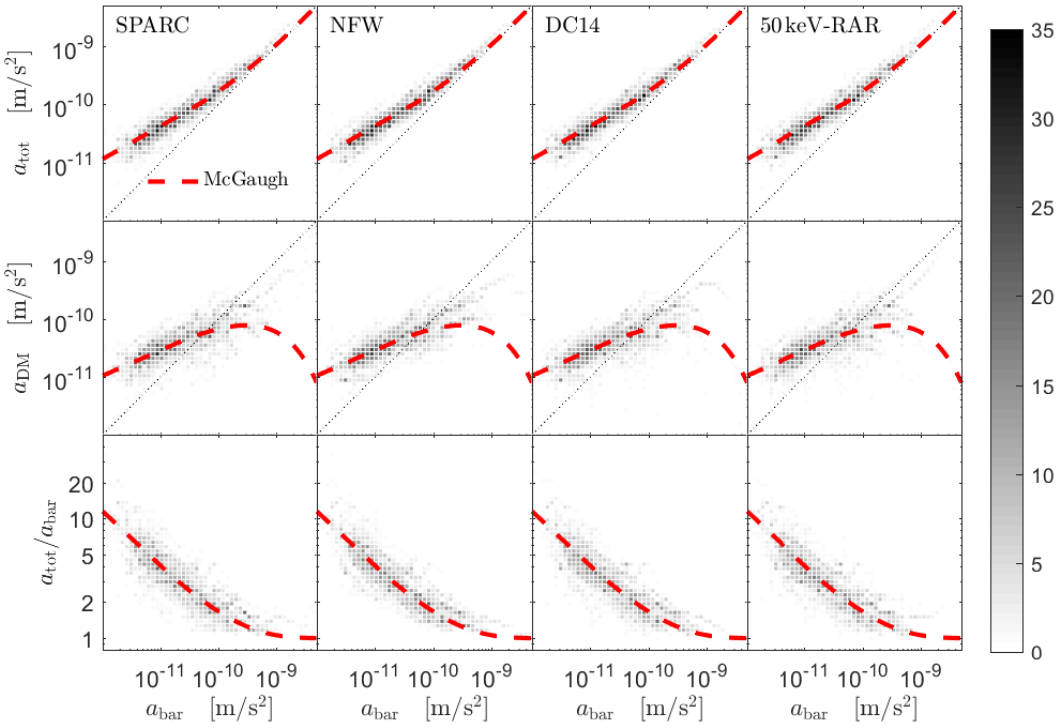

Figure 4.10. Radial acceleration correlations from SPARC data (first row), NFW (second row), DC14 (third) and RAR (forth row). The correlation is presented in three different ways: (top panels) original correlation with focus on the total acceleration $a_{\rm tot}$, (middle panels) correalation with focus on the dark component $a_{\rm DM}$ and (bottom panels) the mass discrepancy acceleration relation with focus on the ratio $a_{\rm tot}/a_{\rm bar}$. The baryonic centripetal acceleration $a_{\rm bar}$ is inferred from luminosity observables while the total acceleration is inferred from velocity fields. Both measurements are independent. For SPARC data the inferred DM acceleration is given by $a_{\rm DM} = a_{\rm obs} - a_{\rm bar}$. In the case of RAR, NFW and DC14 the total acceleration is composed of the predicted dark and the inferred baryonic components. Each plot is divided in 50x50 equal bins showing clearly a non-linear correlation. Note, that the top panels emphasize mainly the dark matter dominated region for accelerations below the particular value $\mathfrak{a}_0 \approx 1.20 \times 10^{-10}{\rm m/s^2}$. Above that acceleration the information about dark matter is hidden due to the baryon dominance, what becomes unveiled in the middle panels. Qualitatively, all considered models (RAR,NFW,DC14) are able to reproduce the radial acceleration correlation, independent of the representations.

is to focus on the dark matter fit of the rotation curves (rather than the inferred acceleration correlation) and assign for each fit numerical values what allows a quantitative comparison of the dark matter models.

Goodness of model

The SPARC galaxies show several phenomena in their rotation curves. Some galaxies indicate a clear cutoff in the outer halo and/or a variation of the inner halo steepness, giving hints of a cored or cuspy halo. Many galaxies show a rising tail implying that the rotation curves are incomplete. This is most probably due to faint stars in the outer most halo region. On the other hand, some galaxies are characterized by a clear oscillation in their flat rotation curve. Of interest is therefore a quantitative description about the goodness of a model fitting the entire galaxy sample.

The goodness of a fit for a single galaxy is well described by the χ^2 value. When competing models with different number of parameters are compared it is appropriate to consider the reduced χ^2 defined as $\chi^2_r = \chi^2/d$ with the degree of freedom $d = N - p$, N the number of observables (for a single galaxy) and p the number of parameters

(of the considered model). The question now arises how to compare the competing models for a population of galaxies. Clearly, the sum of (reduced) χ^2 values for a model would be an inappropriate indicator. Consider the case where a model fits the majority of a population very well (low χ^2 values) but fails extremely (very high χ^2) for just a few galaxies. Thus, the goodness of a model cannot depend on the whole population. Instead, we have to look differentiated at the population. Therefore, we ask *how many* fitted galaxies have a (reduced) χ^2 *lower* than a given one. It turns out that the normalized population curve may be well described by the function

$$\frac{N(\chi_r^2)}{N_{\max}} = \frac{1}{1 + \left[\frac{\chi_r^2}{\hat{\chi}_r^2}\right]^{-n}} \tag{4.15}$$

The parameter $\hat{\chi}_r^2$ cuts the population in half where the first half has a lower reduced χ^2 and the other half has a greater reduced χ^2 compared to the median $\hat{\chi}_r^2$. Exactly this criteria is used to described the goodness of a model for fitting a population of galaxies. Thus, we use $\hat{\chi}_r^2$ to compare the competing models (RAR, DC14, NFW). The secondary parameter n is a descriptor for the population distribution itself. It tells, how bad the first half of the population is fitted and how good the other half. The higher n the steeper is the slope of the curve at $\hat{\chi}_r^2$. A high n value would imply that the fits of most galaxies have a reduced χ^2 slightly greater than the median $\hat{\chi}_r^2$. In other words, a high n value imply that the considered model fits all galaxies similarly good with a reduced χ^2 around the median $\hat{\chi}_r^2$. There would be only few very good fits and same for very bad fits compared to $\hat{\chi}_r^2$. Thus, the descriptor n is a supplemental parameter, which gives further information about a model, but it is not useful to compare different models like $\hat{\chi}_r^2$.

The introduced method is similar to the empirical distribution function when the normalized population is interpreted as a probability depending on the variable χ_r^2.

The goodness of the competing models (RAR, DC14, NFW) in fitting the SPARC galaxy sample is summarized in fig. 4.11. RAR and DC14 are similarly good when the morphological type is ignored. NFW, in contrast, is clearly disfavored here. This picture becomes much more obvious when only megallanic types (Sd,Sdm,Sm,Im) are considered. On the other hand, focusing on non-megallanic types (S0, Sa, Sab, Sb, Sc, Scd, BCD) there is no clear favorite. This implies a connection between dark matter and the morphological type. Moreover, comparing DC14 and NFW implies that baryonic feedback is an important mechanism for galaxy formation. On the other hand, our results show that the RAR model is as good as DC14 although it doesn't consider any baryonic matter contribution nor any baryonic feedback mechanism.

Galaxies of magellanic type which are fitted very well, especially, by the RAR model are NGC0055 (Sm), UGC05986 (Sm), UGC05750 (Sdm), UGC05005 (Im), F565-V2, (Im), UGC06399 (Sm), UGC10310 (Sm), UGC07559 (Im), UGC07690 (Im), UGC05918 (Im) and UGC05414 (Im). This bolsters the results of the goodness of model analysis in fig. 4.11.

A Remarkably good fit with the RAR model (and DC14) is given for NGC0055 (Sm), see figs. 4.12 and 4.13. We now focus on this particular prototype to investigate the large scatter in the radial acceleration correlation. The prototype demonstrates that many galaxies don't follow strictly McGaugh's empirical formula for the acceleration correlation. While in the DM dominated regime ($a_{\text{bar}} < \mathfrak{a}_0$) the acceleration relation seems to be close to McGaugh's fit (despite an offset) we find an abrupt decrease just before the baryon dominated regime. These abrupt decreases we interpret as the source of the increased scatter, especially in form of a *scatter shower* in the low acceleration regime of dark matter. RAR and DC14 can reproduce that abrupt decrease very well, but NFW has serious problems in the baryon dominated regime what is due to its cuspy design. An interesting characteristic of the rotation curve is its slope in the inner halo (baryon dominated region) what shows the nature of the halo: cored

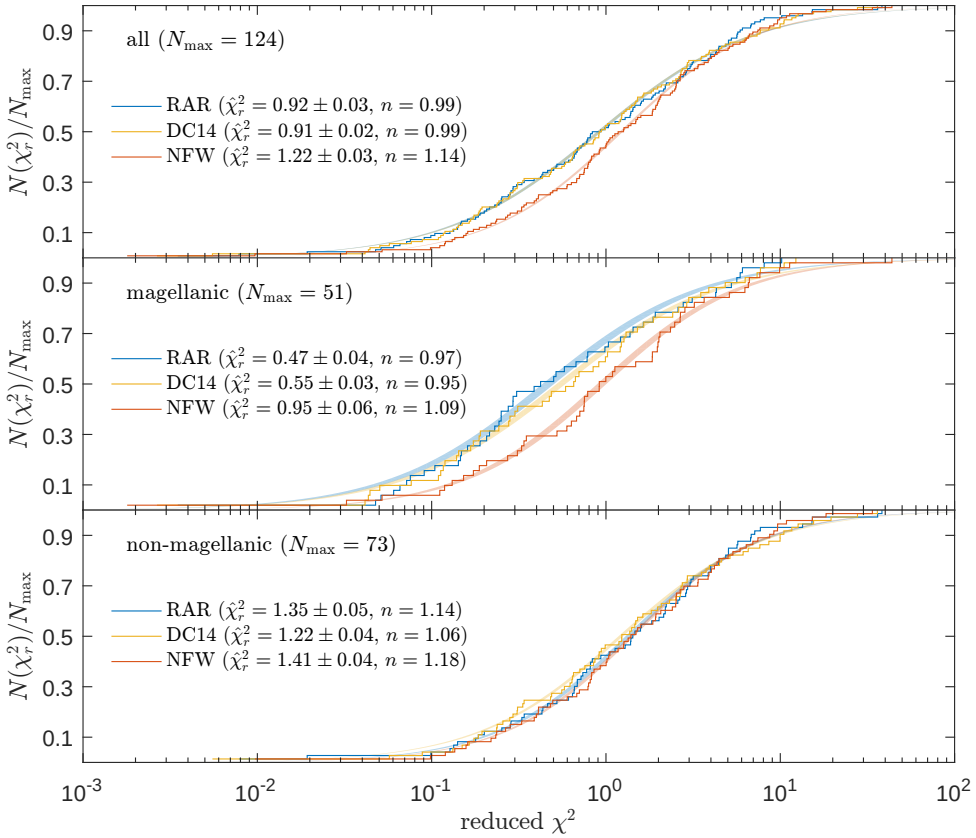

Figure 4.11. Goodness of model analysis for all galaxy types (left), only magellanic (middle) and non-magellanic (right). We count the population of fitted galaxies having a reduced χ^2 smaller than a given one. The normalized population may be well described by the function $1/[1 + (\chi_r^2/\hat{\chi}_r^2)^{-n}]$ with the median $\hat{\chi}_r^2$ and the supplemental descriptor n. RAR and DC14 are similarly good when the galaxy type is ignored. NFW, in contrast, is clearly disfavored here. This picture becomes much more obvious when only megallanic types are considered. On the other hand, focusing on non-megallanic types there is no clear favorite.

or cuspy. The RAR model implies a cored halo and is therefore good in fitting those halos. Contrary, the NFW model gives by design a cuspy halo. For the RAR model (with a well defined halo) as well as for the NFW model those inner halo slopes are fixed while DC14 is more flexible. In summary, the prototype NGC0055 demonstrates clearly that the inner halo shape is important when the relevance of a cuspy or cored halo is considered. It should be now obvious that the new perspective of the radial acceleration correlation ($a_{\rm bar} - a_{\rm DM}$) is preferred compared to the original ($a_{\rm bar} - a_{\rm obs}$) which obscures the inner halo relation.

Another interesting phenomena are oscillations in the rotation curve (RC). Most galaxies, which are poorly fitted by any of the considered models, show *short range* oscillations with more than one maxima in their RC. None of the models can explain that phenomena found mostly in non-magellanic galaxy types: e.g. NGC2403 (Scd), UGC02953 (Sab), NGC6015 (Scd), UGC09133 (Sab), UGC06787 (Sab), UGC11914 (Sab), NGC1003 (Scd), NGC0247 (Sd), UGC08699 (Sab) and UGC03205 (Sab). Indeed, all models show only one maxima in their RC within the range of interest. Phenomenally, in the RAR model it is possible to vary the width of the maxima bump in the RC through the cutoff parameter W_0 in the strong cutoff regime. But without or with weak cutoff the RAR model shows long range oscillations, equivalent to the IS model. However, these oscillations are too long and therefore not a convenient explanation. On the other hand, in the case of strong cutoff we obtain a narrow maxima bump

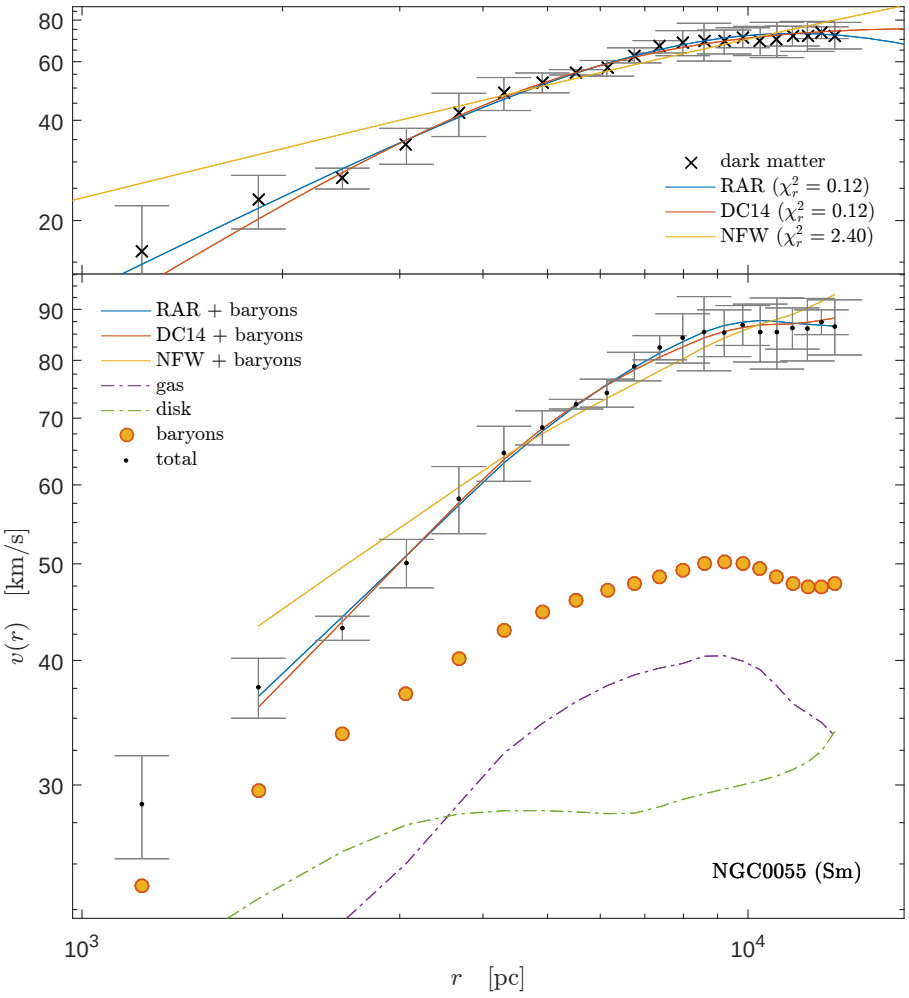

Figure 4.12. Rotation curve of NGC0055 with total velocity and baryonic components (bottom). The sum of dark and baryonic components give the total velocities (thick solid lines). The best fitted DM components (top) are given for RAR, NFW and DC14, being compared with the inferred DM from SPARC data.

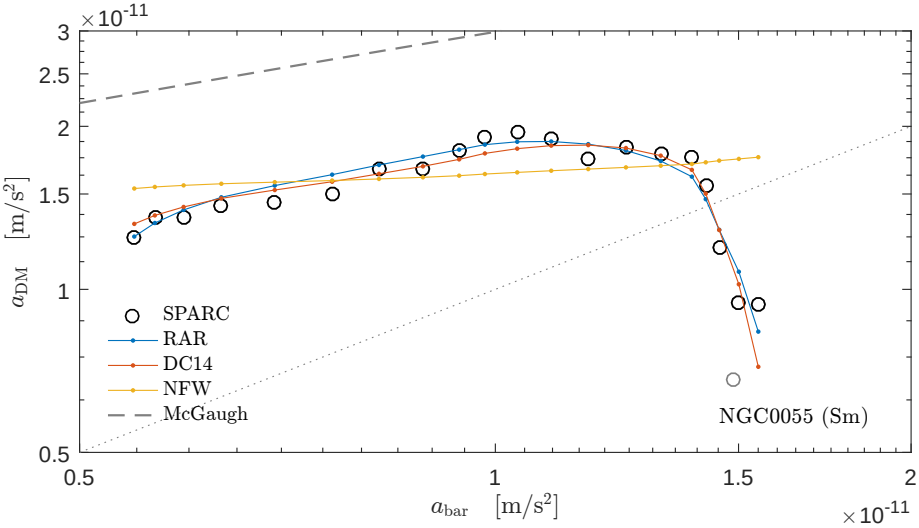

Figure 4.13. Radial acceleration curve of NGC0055 with SPARC data (circles), McGaugh's empirical fit (dashed line) and best fits of the considered DM models. The dotted line describes where dark matter and baryonic acceleration are equal.

necessary for many RCs, especially for galaxies of magellanic type which do not show those oscillations in general, e.g. NGC0055 (Sm), UGC05986 (Sm), UGC07323 (Sdm), KK98-251 (Im), DDO168 (Im), D631-7 (Im), DDO161 (Im), UGCA442 (Sm), DDO154 (Im), F583-1 (Sm), but also for non-magellanic galaxy types, e.g. NGC5585 (Sd), NGC7793 (Sd), UGC06614 (Sa), ESO079-G014 (Sbc), F571-8 (Sc), NGC0891 (Sb), UGC06614 (Sa), UGC09037 (Scd), NGC4217 (Sb), UGC04278 (Sd). NFW has a wide maxima bump and fits therefore oscillating RC well only on average. Same for DC14 since it may vary the maxima bump width. Exactly these oscillations — or a lack of them — may be an interesting hint for the connections between dark matter and the morphological type as suggested by the goodness of model analysis, see fig. 4.11.

χ^2 analysis

We are moving now to a more detailed χ^2 analysis of three selected galaxies, each representing some characteristics of given observational data in relation to the RAR model fit. Thus, we mainly divide the SPARC galaxies in three group through the inferred dark matter component as explained in next.

The first group, represented by NGC0055, clearly shows only a single maxima in its dark matter rotation curve. As shown in fig. 4.14 this typical profile is well fitted by the RAR model with sufficient low cutoff values, corresponding to not negligible surface effects. However, due to the lack of information in the inner halo structures, especially the galactic center, there is some uncertainty in the strength of the cutoff parameter. Although those solutions provide a minimal DM halo mass, the uncertainty is physically better reflected in the core mass M_c, what covers a range of about two orders of magnitude. Higher core masses, given for lower W_0 values, imply cuspier halos what are clearly discarded here. Well disfavored are also higher DM halo masses M_s which corresponding to isothermal-like halos, given for higher W_0 values. In contrast, those solutions provide a minimal core mass M_c with a huge uncertainty in the total mass.

The second group, represented by DDO161, shows a rising part in the rotation curve towards a maximum without a clear turning point, compared to the first group. Fitting those galaxies for different W_0 values does not necessary favor solution with or without surface effects. The variation in the χ^2 value remains rather small, see fig. 4.15. Nevertheless, clearly discarded are cuspy halos just as in the first group. There is a narrow χ^2 minimum for relatively low W_0 values suggesting a best-fit. However, this result should be taken with caution because the obtained minimum depends on the inner data points, keeping in mind that for most galaxies in the SPARC data base the inner data points have a relatively high uncertainty. This is also the case for DDO161.

Finally, the third group, represented by NGC6015, shows some oscillations in the rotation curve, mainly in the outer halo. Following fig. 4.16, those galaxies are clearly better fitted by extended isothermal-like halos compared to the contracted halos, given for lower W_0 values. The extended solutions provide a wide halo maximum followed by a flat rotation curve. This is suitable to fit the oscillations well on average, although the best-fit remains rather poor. The contracted solutions, in contrast, provide only a narrow maximum in the halo, followed by a Keplerian decreasing tail. The latter is clearly disfavored here. It is worth to note that the RAR model (and others such as NFW and DC14) are not appropriate to fit the oscillations, characterized through multiple maxima in the rotation curve.

In summary, we consider galaxies belonging to the first group as *appropriate* candidates because they allow to determine the W_0 value, although with some uncertainty. In contrast, galaxies belonging to the other two groups we consider as *inappropriate* candidates due to either a lack (e.g. DDO161) or an abundance (e.g. NGC6015) of information in the halo. This fact does not allow to determine the cutoff

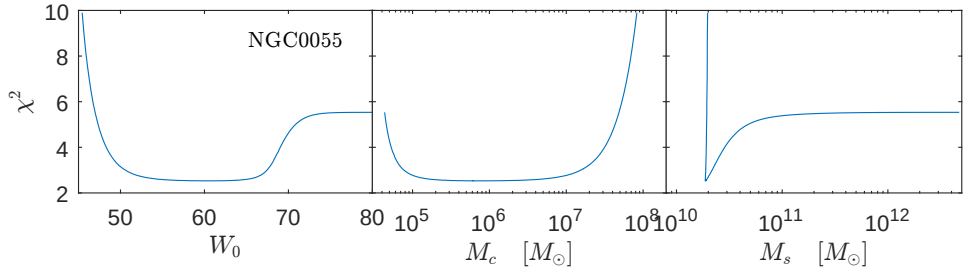

Figure 4.14. χ^2 profiles for NGC0055. There is a clear minimum for a total halo mass of $M_s \approx 2 \times 10^{10} M_\odot$. Due to the lack of information in the inner halo region the minimum corresponds to a valley in the core mass $10^5 \lesssim M_c \lesssim 10^7$, spanning a range of about 2 orders of magnitude. This uncertainty is also reflected in the cutoff parameter W_0. For relatively high values the solutions develop extended isothermal halo tails, which are clearly disfavored here. Solutions with relatively low W_0 values, corresponding here to highly cuspy profiles, are ruled out even stronger. Thus, in favor are solutions with mild surface effects.

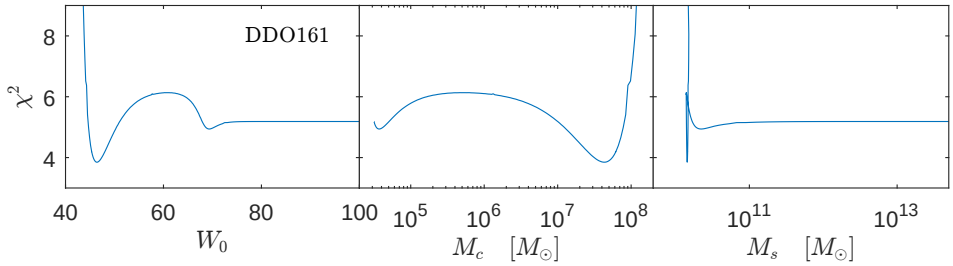

Figure 4.15. χ^2 profiles for DDO161. This galaxy is characterized through a rising rotation curve with a clear turning point. This *deficit* of information in the outer halo region makes is difficult to favor either extended (isothermal-like) or contracted halos. All solutions are suitable for fitting well the rotation curve with a rather small change in the χ^2 value. Solutions with lower W_0 values, corresponding to cuspy halos, are ruled out according to this analysis. With caution has to be taken the local minimum for relatively low W_0 values. This best-fit depends highly on the inner data points which are usually poorly constraint.

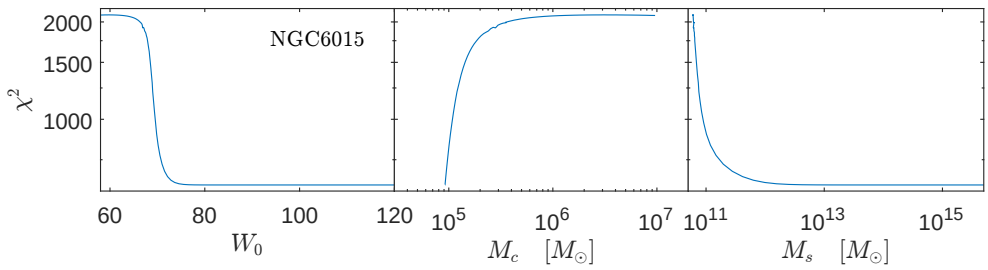

Figure 4.16. χ^2 profiles for NGC6015. This galaxy is characterized through an extended halo tail with oscillations. This *abundance* of information in the outer halo region clearly favors isothermal halos, corresponding to relatively high cutoff values. Those solutions provide extended halo tails with a wide halo maximum, suitable but insufficient for fitting well the rotation curve. Solutions with lower W_0 values are ruled out according to this analysis. The latter corresponds here to profiles with contracted halos without developing isothermal tails due to surface effects.

Table 4.3. Parameter for baryonic components of Milky Way. Note: baryonic and especially disk parameter imply RAR-DM component described by $mc^2 = 50\text{keV}, \theta_0 \approx 37.8, W_0 \approx 66.4$ and $\beta_0 \approx 7.66 \times 10^{-6}$

component	total mass ($M_\odot$)	length scale (kpc)
inner bulge	5.5×10^7	4.07×10^{-3}
main bulge	9.7×10^9	0.137
disk	6.0×10^{10}	2.92

value, especially leaves the upper bound open. Though, in all cases it is possible to set a lower limit what clearly discards cuspy halos within the RAR model. Note that the lower limit in W_0 also sets a specific upper limit for the core mass.

Milky Way

We change now the focus to the Milky Way galaxy which is much better resolved than the SPARC galaxies. In particular, the widely covered radial extent, from the center to the outer halo, gives a better understanding of the mass discrepancy.

The rotation curve for the Milky Way is given by Sofue (2013). In constrast to the SPARC data, the baryonic components (bulge and disk) are given only analytically. The bulge structure is composed of a main and an inner bulge. Each of those two components is given by an exponential sphere model (see appendix A.2). The disk, on the other hand, is given by an exponential disk model (see appendix A.3).

Here, we are mainly interested in the centripetal acceleration given by $a(r) = v^2(r)/r$. The length scales R_b and R_d (for bulge and disk) as well as the masses M_b and M_d, describing the total masses for bulge and disk, are provided in Sofue (2013) and table 4.3. Important attention has to be given to the disk parameters since they depend on the chosen dark matter model and have to be adjusted. Then, the baryonic contribution is the sum of inner bulge, main bulge and disk components. For the total contribution it is necessary to add also the dark matter component.

The rotation curve is given in fig. 4.17. It shows an excellent fit of the given rotation curve observables with the RAR model. For demonstrative purpose it is illustrated for a particle mass of 50 keV. Here, we recall that the RAR model is able to describe the halo and explains simultaneously the compact object in the Galactic center also for other particles masses. For further details concerning the supermassive black hole alternative in the Galactic center are provided in section 4.1.

Regarding the acceleration correlation in the Milky we find fundamental differences compared to McGaugh's empirical fit, see fig. 4.18. In the low acceleration regime (dark matter dominated) we obtain a linear proportionality what is due to the necessary strong cutoff in the halo. After that it follows the transition into the baryonic matter dominated regime with decreasing dark matter acceleration similar to McGaugh. However, in the high acceleration regime we have again an increase of dark matter acceleration because of the degenerate dark matter core, resembling a supermassive dark object, what is a fundamental feature of the RAR model.

For comparison, we have added the NFW model. The results show a similar trend in the low acceleration regime, but diverge towards a constant acceleration of the dark matter component in the high acceleration regime. Thus, all shown predictions (RAR, NFW and McGaugh) have a very different behavior in the baryonic dominated region.

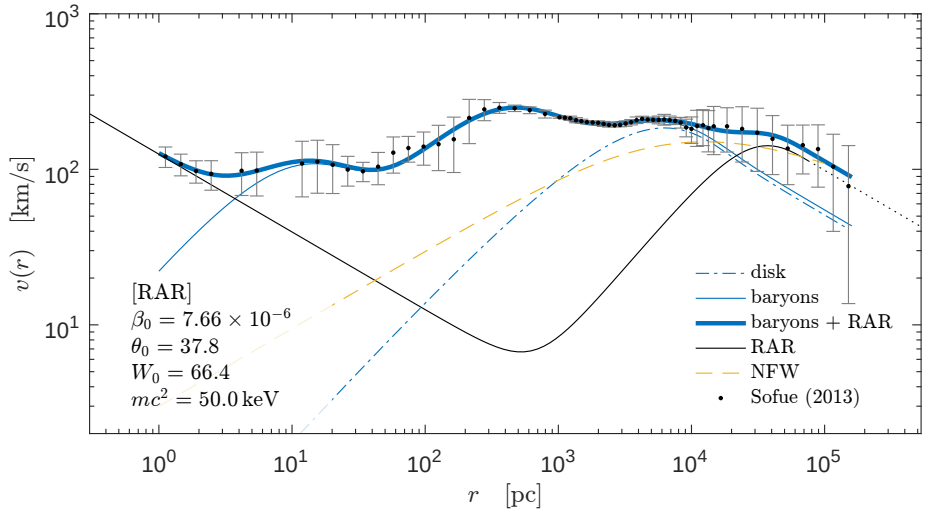

Figure 4.17. Rotation curves for Milky Way galaxy. The observed velocities (black dots with error bars) are compared with the total velocity (thick solid line). The latter is composed of the baryonic component (dashed line), including a disk component (dot-dashed line), and the best-fit of the DM component, modeled with $50\mathrm{keV}$-RAR (thin solid line). For comparison, the NFW profile is added

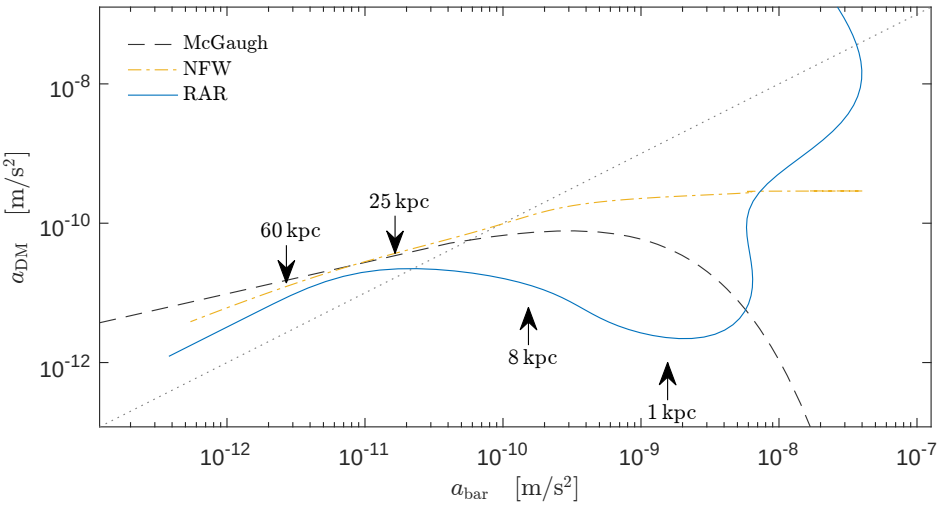

Figure 4.18. Radial acceleration correlation for Milky Way galaxy. The results of the RAR model (solid line) is compared with McGaugh's empirical fit (dashed line) and the results from NFW model (dot-dashed line). The dotted line describes where the centripetal acceleration of dark and baryonic matter are equal. Thus, in the top-left corner is the dark matter dominated region and in the bottom-right corner is the baryonic matter dominated region. The transition appears at about $2 \times 10^{-11}\mathrm{m/s^2}$. In the very high acceleration regime the RAR model predicts an increase of dark matter acceleration due to the degenerate dark matter core in the Galactic center.

Parameter correlations

In this section we analyze different pairs of structural galaxy parameters obtained from the $50\,\mathrm{keV}$-RAR model, such as θ_0 and β_0, the halo radius r_h and mass M_h as well as the core radius r_c and core mass M_c. Further, we are also interested in the total dark matter mass what needs a careful definition here.

Usually, mass distributions infinite in mass and space are truncated for example at a critical radius or density to obtain reasonable values. In that fashion, we define the *boundary mass* $M_b = M(r_b)$, being r_b the boundary radius where the density falls to the critical density of the Local Group ($10^{-5} M_\odot/\mathrm{pc}^3$).

On contrary, the RAR model provides naturally finite mass distributions via the cutoff parameter W_0. Thus, we define the *surface mass* $M_s = M(r_s)$, being r_s the natural surface radius where the density falls to zero. Important, for strong cutoff values we have total masses $M_s \approx M_b$.

It is important to emphasize that appropriate information about the halo, especially the outer halo, are needed to determine the cutoff parameter W_0. Thus, we divide the galaxy sample in two groups: galaxies with

- *appropriate* halo information ($M_{\mathrm{tot}} = M_b \approx M_s$) and
- *inappropriate* halo information ($M_{\mathrm{tot}} = M_b \ll M_s$).

Here, *appropriate* refers to galaxies with sufficient information in the dark matter rotation curve (e.g. a clear maximum) while *inappropriate* refers either to a lack (e.g. no clear maximum) or to an abundance of information (e.g. oscillations in the outer halo).

Additionally, we introduce another group, the so called *flat-tail fits*. All candidates of this group have in common that their whole dark matter distribution is fitted well by the flat tail of the RAR model which implies no (or weak) evaporation. Due to the poor data of those galaxies we consider their results as an artifact of the fitting method. Thus, flat-tail fits produce dark matter distributions with too little halo radii and therefore too high halo and core masses. We speculate therefore that a proper choice of parameters, following the relation

$$\ln \frac{M_h}{M_\odot} \approx 2.02 \ln \frac{r_h}{\mathrm{pc}} + 5.10 \pm 1.54 \tag{4.16}$$

as found in the r_h-M_h plot (see left diagram of fig. 4.19), would produce adequate dark matter profiles, sufficient to describe the rotation curves with slightly different χ^2 values.

All considered solutions of the RAR model have always a degenerate core and a diluted halo. The core is defined as the first maxima in the rotation curve and the halo is defined as the second maxima. We obtain halo radii mainly in the interval $[10^3, 10^5]\mathrm{pc}$ and halo masses in the interval $[10^8, 10^{12}]M_\odot$. For the corresponding cores we obtain radii and masses in the intervals $[10^{-4}, 10^{-2}]\mathrm{pc}$ and $[10^3, 10^7]M_\odot$.

It is important to note that the quantum core is well described by a fully degenerate core. Analytically, we find the simple relation $M_c r_c^3 \sim m^{-8}$. Because we have set the particle mass, the mass-radius relation for the core has no predictive character here.

Of more interest is the core-halo relation for the mass. In that projection we clearly identify a distinction between the appropriate and the inappropriate halo group. Both follow approx. the relation $M_h \sim M_c^2$ while the appropriate halo group shows a higher diversity. Following the best-fit analysis of NGC0055 (see. fig. 4.14), the diversity is most probably due to some uncertainty in the cutoff parameter W_0.

The group distinction with same characteristics is also visible in the θ_0-β_0 parameter space, see fig. 4.19. All best fits have a central degeneracy parameter in the degenerate regime, $\theta_0 \in [20, 50]$. For the central temperature parameter we obtain the

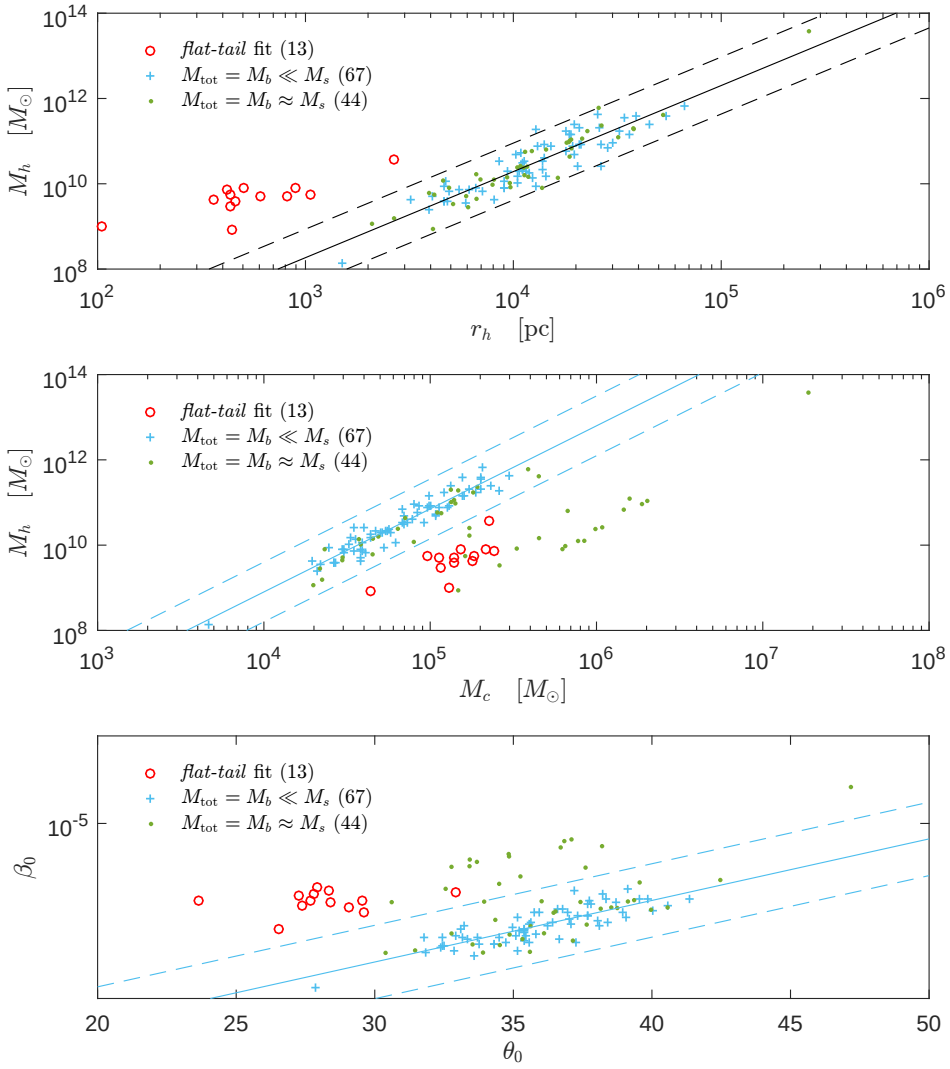

Figure 4.19. Parameter correlations for the best fits of the 50 keV-RAR model. The galaxy sample in every diagram is classified in three groups: (1) galaxies with appropriate halo information ($M_{\rm tot} = M_b \ll M_s$, dots), (2) with inappropriate halo information ($M_{\rm tot} = M_b \ll M_s$, crosses) and (3) with flat-tail fits which are considered as artifacts (open circles). (**left**) In the r_h-M_h plot we find a correlation with approx. $M_h \sim r_h^2$ (dots and crosses). In contrast to this correlation we may interpret the flat-tail fits as false fits. All of them have in common that the whole dark matter distribution was best-fitted with the flat tail of the RAR model, implying no (or weak) cutoff. Only for one galaxy (NGC4088) we find $\beta_0 \sim 10^4$ where pressure effects are not negligible any more. This *outlier* is due to the poor information about the halo where only the cored part without any maxima is available. (**middle**) Focusing on the M_c-M_h plot we clearly identify a distinction between the appropriate (dots) and the inappropriate halo group (crosses). Both follow approx. the relation $M_h \sim M_c^2$ while the appropriate halo group shows a higher diversity. (**left**) The distinction with the same characteristics is also visible in the θ_0-β_0 parameter space.

range $[10^{-9}, 10^{-5}]$ which corresponds to the low temperature regime with negligible pressure effects.

Only for one galaxy (NGC4088) we find $\beta_0 \sim 10^4$ where pressure effects are not negligible any more. But that galaxy has a fundamental lack of information about the halo. Data shows only the inner part of the halo without any trend towards a maxima. This allows only to connect the galaxy with the r_h-M_h correlation group described by eq. (4.16). Without any information about the outer halo (e.g. maxima) it is impossible to predict a narrow window of halo radii and masses. In the following we consider this candidate as an outlier.

Central core vs. total halo mass relation

We move now to the $M_{\rm BH} - M_{\rm tot}$ relation (Bogdán and Goulding, 2015; Ferrarese, 2002; Kormendy and Bender, 2011) where $M_{\rm tot}$ is the total dark matter halo mass and $M_{\rm BH}$ is the mass of the compact dark object at the center of galaxies. Traditionally, the central dark objects are assumed as SMBHs but here interpreted as dark matter quantum cores in the case of inactive galaxies. In the following, we consider $M_{\rm BH} = M_c$, being $M_c = M(r_c)$ the quantum core mass. In section 4.2 it is shown that the RAR model is able to explain this relation for typical dwarf galaxies to normal ellipticals. Here, we extend the results with predictions inferred from disk galaxies of the valid SPARC sample. The results are summarized in fig. 4.20.

Following the two definitions of enclosed mass (M_b and M_c, see above) we focus on the *appropriate* and *inappropriate* groups, excluding flat tail fits and outliers, to demonstrate the natural benefits of the RAR model. Especially the importance of the cutoff parameter W_0. The first group (green circles) corresponds to galaxies where the total mass is given by the surface mass, $M_{\rm tot} = M_s < 10^{14} M_\odot$. The second group (light blue crosses) corresponds to galaxies where the total masses given at the boundary radius, $M_{\rm tot} = M_b \ll M_s$.

The arbitrary upper mass limit $10^{14} M_\odot$ is applied to distinguish between realistic surface masses ($M_s < 10^{14} M_\odot$) and non-realistic ($M_s \geq 10^{14} M_\odot$). Clearly, spirals with masses above $10^{13} M_\odot$ are already highly improbable. And indeed, the prediction of the RAR model tells that SPARC spirals with appropriate halo information have natural total masses mainly below $10^{12} M_\odot$. Only one candidate has few $10^{12} M_\odot$.

Note that due to inappropriate information in the outer halo of the second group it is not possible to constrain the cutoff parameter W_0 what results in extended mass distributions with total masses $M_s \gg 10^{14} M_\odot$, see also fig. 4.16. Thus, it is necessary to truncate those extended mass distribution what results in a misleading narrow correlation in the $M_c - M_{\rm tot}$ relation. Instead, the RAR model predicts a much higher diversity rather than a narrow correlation according to the first group (green circles).

The results suggest that a halo truncation (e.g. at virial radius) describes an upper limit for the total mass, corresponding to a particular core mass. But the cutoff parameter allows to to break this relation by developing either larger core masses for a given total mass or lower total masses for a given core mass. However, respecting the astrophysical condition (e.g. developing a halo maxima in the rotation curve) implies also lower limits for core and halo.

The majority of simulated galaxies has a total dark matter mass between $10^9 M_\odot$ and $10^{12} M_\odot$ while only a few are slightly more massive. The core mass spans a majority range between $10^4 M_\odot$ and few $10^6 M_\odot$. More important, the RAR model predicts here a break in the Ferrarese relation ($M_{\rm tot} \sim M_c^{0.6}$) at about $10^{11} M_\odot$, following $M_{\rm tot} \sim M_c^2$.

We want to emphasize that the second galaxy population (light blue crosses) has to be taken with caution since they don't provide appropriate information about the outer halo. We therefore recommend to rely mainly on the first galaxy population (green circles) with appropriate halo information.

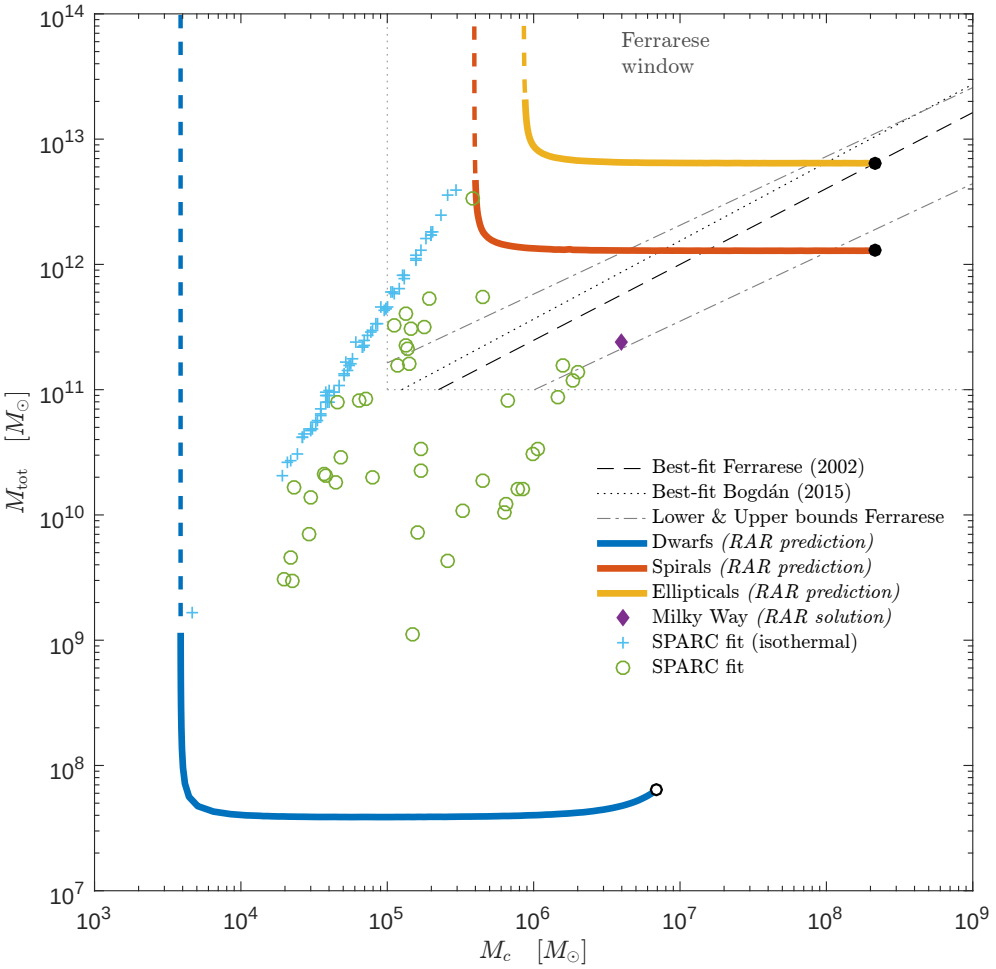

Figure 4.20. Prediction of the M_c-$M_{\rm tot}$ relations within three parametric RAR model (for $mc^2 = 48\,\mathrm{keV}$). The different *predicted* lines read for each galaxy type in correspondence with the astrophysical RAR solutions as given in (see section 4.2 for details). RAR predictions for typical spirals (red) and ellipticals (yellow) together with the Milky Way solution (diamond) lay within the *observable Ferrarese window*. The RAR prediction for typical dwarfs (blue) is located at the lower end of the M_c-$M_{\rm tot}$ plane, where data does not support. The black dots correspond to the critical core masses M_c^{cr} while the black circle indicates the limiting maximum core mass for dwarfs $M_c^{\rm max}$. The SPARC results here are presented in two groups. Green circles correspond to galaxies with total masses $M_{\rm tot} = M_s < 10^{14} M_\odot$, being M_s the natural total mass of the obtained mass distribution. Light blue crosses correspond to total masses given by $M_{\rm tot} = M_b \ll M_s$, being M_b the mass at the boundary radius where the density falls to the critical density of the Local Group ($10^{-5} M_\odot/\mathrm{pc}^3$). Due to inappropriate halo information in the second group (light blue crosses) it is not possible to constrain the cutoff parameter W_0 what results in extended (isothermal) mass distributions with total masses $M_s \gg 10^{14} M_\odot$ which have to be truncated.

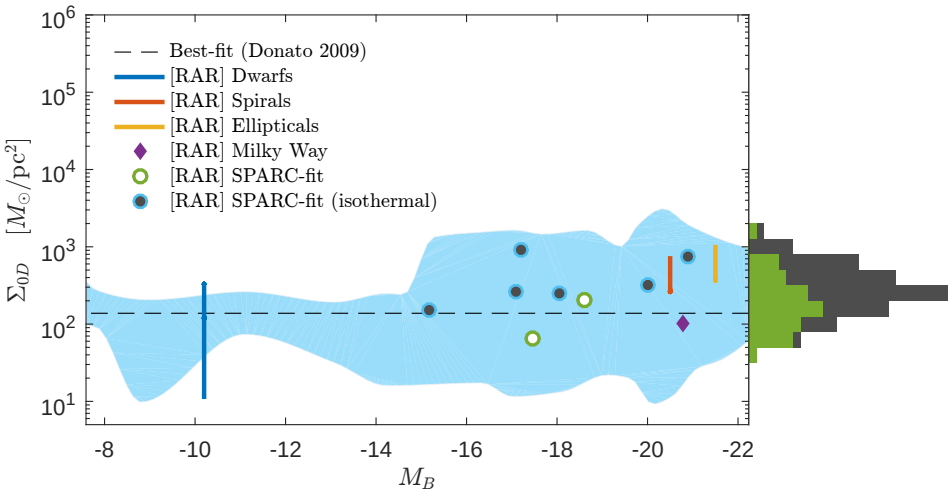

Figure 4.21. RAR Prediction of the DM surface density for disk galaxies of valid SPARC samples. The absolute magnitude was taken from the Carnegie-Irvine Galaxy Survey, providing eight overlapping galaxies. The blue region indicates the delimited area by the 3σ error bars of all the data points used in Donato et al. (2009). The shown candidates include isothermal (blue outlined points) and non-isothermal (green circles) solutions, which are very well in agreement with the DM surface density observations. For comparison, the results are amended by RAR predictions for typical dwarfs, spirals and ellipticals (see section 4.2). Although absolute magnitude information is incomplete, the predicted DM surface densities of the entire valid galaxy sample is within the range of the 3σ area as well. These full results are presented in a histogram (grey bars) with comparison to a subsample, including non-isothermal solutions (green bars). The majority of the latter sample is closer the the observationally inferred mean value of about $140 M_\odot$ pc^{-2}.

DM surface density relation

Finally, we turn to the constant surface density (Donato et al., 2009)

$$\Sigma_{0D} = \rho_{0D} r_0 \approx 140^{+80}_{-50}\, M_\odot/\mathrm{pc}^2 \tag{4.17}$$

This value is valid for about 14 orders of magnitude in absolute magnitude (M_B) where ρ_{0D} and r_0 are the *central* dark matter halo density at the one-halo-scale-length of the Burkert profile.

Note that the *center* in the Burkert model corresponds to the plateau in the RAR model, $\rho_{0D} \approx \rho_{\mathrm{pl}}$ where ρ_{pl} is defined at the first minima in the rotation curve. The relation between both one-halo scale lengths is $r_0 \approx 2/3\, r_h$. We thus calculate the product $2/3\, \rho_{\mathrm{pl}}\, r_h$ for each galaxy.

The absolute magnitude was taken from the Carnegie-Irvine Galaxy Survey, providing eight overlapping galaxies with the SPARC sample. These candidates are very well in agreement with the DM surface density observations, see fig. 4.21.

The central density results of the full galaxy sample (appropriate and inappropriate) is given as a histogram. Thus, the RAR model predicts for all valid candidates *central* surface densities within the 3σ uncertainty. It is worth to note that the spread is relatively high, although not in conflict with observables. This phenomena may be explained by the diversity, similar to the spread in the M_c-M_{tot} relation.

Considering only galaxies with appropriate halo information (green bars), we find that the majority is closer to the mean value of about $140 M_\odot$ pc^{-2}, compared to the full sample (dark gray bars).

4.3.3 Summary

We faced the intricate relation between the mass distribution of dark and baryonic matter for disk galaxies from a different perspective compared to the cosmological ΛCDM principles and MOND. Thus, we considered dark matter as a self-gravitating system composed of elementary fermions while the baryonic component was provided from the SPARC data base.

Acceleration correlation

The radial acceleration correlation (McGaugh, Lelli, and Schombert, 2016b) as well as the equivalent mass discrepancy acceleration relation (McGaugh, 2004; McGaugh, 2014) show clearly a link between the acceleration due to the baryonic matter and the acceleration due to dark matter. In the a_{bar}-a_{DM} projection we found a linear relation between those two acceleration components rather than the proposed empirical fit based on the a_{bar}-a_{tot} projection.

That RAR model is able to reproduce those acceleration correlations together with the their scatter. For comparison, we considered also two more DM models (NFW, DC14) which reproduce the empirical correlation qualitatively as well. In summary, we conclude that all considered DM models reproduce the correlation based on the average of many spiral galaxies of different Hubble type.

Nevertheless, focusing on individual galaxies we may extract more detailed information. Thus, we noticed fundamental deviations compared to the proposed radial acceleration correlation by McGaugh. Based on the representative NGC0055 it shows that many galaxies (of the SPARC database) don't follow strictly the given empirical formula. Despite an offset, NGC055 has a similar behavior to eq. (4.13) in the dark matter dominated region but deviates strongly in the transition into the baryonic matter dominated region with an abrupt decrease of the DM acceleration.

The deviations become more clear in the analysis of the much better resolved Milky Way. Here, we found a linear proportionality in the very low acceleration regime ($\lesssim 10^{-12}\mathrm{m/s^2}$) in contrast to the empirical radial acceleration correlation. This deviation is due to the necessary strong cutoff.

Indeed, compared to the analysis of SPARC galaxies we know that spirals have very different halos regarding the cutoff. Those different cutoffs correspond to different slops of the radial acceleration correlation in the dark matter dominated regime. According to the RAR model we were able to identify several SPARC galaxies with a strong cutoff similar to Milky Way. But those galaxies (among many other) have a lack of information in the very outer halo (e.g. due to faint stars) what keeps the behavior in the very low acceleration regime ($\lesssim 10^{-12}\mathrm{m/s^2}$) in secret.

Moving to the high acceleration regime, representing the baryonic matter dominated region, the prototype NGC0055 demonstrates clearly that the inner halo structure is important when the relevance of a cuspy or cored halo is considered. Thus, the new perspective of the radial acceleration correlation ($a_{\mathrm{bar}} - a_{\mathrm{DM}}$) is preferred compared to the original representation ($a_{\mathrm{bar}} - a_{\mathrm{obs}}$) which obscures the inner halo relation.

Finally, in the very high acceleration regime we predict an increase of the centripetal acceleration due to the quantum core in the galactic center, a fundamental feature of the RAR model. This is in clear contrast to the empirical correlation and the NFW model.

In summary, the unveiled deviations in the low and high acceleration regimes are a satisfying explanation for the large scatter in the radial acceleration correlation. The conclusion of the analysis is that individual galaxies show a more complicated behavior than the empirical radial acceleration correlation suggest and that the RAR model is able to explain this phenomena based on fundamental physical principles.

Goodness of fit

The more profound understanding of the radial acceleration correlation is backed by a goodness of model analysis for 124 filtered galaxies of the SPARC data covering different Hubble types. We found that RAR and DC14 are similarly good while NFW is clearly disfavored here. This picture becomes even more clear when only magellanic galaxies are considered. On the contrary, non-megallanic galaxies are equally bad fitted with all models. This result implies a link between dark matter and the morphological type. Clearly, the type of the inner halo (cored or cuspy) may play an important role.

Spacial attention has to be given to galaxies with an oscillation in the rotation curve. All considered models (RAR as well as NFW and DC14) fail in fitting those rotation curves what appears mostly for non-magellanic types. This is not surprising, since all models have only one maxima bump by design. The oscillations of the RAR model with weak cutoff (or no cutoff in the limit) are too long ranged for a convenient explanation.

Universal relations

Regarding dark-to-dark relations, we enriched the M_c-$M_{\rm tot}$ relation with prediction for disk galaxies of the SPARC data base. The majority of the galaxies has a core mass between $10^4 M_\odot$ and few $10^6 M_\odot$ while the total masses span a range from $10^9 M_\odot$ to few $10^{12} M_\odot$. An important outcome of the results, compared to the $M_{\rm BH}$-$M_{\rm tot}$ relation (Ferrarese, 2002), is a break in the relation at about $10^{11} M_\odot$, the bottom edge of the observable *Ferrarese window*. Of great interest would be therefore the extension of the relation down to dwarf galaxies what is under current investigation in our group.

We want to emphasize that the thinking of a narrow M_c-$M_{\rm tot}$ relation as suggested by Ferrarese (2002) might be misleading according the the predictability analysis of the RAR model, see also Argüelles et al. (2018). In particular, the model predicts a much higher diversity in the M_c-$M_{\rm tot}$ population what is supported by the SPARC results. On the other hand, the diversity is due to some uncertainty in the parameter space (e.g. the cutoff parameter W_0). To narrow those uncertainties better observations in the inner halo are needed.

The *constancy* of the surface density (Donato et al., 2009) for SPARC galaxies is also given within the RAR context. From the Carnegie-Irvine Galaxy Survey we have extracted the absolute magnitude for eight overlapping galaxies. The surface density predictions of that sub-sample are very well in agreement with observations. It is important to emphasize that the predicted surface density range, covering the full sample, remains within the 3σ uncertainty.

4.4 Conclusion

It is now clear from our results that gravitationally bounded systems based on fermionic phase-space distributions, including escape velocity effects and central degeneracy, can explain the DM content in the Galaxy. A key point of the present RAR model with cutoff is the ability to predict Galactic DM halo configurations and simultaneously provide a satisfying explanation of the supermassive dark object in the Galactic center without spoiling the known baryonic (bulge and disk) components, which dominate at intermediate scales. Thus, the regular and continuous distribution of keV fermions can be a natural alternative to the black hole scenario in SgrA*.

This highly compelling result is bolstered by the analysis of typical dwarf to elliptical galaxies and a filtered sample of disk galaxies from the SPARC data base.

Following the template of Randy Olsen (in his book *Housten, we have a narative*), the results of the thesis may be summarized as:

> Nothing in galactic structures makes sense except in the light of fermionic dark matter including relativistic and evaporation effects.

Further details are summarized in next.

Dark matter modeling

From the Milky Way analysis in section 4.1 we obtained a particle mass in the range $mc^2 \sim 48 - 345\,\mathrm{keV}$. This window is constraint through observables on the entire radial extent, ranging from the galactic center, to the halo, to the periphery. The lower bound is imposed by the dynamics of the stellar S-cluster (e.g. S2), while the upper bound corresponds to the last stable configuration before reaching the critical mass for gravitational collapse.

As an interesting example we have discussed in section 4.2 the solutions for $mc^2 = 48\,\mathrm{keV}$, where the model is able to explain the DM halos from typical dSph to normal elliptical galaxies. At the same time the solutions predict the presence of massive compact dark objects from $\sim 10^3 M_\odot$ up to $\sim 10^8 M_\odot$ at the center of the hosting galaxy. Whether or not such full window of compact dark-object masses at the centres of galaxies occur in Nature is a theme of future observational works. In particular, of interest is the case of the smallest (i.e. faintest) dwarf galaxies which don't develop critical core masses.

Nevertheless, the analysis should cover all observed plethora of galactic dark halos with corresponding dark compact central objects. In particular, galaxies with similar halo properties (i.e. total halo mass and radius) can harbor different dark quantum core masses, spanning up to about 3 orders of magnitude. This peculiar feature of the RAR model is an important result, considering that very similar Seyfert-like galaxies have been observed to shown values of M_c that can differ in nearly one order in magnitude ($M_c \sim 10^7 M_\odot$ to $M_c \sim 8 \times 10^7 M_\odot$, see Greene et al., 2010).

Dark and baryonic matter relations

Based on the analysis of a filtered SPARC sample, the RAR model is able to reproduce the radial the acceleration correlation as well as the equivalent MDAR. Qualitatively, the results appear as good as results from the DC14 or NFW model. But a detailed look at individual galaxies shows a more complicated behavior than the empirical correlation suggest. Of special interest, therefore, are deviations on the transition to the baryonic dominated region, which allow to discriminate different dark matter models. Thus, taking the effects in the inner halo more serious shows that the RAR and DC14 models produce comparable fits while NFW clearly has obvious problems.

This profound understanding is backed by a goodness of model analysis, covering the whole considered galaxy sample.

Comparing the RAR model with DC14 yields another interesting hint regarding baryonic-to-dark relations. We may consider DC14, a baryonic feedback motivated model, as an extension of the NFW model. Thus, comparing DC14 and NFW implies that baryonic feedback mechanism is important in galaxy formation. But our RAR model fits the SPARC sample as good as DC14 although it doesn't consider any baryonic matter contribution nor any baryonic feedback mechanism. This leads to the speculation that baryonic feedback might be not so important for disk galaxies. The more probable scenario is that the RAR model enhanced with baryonic feedback mechanism would improve galaxy fitting significantly.

On the other hand, the RAR model is now confronted with the question why dark and baryonic matter distributions arrange in the way they obviously do. That relation seems to be encoded in the acceleration relation, its scatter and, in particular, the *scatter shower* in the low acceleration regime of the dark matter component. The change of perspective from $a_{\rm bar}$-$a_{\rm obs}$ (original) to $a_{\rm bar}$-$a_{\rm DM}$ unveils the acceleration correlation on a wider spatial range and is therefore a good step forward. Since the RAR model considers only dark matter without any baryonic contribution nor feedback this fundamental question has to be answered in a future work.

Dark matter only relations (within the RAR model)

Focusing on the dark-to-dark relations, the RAR model can naturally explain universal relations involving dark components only. This emphasizes the importance of this kind of first principles approaches including quantum statistics, self-gravity and thermodynamics.

The application to different galaxy types (typical spirals and ellipticals) showed that a particle mass of $48\,\mathrm{keV}$ may explain the relation between the masses of the galactic core and the DM halo (Bogdán and Goulding, 2015; Ferrarese, 2002). This observational link has been confirmed only for the more massive galaxies ($\gtrsim 10^{11}\,\mathrm{M}_\odot$), harboring a supermassive core ($\gtrsim 10^{6}\,\mathrm{M}_\odot$). On theoretical ground the SPARC analysis extends the link to lower core masses ($\gtrsim 10^{4}\,\mathrm{M}_\odot$) as well as lower DM halo masses ($\gtrsim 10^{9}\,\mathrm{M}_\odot$). Interestingly, the results predict a break in the power law relation compared to the more massive galaxies, see fig. 4.20 and section 4.3.2. The analysis of typical dwarf galaxies further extends to even less massive DM halos ($\gtrsim 10^{7}\,\mathrm{M}_\odot$) and cores ($\gtrsim 10^{3}\,\mathrm{M}_\odot$).

Moving to the larger elliptical galaxies, it is interesting to note that the maximum quantum core mass $M_c^{cr} \approx 2.2 \times 10^8 M_\odot$, predicted by the RAR model (for $mc^2 = 48\,\mathrm{keV}$), is in striking consistency with the uppermost (sample-representative) central mass $M_{\rm BH}$ obtained in Bogdán and Goulding (2015). The latter result was obtained from an X-ray imaging analysis of more than 3000 isolated and without AGN activity elliptical galaxies. These results, when viewed through the theoretical M_c-$M_{\rm tot}$ relation, give support to the idea that normal elliptical galaxies may harbor dark central objects (not yet BHs) without showing AGN-like activity. Larger SMBHs masses, on the other hand, do show AGN properties and reach the upper end of the M_c-$M_{\rm tot}$ relation.

On top of the successful applications the same results for different galaxies, from dwarfs to ellipticals including the Milky Way galaxy and galaxies from the SPARC data base, are in agreement with the constancy of the *central* surface density (Donato et al., 2009). We recall that the central region of that relation corresponds to the plateau in the RAR model.

General comments on cosmological dark matter (within the RAR model)

An important aspect of the obtained particle mass range (48 to $345\,\mathrm{keV}$) is that it produces basically the same behavior in the power spectrum (down to Mpc scales) from that of standard ΛCDM cosmologies. Therefore, such particle masses, corresponding to the so-called *warm* dark matter, provide the expected large-scale structure (see Boyarsky, Ruchayskiy, and Shaposhnikov, 2009, for details). And as in standard ΛWDM cosmologies it is not *too warm* (i.e. our masses are larger than $mc^2 \sim 1 - 3\,\mathrm{keV}$) to enter in tension with current Ly-α forest constraints (Boyarsky et al., 2009b) and the number of Milky Way satellites (Tollerud et al., 2008).

The introduced fermionic phase-space distribution with a cutoff produces here an extended plateau in the DM density profile on halo scales in a way that they resemble Burkert or cored Einasto profiles (Ruffini, Argüelles, and Rueda, 2015). Our model, therefore, naturally provides cored inner DM halos without developing undesired cuspy density trends on such scales as the ones found in N-body simulations (Navarro, Frenk, and White, 1997). Such a marked difference between both kind of density profiles, cored (RAR) and cuspy (NFW), arises due to the physics involved in the two different approaches. This in turn may provide an important insight to one of the main open problems in standard ΛCDM cosmology, i.e. the so-called *core-cusp problem* (de Blok, 2010).

Our results offer significant support for our keV-scale fermions as DM, which may well co-exist harmonically with other DM species in the universe. These aspects will have to interplay with the physics of elementary particles regarding the nature of those fermions (Majorana neutrinos, supersymmetric particles, sterile neutrinos, etc.) as well as with the possible detection through decaying processes involving weak interactions. Indeed, DM particle masses within the relatively narrow window obtained here ($mc^2 \sim 48 - 345\,\mathrm{keV}$) have also arisen within different microscopic models based on extensions of the standard model. Such models are consistent with all cosmological, large scale structure and X-ray constraints as the ones considered in Boyarsky et al. (2009b) and Patwardhan et al. (2015).

Chapter 5

Future perspective

Motivated by the discovery of new configurations within the RAR model with promising applications beyond the classical candidates (e.g. spirals), the main future goal is a full prediction map which covers all galactic structures in more detail. A first milestone was done in this thesis through the investigation of different galaxy types from dwarfs to ellipticals, including the Milky Way galaxy as well as filtered galaxies from the SPARC dataset.

This objective will need to face individual mass distribution with a re-interpretation of existing observables and concepts (e.g. SMBH). For instance, ultra-compact dwarfs, intermediate massive compact objects and galaxy clusters are clearly interesting candidates to go beyond the scope of the present thesis. Additionally, it is convenient to include also baryonic matter as well as the galactic environment (e.g. background density) to develop a more realistic framework.

Thus, in next I will briefly describe a selected list of further possible application of the RAR model with cutoff as well as convenient model modifications or enhancements to face other astrophysical problems, being a subject of future research.

Ultra-compact dwarfs

The rich varieties of the semi-degenerate configurations, obtained by the RAR model with cutoff, have been only scarcely compared with astrophysical objects. Especially, the importance of the critical cutoff regime, necessary to explain the Milky Way and other galaxy types, is still poorly understood in compact galaxies.

The analysis with focus on dwarfs (e.g. $M_{\rm tot} \sim 10^7\,{\rm M}_\odot$) showed a new family with highly cuspy halos beyond the typical semi-degenerate configuration with cored halos. To recall, typical configurations, which imply a sufficient high central cutoff parameter, are described by mainly three regimes: a central quantum core with a steep decay followed by a long ranged plateau and a diluted Boltzmannian tail with cutoff. The central cutoff parameter (in combination with the other parameters) rules how strong the tail is cut. The smaller the value the more it is cut. The interesting phenomenology appears when the cutoff starts to affect also the plateau. In that case the plateau is shortened and lowered but the halo shows a universal shape. This trend continues until the plateau is completely evaporated (e.g. saddle-point-criteria). The remaining new configurations consist only of a quantum core followed by a power law (instead of a steep decay). This power law may be interpreted as a halo but with a different shape compared to the typical semi-degenerate configuration.

It is therefore convenient to focus on exactly those new configurations. Thus, results of the RAR model predict that dwarfs develop maximal core masses well below the critical core mass as is the case for spirals and ellipticals. Such galactic nuclei correspond to solutions with highly cuspy halos and, consequently, contribute with a high fraction ($\sim 10\%$) to the total DM mass. It is therefore well motivated

that the RAR model with a strong cutoff may explain ultra-compact dwarfs where a similar configuration was observed (Ahn et al., 2017).

Massive compact objects

Comparing the entire window of the M_c-$M_{\rm tot}$ relation, see e.g. fig. 4.20, shows that spirals and ellipticals have similar properties while dwarfs galaxies develop distinct differences. Thus, modeling the dark matter of dwarfs (and small spirals) within the RAR model provides the possibility to harbor core masses at intermediate scales (10^2 $\mathrm{M}_\odot$ to 10^6 $\mathrm{M}_\odot$). Such objects are often associated with intermediate massive black holes. The origin of compact objects within this peculiar mass range is still an open issue.

It is therefore fascinating that the fermionic dark matter model sets the base for intermediate as well as for supermassive compact objects. More important, the RAR model tells that intermediate mass compact objects are mostly limited to less massive galaxies (e.g. dwarfs) while more massive galaxies (e.g. ellipticals) are necessary limited to supermassive compact objects. Thus, fermionic dark matter may provide a natural origin of compact objects on both mass scale, intermediate and supermassive, and may solve the question where the suspected, but currently missing, intermediate massive black holes are populated.

It is very well observed and accepted that ellipticals harbor supermassive compact objects (Padovani et al., 2017), while the situation for dwarfs is still open. For instance, the observational inference of the mass of the central dark region in dwarfs via the dispersion velocity is unclear (see, e.g., Kormendy and Bender, 2011; Valluri et al., 2005, and references therein). However, Valluri et al. (2005) attempted to give an estimate of the dark central object mass in dwarf galaxies obtaining $M_{\rm BH} \sim 10^3$–10^4 $M_\odot$, being in agreement with the values of M_c for the dSphs as analyzed section 4.2.

Recent investigations suggest ultra-compact dwarfs as mentioned above, but also globular clusters and gas clouds may harbor such objects at the intermediate mass scale. A special type of star clusters close to the galactic centre, the nuclear star clusters, seems to be the progenitor of globular clusters but also of massive dark objects in galactic centres.

Active galactic nuclei

The investigated galaxy parameter window might explain why there are low mass active galaxies containing less massive central objects, i.e with $M_c \sim 10^8 M_\odot$, with respect to the more massive active galactic nuclei of $M_{\rm BH} \sim 10^{9-10} M_\odot$ as in the largest elliptical galaxies observed. Though, the majority of the supermassive dark central objects are comprised within $M_c \sim 10^8 M_\odot$ (Gültekin et al., 2009). The more massive objects are most likely SMBHs associated with active galaxies and are characterized by a clear X-ray and radio emissions as well as jets. Such a SMBH may be explained by starting from a BH seed of a critical mass M_c^{cr} formed out of the collapse of critical quantum DM cores. After its formation the BH seed might start a baryonic and/or dark matter accretion process from their massive galactic environment ($M_g \sim 10^{12}$ $M_\odot$). An accretion of $\sim 1\%$ of the (inner) baryonic mass of the galaxy onto the M_c^{cr} core mass, obtained here, would be enough to explain the formation of the largest ($M_{\rm BH} \sim 10^{9-10}$ $M_\odot$) SMBH masses. But, clearly, for a precise answer the accretion onto compact quantum cores needs to be studied in more detail.

To rule all scales — a unified theory

It is worth to emphasize that the introduced dark matter model lead to a successful explanation and reproduction of different astrophysical phenomena. Nevertheless, due to the limitation on galactic scales (e.g. dwarfs to ellipticals) only a limited range of the parameter space was seriously investigated.

Therefore, I propose to make use of the full potential of the RAR model: a full predictability analysis and summary of the results in (at least) one full prediction map including, for instance, the core and the total dark matter mass (e.g. M_c-$M_{\rm tot}$). It is expected that this analysis will cover galactic structures below dwarfs scales as well as scales above elliptical galaxies, targeting for example clusters of galaxies in the latter case. The impact can already be estimated in fig. 4.20 by an extrapolation of the behavior for lower as well as higher masses.

This investigation implies a careful analysis of one (or two) parameter families where the remaining parameters are fixed. Although a particle mass of about $50\,\mathrm{keV}$ is a promising candidate, it may be more convenient to consider dimensionless solutions, equivalent to particle mass independent. The choice of the remaining configuration parameters is not limited to the original parameters (β_0, θ_0, W_0). Instead, it is convenient also to consider scale invariant structural observables (e.g. defined by extrema) at the core, plateau, halo or surface.

It is expected that such a full prediction map will then summarize the rich diversity of mass distributions predicted by the RAR model. Of course, it has to be filled and compared with observables (e.g. from existing literature) to demonstrate their applicability with the aim to check, if the model covers all observed galactic structural phenomena. This would allow a deeper understanding of the formation of galactic structures within the framework of fermionic dark matter. For instance, a fundamental question is the particle mass of dark matter that has great impact on astro-particle physics (e.g. sterile neutrino) as well as on cosmology (e.g WDM).

Further, focusing on the very different configurations and their application to real observations would expand the knowledge of astrophysical and astronomical phenomena. This would clearly push the fermionic dark matter model (or slightly variations of it, see below) to a unified theory which will probably cover different fields, ranging from astro-particle physics, to compact objects and galactic structures and finally to cosmology.

Apart the promising opportunity to cover different field, this proposal focuses mainly on galactic structures in combination with central compact objects as a starting point. Not explicitly intended but future results may have also an impact on gravitational lensing applications and the recently discovered gravitational waves as well.

Galaxy formation

In order to attempt to answer the question why the nature constrains the RAR model free parameters to the specific values, it would need the extension of the present analysis into a broader theoretical context such as the formation and evolution of galaxies. Such an insight may be likely gained through a detailed study of a dynamical theory of collisionless relaxation, including a full statistical/thermodynamical analysis of the condition under which (quasi) DM halo relaxation is reached. Considerations based on maximization entropy approaches for given total mass (with corresponding running of the free model parameters), as the one analyzed in similar self-gravitating systems in Chavanis, Lemou, and Méhats (2015) (and references therein), could help in this direction.

Environment contribution

Motivated by the preliminarily investigation in this thesis it is promising to focus on the total mass (or radius) of the total dark matter distribution and include also the environment into account. The former (e.g. surface) is well characterized through the value of the cutoff parameter at the plateau implying a maximum mass and radius for the dark matter halo. For the latter (environment) it is convenient to focus on the density profiles where the density at the plateau plays an important role when the background density is taken into account. Especially, when the plateau density is comparable to the density of the underlying environment where galactic structures are embedded. Note that such background densities have been neglected in this thesis, implying that plateau densities are well above. This, a more realistic model needs to consider also the environment. A promising way to include this component is to describe the density through two components,

$$\rho(r) = \rho_{\rm bg} + \rho_{\rm dm}(r) \tag{5.1}$$

where $\rho_{\rm bg}$ is a (constant) background and $\rho_{\rm dm}(r)$ describes the fermionic dark matter (e.g. as introduced in chapter 2).

Based on this environment ansatz we may set the critical density of the universe as an absolute lower limit, e.g. $\rho_{\rm bg} = \rho_{\rm cr}$. Indeed, for the Local Group it is common to expect a value two orders of magnitude higher (a factor of 200 is often chosen). Further, it is well known that small substructures are embedded in larger structures what implies an environment with increased background density. Thus, this approach does not only allow prediction of galactic structures beyond the classical one (e.g. spirals), it also may give predictions for specific galactic structures based on the environment what is believed to be a key component in hierarchical growing.

Information filter

I remind to interpret the SPARC results, corresponding to isothermal galaxies (e.g. $M_{\rm tot} = M_b \ll M_s$), with caution. Compared to the the remaining galaxies they have either a lack of information or short ranged oscillations in the outer halo what prohibits to constrain the cutoff parameter with certainty. The lack of information may be simply solved with future surveys while the oscillations, what may be regarded as an abundance of information, requires further investigations. A truncation (information filter) shortly after the first maxima in the rotation curve would certainly allow to compare with other galaxies, which provide only one maxima bump at best. We expect that such analysis will unveil more profound connections between the dark matter and the morphological type.

Multi-component model

Although, the very different oscillations, as found in galaxies of the SPARC dataset, may be due to ongoing relaxation processes it might be worth to consider also multi-component halo models. It is probable that the RAR model enhanced with baryonic contributions and/or additional DM components (e.g. from merging) will help to understand galactic structures. However, it is important to keep the additions as small as possible in order to maintain the model simple enough and, more important, not to loose the predictability through an over-abundance of parameters.

Dynamical classification

Kalinova et al. (2017) introduced recently a new dynamical classification of galaxies based on circular velocity curves. In analogy, a classification based on inferred

dark matter rotation curves would be an interesting alternative to the traditional morphological classification (e.g. Hubble), which seems to be linked to dark matter profiles. Further, it is probable that such a dark classification, including dark compact objects if possible, will reveal new set of galaxy types. Though, it is hard to say if such an galaxy set will give more insight about galactic structures compared to classifications based on baryonic matter.

Appendix A

Other important models

A.1 Phenomenological dark matter

In this thesis the RAR model is compared with other more dark matter models which are described in next. Note that NFW and DC14 use the folowing scaling factors: $R_{\rm N}$, $\rho_{\rm N}$, $\sigma_{\rm N}^2 = GM_{\rm N}/R_{\rm N}$ and $M_{\rm N} = 4\pi\rho_{\rm N}R_{\rm N}^3$ for length, density, velocity and mass.

NFW

The NFW model is simply given by (Navarro, Frenk, and White, 1996)

$$\frac{\rho(r)}{\rho_{\rm N}} = \left[\frac{r}{R_{\rm N}}\right]^{-1}\left[1+\frac{r}{R_{\rm N}}\right]^{-2} \tag{A.1}$$

with the circular velocity

$$\frac{v^2(r)}{\sigma_{\rm N}^2} = \frac{\ln(1+r/R_{\rm N})}{r/R_{\rm N}} - \frac{1}{1+r/R_{\rm N}} \tag{A.2}$$

DC14

The DC14 model is given by a slightly modified Hernquist model which includes the influence of galaxy formation based on more profound baryonic feedback mechanism (Cintio et al., 2014; Hernquist, 1990; Katz et al., 2016)

$$\frac{\rho(r)}{\rho_{\rm N}} = \left[\frac{r}{R_{\rm N}}\right]^{-\gamma}\left[1+\left[\frac{r}{R_{\rm N}}\right]^{\alpha}\right]^{-\frac{\beta-\gamma}{\alpha}} \tag{A.3}$$

The three parameters (α, β, γ) are related through the stellar-to-dark matter ratio encoded via $X = \log_{10}(M^*/M_{\rm halo})$,

$$\alpha = 2.94 - \log_{10}\left[(10^{X+2.33})^{-1.08} + (10^{X+2.33})^{2.29}\right] \tag{A.4}$$

$$\beta = 4.23 + 1.34X + 0.26X^2 \tag{A.5}$$

$$\gamma = -0.06 - \log_{10}\left[(10^{X+2.56})^{-0.68} + 10^{X+2.56}\right] \tag{A.6}$$

The velocity is described by a hyper geometric function,

$$\frac{v^2(r)}{\sigma_{\rm N}^2} = \frac{1}{3-\gamma}\left[\frac{r}{R_{\rm N}}\right]^{3-\gamma} {}_2F_1(p_1, p_2;\, q_1;\, -[r/R_{\rm N}]^{\alpha}) \tag{A.7}$$

with

$$\begin{aligned} p_1 &= (3-\gamma)/\alpha \\ p_2 &= (\beta-\gamma)/\alpha \\ q_1 &= 1+(3-\gamma)/\alpha \end{aligned}$$

A.2 Exponential Sphere

The exponential sphere model is defined through the density

$$\frac{\rho(r)}{\rho_b} = \mathrm{e}^{-r/R_b} \tag{A.8}$$

with a central density ρ_b and a length scale R_b. The mass is then given by $M(r) = \int_0^r 4\pi r^2 \rho(r)\,\mathrm{d}r$ and the circular velocity becomes

$$\frac{v^2(r)}{\sigma_b^2} = \frac{M(r)}{M_b}\frac{R_b}{r} \tag{A.9}$$

The scale factors are defined by $M_b = 4\pi\rho_b R_b^3$ and $\sigma_b^2 = GM_b/R_b$.

A.3 Exponential Disk

The exponential disk model is defined through the surface density, which follows an exponential law,

$$\frac{\Sigma(r)}{\Sigma_d} = \mathrm{e}^{-r/R_d} \tag{A.10}$$

with the parameters Σ_d and R_d. The mass is then given by $M(r) = \int_0^r 2\pi r\Sigma(r)\,\mathrm{d}r$. Since the dynamics for an axial symmetric mass distribution differ from a spherical symmetric mass distribution it is necessary to use the circular velocity (on the equatorial plane) given by

$$\frac{v^2(r)}{\sigma_d^2} = 2y^2\left[I_0(y)K_0(y) - I_1(y)K_1(y)\right] \tag{A.11}$$

with the substitution $y = r/(2R_d)$ and the modified Bessel functions $I_n(x)$ and $K_n(x)$ (Binney and Tremaine, 2008). The scale factors are defined by $M_d = 2\pi\Sigma_d R_d^2$ and $\sigma_d^2 = GM_d/R_d$.

Abbreviations

DM	Dark Matter
SM	Standard Model of Particle Physics
SUSY	Supersymmetric Standard Model
FRW	Friedman-Robertson-Walker
TOV	Tolman-Oppenheimer-Volkoff
OV	Oppenheimer-Volkoff
ISCO	Innermost Stable Circular Orbit

Dark Matter candidates

MACHO	Massive Compact Halo Object
WIMP	Weakly Interacting Massive Particle
FDM	Fermionic Dark Matter

Cosmological Dark Matter schemes

HDM	Hot Dark Matter
WDM	Warm Dark Matter
CDM	Cold Dark Matter
ΛCDM	Λ Cold Dark Matter
ΛWDM	Λ Warm Dark Matter
SIDM	Self-Interacting Dark Matter

Dark Matter models

NFW	Navarro-Frenk-White
DC14	A mass-dependent density profile for dark matter halos including the influence of galaxy formation (Di Cintio et al., 2014)
RAR	Ruffini-Argüelles-Rueda
IS	Isothermal Sphere

Modified Gravity

MOND	Modified Newtonian Dynamics
AQUAL	Aquadratic Lagrangian theory
RAQUAL	Relativistic Aquadratic Lagrangian theory
TeVeS	Tensor-Vector-Scalar gravity

Gravitationally bound systems

S	spiral galaxy
SB	barred spiral galaxy
S0	lenticular galaxy
E	elliptical galaxy
Irr	irregular galaxy

Compact objects

BH	Black Hole
SMBH	Supermasive Black Hole
IMBH	Intermediate Massive Black Hole

Astronomical Phenomena

SgrA*	Sagittarius A*
AGN	Active Galactic Nuclei
CMB	Cosmic Microwave Background

Observation instruments

HST	Hubble Space Telescope
SST	Spitzer Space Telescope
EHT	Event Horizon Telescope

Surveys

WMAP	Wilkinson Microwave Anisotropy Probe
THINGS	The HI Nearby Galaxy Survey
SPARC	Spitzer Photometry & Accurate Rotation Curves

Symbols

$\nu(r)$	metric potential (00 component)
$\lambda(r)$	metric potential (11 component)
$\rho(r)$	density
$P(r)$	pressure
$M(r)$	enclosed mass (within the radius r)
$\sigma(r)$	velocity dispersion
$\varsigma(r)$	effective velocity dispersion
$\varphi(r)$	compactness
$v(r)$	proper circular velocity
$v(r)$	circular velocity (classical)
$f(r, \epsilon)$	phase-space distribution function
$\beta(r)$	temperature variable
$T(r)$	temperature
$\alpha(r)$	chemical potential
$\mu(r)$	chemical potential (rest-mass subtracted)
$\varepsilon(r)$	escape/cutoff energy
$E_\infty(r)$	kinetic particle escape energy
$\theta(r)$	degeneracy variable
$W(r)$	cutoff variable
ϵ	particle energy
m	particle mass
g	particle degeneracy
$\hbar$	Planck's constant
G	gravitational constant
c	speed of light
k_B	Boltzmann constant

Bibliography

Adhikari, R. et al. (2017). "A White Paper on keV sterile neutrino Dark Matter". In: *J. Cosmology Astropart. Phys.* 1, 025, p. 025. DOI: 10.1088/1475-7516/2017/01/025. arXiv: 1602.04816 [hep-ph].

Ahn, C. P. et al. (2017). "Detection of Supermassive Black Holes in Two Virgo Ultra-compact Dwarf Galaxies". In: *ApJ* 839, 72, p. 72. DOI: 10.3847/1538-4357/aa6972. arXiv: 1703.09221.

Alcock, C. et al. (2000). "The MACHO Project: Microlensing Results from 5.7 Years of Large Magellanic Cloud Observations". In: *ApJ* 542, pp. 281–307. DOI: 10.1086/309512. eprint: astro-ph/0001272.

Alpher, R. A., H. Bethe, and G. Gamow (1948). "The Origin of Chemical Elements". In: *Physical Review* 73, pp. 803–804. DOI: 10.1103/PhysRev.73.803.

Angulo, R. E., O. Hahn, and T. Abel (2013). "The warm dark matter halo mass function below the cut-off scale". In: *MNRAS* 434, pp. 3337–3347. DOI: 10.1093/mnras/stt1246. arXiv: 1304.2406.

Argüelles, C. R. and R. Ruffini (2014). "Are the most super-massive dark compact objects harbored at the center of dark matter halos?" In: *International Journal of Modern Physics D* 23, 1442020, p. 1442020. DOI: 10.1142/S0218271814420206. arXiv: 1405.7505.

Argüelles, C. R., R. Ruffini, and B. M. O. Fraga (2014). "Critical configurations for a system of semidegenerate fermions". In: *Journal of Korean Physical Society* 65, pp. 809–813. DOI: 10.3938/jkps.65.809. arXiv: 1402.1329.

Argüelles, C. R. et al. (2014). "On the distribution of dark matter in galaxies: Quantum treatments". In: *Journal of Korean Physical Society* 65, pp. 801–804. DOI: 10.3938/jkps.65.801. arXiv: 1402.0700.

Argüelles, C. R. et al. (2016). "The role of self-interacting right-handed neutrinos in galactic structure". In: *J. Cosmology Astropart. Phys.* 4, 038, p. 038. DOI: 10.1088/1475-7516/2016/04/038. arXiv: 1502.00136.

Argüelles, C. R. et al. (2018). "Novel constraints on fermionic dark matter from galactic observables". In: *ArXiv e-prints*. arXiv: 1606.07040.

Asaka, T., S. Blanchet, and M. Shaposhnikov (2005). "The νMSM, dark matter and neutrino masses [rapid communication]". In: *Physics Letters B* 631, pp. 151–156. DOI: 10.1016/j.physletb.2005.09.070. eprint: hep-ph/0503065.

Baldeschi, M. R., G. B. Gelmini, and R. Ruffini (1983). "On massive fermions and bosons in galactic halos". In: *Physics Letters B* 122, pp. 221–224. DOI: 10.1016/0370-2693(83)90688-3.

Bekenstein, J. D. (2004). "Relativistic gravitation theory for the modified Newtonian dynamics paradigm". In: *Phys. Rev. D* 70.8, 083509, p. 083509. DOI: 10.1103/PhysRevD.70.083509. eprint: astro-ph/0403694.

Bekenstein, J. and M. Milgrom (1984). "Does the missing mass problem signal the breakdown of Newtonian gravity?" In: *ApJ* 286, pp. 7–14. DOI: 10.1086/162570.

Belokurov, V. et al. (2014). "Precession of the Sagittarius stream". In: *MNRAS* 437, pp. 116–131. DOI: 10.1093/mnras/stt1862. arXiv: 1301.7069 [astro-ph.GA].

Bertone, G. and D. Hooper (2016). "A History of Dark Matter". In: *ArXiv e-prints*. arXiv: 1605.04909.

Bethe, H. A. (1939). "Energy Production in Stars". In: *Physical Review* 55, pp. 434–456. DOI: 10.1103/PhysRev.55.434.

Bilic, N. et al. (2002). "The dynamics of stars near Sgr A* and dark matter at the center and in the halo of the galaxy". In: *Progress in Particle and Nuclear Physics* 48, pp. 291–300. DOI: 10.1016/S0146-6410(02)00136-9.

Binney, James and Scott Tremaine (2008). *Galactic Dynamics*. 2nd ed. Princeton University Press, p. 920.

Blumenthal, G. R. et al. (1984). "Formation of galaxies and large-scale structure with cold dark matter". In: *Nature* 311, pp. 517–525. DOI: 10.1038/311517a0.

Bode, P., J. P. Ostriker, and N. Turok (2001). "Halo Formation in Warm Dark Matter Models". In: *ApJ* 556, pp. 93–107. DOI: 10.1086/321541. eprint: astro-ph/0010389.

Bogdán, Á. and A. D. Goulding (2015). "Connecting Dark Matter Halos with the Galaxy Center and the Supermassive Black Hole". In: *ApJ* 800, 124, p. 124. DOI: 10.1088/0004-637X/800/2/124. arXiv: 1502.05043.

Bondi, H. (1964). "The Contraction of Gravitating Spheres". In: *Proceedings of the Royal Society of London Series A* 281, pp. 39–48. DOI: 10.1098/rspa.1964.0167.

Borriello, A. and P. Salucci (2001). "The dark matter distribution in disc galaxies". In: *MNRAS* 323, pp. 285–292. DOI: 10.1046/j.1365-8711.2001.04077.x. eprint: astro-ph/0001082.

Bosma, A. (1978). "The distribution and kinematics of neutral hydrogen in spiral galaxies of various morphological types". PhD thesis. PhD Thesis, Groningen Univ., (1978).

Boyarsky, A., O. Ruchayskiy, and M. Shaposhnikov (2009). "The Role of Sterile Neutrinos in Cosmology and Astrophysics". In: *Annual Review of Nuclear and Particle Science* 59, pp. 191–214. DOI: 10.1146/annurev.nucl.010909.083654. arXiv: 0901.0011 [hep-ph].

Boyarsky, A. et al. (2009a). "New evidence for dark matter". In: *ArXiv e-prints*. arXiv: 0911.1774 [astro-ph.CO].

Boyarsky, A. et al. (2009b). "Realistic Sterile Neutrino Dark Matter with KeV Mass does not Contradict Cosmological Bounds". In: *Physical Review Letters* 102.20, 201304, p. 201304. DOI: 10.1103/PhysRevLett.102.201304. arXiv: 0812.3256 [hep-ph].

Boylan-Kolchin, M., J. S. Bullock, and M. Kaplinghat (2011). "Too big to fail? The puzzling darkness of massive Milky Way subhaloes". In: *MNRAS* 415, pp. L40–L44. DOI: 10.1111/j.1745-3933.2011.01074.x. arXiv: 1103.0007 [astro-ph.CO].

— (2012). "The Milky Way's bright satellites as an apparent failure of ΛCDM". In: *MNRAS* 422, pp. 1203–1218. DOI: 10.1111/j.1365-2966.2012.20695.x. arXiv: 1111.2048 [astro-ph.CO].

Buchdahl, H. A. (1959). "General Relativistic Fluid Spheres". In: *Physical Review* 116, pp. 1027–1034. DOI: 10.1103/PhysRev.116.1027.

— (1966). "General Relativistic Fluid Spheres. II. General Inequalities for Regular Spheres". In: *ApJ* 146, p. 275. DOI: 10.1086/148875.

Bullock, J. S. and M. Boylan-Kolchin (2017). "Small-Scale Challenges to the ΛCDM Paradigm". In: *ARA&A* 55, pp. 343–387. DOI: 10.1146/annurev-astro-091916-055313. arXiv: 1707.04256.

Burbidge, E. M. et al. (1957). "Synthesis of the Elements in Stars". In: *Reviews of Modern Physics* 29, pp. 547–650. DOI: 10.1103/RevModPhys.29.547.

Burles, S. and D. Tytler (1998a). "The Deuterium Abundance toward Q1937-1009". In: *ApJ* 499, pp. 699–712. DOI: 10.1086/305667. eprint: astro-ph/9712108.

— (1998b). "The Deuterium Abundance toward QSO 1009+2956". In: *ApJ* 507, pp. 732–744. DOI: 10.1086/306341. eprint: astro-ph/9712109.

Cappellari, M. et al. (2011). "The ATLAS^{3D} project - I. A volume-limited sample of 260 nearby early-type galaxies: science goals and selection criteria". In: *MNRAS* 413, pp. 813–836. DOI: 10.1111/j.1365-2966.2010.18174.x. arXiv: 1012.1551.

Chae, K.-H., M. Bernardi, and R. K. Sheth (2017). "Radial Acceleration Relation by Dark Matter and Baryons in the Intermediate Acceleration Regime". In: *ArXiv e-prints*. arXiv: 1707.08280.

Chandrasekhar, S. (1939). *An introduction to the study of stellar structure*.

— (1942). *Principles of stellar dynamics*.

— (1967). *An introduction to the study of stellar structure*. Dover Publications, Inc.

Chavanis, P.-H. (2002). "Phase transitions in self-gravitating systems: Self-gravitating fermions and hard-sphere models". In: *Phys. Rev. E* 65.5, 056123, p. 056123. DOI: 10.1103/PhysRevE.65.056123. eprint: cond-mat/0109294.

— (2004). "Generalized thermodynamics and kinetic equations: Boltzmann, Landau, Kramers and Smoluchowski". In: *Physica A Statistical Mechanics and its Applications* 332, pp. 89–122. DOI: 10.1016/j.physa.2003.09.061. eprint: cond-mat/0304073.

— (2006). "Quasi-stationary states and incomplete violent relaxation in systems with long-range interactions". In: *Physica A Statistical Mechanics and its Applications* 365, pp. 102–107. DOI: 10.1016/j.physa.2006.01.006. eprint: cond-mat/0509726.

Chavanis, P.-H., M. Lemou, and F. Méhats (2015). "Models of dark matter halos based on statistical mechanics: The fermionic King model". In: *Phys. Rev. D* 92.12, 123527, p. 123527. DOI: 10.1103/PhysRevD.92.123527. arXiv: 1409.7840.

Chavanis, P.-H. and J. Sommeria (1998). "Degenerate equilibrium states of collisionless stellar systems". In: *MNRAS* 296, pp. 569–578. DOI: 10.1046/j.1365-8711.1998.01414.x.

Cintio, Arianna Di et al. (2014). "A mass-dependent density profile for dark matter haloes including the influence of galaxy formation". In: *Monthly Notices of the Royal Astronomical Society* 441.4, pp. 2986–2995. DOI: 10.1093/mnras/stu729. eprint: /oup/backfile/content_public/journal/mnras/441/4/10.1093/mnras/stu729/2/stu729.pdf. URL: +http://dx.doi.org/10.1093/mnras/stu729.

Clifton, T. et al. (2012). "Modified gravity and cosmology". In: *Phys. Rep.* 513, pp. 1–189. DOI: 10.1016/j.physrep.2012.01.001. arXiv: 1106.2476.

Clowe, D. et al. (2006). "A Direct Empirical Proof of the Existence of Dark Matter". In: *ApJ* 648, pp. L109–L113. DOI: 10.1086/508162. eprint: astro-ph/0608407.

Cowsik, R. and J. McClelland (1972). "An Upper Limit on the Neutrino Rest Mass". In: *Physical Review Letters* 29, pp. 669–670. DOI: 10.1103/PhysRevLett.29.669.

Davé, R. et al. (2001). "Halo Properties in Cosmological Simulations of Self-interacting Cold Dark Matter". In: *ApJ* 547, pp. 574–589. DOI: 10.1086/318417. eprint: astro-ph/0006218.

Davis, M. et al. (1982). "A survey of galaxy redshifts. II - The large scale space distribution". In: *ApJ* 253, pp. 423–445. DOI: 10.1086/159646.

Davis, M. et al. (1985). "The evolution of large-scale structure in a universe dominated by cold dark matter". In: *ApJ* 292, pp. 371–394. DOI: 10.1086/163168.

De Paolis, F. et al. (2001). "Astrophysical constraints on a possible neutrino ball at the Galactic Center". In: *A&A* 376, pp. 853–860. DOI: 10.1051/0004-6361:20010929. eprint: astro-ph/0107497.

Del Popolo, A. and M. Le Delliou (2017). "Small Scale Problems of the ΛCDM Model: A Short Review". In: *Galaxies* 5, p. 17. DOI: 10.3390/galaxies5010017. arXiv: 1606.07790.

Diemand, J., B. Moore, and J. Stadel (2004). "Convergence and scatter of cluster density profiles". In: *MNRAS* 353, pp. 624–632. DOI: 10.1111/j.1365-2966.2004.08094.x. eprint: astro-ph/0402267.

Donato, F. et al. (2009). "A constant dark matter halo surface density in galaxies". In: *MNRAS* 397, pp. 1169–1176. DOI: 10.1111/j.1365-2966.2009.15004.x. arXiv: 0904.4054.

Einasto, J., A. Kaasik, and E. Saar (1974). "Dynamic evidence on massive coronas of galaxies". In: *Nature* 250, pp. 309–310. DOI: 10.1038/250309a0.

Einasto, J. et al. (1974). "Missing mass around galaxies - Morphological evidence". In: *Nature* 252, pp. 111–113. DOI: 10.1038/252111a0.

Faber, S. M. and J. S. Gallagher (1979). "Masses and mass-to-light ratios of galaxies". In: *ARA&A* 17, pp. 135–187. DOI: 10.1146/annurev.aa.17.090179.001031.

Ferrarese, L. (2002). "Beyond the Bulge: A Fundamental Relation between Supermassive Black Holes and Dark Matter Halos". In: *ApJ* 578, pp. 90–97. DOI: 10.1086/342308. eprint: astro-ph/0203469.

Ferrarese, L. and D. Merritt (2000). "A Fundamental Relation between Supermassive Black Holes and Their Host Galaxies". In: *ApJ* 539, pp. L9–L12. DOI: 10.1086/312838. eprint: astro-ph/0006053.

Gao, J. G., M. Merafina, and R. Ruffini (1990). "The semidegenerate configurations of a selfgravitating system of fermions". In: *A&A* 235, pp. 1–7.

Gebhardt, K. et al. (2000). "A Relationship between Nuclear Black Hole Mass and Galaxy Velocity Dispersion". In: *ApJ* 539, pp. L13–L16. DOI: 10.1086/312840. eprint: astro-ph/0006289.

Genzel, R., F. Eisenhauer, and S. Gillessen (2010). "The Galactic Center massive black hole and nuclear star cluster". In: *Reviews of Modern Physics* 82, pp. 3121–3195. DOI: 10.1103/RevModPhys.82.3121. arXiv: 1006.0064.

Gershtein, S. S. and Y. B. Zel'dovich (1966). "Rest Mass of Muonic Neutrino and Cosmology". In: *Soviet Journal of Experimental and Theoretical Physics Letters* 4, pp. 120–122.

Gibbons, S. L. J., V. Belokurov, and N. W. Evans (2014). "'Skinny Milky Way please', says Sagittarius". In: *MNRAS* 445, pp. 3788–3802. DOI: 10.1093/mnras/stu1986. arXiv: 1406.2243.

Gillessen, S. et al. (2009a). "Monitoring Stellar Orbits Around the Massive Black Hole in the Galactic Center". In: *ApJ* 692, pp. 1075–1109. DOI: 10.1088/0004-637X/692/2/1075. arXiv: 0810.4674.

Gillessen, S. et al. (2009b). "The Orbit of the Star S2 Around SGR A* from Very Large Telescope and Keck Data". In: *ApJ* 707, pp. L114–L117. DOI: 10.1088/0004-637X/707/2/L114. arXiv: 0910.3069.

Gnedin, O. Y. and J. R. Primack (2004). "Dark Matter Profile in the Galactic Center". In: *Physical Review Letters* 93.6, 061302, p. 061302. DOI: 10.1103/PhysRevLett.93.061302. eprint: astro-ph/0308385.

Gómez, L. G. and J. A. Rueda (2017). "Dark matter dynamical friction versus gravitational wave emission in the evolution of compact-star binaries". In: *Phys. Rev. D* 96.6, 063001, p. 063001. DOI: 10.1103/PhysRevD.96.063001. arXiv: 1706.06801.

Gómez, L. G. et al. (2016). "Strong lensing by fermionic dark matter in galaxies". In: *Phys. Rev. D* 94.12, 123004, p. 123004. DOI: 10.1103/PhysRevD.94.123004. arXiv: 1610.03442.

Gondolo, P. and J. Silk (1999). "Dark Matter Annihilation at the Galactic Center". In: *Physical Review Letters* 83, pp. 1719–1722. DOI: 10.1103/PhysRevLett.83.1719. eprint: astro-ph/9906391.

Gonzalez-Garcia, M. C. and Y. Nir (2003). "Neutrino masses and mixing: evidence and implications". In: *Reviews of Modern Physics* 75, pp. 345–402. DOI: 10.1103/RevModPhys.75.345. eprint: hep-ph/0202058.

Greene, J. E. et al. (2010). "Precise Black Hole Masses from Megamaser Disks: Black Hole-Bulge Relations at Low Mass". In: *ApJ* 721, pp. 26–45. DOI: 10.1088/0004-637X/721/1/26. arXiv: 1007.2851.

Gültekin, K. et al. (2009). "The M-σ and M-L Relations in Galactic Bulges, and Determinations of Their Intrinsic Scatter". In: *ApJ* 698, pp. 198–221. DOI: 10.1088/0004-637X/698/1/198. arXiv: 0903.4897 [astro-ph.GA].

Haller, J. W. et al. (1996). "Stellar Kinematics and the Black Hole in the Galactic Center". In: *ApJ* 456, p. 194. DOI: 10.1086/176640.

Hannestad, S. (2010). "Neutrino physics from precision cosmology". In: *Progress in Particle and Nuclear Physics* 65, pp. 185–208. DOI: 10.1016/j.ppnp.2010.07.001. arXiv: 1007.0658 [hep-ph].

Hawking, S. W. (1975). "Particle creation by black holes". In: *Communications in Mathematical Physics* 43, pp. 199–220. DOI: 10.1007/BF02345020.

Hernquist, L. (1990). "An analytical model for spherical galaxies and bulges". In: *ApJ* 356, pp. 359–364. DOI: 10.1086/168845.

Hinshaw, G. et al. (2013). "Nine-year Wilkinson Microwave Anisotropy Probe (WMAP) Observations: Cosmological Parameter Results". In: *ApJS* 208, 19, p. 19. DOI: 10.1088/0067-0049/208/2/19. arXiv: 1212.5226.

Hoekstra, H. et al. (2005). "Virial Masses and the Baryon Fraction in Galaxies". In: *ApJ* 635, pp. 73–85. DOI: 10.1086/496913. eprint: astro-ph/0510097.

Hu, W., R. Barkana, and A. Gruzinov (2000). "Fuzzy Cold Dark Matter: The Wave Properties of Ultralight Particles". In: *Physical Review Letters* 85, pp. 1158–1161. DOI: 10.1103/PhysRevLett.85.1158. eprint: astro-ph/0003365.

Hui, L. et al. (2017). "Ultralight scalars as cosmological dark matter". In: *Phys. Rev. D* 95.4, 043541, p. 043541. DOI: 10.1103/PhysRevD.95.043541. arXiv: 1610.08297.

Humphrey, P. J. et al. (2006). "A Chandra View of Dark Matter in Early-Type Galaxies". In: *ApJ* 646, pp. 899–918. DOI: 10.1086/505019. eprint: astro-ph/0601301.

Ingrosso, G. et al. (1992). "System of self-gravitating semidegenerate fermions with a cutoff of energy and angular momentum in their distribution function". In: *A&A* 258, pp. 223–233.

Iocco, F., M. Pato, and G. Bertone (2015). "Evidence for dark matter in the inner Milky Way". In: *Nature Physics* 11, pp. 245–248. DOI: 10.1038/nphys3237. arXiv: 1502.03821.

Irwin, M. and D. Hatzidimitriou (1995). "Structural parameters for the Galactic dwarf spheroidals". In: *MNRAS* 277, pp. 1354–1378. DOI: 10.1093/mnras/277.4.1354.

Jeans, J. H. (1922). "The Motions of Stars in a Kapteyn Universe". In: *MNRAS* 82, pp. 122–132. DOI: 10.1093/mnras/82.3.122.

Kalinova, V. et al. (2017). "Towards a new classification of galaxies: principal component analysis of CALIFA circular velocity curves". In: *MNRAS* 469, pp. 2539–2594. DOI: 10.1093/mnras/stx901. arXiv: 1509.03352.

Karachentsev, I. D. et al. (2004). "A Catalog of Neighboring Galaxies". In: *AJ* 127, pp. 2031–2068. DOI: 10.1086/382905.

Katz, H. et al. (2016). "Testing Feedback-Modified Dark Matter Haloes with Galaxy Rotation Curves: Estimation of Halo Parameters and Consistency with ΛCDM". In: *ArXiv e-prints*. arXiv: 1605.05971.

Keller, B. W. and J. W. Wadsley (2016). "{\Lambda} CDM is Fully Consistent with SPARC Acceleration Law". In: *ArXiv e-prints*. arXiv: 1610.06183.

King, I. R. (1966). "The structure of star clusters. III. Some simple dynamical models". In: *AJ* 71, p. 64. DOI: 10.1086/109857.

King, I. (1962). "The structure of star clusters. I. an empirical density law". In: *AJ* 67, p. 471. DOI: 10.1086/108756.

Klein, O. (1949). "On the Thermodynamical Equilibrium of Fluids in Gravitational Fields". In: *Reviews of Modern Physics* 21, pp. 531–533. DOI: 10.1103/RevModPhys.21.531.

Klypin, A. et al. (1999). "Where Are the Missing Galactic Satellites?" In: *ApJ* 522, pp. 82–92. DOI: 10.1086/307643. eprint: astro-ph/9901240.

Kormendy, J. and R. Bender (2011). "Supermassive black holes do not correlate with dark matter haloes of galaxies". In: *Nature* 469, pp. 377–380. DOI: 10.1038/nature09695. arXiv: 1101.4650.

Kuzio de Naray, R. and T. Kaufmann (2011). "Recovering cores and cusps in dark matter haloes using mock velocity field observations". In: *MNRAS* 414, pp. 3617–3626. DOI: 10.1111/j.1365-2966.2011.18656.x. arXiv: 1012.3471.

Lee, B. W. and S. Weinberg (1977). "Cosmological lower bound on heavy-neutrino masses". In: *Physical Review Letters* 39, pp. 165–168. DOI: 10.1103/PhysRevLett.39.165.

Lelli, F., S. S. McGaugh, and J. M. Schombert (2016). "SPARC: Mass Models for 175 Disk Galaxies with Spitzer Photometry and Accurate Rotation Curves". In: *AJ* 152, 157, p. 157. DOI: 10.3847/0004-6256/152/6/157. arXiv: 1606.09251.

Lelli, F. et al. (2017). "One Law to Rule Them All: The Radial Acceleration Relation of Galaxies". In: *ApJ* 836, 152, p. 152. DOI: 10.3847/1538-4357/836/2/152. arXiv: 1610.08981.

Lisanti, M. (2017). "Lectures on Dark Matter Physics". In: *New Frontiers in Fields and Strings (TASI 2015) - Proceedings of the 2015 Theoretical Advanced Study Institute in Elementary Particle Physics. Edited by POLCHINSKI JOSEPH ET AL. Published by World Scientific Publishing Co. Pte. Ltd., 2017. ISBN #9789813149441, pp. 399-446*. Ed. by J. Polchinski and et al., pp. 399–446. DOI: 10.1142/9789813149441_0007. arXiv: 1603.03797 [hep-ph].

Lobanov, A. (2017). "Beyond the event horizon or altogether without it?" In: *Nature Astronomy* 1, 0069, p. 0069. DOI: 10.1038/s41550-017-0069.

Longair, M. S. (2008). *Galaxy Formation*.

Lovell, M. R. et al. (2012). "The haloes of bright satellite galaxies in a warm dark matter universe". In: *MNRAS* 420, pp. 2318–2324. DOI: 10.1111/j.1365-2966.2011.20200.x. arXiv: 1104.2929.

Lynden-Bell, D. (1967). "Statistical mechanics of violent relaxation in stellar systems". In: *MNRAS* 136, p. 101. DOI: 10.1093/mnras/136.1.101.

Lynden-Bell, D. and R. M. Lynden-Bell (1977). "On the negative specific heat paradox". In: *MNRAS* 181, pp. 405–419. DOI: 10.1093/mnras/181.3.405.

— (1995). "Ghostly streams from the formation of the Galaxy's halo". In: *MNRAS* 275, pp. 429–442. DOI: 10.1093/mnras/275.2.429.

Lynden-Bell, D. and M. J. Rees (1971). "On quasars, dust and the galactic centre". In: *MNRAS* 152, p. 461. DOI: 10.1093/mnras/152.4.461.

Lynden-Bell, D. and R. Wood (1968). "The gravo-thermal catastrophe in isothermal spheres and the onset of red-giant structure for stellar systems". In: *MNRAS* 138, p. 495. DOI: 10.1093/mnras/138.4.495.

Marrodán Undagoitia, T. and L. Rauch (2016). "Dark matter direct-detection experiments". In: *Journal of Physics G Nuclear Physics* 43.1, 013001, p. 013001. DOI: 10.1088/0954-3899/43/1/013001. arXiv: 1509.08767 [physics.ins-det].

McGaugh, S. S. (2004). "The Mass Discrepancy-Acceleration Relation: Disk Mass and the Dark Matter Distribution". In: *ApJ* 609, pp. 652–666. DOI: 10.1086/421338. eprint: astro-ph/0403610.

McGaugh, S. S., F. Lelli, and J. M. Schombert (2016a). "Radial Acceleration Relation in Rotationally Supported Galaxies". In: *Physical Review Letters* 117.20, 201101, p. 201101. DOI: 10.1103/PhysRevLett.117.201101. arXiv: 1609.05917.

McGaugh, S. S. et al. (2000). "The Baryonic Tully-Fisher Relation". In: *ApJ* 533, pp. L99–L102. DOI: 10.1086/312628. eprint: astro-ph/0003001.

McGaugh, S. (2014). "The Third Law of Galactic Rotation". In: *Galaxies* 2, pp. 601–622. DOI: 10.3390/galaxies2040601. arXiv: 1412.3767.

McGaugh, S., F. Lelli, and J. Schombert (2016b). "The Radial Acceleration Relation in Rotationally Supported Galaxies". In: *ArXiv e-prints*. arXiv: 1609.05917.

Merafina, M. and R. Ruffini (1989). "Systems of selfgravitating classical particles with a cutoff in their distribution function". In: *A&A* 221, pp. 4–19.

Michie, R. W. (1963). "On the distribution of high energy stars in spherical stellar systems". In: *MNRAS* 125, p. 127.

Milgrom, M. (1983a). "A Modification of the Newtonian Dynamics - Implications for Galaxy Systems". In: *ApJ* 270, p. 384. DOI: 10.1086/161132.

— (1983b). "A modification of the Newtonian dynamics - Implications for galaxies". In: *ApJ* 270, pp. 371–389. DOI: 10.1086/161131.

— (1983c). "A modification of the Newtonian dynamics as a possible alternative to the hidden mass hypothesis". In: *ApJ* 270, pp. 365–370. DOI: 10.1086/161130.

Navarro, J. F., C. S. Frenk, and S. D. M. White (1996). "The Structure of Cold Dark Matter Halos". In: *ApJ* 462, p. 563. DOI: 10.1086/177173. eprint: astro-ph/9508025.

— (1997). "A Universal Density Profile from Hierarchical Clustering". In: *ApJ* 490, pp. 493–508. eprint: astro-ph/9611107.

Navarro, J. F. et al. (2016). "The origin of the mass discrepancy-acceleration relation in ΛCDM". In: *ArXiv e-prints*. arXiv: 1612.06329.

O'Meara, J. M. et al. (2001). "The Deuterium to Hydrogen Abundance Ratio toward a Fourth QSO: HS 0105+1619". In: *ApJ* 552, pp. 718–730. DOI: 10.1086/320579. eprint: astro-ph/0011179.

Oort, J. H. (1932). "The force exerted by the stellar system in the direction perpendicular to the galactic plane and some related problems". In: *Bull. Astron. Inst. Netherlands* 6, p. 249.

Oppenheimer, J. R. and G. M. Volkoff (1939). "On Massive Neutron Cores". In: *Physical Review* 55, pp. 374–381. DOI: 10.1103/PhysRev.55.374.

Ostriker, J. P. and P. J. E. Peebles (1973). "A Numerical Study of the Stability of Flattened Galaxies: or, can Cold Galaxies Survive?" In: *ApJ* 186, pp. 467–480. DOI: 10.1086/152513.

Padovani, P. et al. (2017). "Active galactic nuclei: what's in a name?" In: *A&A Rev.* 25, 2, p. 2. DOI: 10.1007/s00159-017-0102-9. arXiv: 1707.07134.

Patwardhan, A. V. et al. (2015). "Diluted equilibrium sterile neutrino dark matter". In: *Phys. Rev. D* 92.10, 103509, p. 103509. DOI: 10.1103/PhysRevD.92.103509. arXiv: 1507.01977.

Peebles, P. J. E. (1982). "Primeval adiabatic perturbations - Effect of massive neutrinos". In: *ApJ* 258, pp. 415–424. DOI: 10.1086/160094.

Peter, A. H. G. et al. (2013). "Cosmological simulations with self-interacting dark matter - II. Halo shapes versus observations". In: *MNRAS* 430, pp. 105–120. DOI: 10.1093/mnras/sts535. arXiv: 1208.3026.

Planck Collaboration et al. (2016). "Planck 2015 results. XIII. Cosmological parameters". In: *A&A* 594, A13, A13. DOI: 10.1051/0004-6361/201525830. arXiv: 1502.01589.

Pontecorvo, B. (1958). "Mesonium and Antimesonium". In: *Soviet Journal of Experimental and Theoretical Physics* 6, p. 429.

Portail, M. et al. (2017). "Dynamical modelling of the galactic bulge and bar: the Milky Way's pattern speed, stellar and dark matter mass distribution". In: *MNRAS* 465, pp. 1621–1644. DOI: 10.1093/mnras/stw2819. arXiv: 1608.07954.

Press, W. H. and P. Schechter (1974). "Formation of Galaxies and Clusters of Galaxies by Self-Similar Gravitational Condensation". In: *ApJ* 187, pp. 425–438. DOI: 10.1086/152650.

Read, J. I. (2014). "The local dark matter density". In: *Journal of Physics G Nuclear Physics* 41.6, 063101, p. 063101. DOI: 10.1088/0954-3899/41/6/063101. arXiv: 1404.1938.

Reeves, H. et al. (1973). "On the Origin of Light Elements". In: *ApJ* 179, pp. 909–930. DOI: 10.1086/151928.

Rephaeli, Y. (1982). "Neutrino halos". In: *Phys. Rev. D* 26, pp. 770–774. DOI: 10.1103/PhysRevD.26.770.

Rocha, M. et al. (2013). "Cosmological simulations with self-interacting dark matter - I. Constant-density cores and substructure". In: *MNRAS* 430, pp. 81–104. DOI: 10.1093/mnras/sts514. arXiv: 1208.3025.

Romanowsky, A. J. and C. S. Kochanek (2001). "Dynamics of Stars and Globular Clusters in M87". In: *ApJ* 553, pp. 722–732. DOI: 10.1086/320947. eprint: astro-ph/0008062.

Rubin, V. C. and W. K. Ford Jr. (1970). "Rotation of the Andromeda Nebula from a Spectroscopic Survey of Emission Regions". In: *ApJ* 159, p. 379. DOI: 10.1086/150317.

Rubin, V. C., W. K. Ford Jr., and N. Thonnard (1980). "Rotational properties of 21 SC galaxies with a large range of luminosities and radii, from NGC 4605 /R = 4kpc/ to UGC 2885 /R = 122 kpc/". In: *ApJ* 238, pp. 471–487. DOI: 10.1086/158003.

Ruffini, R., C. R. Argüelles, and J. A. Rueda (2015). "On the core-halo distribution of dark matter in galaxies". In: *MNRAS* 451, pp. 622–628. DOI: 10.1093/mnras/stv1016. arXiv: 1409.7365.

Ruffini, R. and S. Bonazzola (1969). "Systems of Self-Gravitating Particles in General Relativity and the Concept of an Equation of State". In: *Physical Review* 187, pp. 1767–1783. DOI: 10.1103/PhysRev.187.1767.

Ruffini, R. and L. Stella (1983). "On semi-degenerate equilibrium configurations of a collisionless self-gravitating Fermi gas". In: *A&A* 119, pp. 35–41.

Salpeter, E. E. (1964). "Accretion of Interstellar Matter by Massive Objects." In: *ApJ* 140, pp. 796–800. DOI: 10.1086/147973.

Salucci, P. (2016). "Dark Matter Strikes Back". In: *ArXiv e-prints*. arXiv: 1612.08857.

Salucci, P. et al. (2010). "The dark matter density at the Sun's location". In: *A&A* 523, A83, A83. DOI: 10.1051/0004-6361/201014385. arXiv: 1003.3101.

Sanders, R. H. (1992). "The case against a massive black hole at the Galactic Centre". In: *Nature* 359, p. 131. DOI: 10.1038/359131a0.

Schramm, D. N. and G. Steigman (1981). "Relic Neutrinos and the Density of the Universe". In: *ApJ* 243, p. 1. DOI: 10.1086/158559.

Shapiro, S.L. and S.A. Teukolsky (2008). *Black Holes, White Dwarfs and Neutron Stars: The Physics of Compact Objects*. Wiley. ISBN: 978-3-527-61767-8. URL: https://books.google.it/books?id=CB2kZ-vMhaoC.

Shaposhnikov, M. (2009). "Baryon Asymmetry of the Universe and Neutrinos". In: *Progress of Theoretical Physics* 122, pp. 185–203. DOI: 10.1143/PTP.122.185.

Shi, X. and G. M. Fuller (1999). "New Dark Matter Candidate: Nonthermal Sterile Neutrinos". In: *Physical Review Letters* 82, pp. 2832–2835. DOI: 10.1103/PhysRevLett.82.2832. eprint: astro-ph/9810076.

Silk, J. and M. J. Rees (1998). "Quasars and galaxy formation". In: *A&A* 331, pp. L1–L4. eprint: astro-ph/9801013.

Siutsou, I., C. R. Argüelles, and R. Ruffini (2015). "Dark matter massive fermions and Einasto profiles in galactic haloes". In: *Astronomy Reports* 59, pp. 656–666. DOI: 10.1134/S1063772915070124. arXiv: 1402.0695.

Sofue, Y. (2012). "Grand Rotation Curve and Dark Matter Halo in the Milky Way Galaxy". In: *PASJ* 64, 75, p. 75. DOI: 10.1093/pasj/64.4.75. arXiv: 1110.4431.

— (2013). "Rotation Curve and Mass Distribution in the Galactic Center - From Black Hole to Entire Galaxy". In: *PASJ* 65, p. 118. DOI: 10.1093/pasj/65.6.118. arXiv: 1307.8241 [astro-ph.GA].

Spergel, D. N. and P. J. Steinhardt (2000). "Observational Evidence for Self-Interacting Cold Dark Matter". In: *Physical Review Letters* 84, pp. 3760–3763. DOI: 10.1103/PhysRevLett.84.3760. eprint: astro-ph/9909386.

Stasielak, J., P. L. Biermann, and A. Kusenko (2007). "Sterile Neutrinos and Structure Formation". In: *Acta Physica Polonica B* 38, p. 3869. arXiv: 0710.5431.

Steigman, G. (2006). "Primordial Nucleosynthesis:. Successes and Challenges". In: *International Journal of Modern Physics E* 15, pp. 1–35. DOI: 10.1142/S0218301306004028. eprint: astro-ph/0511534.

Strigari, L. E. et al. (2008). "A common mass scale for satellite galaxies of the Milky Way". In: *Nature* 454, pp. 1096–1097. DOI: 10.1038/nature07222. arXiv: 0808.3772.

Tollerud, E. J. et al. (2008). "Hundreds of Milky Way Satellites? Luminosity Bias in the Satellite Luminosity Function". In: *ApJ* 688, 277-289, pp. 277–289. DOI: 10.1086/592102. arXiv: 0806.4381.

Tolman, R. C. and P. Ehrenfest (1930). "Temperature Equilibrium in a Static Gravitational Field". In: *Physical Review* 36, pp. 1791–1798. DOI: 10.1103/PhysRev.36.1791.

Tremaine, S. and J. E. Gunn (1979). "Dynamical role of light neutral leptons in cosmology". In: *Physical Review Letters* 42, pp. 407–410. DOI: 10.1103/PhysRevLett.42.407.

Tsiklauri, D. and R. D. Viollier (1998). "Dark Matter Concentration in the Galactic Center". In: *ApJ* 500, pp. 591–595. DOI: 10.1086/305753. eprint: astro-ph/9805273.

Tulin, S. and H.-B. Yu (2018). "Dark matter self-interactions and small scale structure". In: *Phys. Rep.* 730, pp. 1–57. DOI: 10.1016/j.physrep.2017.11.004. arXiv: 1705.02358 [hep-ph].

Tully, R. B. and J. R. Fisher (1977). "A new method of determining distances to galaxies". In: *A&A* 54, pp. 661–673.

Turner, M. S. (2003). "Dark Matter and Dark Energy: The Critical Questions". In: *Hubble's Science Legacy: Future Optical/Ultraviolet Astronomy from Space*. Ed. by K. R. Sembach et al. Vol. 291. Astronomical Society of the Pacific Conference Series, p. 253. eprint: astro-ph/0207297.

Valluri, M. et al. (2005). "The Low End of the Supermassive Black Hole Mass Function: Constraining the Mass of a Nuclear Black Hole in NGC 205 via Stellar Kinematics". In: *ApJ* 628, pp. 137–152. DOI: 10.1086/430752. eprint: astro-ph/0502493.

Vasiliev, E. and M. Zelnikov (2008). "Dark matter dynamics in the galactic center". In: *Phys. Rev. D* 78.8, 083506, p. 083506. DOI: 10.1103/PhysRevD.78.083506. arXiv: 0803.0002.

Walker, M. G. et al. (2009). "A Universal Mass Profile for Dwarf Spheroidal Galaxies?" In: *ApJ* 704, pp. 1274–1287. DOI: 10.1088/0004-637X/704/2/1274. arXiv: 0906.0341 [astro-ph.CO].

White, S. D. M., C. S. Frenk, and M. Davis (1983). "Clustering in a neutrino-dominated universe". In: *ApJ* 274, pp. L1–L5. DOI: 10.1086/184139.

Zwicky, F. (1933). "Die Rotverschiebung von extragalaktischen Nebeln". In: *Helvetica Physica Acta* 6, pp. 110–127.

— (1937). "On the Masses of Nebulae and of Clusters of Nebulae". In: *ApJ* 86, p. 217. DOI: 10.1086/143864.

de Blok, W. J. G. (2010). "The Core-Cusp Problem". In: *Advances in Astronomy* 2010, 789293, p. 789293. DOI: 10.1155/2010/789293. arXiv: 0910.3538.

de Blok, W. J. G., A. Bosma, and S. McGaugh (2003). "Simulating observations of dark matter dominated galaxies: towards the optimal halo profile". In: *MNRAS*

340, pp. 657–678. DOI: 10.1046/j.1365-8711.2003.06330.x. eprint: astro-ph/0212102.

de Blok, W. J. G. et al. (2001). "Mass Density Profiles of Low Surface Brightness Galaxies". In: *ApJ* 552, pp. L23–L26. DOI: 10.1086/320262. eprint: astro-ph/0103102.

de Blok, W. J. G. et al. (2008). "High-Resolution Rotation Curves and Galaxy Mass Models from THINGS". In: *AJ* 136, 2648, pp. 2648–2719. DOI: 10.1088/0004-6256/136/6/2648. arXiv: 0810.2100.

van den Bosch, F. C. and R. A. Swaters (2001). "Dwarf galaxy rotation curves and the core problem of dark matter haloes". In: *MNRAS* 325, pp. 1017–1038. DOI: 10.1046/j.1365-8711.2001.04456.x. eprint: astro-ph/0006048.

van den Bosch, F. C. et al. (2000). "Constraints on the Structure of Dark Matter Halos from the Rotation Curves of Low Surface Brightness Galaxies". In: *AJ* 119, pp. 1579–1591. DOI: 10.1086/301315. eprint: astro-ph/9911372.

Acknowledgments

I warmly thank my family for all their unconditional support. They have contributed with a trustfully and solid basis to my personal development. I warmly thank also my dearest friends. They maintained our friendship regularly despite the long distance.

Thanks to the PhD I met beautiful people all over the world. Many joint activities tightened the relationship and I am happy that during this time I found new friends. Friends, who gave me the feeling of a second home.

An important acknowledgments belongs to my supervisor Carlos (a.k.a. Charly). Without any doubt, his great enthusiasm for DM and galactic structures rubbed on me. I thank him for a smooth introduction in this complex and fascinating topic as well as a fruitful support during all the time. I am glad I had the opportunity to combine many of my interests with a constitutive contribution to the scientific community.

I would like to devote my special thanks to everybody who contributes to a comfortable hospitality. In particular, for visitors from a foreign country. This friendly gesture makes the world clearly a better place.

Finally, I have to note that the PhD would be not possible without the financial support by the Erasmus Mundus Joint Doctorate Program by Grants Number 2014-0707 from the agency EACEA of the European Commission.